

# Impact of High Electric Fields on the Behavior of Water Droplets under Various Ambient Conditions: Experiments and Theory

Vom Fachbereich Maschinenbau  
an der Technischen Universität Darmstadt  
zur  
Erlangung des Grades eines Doktor-Ingenieurs (Dr.-Ing.)  
genehmigte

D i s s e r t a t i o n

vorgelegt von

**Jens-Michael Löwe, M.Sc.**

aus Bad Soden am Taunus, Deutschland

Berichterstatter:	Prof. Dr.-Ing. C. Tropea
Mitberichterstatter:	Prof. Dr.-Ing. V. Hinrichsen
	Prof. Dr. rer. nat. S. Hardt
Tag der Einreichung:	05.10.2021
Tag der mündlichen Prüfung:	22.02.2022

Darmstadt 2022  
D17 (Diss. Darmstadt)

Löwe, Jens-Michael:

Impact of High Electric Fields on the Behavior of Water Droplets under Various Ambient Conditions: Experiments and Theory  
Darmstadt, Technische Universität Darmstadt

Jahr der Veröffentlichung: 2022

Veröffentlichung der Dissertation auf TUprints:

URN: urn:nbn:de:tuda-tuprints-208834

URI: <https://tuprints.ulb.tu-darmstadt.de/id/eprint/20883>

Tag der mündlichen Prüfung: 22. Februar 2022



Veröffentlicht unter CC BY-NC-SA 4.0 International:  
Namensnennung - Keine kommerzielle Nutzung - Weitergabe unter gleichen Bedingungen

*Dedicated to my family and friends.*

*What we know is a drop, what we don't know is an ocean.*  
(Sir Isaac Newton, 1643 - 1727)



Hiermit versichere ich, die vorliegende Doktorarbeit unter der Betreuung von Prof. Dr.-Ing. C. Tropea und Prof. Dr.-Ing. V. Hinrichsen nur mit den in ihr angegebenen Hilfsmitteln und Quellen selbstständig angefertigt zu haben (§9 Abs.1 PO/AT). Die Arbeit hat bisher noch nicht zu Prüfungszwecken gedient (§9 Abs.2 PO/AT). Außerdem versichere ich, dass die vorgelegte elektronische mit der schriftlichen Version der Dissertation übereinstimmt (§8 Abs.1 lit. c PO/AT) und zu einem vorherigen Zeitpunkt noch keine Promotion versucht wurde (§8 Abs.1 lit. d PO/AT).

Darmstadt, den 05. Oktober 2021



# Abstract

The interaction of water droplets and electric fields is present in various applications like electrowetting, electrostatic lenses or high-voltage composite insulators. Depending on the application, the electric field is used to actively control the behaviour of the liquid as for example for electrostatic lenses, or is only considered as a boundary condition which has a negative influence on, as for instance, the properties of high-voltage composite insulators. The understanding of the underlying physical mechanisms is essential to predict and control the behaviour of liquids under the impact of electric fields. Even though the general behaviour of water under the impact of constant, alternating and transient electric fields was already investigated experimentally, theoretical and numerically in the past, the influence of electric charges on the behaviour of water droplets or the interaction of nearby droplets under the impact of transient electric fields are still not completely clear. It is well known that water droplets are significantly influenced by external electric fields, resulting in oscillations or deformations. Hence, the presence of electric fields might indirectly impact other physical mechanism like ice nucleation, which is controversially discussed and not unambiguously proven.

The present work aims to expand the knowledge of the impact of electric fields on sessile droplets under various ambient conditions. Therefore, the influence of electric charges on the motion of single droplets and the inception field strength for electrical partial discharges for single and multiple droplets are experimentally investigated depending on the electric field strength, droplet volume as well as frequency of the electric field. The oscillation behaviour and partial discharge inception of water droplets are significantly influenced by electric charges. In addition, the interaction of nearby droplets under the impact of transient electric fields is determined and the behaviour is categorized depending on the influencing factors.

Furthermore, it is confirmed that heterogeneous ice nucleation can be clearly promoted by the presence of electric fields. While constant electric fields have an almost negligible influence, alternating and transient electric fields significantly promote ice nucleation depending on the frequency, type and strength of the electric field.

This present experimental work expands the understanding of the impact of electric fields on water droplets under various boundary conditions and might help to improve and optimize applications like the operation of high-voltage composite insulators at ambient and cold conditions.



# Kurzfassung

Die Interaktion von Wassertropfen und elektrischen Feldern beeinflusst viele technischen Anwendungen wie z. B. elektrostatische Linsen oder Verbundisolatoren. Dabei können elektrische Felder aktiv zum gezielten Kontrollieren von Flüssigkeiten genutzt werden (z. B. elektrostatische Linsen) oder nehmen passiv und ggf. ungewollt Einfluss auf die Anwendung (z. B. Alterung von Verbundisolatoren). Die Kenntnis der zugrunde liegenden physikalischen Mechanismen ist essenziell für Verständnis des Verhaltens von Flüssigkeiten unter Einfluss elektrischer Felder. Obwohl das Verhalten von Wassertropfen unter Einfluss konstanter, alternierender und transientser elektrischer Felder bereits theoretisch, numerisch sowie experimentell untersucht wurde, ist beispielsweise der Einfluss der elektrischen Ladung oder die Koaleszenz von Tropfen unter Einfluss transienter elektrischer Felder bisher nicht ausreichend erforscht. Aufgrund der Interaktion zwischen elektrischen Feldern und Wassertropfen, die zu Oszillationen oder Deformation der Wassertropfen führen können, werden möglicherweise auch weitere physikalische Mechanismen wie die Eisnukleation beeinflusst. Dieser Einfluss wird jedoch kontrovers in bestehender Literatur diskutiert und ist bisher nicht eindeutig bestätigt.

Der Fokus dieser Arbeit ist die Untersuchung des Einflusses elektrischer Felder auf das Verhalten von Wassertropfen unter verschiedensten Umgebungsbedingungen. Dazu wurde der Einfluss elektrischer Ladung auf das Verhalten einzelner und mehrerer Wassertropfen in elektrischen Feldern sowie deren Einsetzfeldstärke für Teilentladungen experimentell unter Berücksichtigung der Feldstärke, Frequenz, elektrischen Ladung, Tropfeninteraktion und des Tropfenvolumens untersucht. Besonders elektrische Ladungen beeinflussen das Verhalten von Wassertropfen in elektrischen Feldern und das Auftreten von Teilentladungen maßgeblich. Des Weiteren wurde gezeigt, dass heterogene Eisnukleation durch die Präsenz von elektrischen Feldern begünstigt werden kann. Während der Einfluss konstanter elektrischer Felder auf die Eisnukleation vernachlässigbar gering ist, haben alternierende und transiente elektrische Felder in Abhängigkeit der Frequenz, des Typs sowie der Stärke des elektrischen Feldes einen großen Einfluss und begünstigen das Gefrieren von Wasser.

Diese umfassende experimentelle Arbeit erweitert das Verständnis des Einflusses elektrischer Felder auf Wassertropfen unter verschiedensten Umgebungsbedingungen und kann somit zur Optimierung von Anwendungen wie z. B. dem Betrieb von Verbundisolatoren beitragen.



# Acknowledgments

This work would not be possible without the continuous support and assistance of my supervisors, colleagues, friends and family throughout my entire work at the *High-Voltage Laboratories* at the *Technical University of Darmstadt*. Their support significantly contributed to the existence, quality and success of this work. I am very grateful for the opportunity to accomplish a doctorate and I would like to use this chance to thank in particular:

**Prof. Dr.-Ing. Cameron Tropea** for the continuous support and supervision during doctorate. I enjoyed working together and appreciate his expertise and professional experience from that I could benefit in various situations. Furthermore, without his commitment and confidence in my personal performance I would not have had the opportunity to work at the *High-Voltage Laboratories* at the *Technical University Darmstadt*. The interdisciplinary work and occurring challenges enabled me to broaden my expertise and get to know other points of view.

**Prof. Dr.-Ing. Volker Hinrichsen** for the opportunity to work at the *High-Voltage Laboratories* at the *Technical University of Darmstadt* and his steady trust in my performance and ability. His support throughout my doctorate significantly contributed to the success of this work. Particularly, I valued the delegated responsibility with respect to the research project and the freedom of research which promoted my creativity.

**Prof. Dr. rer. nat. Steffen Hardt** for appraising my work, especially due to the short-term assignment as an appraiser. I really appreciate his expertise and the suggestions to improve this work.

**Apl. Prof. Dr. Ilia Roisman** for his support during my scientific carrier including my academic studies and my doctorate. I highly enjoyed the collaboration and his scientific expertise which significantly contributed to the scientific quality of this work. His ideas always enabled the possibility to generate new solutions to complex scientific problems. In addition, without his engagement, support and trust in my expertise the stay at the *University of Illinois at Chicago* would not have been possible.

**Prof. PhD Alexander Yarin** for facilitating my research period at the *Multiscale Mechanics and Nanotechnology Laboratory* at the *University of Illinois at Chicago*. I appreciate the collaboration with him and his

students which contributed to broadening my scientific and professional experience. The stay in the USA was exciting and a great experience. I always like to remember that time.

The workshop of *High-Voltage Laboratories* and the *Institute of Fluid Mechanics and Aerodynamics* at the *Technical University of Darmstadt*, in particular **Ulrich Veith** and **Christian Homa**. Without their accurate work and support, the experiments could not have been performed. Furthermore, their know-how significantly contributed to the solutions of mechanical, electrical and various other problems.

**Birgit Neuthe, Corinna Neumann, Cornelia Richter-Steinmetz** and **Ulla Brunner** for their support in all administrative matters.

My colleagues and friends at the *Technical University Darmstadt* and *University of Illinois at Chicago* for the beautiful and enjoyable time at the universities. Special thanks go to **Dr.-Ing. Markus Schremb, Dr.-Ing. Maximilian Secklehner, Dr.-Ing. Rashid Hussain, David Chistropher Kothe, Peter Hock, Benjamin Surges, Florian Pabst, Dr.-Ing. Maik Bröker, Christian Dorsch, Jevon Plog** and **PhD Patrick M. Comiskey** for their fruitful discussions and contributions of the various scientific publications as well as the great times besides work. These colleagues are the main reason that I enjoyed my work at the university. In addition, I would like to thank **Dr.-Ing. Daniel Kintea** who supervised my Bachelor and Master theses and taught me the basics of scientific work.

A big thanks goes to all the students I supervised, in particular to **Jan Engelhardt, Franziska Zajonz, David Zöller, Marvin Dietzmann-Kolbe, Henrik Scholz, Johannes Franz Alois Hollerith, Duygu Cicekdagli, Tim Dorau, Moritz Hülsebrock, Patrick Weis** and **Julia Wenzel**, who contributed to this work with their theses and work at the *High-Voltage Laboratories*. Without their participation and dedication the various time-consuming experiments would not have been possible.

I would like to thank the **Deutsche Forschungsgemeinschaft (DFG)** for financial support of the project within the Collaborative Research Centre SFB-TRR 75, Project No. 84292822. I always enjoyed the work at this interdisciplinary project and the scientific knowledge exchange of the several projects during the annual meetings.

Furthermore, I would like to thank my girlfriend **Franziska Schmitt** and all my friends for their continuous support and encouragement. I am

very grateful to have such wonderful people in my life. Especially, I want to acknowledge the contribution of **Jennifer Spicer**, who proofread this work.

Last but not least, I would like to thank my family, especially my mother **Christa Löwe** and my father **Michael Manfred Löwe**. Their enduring support, encouragement and belief in my abilities significantly contributed to my academic achievements and to the quality and success of this work. It is by far the most important contribution. I am very grateful for my family and dedicate this work to them.

Liederbach, den 05.10.2021

Jens-Michael Löwe

The author thanks the International Electrotechnical Commission (IEC) for permission to reproduce Information from its International Standards. All such extracts are copyright of IEC, Geneva, Switzerland. All rights reserved. Further information on the IEC is available from [www.iec.ch](http://www.iec.ch). IEC has no responsibility for the placement and context in which the extracts and contents are reproduced by the author, nor is IEC in any way responsible for the other content or accuracy therein.



# Nomenclature

## Latin letters, lower-case

Symbol	Unit	Meaning
$a$	m	Radius of nucleus
$c$	kg/m <sup>3</sup>	Solubility
$d$	-	Derivative
$d$	m	Diameter
$\vec{e}$	m	Unity vector
$f$	Hz	Frequency
$g$	m <sup>2</sup> /s	Gravitational acceleration
$h$	m	Distance
$i$	-	Variable
$k_b$	m <sup>2</sup> kg/(s <sup>2</sup> K)	Boltzmann constant, $k_b = 1.381 \cdot 10^{-23} \text{ m}^2 \text{ kg}/(\text{s}^2 \text{ K})$
$m$	kg	Mass
$n$	1/m <sup>2</sup>	Nucleation site density
$n_0$	1/m <sup>2</sup>	Initial nucleation site density (singular nucleation model - constant)
$p$	Pa	Pressure
$q$	C/m <sup>3</sup>	Charge density
$r$	m	Coordinate in radial direction
$s$	m	Length
$t$	s	Time
$x$	m	Coordinate in x-direction

Continued on next page

**Latin letters (lower-case) continued from previous page**

<b>Symbol</b>	<b>Unit</b>	<b>Meaning</b>
<i>y</i>	m	Coordinate in y-direction
<i>z</i>	m	Coordinate in z-direction
Concluded		

**Latin letters, upper-case**

<b>Symbol</b>	<b>Unit</b>	<b>Meaning</b>
<i>A</i>	m <sup>2</sup>	Area
<i>B</i>	T, V s/m <sup>2</sup>	Magnetic flux density
<i>C</i>	-	Cluster number
<i>C</i>	F, A s/V	Capacitance
<i>D</i>	C/m <sup>2</sup> , A s/m <sup>2</sup>	Displacement field
<i>D</i>	m <sup>2</sup> /s	Diffusion coefficient
<i>E</i>	V/m	Electric field
<i>F</i>	N	Force
<i>G</i>	J	Gibb's free energy
<i>H</i>	A/m	Magnetic field strength
<i>J</i>	1/(m <sup>3</sup> s)	Nucleation rate
<i>J</i>	A/m <sup>2</sup>	Current density
<i>L<sub>V</sub></i>	J/m <sup>3</sup>	Latent heat of fusion per volume
<i>N</i>	-	Number
Continued on next page		

**Latin letters (upper-case) continued from previous page**

<b>Symbol</b>	<b>Unit</b>	<b>Meaning</b>
$N_A$	1/mol	Avogadro constant, $N_A = 6.022 \cdot 10^{23}$ 1/mol
$\mathcal{N}$	-	Mode number
$\mathcal{P}$	-	Probability
$Q$	C, A s	Charge
$R$	m	Radius
$S$	-	Contact angle function
$\mathcal{S}$	-	Single-sided amplitude spectrum
$T$	K	Temperature
$\mathcal{T}_0$	K	Characteristic temperature (singular nucleation model - constant)
$\dot{T}$	K/min	Cooling rate
$U$	V	Voltage
$\mathcal{U}$	m/s	Velocity
$V$	m <sup>3</sup>	Volume
$W$	J	Work
Concluded		

## Greek letters

Symbol	Unit	Meaning
$\alpha$	$^{\circ}$	Angle
$\Delta$	-	Difference
$\nabla$	-	Nabla operator
$\delta$	-	Small increment
$\partial$	-	Partial derivative
$\varepsilon$	A s/(V m)	Permittivity
$\varepsilon_0$	A s/(V m)	Vacuum permittivity (constant), $\varepsilon_0 = 8.854 \cdot 10^{-12}$ A s/(V m)
$\varepsilon_r$	-	Relative permittivity
$\eta$	N s/m <sup>2</sup>	Dynamic viscosity
$\theta$	$^{\circ}$	Contact angle
$\vartheta$	$^{\circ}$ C	Temperature
$\kappa$	S/m, A/(V m)	Electrical conductivity
$\lambda$	W/(m·K)	Heat conductivity
$\nu$	m <sup>2</sup> /s	Kinematic viscosity
$\xi$	-	Characteristic ratio of electric forces
$\rho$	kg/m <sup>3</sup>	Density
$\gamma$	N/m	Surface/interfacial tension
$\tau$	s	Characteristic time
$\varphi$	$^{\circ}$	Angle in spherical coordinates
$\phi$	V	Electric potential
$\Psi$	-	Function of permittivities
$\omega$	1/s	Angular frequency

Concluded

## Dimensionless groups

Symbol	Name	Definition and Meaning
$B_o$	Bond number	$B_o = \frac{\rho g d_d}{\gamma} \hat{=} \frac{\text{Force of gravity}}{\text{Force of surface tension}}$
$B_{o_{el}}$	Electrical Bond number	$B_{o_{el}} = \frac{\varepsilon_0 U^2}{\gamma h_{d-d}} \hat{=} \frac{\text{Force of electric field}}{\text{Force of surface tension}}$
$\xi$	Charac. ratio of electric forces	$\xi = \frac{Q}{\varepsilon_0 E d_d^2} \hat{=} \frac{\text{Coulomb force}}{\text{Dielectr./electrostr. force}}$
Concluded		

## Superscripts

Superscripts	Meaning
$\wedge$	Amplitude
$-$	Mean value
$\rightarrow$	Vector (in combination with bold symbol)
$*$	Critical/onset quantity
$\sim$	Test quantity
$\cdot$	Derivation with respect to time
$  $	Norm/Strength of vector quantity
Concluded	

## Subscripts

Subscripts	Meaning
0	Reference/initial condition
A	Avogadro
AC	Alternating current
adv	Advancing
air	Air
app	Apparent
b	Boltzmann
bub	Bubble
cer	Ceramic
char	Characteristic
DC	Direct current
d	Droplet
d-d	Droplet-droplet
el	Electrical
ep	Epoxy
F	Front
g	Gas
gel	Gelatin
gla	Glass
gly	Glycerol

Continued on next page

**Subscripts continued from previous page**

<b>Subscripts</b>	<b>Meaning</b>
gro	Groove
het	Heterogeneous
hole	Hole
hom	Homogeneous
ice	Ice
in	Inception
<i>l</i>	Liquid
left	Left
life	Lifetime
m	Melting
max	Maximum
min	Minimum
mix	Mixture
mol	Molecule
n	Normal
nuc	Nucleation
oil	Oil
PD	Partial discharge
pot	Potential
proj	Projected
rec	Receding
r	Relative
right	Right

Continued on next page

**Subscripts continued from previous page**

<b>Subscripts</b>	<b>Meaning</b>
RMS	Root mean square
rod	Rod
s	Solid
sil	Silicone
single	Single
si	Site
surf	Surface
surr	Surrounding
T	Tail
t	Tangential
tar	Target
tot	Total
two	Two
w	Wall/Substrate
wet	Wetted
wa	Water

Concluded

# Abbreviations

Abbreviation	Meaning
AC	Alternating current
App.	Appendix
CAD	Computer aided design
Chap.	Chapter
Charac.	Characteristic
CNT	Classical nucleation theory
DC	Direct current
Dielectr.	Dielectric
Elec.	Electric
Electrostr.	Electrostrictive
EQS	Electro quasi-static
FFT	Fast Fourier Transformation
ID	(Droplet) Identification number
IEC	International Electrotechnical Commission
INP	Ice nucleating particle
INPs	Ice nucleating particles
LED	Light emitting diode
LI	Lightning impulse
PD	Electrical partial discharge
PEEK	Polyetheretherketone
PMMA	Poly(methylmethacrylate)
SAPPHIRE	Semi-automatic APPAratus for High-voltage Ice nucleation REsearch

Continued on next page

**Abbreviations continued from previous page**

<b>Abbreviation</b>	<b>Meaning</b>
Sec.	Section
Subsec.	Subsection
SI	Switching impulse
Concluded	

# Contents

<b>Abstract</b>	<b>i</b>
<b>Kurzfassung</b>	<b>iii</b>
<b>Acknowledgements</b>	<b>v</b>
<b>Nomenclature</b>	<b>ix</b>
<b>I Opening</b>	<b>1</b>
<b>1 Introduction</b>	<b>3</b>
1.1 Motivation . . . . .	4
1.2 Aims and outline of thesis . . . . .	7
<b>II Fundamentals</b>	<b>9</b>
<b>2 Hydrodynamic and electrohydrodynamic phenomena</b>	<b>11</b>
2.1 Sessile droplets . . . . .	11
2.2 The electric field . . . . .	16
2.3 Microscopic interaction of sessile droplets and electric fields	24
2.4 Macroscopic interaction of sessile droplets and the electric field . . . . .	29
<b>3 Ice nucleation</b>	<b>41</b>
3.1 Homogeneous ice nucleation . . . . .	42
3.2 Heterogeneous ice nucleation . . . . .	49
3.3 Ice nucleation models . . . . .	53
3.3.1 Classical (stochastic) nucleation model . . . . .	54
3.3.2 Singular nucleation model . . . . .	56
3.3.3 Further nucleation models . . . . .	57
3.4 Influence of electric fields on ice nucleation . . . . .	58

<b>III Electrohydrodynamics of sessile droplets</b>	<b>65</b>
<b>4 Experimental details</b>	<b>67</b>
4.1 Experimental setup . . . . .	68
4.1.1 Motion and oscillation of droplets . . . . .	72
4.1.2 Measurement of partial discharges . . . . .	73
4.2 Preparation . . . . .	74
4.3 Procedure . . . . .	76
4.3.1 Generation of charged and uncharged droplets . . . . .	76
4.3.2 Generation of inflexible gelatin droplets . . . . .	81
4.3.3 Positioning of the droplets . . . . .	83
4.3.4 Analysis of the droplet motion experiments . . . . .	84
4.3.5 Analysis of the partial discharge experiments . . . . .	88
<b>5 Motion of charged and uncharged sessile droplets</b>	<b>91</b>
5.1 General . . . . .	91
5.2 Motion of droplets in first resonance mode . . . . .	95
5.3 Motion of droplets in second resonance mode . . . . .	98
5.4 Motion of droplets in third resonance mode . . . . .	105
5.5 Conclusions . . . . .	110
<b>6 Partial discharges generated by sessile droplets</b>	<b>113</b>
6.1 General . . . . .	113
6.2 PD inception field strength of single inflexible droplets . . . . .	119
6.3 PD inception field strength of two adjacent inflexible droplets	121
6.4 PD inception field strength for charged and uncharged water droplets . . . . .	124
6.5 Conclusions . . . . .	130
<b>7 Droplets under the impact of transient electric fields</b>	<b>133</b>
7.1 General . . . . .	133
7.2 Single droplet behaviour . . . . .	135
7.3 Coalescence of neighbouring droplets . . . . .	139
7.3.1 Standard lightning impulse voltage . . . . .	143
7.3.2 Standard switching impulse voltage . . . . .	145
7.4 Conclusions . . . . .	147

<b>IV</b>	<b>Ice nucleation of supercooled droplets</b>	<b>149</b>
<b>8</b>	<b>Experimental details</b>	<b>151</b>
8.1	Experimental setup . . . . .	151
8.1.1	Temperature control . . . . .	153
8.1.2	Temperature measurement . . . . .	155
8.1.3	Observation system . . . . .	160
8.1.4	Electric field generation . . . . .	161
8.1.4.1	Constant electric fields . . . . .	164
8.1.4.2	Alternating electric fields . . . . .	164
8.1.4.3	Transient electric fields . . . . .	165
8.1.4.4	Electric field strengths present in applica- tions . . . . .	167
8.1.5	Boundary conditions . . . . .	168
8.1.5.1	Surrounding fluid . . . . .	168
8.1.5.2	Electric charges on the droplet and the substrate . . . . .	172
8.2	Preparation and Procedure . . . . .	174
8.2.1	Generation of sessile droplets . . . . .	174
8.2.2	Generation of emulsified droplets . . . . .	176
8.2.3	Experimental procedure . . . . .	178
8.2.4	Analysis of the experiments . . . . .	182
<b>9</b>	<b>Results using supercooled sessile droplets</b>	<b>185</b>
9.1	Four stages of ice nucleation experiments . . . . .	186
9.2	Constant electric fields . . . . .	192
9.2.1	Impact of the electric field strength . . . . .	193
9.2.2	Singular behaviour of ice nucleation . . . . .	197
9.2.3	Droplet hydrodynamics in electric fields . . . . .	200
9.2.4	Conclusions . . . . .	202
9.3	Alternating electric fields . . . . .	202
9.3.1	Influence of the electric field strength . . . . .	204
9.3.2	Time effects regarding the electric field strength . . . . .	210
9.3.3	Singular ice nucleation . . . . .	215
9.3.4	Influence of the frequency of the electric field . . . . .	223
9.3.5	Conclusions . . . . .	228
9.4	Transient electric fields . . . . .	229
9.4.1	Impact of standard lightning impulse voltages . . . . .	231
9.4.2	Impact of standard switching impulse voltages . . . . .	235
9.4.3	Singular vs. stochastic behaviour . . . . .	241

*Contents*

9.4.4	Conclusions . . . . .	247
<b>10</b>	<b>Results of emulsified supercooled droplets</b>	<b>249</b>
10.1	Constant electric fields . . . . .	250
10.2	Alternating and transient electric fields . . . . .	254
<b>V</b>	<b>Remarks and outlook</b>	<b>255</b>
<b>11</b>	<b>Summary</b>	<b>257</b>
<b>12</b>	<b>Conclusions and outlook</b>	<b>265</b>
<b>Appendix</b>		<b>269</b>
A	Electrical circuit for the measurement of partial discharges	269
B	Measurement setup to determine the electric surface potential on silicone rubber . . . . .	270
C	Electric surface potential measurement on silicone rubber	272
D	Calibration of the electric charge measurement . . . . .	273
E	Additional data for charged and uncharged droplets under the influence of alternating electric fields . . . . .	275
F	Measurement of electrical properties of gelatin droplets . .	277
G	Accuracy of image processing and droplet motion analysis	279
H	Measurement of electric charge of raindrops . . . . .	283
I	Measurement of electrical properties of ice . . . . .	284
J	Distorted electric field distribution . . . . .	286
K	Literature review of ice nucleation investigations . . . . .	288
L	Temperature calibration for emulsified droplets . . . . .	290
<b>Bibliography</b>		<b>295</b>
<b>List of own publications</b>		<b>329</b>
<b>List of supervised theses</b>		<b>331</b>

**Part I**

**OPENING**



# 1 Introduction

Over 70% of the earth surface is covered with water [220]. Hence, water is omnipresent and interacts with various technical systems. The interaction between technical systems and water can be used in a targeted manner or is unintentionally given as a boundary condition. The kind of interaction is mainly determined by the application itself and the boundary conditions. Various technical systems are specially designed to interact with fluids, more specifically with water or similar liquids, such as hydropower plants [26, 199], electrostatic lenses [16, 38, 178, 191], electowetting systems [183, 262], displays [10, 124], atomization and spray systems [88, 282, 285] or processes in food industry [44, 112, 245]. In contrast, the unintended interaction between an electric field and water can significantly affect the reliability of the technical system as it occurs, e.g. during the operation of high-voltage insulators [2, 207, 225] or can even cause serious safety risks, as for instance aquaplaning of cars and aircraft [77, 89, 135]. Besides liquid water at ambient temperature, ice also affects many applications, especially in cold regions, like aircraft [8, 35], ships [49, 221], wind turbines [3, 202], photo-voltaic systems [111], structures such as bridges [125], or components of power transmission and distribution [62, 63, 65]. Consequently, applications and technical systems are affected by water independent of the aggregation state of water. In general, a safe and reliable operation is the number one priority which has to be ensured by technical solutions.

The various mentioned applications involve physics of different research areas such as the hydrodynamics of droplet impact and movement, droplet-droplet interaction, surface wetting, phase change or heat transfer. The presence of these different phenomena lead to complex interactions and physical mechanisms. In addition, external influences like electric fields even complicate the underlying physics. Simultaneously, the use of electric fields enables new opportunities to actively control fluid dynamic processes and optimize already present applications. This results in more reliable, efficient and safe operation, and thus is beneficial with respect to sustainable applications. However, the operation of the electric fields must be safe to use and should not have a negative impact on the application. The undesired influence of the electric field might reduce the reliability, efficiency and/or lifetime of the technical system, which should definitely be avoided. A detailed knowledge of the physical mech-

## 1 Introduction

anisms involved with droplets under the impact of electric fields is a key to improve the reliability of technical applications and to ensure a safe operation. Even though the influence of electric fields is already widely used in applications and research, the general influence of electric fields on the behaviour of water under various boundary conditions is not yet completely understood. Thus, the underlying physics has to be investigated in detail depending on different boundary conditions to improve the understanding of the complicated interrelationships.

Consequently, the main focus of this study is to determine the impact of electric fields on the behaviour of water droplets under various ambient conditions.

### 1.1 Motivation

Electric power transmission and distribution relies on the quality of the components used, as for instance high-voltage insulators. The insulators are specially designed equipment to withstand different environmental stresses such as liquid water present as rain, ice, UV-radiation or different temperatures [123]. In general, the components are designed to operate up to 40 years [92] without a significant loss of performance and reliability. The main task of the insulators is to insulate the high-voltage from the ground potential for safety reasons and to avoid short circuits [86]. Nowadays, composite insulators are favoured compared to glass or ceramic due to several advantages. The insulator consists of a fibreglass rod covered by weather sheds made out of silicone rubber, resulting in a lightweight and robust design [86, 201]. In addition, the silicone rubber leads to hydrophobic surface properties [86], which prevents the formation of a liquid layer on the surface. An electrical conductive liquid layer on the surface promotes the formation of significant creeping currents, and therefore reduces the efficiency of the system. In contrast, only single sessile droplets are formed on a hydrophobic surface. Even though the formation of single droplets is beneficial in terms of the formation of electrical conductive layers on the surface, the individual sessile droplets generate electrically critical regions near the three-phase contact line [270]. The electric field is suppressed or vanishes inside the water droplet and enhanced in the material with the lowest relative permittivity, generally air. The local field enhancement can lead to the generation of partial discharges, which deteriorate the surface due to the generated heat and UV-light. Thus, the

ageing of the insulator surface is accelerated [2, 87]. The phenomena are influenced by different parameters such as strength, frequency or type of the electric field as well as electric charges. Various parameters like the droplet volume, electric field strength, frequency of the electric field or influence of the fluid as well as the general impact of electric fields on liquids have already been investigated in detail, amongst others by Fujii et al. [75, 76], Nazemi [187], Phillips et al. [207], Rayleigh [223], Schütte and Hornfeldt [237] and Taylor [259]. Nevertheless, most studies reported in literature are performed on complex specimens as for instance on the high-voltage insulator itself [81, 179, 208, 228, 271], and therefore investigate the overall performance of the insulator. Even though several influencing factors have been identified, no reliable prediction model for the ageing of high-voltage insulators could be developed. The high complexity of the specimens and the neglect of possibly important influencing parameters such as the electric charge might mask physical processes and possible influences. Hence, the underlying physical mechanisms have to be first determined using simpler arrangements, like a generic specimen and a single water droplet with well-defined boundary conditions, which can then be transferred to more complex arrangements. Such simple arrangements are more appropriate to determine the impact of each influencing factor, even if the impact is small. Especially, the impact of electric charges on the movement and the generation of partial discharges is not carefully controlled or almost neglected in literature. Thus, various previously performed studies might have unintentionally used charged water droplets, which are assumed to influence the outcome of the investigations. Consequently, in this study the impact of electric charges on the motion of a single sessile droplet and the generation of partial discharges is investigated under well-defined conditions to improve the understanding of the ageing mechanisms of high-voltage composite insulators.

Besides the accelerated ageing caused by the presence of liquid sessile water droplets under ambient conditions, high-voltage insulators and line conductors are significantly affected by ice accretion [63], especially in cold regions. Even though high-voltage insulators are affected by accreted ice, the impact of electric fields on ice nucleation is still not completely understood. Snow or ice generated by freezing of supercooled water droplets can adhere on the weather sheds of the insulator or the line conductor. Accordingly, the ice alters the shape of the insulator and can lead to bridging of the weather sheds, which reduces the insulation distance and induce undesired creeping currents or a flashover in the worst case [64, 65].

## 1 Introduction

In addition, the accreted ice causes additional static (weight of ice and snow) and dynamic (by line galloping) loads acting on the pylons, which might result in a collapse of the pylons in the worst case [65]. Any undesired modification of the technical systems significantly reduce the efficiency and reliability of the system. Icing is initiated by ice nucleation, which is influenced by several influencing factors like the temperature, substrate or droplet size as shown, e.g. by Holden et al. [103], Kuhn et al. [134], Vali [265] and Wang et al. [274]. Many of these influencing factors are already investigated and widely known. Nevertheless, the impact of electric fields on ice nucleation, which is often called *Electrofreezing*, is still not completely understood. Even though several investigations under different boundary conditions were already performed, the impact of the electric field is still not clear and even contrarily discussed in literature [1, 53, 120, 197, 217, 277, 279]. The small influence of the electric field might be masked by other influencing factors or the statistical nature of ice nucleation [193]. Especially, the impact of alternating and transient electric fields depending on the electric field strength and frequency were rarely investigated in the past. As a consequence, a clean and careful experiment is necessary to ensure well-defined boundary conditions and to investigate the impact of electric fields. While such experimental setups are already available to investigate ice nucleation depending on, e.g. the cooling rate, droplet size or different contamination with ice nucleating particles [9, 28, 46, 94, 175, 240, 278, 280], an experimental setup to investigate the impact of electric fields on homogeneous and heterogeneous ice nucleation under various (type, orientation, frequency and strength of the electric field) but well-defined boundary conditions is still not available. The previous experimental setups only cover specific boundary conditions, such as shown in [197]. Hence, a new experimental setup is developed in this study to determine the impact of electric fields on ice nucleation under well-defined conditions, which improves the understanding of icing mechanisms.

In summary, high-voltage insulators are highly affected by the interaction of water and electric fields under various ambient conditions. The insulator is exposed to water in different aggregation states, namely liquid water or ice, depending on the boundary conditions. The main focus of the present study is to investigate the fundamental physical mechanisms influencing the behaviour of water droplets under the impact of electric fields for different boundary conditions. The results aim to improve the understanding of the behaviour of water droplets inside electric fields and help

to improve the efficiency of high-voltage insulators. Due to the large variety of boundary conditions, the results are related to other research fields like, electrowetting, atomization, food science or atmospheric physics.

## 1.2 Aims and outline of thesis

The main goal of the present study is to improve the understanding of the behaviour of water droplets under the impact of electric fields. The thesis has two main emphases: First, to determine the impact of electric fields on the behaviour of sessile droplets under ambient conditions and second, to investigate the impact of electric fields on ice nucleation. Hence, the thesis is divided into two main topics, which are presented in separate chapters.

The literature presented in the previous section revealed the research gaps for both topics. Based on the research gaps, the following objectives are defined, which will be addressed in this thesis.

### *Droplets under ambient conditions*

- Determine the impact of electric charges on the motion and oscillation of sessile droplets depending on the droplet volume, droplet charge, electric field strength, frequency and type of the electric field.
- Identify the impact of electric charge on the partial discharge inception field strength of single and multiple sessile droplets depending on the droplet volume, droplet charge, electric field strength and frequency of the electric field.
- Investigate the interaction of two nearby droplets under the impact of transient electric fields depending on the electric field strength, impulse type, droplet volume and droplet-droplet separation.

### *Supercooled droplets - ice nucleation*

- Development and construction of an experimental setup to investigate the impact of electric fields on ice nucleation under well-defined conditions with respect to the electric field and temperature.
- Determine the influence of electric fields on ice nucleation depending

## 1 Introduction

on the electric field strength, type of the electric field, frequency, droplet ensemble and temperature.

- Investigate the difference between homogeneous and heterogeneous ice nucleation under the impact of electric fields.

The defined objectives are categorized by the boundary conditions with respect to the temperature. This structure is maintained for the entire thesis, which leads to five parts.

Part I contains *Chap. 1*, which introduces and motivates the present thesis. Furthermore, the research gap and the main objectives of the thesis are defined.

Part II summarizes the theoretical background. The part is divided into two chapters. *Chapter 2* recapitulates the droplet hydrodynamics and describes the interaction of water droplets and electric fields, namely the electrohydrodynamic phenomena. In addition, *Chap. 3* introduces the theoretical background for supercooled droplets and ice nucleation.

The results of the experimental investigations are presented in Part III and Part IV. The subject of Part III is the behaviour of water droplets under the influence of electric fields under ambient conditions. The experimental setup used for all experiments is shown in *Chap. 4*. Subsequently, the influence of electric fields on the motion/oscillation of sessile droplets and the partial discharge inception are described in *Chap. 5* and *Chap. 6* respectively. Furthermore, the droplet coalescence of neighbouring droplets under the impact of transient electric fields is presented in *Chap. 7*.

Part IV contains the results of the investigation of ice nucleation under the influence of electric fields. The part begins with the presentation of the experimental setup and procedure in *Chap. 8*. The results of heterogeneous ice nucleation and homogeneous ice nucleation under various different conditions with respect to the type of the electric field are presented in *Chap. 9* and *Chap. 10* respectively.

Part V concludes this study and provides a summary of the presented investigation in *Chap. 11* and an outlook in *Chap. 12*. The major outcomes of this study are summarized, and open questions for further research are defined.

**Part II**

**FUNDAMENTALS**



## 2 Hydrodynamic and electrohydrodynamic phenomena

The word hydrodynamics originates from the Latin word *Hydrodynamica* introduced by Bernoulli [17] and describes the motion of fluids. The motion of a fluid is determined by the forces acting on the fluid and the fluid properties. Even in equilibrium and at rest, forces can act on the fluid. The interaction of liquids in motion (hydrodynamics) and electric fields is called *electrohydrodynamics* [263]. First studies of electrohydrodynamic phenomena were performed, among others by Taylor [259, 260] and Melcher [172]. Subsequently, the effect of electric fields on the behaviour of different liquids was extensively studied experimentally and theoretically. Nowadays, many applications like electrowetting [183], electrostatic atomization [88], inkjet printing [171], electrostatic lenses [38] or electrostatic painting [248] actively use an electric field to manipulate the fluid flow and motion of the liquid. The following sections summarize the fundamentals of the hydrodynamics of single sessile droplets. In addition, the fundamentals of the electric field and the corresponding electric quantities are discussed in detail. Based on the definition of the electric field, the interaction of liquids and the electric field is explained with respect to the electric field distribution and the resulting forces caused by the electric field.

### 2.1 Sessile droplets

A sessile droplet consists of a liquid resting on a substrate in equilibrium. Hence, the liquid is in contact with additional materials like the substrate and the surrounding fluid or gas. The different media are separated by an interface, which can be characterized by a thin surface with negligible thickness and discontinuous thermodynamic properties in a macroscopic point of view [73]. The interface between the liquid and a gas is called a surface [73]. A phenomenon associated with the interface is the *interfacial* or *surface tension*. Thermodynamically the surface tension  $\gamma$  is defined as energy per unit surface area, which leads to [48, 73]

$$\gamma = \left( \frac{dW}{dA} \right)_{V,T,N_{\text{mol}}}, \quad (2.1)$$

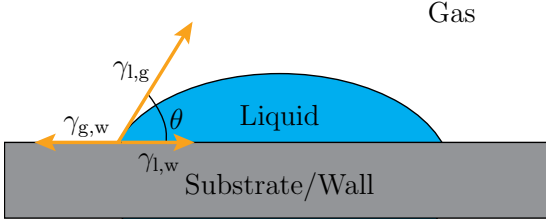


Figure 2.1: Principle of a sessile droplet and the corresponding interfacial tensions  $\gamma$  including the definition of the contact angle  $\theta$ . Any influence of gravity is neglected.

where  $W$  is the surface energy or work and  $A$  is the surface area for constant volume  $V$ , temperature  $T$  and number of molecules  $N_{\text{mol}}$ . The surface tension describes the change of energy necessary to change the surface area [48] and is always defined with respect to the involved materials. The unit of the surface tension is  $\text{J}/\text{m}^2$  or  $\text{N}/\text{m}$ . In the following work the tension at the interface between a liquid and a gas is called surface tension while the tension on the interface between different liquids or liquids and solids is named interfacial tension or interfacial energy. From a molecular perspective the forces on a molecule being in the bulk differ from the forces acting on a molecule near or at the surface [263]. A molecule inside the bulk experiences forces from the surrounding molecules from all directions leading to a zero net force on the molecule. In contrast, a molecule at the surface of the liquid only experiences forces from the liquid bulk, which leads to an attraction of the molecule towards the bulk and a non-zero net force on the molecule. In consequence, the energy of a molecule located at the surface has to be different compared to that of a molecule in the bulk [263]. Gibbs et al. [82] developed the definition of the surface tension by specifying the surface tension as the difference between the energy of the system and the sum of energies of its components under the assumption that there is no interface between the different media, which leads to the definition of Eq. (2.1) [263]. Generally, each thermodynamic system tries to minimize its free energy [29], and consequently the shape of the liquid is determined by the state of the lowest possible surface energy, which is correlated to a low surface area. In case of a droplet levitating in the air the droplet adopts a spherical shape because of the minimum surface area of a given volume associated with a spherical shape [48]. In contrast to a

levitating droplet, the shape of a sessile droplet is more complicated, because of the substrate present, which leads to additional interfaces. Each interface leads to an interfacial tension, which determines the shape of the sessile droplet. Figure 2.1 illustrates a sessile droplet and the three interfacial tensions on the different interfaces by neglecting any influence of gravity. Note that the principle is still valid for inclined substrates or vertical walls. The force balance of the interfacial tension directly at the three-phase contact line leads to the Young equation [291]

$$\gamma_{g,w} = \gamma_{\ell,w} + \gamma_{\ell,g} \cos(\theta), \quad (2.2)$$

which relates the static contact angle  $\theta$  and the surface tension between the liquid and gas  $\gamma_{\ell,g}$ , the interfacial tension between the substrate (or wall as a abbreviation) and the liquid  $\gamma_{\ell,w}$  and the interfacial tension between the gas and the substrate  $\gamma_{g,w}$ . This equation is only valid for an ideal solid substrate, which is perfectly smooth, rigid, chemically homogeneous, insoluble and non-reactive [263]. The static contact angle is always defined within the liquid as shown in Fig. 2.1.

The shape of the droplet is affected by different influencing factors like the substrate properties or external forces, as for instance electric fields. As an example, the roughness of the surface influences the wettability of the substrate [218] and therefore the shape of the droplet. Figure 2.2 shows the principle shape of a droplet on a hydrophilic and a hydrophobic substrate. The wettability of a substrate is characterized by the properties of a fluid to wet the surface, which can be characterized by the static contact angle. Generally, the higher the static contact angle, the lower is the wettability of the surface and vice versa. Thus, substrates with a static contact angle of  $\theta < 90^\circ$  and  $\theta > 90^\circ$  are called hydrophilic and hydrophobic [141] respectively. Substrates with static contact angles  $\theta > 150^\circ$  are called superhydrophobic [276].

In practice, an ideal surface does not exist so that no distinct contact angles can be observed, rather a range of contact angles. The measurement of the static contact angle requires a pinned contact line, which is partially given for different contact angles. The range of the static contact angle  $\Delta\theta$  is defined by the advancing and receding contact angle and is named contact angle hysteresis [85]

$$\Delta\theta = \theta_{\text{adv}} - \theta_{\text{rec}}, \quad (2.3)$$

where  $\theta_{\text{adv}}$  is the advancing and  $\theta_{\text{rec}}$  is the receding contact angle. As long as the contact line of a droplet is pinned, the contact angle can have

## 2 Hydrodynamic and electrohydrodynamic phenomena

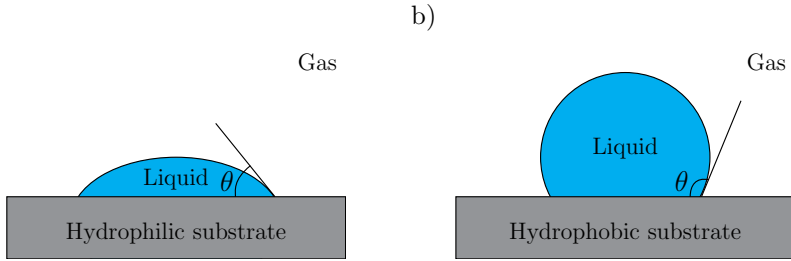


Figure 2.2: Principle shape of a droplet depending on the wetting properties of the substrate and the corresponding contact angle  $\theta$  for a) droplet on a hydrophilic substrate and b) on a hydrophobic substrate.

different values. However, if the static contact angle reaches a critical angle the contact line moves on the substrate. In case of an extension of the droplet and an outward motion the lowest possible angle for the motion is called advancing contact angle. In addition, the lowest possible contact angle, which leads to a retraction characterized by an inward motion of the droplet is called receding contact angle. In practice, the advancing and receding contact angle are measured using a syringe immersed in a droplet. The liquid is fed or retracted from the droplet, and the contact angle is optically measured to determine the contact angle for the extension or retraction of the droplet. The difference between the advancing and receding contact angle for water strongly depends on the properties of the substrate and can reach values of up to  $\Delta\theta \approx 50^\circ$  [273]. A visualization of the contact angle hysteresis and the different conditions of the contact line with respect to its motion is shown in Fig. 2.3. A pinned contact line prevents the contact line motion and is indicated by zero on the abscissa. The contact angle can have different values without a motion of the contact line. If the contact angle exceeds the advancing contact angle the contact line starts to move. Note that the contact angle might change during the motion of the contact line because the contact angle depends on the velocity of the contact line [85]. In contrast, if the contact angle is lower than the receding contact angle the droplet recedes. Similar to the advancing of the droplet, the contact angle during receding might vary because it depends on the receding rate. Due to the fact that both, the receding and the advancing contact angle, depend on the con-

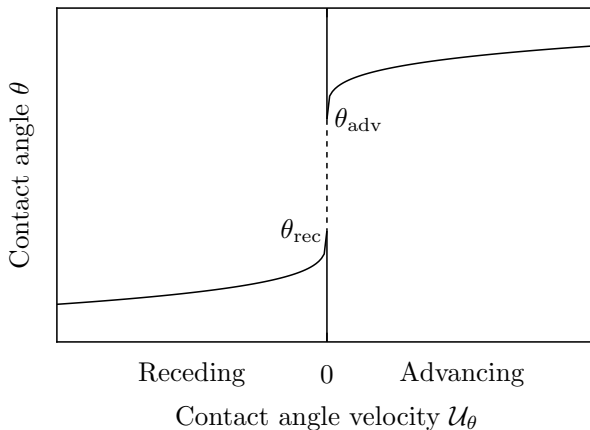


Figure 2.3: Schematic of the contact angle hysteresis. Contact angle  $\theta$  depending on the different states of the droplet. A movement of the contact line is observable in the advancing (adv) and receding (rec) region.

tact line velocity the critical advancing and receding contact angle have to be determined during the initial movement of the contact line. The static contact angle can have any value between advancing and receding contact angle, which mainly depends on the local wetting properties of the substrate [27]. The pinning of the contact line, which is caused by a non-homogeneous surface with respect to the wetting properties, leads to the contact angle hysteresis [48]. For such condition, which is described by the Young-Laplace equation, the contact line is in a meta-stable (locally stable) state [27]. Any disturbances like locally changed surface roughness, surface contamination or surface heterogeneity influence the observed contact angle [15, 27]. Thus, the contact angle hysteresis can be interpreted as a characterization of the activation energy to cause droplet movement from one meta-stable state into another [78]. Microscopically, the activation energy is given by the distortion of the droplet and leads to change of the free interfacial energy [78]. Hence, the shape of the droplet is mainly influenced by the local wetting properties of the substrate, as for instance the roughness or surface heterogeneity.

In addition, electric charges can influence the equilibrium shape of a droplet. While the surface tension tends to minimize the surface area,

## 2 Hydrodynamic and electrohydrodynamic phenomena

electric charges with same polarity as nearby electric charges generate a repulsion force, which tends to increase the surface area. A force balance between the repulsion force of the electric charge and the surface tension leads to the assumption that the charge of a droplet is limited. The maximum charge  $Q_{\max}$  depends on the volume of the (free floating) droplet and is given by the Rayleigh limit [223]

$$Q_{\max} = \sqrt{48\pi\varepsilon_0\gamma V}, \quad (2.4)$$

where  $V$  is the volume of the droplet and  $\varepsilon_0$  is the vacuum permittivity. Increasing the electric charge on a droplet causes a deformation of the droplet [259]. As soon as the Rayleigh limit is reached the repulsion force of the electric charge exceeds the surface tension, which results in a disintegration of the droplet [55, 223]. Hence, the droplet is not stable any more.

### 2.2 The electric field

The electric field  $\vec{E}$  is derived from the Coulomb law, which defines the force between two charges [74, 131]. The force  $\vec{F}_2$  acting on a charge  $Q_2$  resulting from a charge  $Q_1$  in the distance  $r$  is given by [131]

$$\vec{F}_2 = Q_2 \cdot \underbrace{\frac{Q_1}{4\pi\varepsilon r^2}}_{\vec{E}} \cdot \vec{e}_r, \quad (2.5)$$

where  $\varepsilon$  is the permittivity and  $\vec{e}_r$  is the unit vector in radial direction. The permittivity  $\varepsilon$  is defined by  $\varepsilon = \varepsilon_0\varepsilon_r$ , where  $\varepsilon_r$  is the relative permittivity and  $\varepsilon_0$  is the vacuum permittivity. The vacuum permittivity is a constant and yields  $\varepsilon_0 = 8.854 \cdot 10^{-12} \text{ A s}/(\text{V m})$  [90]. In contrast, the relative permittivity  $\varepsilon_r$  depends on the dielectric properties of the material and is dimensionless. Equation (2.5) assigns an electric field to the charge  $Q_1$ , which decreases quadratically in radial direction. Consequently, the force on the charge  $Q_2$  can be described by means of an electric field instead of explicitly using the origin ( $Q_1$ ) [131]. In general, the electric field can be defined by the force  $\vec{F}$  acting on a positive test charge  $\tilde{Q}$  [173]

$$\vec{E} = \frac{\vec{F}}{\tilde{Q}}. \quad (2.6)$$

The test charge is introduced because the electric field can only be determined by the force on a specific charge. An object containing a positive charge  $\tilde{Q}$  is affected by the force  $\vec{F}$  inside an electric field  $\vec{E}$ . Both the force  $\vec{F}$  and the electric field  $\vec{E}$  are vector quantities, which are defined by their magnitude and direction.

Instead of using the exact charge on an electrode, more commonly the applied electric potential or potential difference is used to characterize the electrical arrangement. Hence, the electric potential is introduced to determine the electric field without explicitly mentioning the electric charge.

The electric potential  $\phi$  is defined by the potential energy  $W_{\text{pot}}$  per test charge  $\tilde{Q}$  [133, 173]

$$\phi = \frac{W_{\text{pot}}}{\tilde{Q}}. \quad (2.7)$$

Inserting the definition of the potential energy

$$W = \int \vec{F} d\vec{s}, \quad (2.8)$$

where the force  $\vec{F}$  is acting along the vector  $\vec{s}$ , in Eq. (2.7) yields

$$\phi = \frac{1}{\tilde{Q}} \int \vec{F} d\vec{s}. \quad (2.9)$$

Using Eq. (2.6) the electric potential can be expressed with respect to the electric field

$$\phi = \frac{1}{\tilde{Q}} \int \vec{E} \tilde{Q} d\vec{s}. \quad (2.10)$$

This equation can also be expressed in differential form, which leads to

$$\vec{E} = -\nabla\phi, \quad (2.11)$$

where  $\nabla$  is the Nabla operator [133, 173]. The components of an electric field are calculated by the partial derivatives of the electric potential with respect to the unit vectors of the corresponding coordinate system.

The electric potential is always defined with respect to a reference potential  $\phi_0$ . A potential difference

$$U = \phi_1 - \phi_2, \quad (2.12)$$

## 2 Hydrodynamic and electrohydrodynamic phenomena

is named voltage  $U$  and is often used to characterize the difference in electric potential between two electrodes.

The electric field can arise from two different sources [133]. First, the occurrence of charges, which are sources (positive charges) and sinks (negative charges) of the electric field. In this case the electric field is also called *electro-static field*. Second, the electric field can be generated by a time-varying magnetic field as defined by the induction law (second Maxwell equation). Both physical mechanisms can be described by the Maxwell equations, which characterize electromagnetic fields in general [238] and can be used to determine the electric potential for a specific geometry so that the electric field distribution can be calculated. These general equations can be simplified by only taking into account slow changes of the field (low frequencies). The resulting equations describe electric and magnetic quasi-static fields. Furthermore, neglecting temporal changes of the magnetic flux density  $\partial \vec{B} / \partial t = 0$  leads to the electric quasi-static (EQS) field, which is described in detail hereafter. The assumption of an EQS field results in the following simplified Maxwell equations

$$\oint \vec{H} \, d\vec{s} = \oint\!\!\!\oint_A \left( \vec{J} + \frac{\partial \vec{D}}{\partial t} \right) d\vec{A}, \quad (2.13)$$

$$\oint \vec{E} \, d\vec{s} = 0, \quad (2.14)$$

$$\oint\!\!\!\oint_A \vec{B} \, d\vec{A} = 0, \quad (2.15)$$

$$\oint\!\!\!\oint_A \vec{D} \, d\vec{A} = \iiint_V q \, dV, \quad (2.16)$$

where  $\vec{H}$  is the magnetic field strength,  $\vec{J}$  is the current density,  $\vec{D}$  is the field displacement,  $t$  is the time,  $\vec{B}$  is the magnetic flux density,  $q$  is the charge density per volume with  $V$  being the corresponding volume,  $\vec{A}$  is the surface area pervaded by the field quantities and  $\vec{s}$  is the integration path along a closed curve. Equation (2.13) states that the circular integral of the magnetic field equals the enclosed current, which is given by the current and a time variable field displacement. In addition, Eq. (2.14) defines that the electric field is an irrotational field. Equation (2.16) is called Gauss's Law and defines that the envelope surface integral of

the field displacement equals the enclosed charge [238]. The Maxwell equations can also be written in differential form

$$\nabla \times \vec{H} = \vec{J} + \frac{\partial \vec{D}}{\partial t}, \quad (2.17)$$

$$\nabla \times \vec{E} = 0, \quad (2.18)$$

$$\nabla \cdot \vec{B} = 0, \quad (2.19)$$

$$\nabla \cdot \vec{D} = q. \quad (2.20)$$

The Maxwell equations connect the different field quantities, but cannot be solved without the correlation between the field strengths and the flux densities. Hence, the material specific correlations for  $\vec{D}$ ,  $\vec{J}$  and  $\vec{E}$  are introduced, which are given by [95]

$$\vec{D} = \varepsilon_0 \varepsilon_r \vec{E}, \quad (2.21)$$

$$\vec{J} = \kappa \vec{E}, \quad (2.22)$$

where  $\kappa$  is the electrical conductivity of the material. Using the differential form of the Maxwell equations, Eq. (2.11), Eq. (2.21) and Eq. (2.22) the general equation for the electric potential of the EQS field can be derived. Inserting Eq. (2.11) and Eq. (2.21) into Eq. (2.20) yields

$$\nabla \cdot (\varepsilon_0 \varepsilon_r \nabla \phi) = -q. \quad (2.23)$$

After calculating the divergence of Eq. (2.17) the equation is given by [95]

$$\nabla \cdot \vec{J} + \frac{\partial q}{\partial t} = 0. \quad (2.24)$$

Note that  $\nabla \cdot (\nabla \times \vec{H}) = 0$ . Inserting Eq. (2.23) in Eq. (2.24) results in the equation of the electric potential for the EQS field

$$\nabla \cdot \left( \kappa \nabla \phi + \frac{\partial}{\partial t} \varepsilon_0 \varepsilon_r \nabla \phi \right) = 0. \quad (2.25)$$

The solution of this equation yields the electric potential, which can be used to calculate the electric field strength without knowing the charge distribution. Calculating the electric potential is generally more convenient because the electric charge distribution is unknown while the electric

## 2 Hydrodynamic and electrohydrodynamic phenomena

potential is often defined by the applied voltage and the geometric arrangement. As already mentioned, the electro quasi-static field describes time-variant electric fields with slow changes [133]. Such electric fields are generated by power-frequency voltages (AC, originates from alternating current) or switching impulse (SI) as well as lightning impulse (LI) voltages [133]. Electric fields in dielectrics cause displacement currents to be much larger than the conduction currents  $\partial\vec{D}/\partial t \gg \vec{J}$  [133]. Hence, Eq. (2.25) can be further simplified to

$$\nabla \cdot (\varepsilon_0 \varepsilon_r \nabla \phi) = 0, \quad (2.26)$$

which defines the electric potential distribution in absence of charges. As shown by Eq. (2.26) the electric field distribution is mainly influenced by the relative permittivities of the involved materials. A special case of the EQS field is the static electric field, which is time-invariant and generated using a constant voltage (DC, originates from direct current). In this case the temporal dependence of all quantities vanishes, so that  $\partial\vec{D}/\partial t \ll \vec{J}$  is valid [133]. Taking into account this assumption leads to the following potential equation

$$\nabla \cdot (\kappa \nabla \phi) = 0. \quad (2.27)$$

In the case of a constant electric field the electric field distribution is characterized by the electrical conductivities of the involved materials instead of the relative permittivities. Generally, the field distribution depends on the electrical properties of the involved materials. Whether the relative permittivity or the electrical conductivity of the materials characterizes the field distribution is defined by the type of the electric field. The characteristic time for the charge relaxation  $\tau_{el} = \varepsilon/\kappa$  [108] and the characteristic time of the problem  $\tau_{char}$ , which can be defined by the frequency of the electric field (e.g.  $\tau_{char} = 1/f_{AC}$ , with  $f_{AC}$  as the frequency of an alternating electric field) or the hydrodynamic timescale, can be used to determine the dominant physical mechanism. For  $\tau_{el}/\tau_{char} \gg 1$  the electric field is characterized by the relative permittivities, while for  $\tau_{el}/\tau_{char} \ll 1$  the electric field is determined by the electrical conductivities [211]. Note that  $\tau_{el}/\tau_{char}$  in the order of one leads to a field distribution defined by both, the electrical conductivities and the relative permittivities.

Assuming a constant permittivity  $\varepsilon$  or electrical conductivity  $\kappa$  the equations for the electric potential can be further simplified to

$$\nabla^2 \phi = 0, \quad (2.28)$$

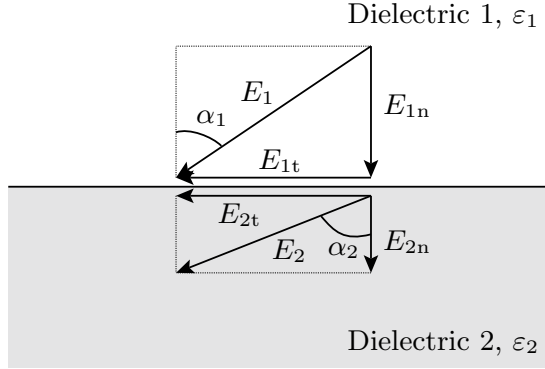


Figure 2.4: Principle behaviour of the electric field  $E$  and its components at an interface of two different dielectrics ( $\varepsilon_2 > \varepsilon_1$ ). The refraction of the electric field is characterized by the angles  $\alpha$ . Adapted by permission from Springer Nature: Springer Vieweg, *High-Voltage Engineering - Electric Stresses* by Andreas Küchler, copyright (2018).

which is called Laplace equation [133, 139]. The more general case of the Laplace equation is the Poisson equation, which also takes into account external charges. For  $\tau_{\text{el}}/\tau_{\text{char}} \gg 1$  the Poisson equation is given by [133, 139]

$$\nabla^2 \phi = -\frac{q}{\varepsilon_0 \varepsilon_r}. \quad (2.29)$$

The solution of the Poisson or Laplace equation can be determined for a specific geometry and known boundary conditions such as the electric potential at the electrodes and yields the electric potential distribution. Furthermore, the electric potential can be used to determine the electric field. Generally, the electric potential and the geometric arrangement of the electrodes is known, so that the electric field is determined by solving the Poisson or Laplace equation. Especially for geometrical arrangements with multiple dielectrics the electric field distribution has to be determined with respect to the boundary conditions at the interfaces between the different dielectrics. These interfaces and the properties of the dielectric materials are essential for the electric field distribution. The principle behaviour of the electric field at the interface between two different dielectrics is shown in Fig. (2.4). The electric field  $\vec{E}_1$  in the dielectric 1

## 2 Hydrodynamic and electrohydrodynamic phenomena

is inclined with respect to the interface. The angle between the electric field and the interface is characterized by  $90^\circ - \alpha_1$ . Hence, the electric field  $\vec{E}_1$  can be divided into two components, which are tangential  $\vec{E}_{1t}$  and perpendicular  $\vec{E}_{1n}$  to the interface. The Maxwell equations determine the conditions at the interface. Using Eq. (2.14) and defining an infinitesimally small area around the interface yields [133]

$$E_{1t} = E_{2t}. \quad (2.30)$$

According to this equation, the tangential electric field strength at the interface is constant and independent of the relative permittivity of the materials. Furthermore, using the Gauss law (Eq. (2.16)) and neglecting any accumulated charges at the interface leads to [133]

$$D_{1n} = D_{2n}. \quad (2.31)$$

Thus, the dielectric field displacement perpendicular to the interface is constant. Taking into account the correlation between the dielectric displacement and the electric field results in

$$\frac{E_{1n}}{E_{1n}} = \frac{\varepsilon_2}{\varepsilon_1}, \quad (2.32)$$

so that the electric field strengths inside the different dielectrics depend on the ratio of the permittivities [133]. Assuming a perpendicular electric field to the interface ( $\alpha = 0$ ) the electric field strength is given by [133]

$$\frac{E_1}{E_2} = \frac{\varepsilon_2}{\varepsilon_1}. \quad (2.33)$$

The electric field strength is higher in the dielectric with the lower permittivity, so that for  $\varepsilon_2 > \varepsilon_1$  the electric field strength  $E_1$  is larger than  $E_2$ . The decrease of the electric field strength in the dielectric material with the higher permittivity and the increase of the electric field strength in the dielectric material with the lower permittivity is called *field displacement* [133]. The field displacement is illustrated by Fig. 2.5 with  $U = U_1 + U_2$  and  $h = h_1 + h_2$  being the applied voltage and the distance between the plates, respectively. The actual field strength in the individual dielectric layers are not only given by the ratio of the permittivities but also depends on the thickness of the different layers and can be expressed as [133]

$$E_1 = \frac{U}{h_1 + h_2 \frac{\varepsilon_1}{\varepsilon_2}} \quad (2.34)$$

$$E_2 = \frac{U}{h_1 \frac{\varepsilon_2}{\varepsilon_1} + h_2}. \quad (2.35)$$

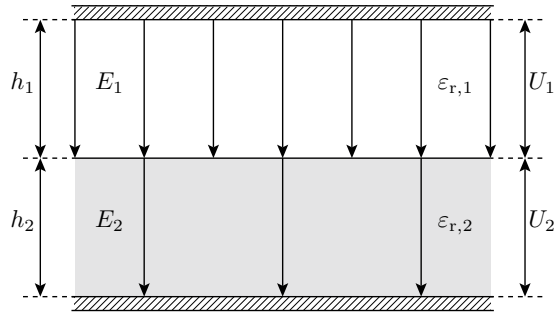


Figure 2.5: Principle electric field distribution between two electrical conductive plates with two different dielectric materials ( $\varepsilon_2 > \varepsilon_1$ ). Adapted by permission from Springer Nature: Springer Vieweg, *High-Voltage Engineering - Electric Stresses* by Andreas Küchler, copyright (2018).

The smaller the thickness of a layer  $h_i$  the higher the electric field strength. Consequently, the actual electric field strength strongly depends on the layer thickness. For the limit case of a negligible layer thickness  $h_1$  ( $h_1 \ll h_2$ ) the ratio of the electric field strengths of the individual layers converge towards the ratio presented in Eq. (2.33). In case of an arrangement consisting of a single dielectric material with vanishing thickness the electric field strength tends towards infinity (as indicated by  $E = U/h$ ). Note that the field displacement is visualized by the higher density of the electric field lines in Fig. 2.5.

For the more general case ( $\alpha \neq 0$ ), as shown in Fig. 2.4, Eq. (2.32) is still valid. Taking into account the tangential and normal components of the electric field the correlation between the different angles  $\alpha_1$  and  $\alpha_2$  can be determined and yields [133]

$$\frac{\tan \alpha_1}{\tan \alpha_2} = \frac{\varepsilon_1}{\varepsilon_2}. \quad (2.36)$$

The electric field is refracted at the interface as indicated by Eq. (2.36). The reason for this refraction of the electric field is caused by a constant tangential component of the electric field in both dielectric materials, so that only the normal component of the electric field is affected by the field displacement. The angle between the interface and the resulting electric field is determined by the ratio of the permittivities  $\varepsilon_1/\varepsilon_2$ . For  $\varepsilon_2 > \varepsilon_1$  it yields  $\alpha_2 > \alpha_1$  so that the electric field is refracted towards the interface.

In case of  $\partial\vec{D}/\partial t \ll \vec{J}$  Eq. (2.31) becomes [133]

$$J_{1n} = J_{2n}. \quad (2.37)$$

Consequently, the electric field is defined by the ratio of the electrical conductivities instead of the relative permittivities. The derived correlations are still valid in the same manner and only have to be adapted with respect to the used quantities. So,  $J$  has to be used instead of  $D$ , resulting in a correlation of the electric field strength and the electrical conductivities.

### 2.3 Microscopic interaction of sessile droplets and electric fields

Droplets exposed to electric fields affect the field distribution due to the dielectric properties of the fluid. Especially, water droplets highly affect the field distribution because of their high relative permittivity of  $\varepsilon_{r,wa} \approx 81$  and generally high electrical conductivity. As already shown, the electric field distribution depends on the electrical properties of the involved materials as well as the geometric arrangement. So the droplet can be in direct contact with one or multiple electrodes or only in contact with a dielectric material [183, 190]. Depending on the geometric arrangement the electric field is influenced. A droplet, which is in contact with an electrode can be assumed as an extension of the electrode, and thus has the same electric potential as the electrode, if the electrical conductivity of the droplet is higher than that of the surrounding air. In contrast, the electric potential of a droplet resting on a dielectric material is determined by the local electric field strength at the droplet position. In the following only droplets isolated from the electrodes are considered. The electric potential and the behaviour of the droplet mainly depends on the geometrical arrangement, and thus on the orientation of the electric field.

The orientation of the electric field can be characterized with respect to the substrate. Figure 2.6 shows two different orientations of the electric field for an axisymmetric droplet surrounded by air, where a) shows a normal orientation of the electric field and b) shows a tangential orientation of the electric field with respect to the substrate. In addition, any other direction of the electric field is possible, but can be expressed by a combi-

### 2.3 Microscopic interaction of sessile droplets and electric fields

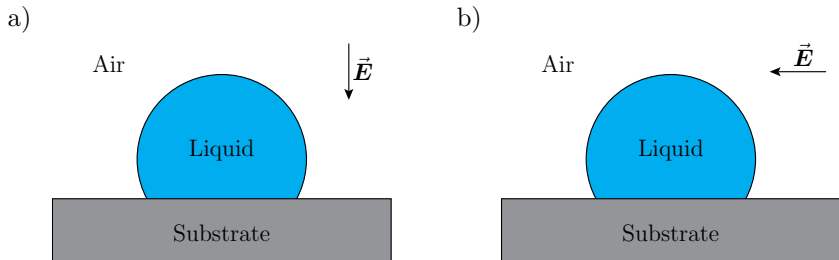


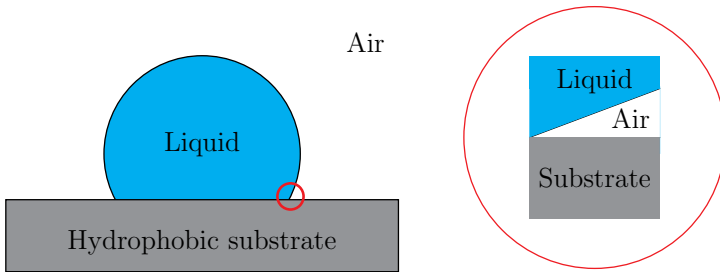
Figure 2.6: Droplet surrounded by air and different orientations of the electric field  $\vec{E}$ : a) normal orientation and b) tangential orientation with respect to the substrate.

nation of the presented cases (only valid for axisymmetric droplets). Both arrangements shown in Fig. 2.6 were already investigated in the past, and it was found that tangentially aligned electric fields have a higher impact on the droplet behaviour compared to the normal orientation [233]. Consequently, only tangentially aligned electric fields are investigated in detail in this study.

The electric field distribution mainly depends on the dielectric properties of the involved materials and the geometrical arrangement. As an example, the arrangement shown in Fig. 2.6 involves three different dielectric materials, namely a surrounding medium, a liquid and the substrate. In case of a high-voltage insulator the liquid is given by water (e.g. rain), and the substrate may consist of silicone rubber. The air, water and silicone rubber have different relative permittivities of  $\varepsilon_{r,\text{air}} = 1$ ,  $\varepsilon_{r,\text{wa}} \approx 81$  and  $\varepsilon_{r,\text{sil}} \approx 2 - 3$  [133], respectively. Hence, based on a permittivity dominated description of the field distribution, the electric field is suppressed inside the liquid and enhanced inside the air because of the field displacement. Due to the relatively high electrical conductivity of the water (e.g.  $\kappa_{\text{wa}} = 5.5 \cdot 10^{-6} \text{ S/m}$  for the high purity water used in these investigations) the droplet can be assumed as a perfect conductor for sufficiently low frequencies. For water the ratio of the charge relaxation time and the characteristic time yields  $\tau_{\text{el}}/\tau_{\text{char}} \ll 1$  for all frequencies of alternating fields investigated in this work ( $f_{\text{AC}} < 200 \text{ Hz}$ ), so that the surface of the droplet is an equipotential surface. The field enhancement is influenced by the geometric arrangement, and therefore by the wetting properties of the substrate.

## 2 Hydrodynamic and electrohydrodynamic phenomena

a)



b)

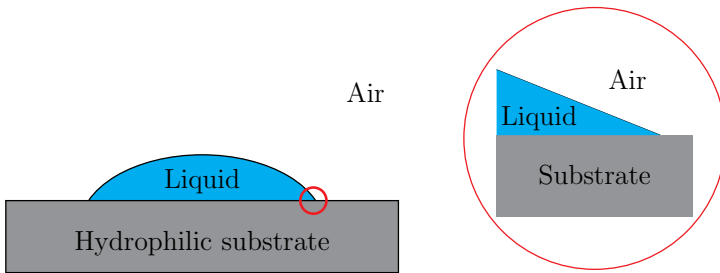


Figure 2.7: Close-up of region near the three-phase contact line for a) hydrophobic substrate ( $\theta > 90^\circ$ ) and b) hydrophilic substrate ( $\theta < 90^\circ$ ) showing the geometrical arrangement of the involved materials. a) Thin air gap between the conducting water and dielectric substrate and b) wedge-like form of the conducting water resulting in a sharp tip.

The most critical region is located directly at the three-phase contact line. Figure 2.7 illustrates the critical region near the three-phase contact line for two different contact angles. In case of a hydrophobic or superhydrophobic surface the contact angle is larger than  $\theta > 90^\circ$  [141], which leads to the arrangement shown in Fig. 2.7a. The close-up of the region near the three-phase contact line shows a narrowing air gap between the water and the substrate, which finally ends up at the three-phase contact line. Regardless of whether the liquid is assumed as a perfect conductor or a leaky dielectric, an electric field is present in the air gap. The electric field strength increases with decreasing thickness of the air layer. Due to the fact that the thickness of the air gap tends towards zero the field en-

### 2.3 Microscopic interaction of sessile droplets and electric fields

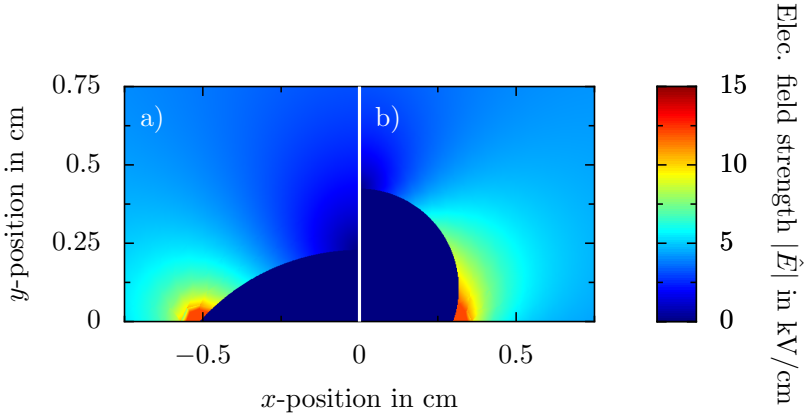


Figure 2.8: Electric field distribution around a droplet with  $V = 100 \mu\text{l}$  on a) a hydrophilic substrate and b) a hydrophobic substrate. The undisturbed electric field is tangentially aligned to the substrate and has a field strength of  $\hat{E}_0 = 4 \text{ kV/cm}$ . Based on the axis-symmetry only one half of each droplet is shown.

hancement in the air is tremendous, especially at the three-phase contact line. In contrast, Fig. 2.7b shows the hydrophobic case for  $\theta < 90^\circ$  [141]. In this case the sharp edge formed by the droplet generates high electric field strength.

The field distribution for both geometrical arrangements is shown in Fig. 2.8. The electric field is obtained by numerical simulation (COM-SOL Multiphysics<sup>®</sup>) for sessile droplets under the impact of an electric field tangentially aligned to the substrate. The substrate is given by silicone rubber and is located at  $y = 0$ . The following material properties are used for water, air and silicone to calculate the electric field distribution:  $\varepsilon_{r,wa} = 81$ ,  $\kappa_{wa} = 5.5 \cdot 10^{-6} \text{ S/m}$ ,  $\varepsilon_{r,air} = 1$ ,  $\kappa_{air} = 1 \cdot 10^{-20} \text{ S/m}$ ,  $\varepsilon_{r,sil} = 2.9$ ,  $\kappa_{sil} = 1 \cdot 10^{-15} \text{ S/m}$ . Note that the maximum electric field strength is limited to  $\hat{E}_{\text{max}} = 15 \text{ kV/cm}$  for better visualization of the field distribution. Therefore, it is not necessary to calculate the exact field strength at the three-phase contact line, which would be very difficult due to the singularity of the electric field. However, to determine accurate results, the mesh is refined in the region close to the three-phase contact line. The field distribution confirms that the highest electric field

## 2 Hydrodynamic and electrohydrodynamic phenomena

strength is located at the three-phase contact line in both cases. Furthermore, the narrowing air gap produced by sessile droplets on a hydrophobic substrate leads to an increasing electric field strength with decreasing air gap size.

Analytic solutions of the Laplace equation (Eq. (2.28)) for a sessile droplet on a hydrophobic substrate also confirms the strong field enhancement directly at the three-phase contact line. The field enhancement results from a singularity directly at the three-phase contact line [18, 206, 270]. Hence, the electric field strength should be infinite according to field theory. However, in reality the electric field strength cannot be infinite because of the limited dielectric strength of the materials, which is not taken into account in the classical field theory. The electric field near the three-phase contact line is significantly enhanced (as shown in Fig. 2.8) and might locally exceed the dielectric strength of the surrounding air which causes the generation of *partial discharges*. Partial discharges are only locally electric discharges, which does not necessarily result in a complete breakdown of the insulation distance [133]. In reality, the appearance of partial discharges limits the electric field strength. If only the geometrical arrangement and the dielectric properties would define the maximum field strength, any electric field strength would produce partial discharges caused by the singularity at the three-phase contact line. However, partial discharges only occur for sufficiently high electric field strengths, which are higher than the inception field strength. Thus, the classical field theory does not take into account all physical influencing parameters. An explanation might be that the macroscopic contact angle and the microscopic contact angle are not the same so that the region of the three-phase contact line is not adequately covered by the theory [69]. Furthermore, charges generated by the partial discharges affect the local field distribution, but are not taken into account by the classical field theory.

Even if partial discharges do not lead to a full breakdown of the insulation distance, the discharges affect the insulation performance of nearby insulation materials. Partial discharges mostly occur as locally concentrated and repetitive discharge impulses accompanied by the generation of UV-light and heat, which promote electrical or thermal erosion [128, 133]. This deteriorates the insulation performance and might cause an accelerated ageing of the insulating material. Therefore, partial discharges have to be avoided, especially in high-voltage engineering.

Due to the importance to avoid partial discharges in high-voltage engi-

## 2.4 Macroscopic interaction of sessile droplets and the electric field

neering, the behaviour of water droplets under the influence of electric fields and the corresponding inception field strength for the generation of partial discharges was already investigated by several authors. For instance, the origin of the partial discharges was theoretically examined for a specific experimental setup, where the droplet is in direct contact with the electrode, by Vallet et al. [270]. Besides the theoretical investigations several authors have experimentally explored the partial discharge behaviour of single sessile droplets [25, 186, 187, 189, 207] and multiple droplets [99, 121, 148, 186, 187]. They identified different influencing factors like the electric field strength, volume of the droplet, inclination of the surface, droplet distance as well as the wettability of the substrate. With increasing droplet volume the inception field strength of partial discharges is lowered. The same tendency is given for a decreasing distance between two nearby droplets. Furthermore, the inclination of the surface has an impact on the inception of partial discharges and can lead to larger inception field strength with increasing inclination angle. In addition to this fundamental research on single droplets, the impact of partial discharges on high-voltage insulators was also examined using more realistic geometries such as used in [37, 208, 210]. Based on these investigations partial discharges were identified to accelerate the ageing of silicone rubber surfaces which causes erosion, change of surface colour, loss of hydrophobicity or reduced electrical performance without a visual indication [4, 181, 182, 225, 295].

## 2.4 Macroscopic interaction of sessile droplets and the electric field

Besides the electrical field enhancement near the three-phase contact line, the electric field causes a force on dielectric and charged bodies. Hence, a droplet placed inside an electric field experiences a force depending on the electric field strength and the orientation of the electric field. The force generated by the electric field is a volume force similar to gravity and has to be considered in the momentum equation [263]. Assuming an electrostatic field the force per volume that acts on the dielectric body can be derived using a virtual process [200]. The following derivation of the force is recapitulated according to Panofsky and Phillips [200]. Equation (2.8) defines the work of a force  $\vec{F}$  acting along the distance  $\vec{s}$ .

## 2 Hydrodynamic and electrohydrodynamic phenomena

According to this definition the incremental work  $\delta W$  resulting from the virtual displacement  $\delta \vec{x}$  in the absence of additional mechanical work is defined by

$$\delta W = - \int \vec{F}_V \cdot \delta \vec{x} dV, \quad (2.38)$$

where  $\vec{F}_V$  is the force per volume,  $\delta \vec{x}$  is the virtual displacement and  $V$  is the considered volume. The incremental work is negative because energy has to be provided in order to cause the virtual displacement. Accordingly, this work equals a change of the energy in the system. A different representation is given by the rate of change of energy, which is given by

$$\frac{dW}{dt} = - \int \vec{F}_V \cdot \vec{U} dV, \quad (2.39)$$

where  $\vec{U} = d\vec{x}/dt$  and defines an arbitrary velocity field in the dielectric. The change of energy resulting from the virtual displacement  $\delta \vec{x}$  can also be expressed in terms of the electric field  $\vec{E}$  and field displacement  $\vec{D}$  as stated in the following equation

$$\delta W = \frac{1}{2} \delta \int \vec{E} \cdot \vec{D} dV. \quad (2.40)$$

Using the correlation between the electric field and the field displacement given by Eq. (2.21) the incremental work can be expressed by

$$\delta W = \frac{1}{2\epsilon_0} \int D^2 \delta(1/\epsilon_r) dV + \int \vec{E} \cdot \delta \vec{D} dV \quad (2.41)$$

$$= -\frac{\epsilon_0}{2} \int E^2 \delta \epsilon_r dV + \int \vec{E} \cdot \delta \vec{D} dV. \quad (2.42)$$

The first term on the right-hand side of Eq. (2.42) represents the change in energy by an incremental change of the relative permittivity. The second term on the right-hand side determines the change of energy by the change of the displacement field and can be expressed in terms of the electric potential and charge density instead of the electric field and field displacement by using Eqs. (2.11) and (2.20) which yields

$$\int \vec{E} \cdot \delta \vec{D} dV = - \int \nabla \phi \cdot \delta \vec{D} dV = \int \phi \delta q dV. \quad (2.43)$$

Inserting Eq. (2.43) in Eq. (2.42) results in [200]

$$\delta W = \int \left( \phi \delta q - \frac{\epsilon_0}{2} E^2 \delta \epsilon_r \right) dV. \quad (2.44)$$

## 2.4 Macroscopic interaction of sessile droplets and the electric field

Based on this equation the rate of change of energy can be calculated by differentiating the equation with respect to time:

$$\frac{dW}{dt} = \int \left( \phi \frac{\partial q}{\partial t} - \frac{\varepsilon_0}{2} E^2 \frac{\partial \varepsilon_r}{\partial t} \right) dV. \quad (2.45)$$

To further simplify Eq. (2.45) the expressions for  $\partial q/\partial t$  and  $\partial \varepsilon_r/\partial t$  have to be determined depending on the arbitrary velocity field  $\vec{\mathbf{u}}$ . According to Panofsky and Phillips [200] the partial derivatives of the relative permittivity and the charge density can be determined using the conservation equations for charge and mass as well as the total derivative of both quantities. This results in the following expressions

$$\frac{\partial q}{\partial t} = -\nabla \cdot (q\vec{\mathbf{u}}), \quad (2.46)$$

$$\frac{\partial \varepsilon_r}{\partial t} = -\frac{d\varepsilon_r}{d\rho} \rho \left( \nabla \cdot \vec{\mathbf{u}} \right) - (\nabla \varepsilon_r) \cdot \vec{\mathbf{u}}. \quad (2.47)$$

Inserting Eq. (2.46) and Eq. (2.47) in Eq. (2.45) yields

$$\begin{aligned} \frac{dW}{dt} = \int \left[ -\phi \nabla \cdot (q\vec{\mathbf{u}}) \right. \\ \left. + \frac{\varepsilon_0}{2} E^2 \left( \frac{d\varepsilon_r}{d\rho} \rho \right)_T \left( \nabla \cdot \vec{\mathbf{u}} + \left( \frac{\varepsilon_0}{2} E^2 \nabla \varepsilon_r \right) \cdot \vec{\mathbf{u}} \right) \right] dV. \end{aligned} \quad (2.48)$$

Simplifying this equation and using the correlation defined in Eq. (2.11) results in the rate of change of energy depending on the electric field, the electric charge and the material properties

$$\frac{dW}{dt} = \int \left[ q\vec{\mathbf{E}} + \frac{\varepsilon_0}{2} E^2 \nabla \varepsilon_r - \frac{\varepsilon_0}{2} \nabla \left( \rho E^2 \left( \frac{d\varepsilon_r}{d\rho} \right)_T \right) \right] \cdot \vec{\mathbf{u}} dV. \quad (2.49)$$

A comparison of Eqs. (2.49) and (2.39) yields the force per volume  $\vec{\mathbf{F}}_V$  [200, 263]

$$\vec{\mathbf{F}}_V = \underbrace{q\vec{\mathbf{E}}}_{\text{Coulomb force}} - \underbrace{\frac{\varepsilon_0}{2} E^2 \nabla \varepsilon_r}_{\text{Dielectric force}} + \underbrace{\frac{\varepsilon_0}{2} \nabla \left[ \rho E^2 \left( \frac{d\varepsilon_r}{d\rho} \right)_T \right]}_{\text{Electrostrictive force}}, \quad (2.50)$$

where the first term on the right-hand side describes the *Coulomb force*, which determines the force per volume on a body containing electric

## 2 Hydrodynamic and electrohydrodynamic phenomena

charges and is the most dominant force in constant electric fields [263]. Furthermore, the second term is called *dielectric force*, which defines the force on a non-homogeneous dielectric liquid. This term only dominates in case of alternating electric fields if the inverse of the frequency is much smaller than the charge relaxation time of the liquid  $1/f \ll \tau_{\text{el}} = \varepsilon/\kappa$  [263]. Furthermore, the charge of the droplet has to be sufficiently small. The third term is called *electrostrictive force*, which only occurs in dielectric materials and can be interpreted as a modification of the fluid pressure in terms of liquid [263]. In case of an incompressible fluid, the electrostrictive force can be neglected [80]. Note that the Nabla operator is a vector, and thus Eq. (2.50) is a regular vectorial equation.

In case of a perfectly conducting liquid ( $\tau_{\text{el}}/\tau_{\text{char}} \ll 1$ ) the droplet itself is field-free because of electric induction [18]. The net charges of the droplet are located at the interface of the droplet due to the repulsive force of charges with the same polarity. As a consequence, the electric field lines and the force resulting from the electric field are perpendicular to the surface of the droplet [18]. The reason for this are the vanishing electric field inside the droplet and the continuity conditions of the tangential component of the electric field on the interface of the droplet, which results in a vanishing electric field tangentially aligned on the surface. Due to symmetry, a perfectly symmetric droplet would always experience a net force of zero. However, small disturbances of the homogeneous electric field are always present. These disturbances are caused by the net charge distribution inside the droplet or the experimental setup and cause a non-homogeneous electric field resulting in a non-zero force acting on the droplet. The resulting force induces a distortion of the droplet and can also be interpreted in terms of an increased pressure inside the droplet, which is often referred to the *electrostatic pressure*. In case of a perfect dielectric ( $\tau_{\text{el}}/\tau_{\text{char}} \gg 1$ ) the electric field inside the droplet does not completely vanish. However, due to the high relative permittivity of water compared to air and most substrates the electric field is strongly depressed in the droplets, which leads to an almost field-free droplet.

The force on the surface of the droplet has two components, namely a normal and a perpendicular component, which satisfy the boundary conditions at the interface as defined by Eqs. (2.30) and (2.31). Note, that the high purity water used in this study can be assumed as a perfect conductor in case of alternating and constant electric fields because the relaxation time ( $\tau_{\text{el}} = \varepsilon/\kappa$ ) is in the order of  $10^{-6}$  s to  $10^{-4}$  s, and therefore much lower than the order of the characteristic time of the electric fields ( $10^{-2}$  s

## 2.4 Macroscopic interaction of sessile droplets and the electric field

to 1 s) tested in this investigation. Nevertheless, in electro-hydrodynamics electrical and hydrodynamic phenomena are coupled so that the hydrodynamic timescale is also important. Both characteristic times determine the behaviour of the droplet. Fast hydrodynamic processes like a droplet impact can take place on a smaller timescale compared to the charge relaxation time so that the droplet is assumed as a dielectric during impact. In contrast, a resting droplet with an almost infinite characteristic hydrodynamic time has to be assumed as a perfect conductor because charges have enough time to adjust themselves to the boundary conditions [211].

The force resulting from the electric field is directly coupled with the momentum equation of the droplet. Consequently, the electric field can produce a droplet motion, deformation or oscillation depending on the type of the electric field. Droplets exposed to constant electric fields experience a constant force because the electric field strength is constant. The constant force leads to a deformation which might result in a movement of the droplet [13]. In contrast, an alternating electric field results in an alternating force. The frequency of the force acting on the droplet mainly depends on the dominant physical mechanism and the dominant force with respect to the Coulomb, dielectric and electrostrictive force. In case of a large charge  $Q$  on the droplet and a sufficiently small electric field strength, the Coulomb force, which is directly proportional to the electric field, is dominant. Hence, the force on the droplet has the same frequency as the applied electric field. In contrast, an uncharged droplet is not affected by the Coulomb force and only experiences the dielectric force. The electrostriction term does not cause a net force on the droplet by integrating the relevant term of Eq. (2.50) over a large portion of the dielectric with extremities in a field-free region [200]. Under this assumption the electrostriction term vanishes and can be neglected. The dielectric force is proportional to the square of the electric field, so that the force acting on the droplet is proportional to the doubled frequency of the electric field.

Figure 2.9 illustrates the correlation between the individual fractions of the force depending on the electric field strength and the charge of the droplet. Applying a sinusoidal voltage with a frequency  $f_{AC}$  leads to an electric field of the form  $\vec{E}(t) = \hat{E} \sin(\omega t) \vec{e}$ , where  $\hat{E}$  is the amplitude of the electric field,  $\omega$  is the angular frequency and  $\vec{e}$  is the unit vector. The two regimes shown in Fig. 2.9 characterize the different regimes for charged and uncharged droplets. Both the Coulomb and the dielectric force are acting on the droplet simultaneously, but usually one force is

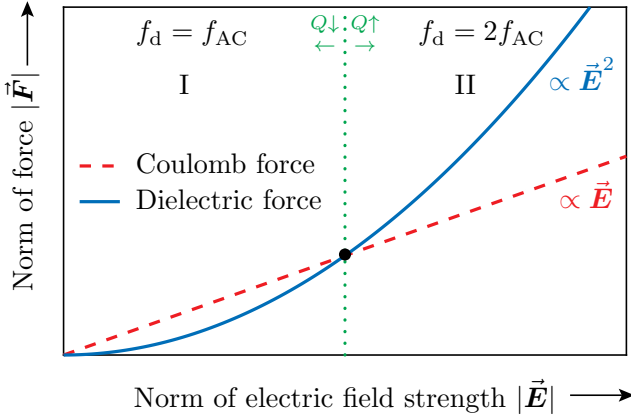


Figure 2.9: Principle of forces  $\vec{F}$  acting on a dielectric body depending on the electric charge  $Q$  and the electric field strength  $E$  resulting from an alternating electric field. The two different regimes I and II characterize the oscillation frequency of the droplet  $f_d$  depending on the frequency of the applied voltage  $f_{AC}$ . Reprinted (adapted) with permission from [150], © 2019 IEEE.

dominant. Regime I defines the regime for charged droplets. The amount of charge on the droplet is large enough so that the Coulomb force is dominant. In this case the droplet oscillates with the same frequency as the applied electric field, due to  $f_d \propto \vec{F}_V \propto \vec{E} \propto \sin(\omega t)$ . This behaviour can be observed for low electric field strengths and a sufficient amount of charge. Increasing the electric field strength leads to a different behaviour which is characterized by regime II. In this regime the dielectric force is dominant and induces droplet oscillations with twice the frequency of the applied electric field, due to  $f_d \propto \vec{F}_V \propto \vec{E}^2 \propto 1 - \cos(2\omega t)$ . The resulting force on the droplet contains both the Coulomb and the dielectric force. As a consequence, the behaviour of the droplet is determined by the electric field strength and the electric charge of the droplet. The size of the two regimes is also influenced by the electric charge and electric field strength. The higher the electric charge, the larger is the gradient of the linear slope (dashed line in Fig. 2.9) of the Coulomb force, which leads to an intersection of both forces at higher electric field strength. Conse-

## 2.4 Macroscopic interaction of sessile droplets and the electric field

quently, increasing the electric charge increases regime I for a constant electric field strength and vice versa. However, sufficiently high electric field strengths always cause a dominant dielectric force resulting from the quadratic dependence of the force on the electric field strength.

Besides the electric field strength and the electric charge, the droplet volume significantly influences the droplet movement. The oscillatory force generated by the electric field can cause resonance of the droplet, which can finally result in droplet movement for large amplitudes caused by high electric field strengths. The resonance frequencies of a liquid droplet (consisting, for instance, of water) surrounded by a fluid having a much lower density ( $\rho_d \gg \rho_{\text{air}}$ ) such as air under the impact of an electric field are given by [138, 237]

$$f_{\mathcal{N}} = \left[ \frac{\mathcal{N}(\mathcal{N} - 1)(\mathcal{N} + 2)\gamma}{12V_d\pi\rho_d} \right]^{1/2} \quad \text{for } \mathcal{N} \geq 2, \quad (2.51)$$

where  $\mathcal{N}$  is an integer corresponding to the different modes,  $\rho_d$  is the droplet density and  $\gamma$  is the surface tension of the water droplet with respect to the surrounding fluid (air). Note that any viscosity effects are neglected, which mainly damp the oscillation of the droplet. Equation (2.51) is only valid for small oscillations, i.e. only for low electric field strengths. High electric field strengths generate large droplet deformations, which are not covered by the theoretical model. For a surrounding medium with a similar density compared to water ( $\rho_d \approx \rho_{\text{surr}}$ ), like oil, the resonance frequencies are defined by a more general relation [138]

$$f_{\mathcal{N}} = \left[ \frac{\mathcal{N}(\mathcal{N} + 1)(\mathcal{N} - 1)(\mathcal{N} + 2)\gamma}{12V_d\pi[(\mathcal{N} + 1)\rho_d + \mathcal{N}\rho_{\text{surr}}]} \right]^{1/2} \quad \text{for } \mathcal{N} \geq 2. \quad (2.52)$$

As found by Schütte and Hornfeldt [237], the resonance frequencies of a free droplet, which is described by Eq. (2.51), can also be used to accurately determine the resonance frequencies of a sessile droplet on a hydrophobic substrate. However, the different boundary conditions, namely the broken symmetry, produce additional resonance frequencies in case of a sessile droplet [237]. The mode number is defined by  $\mathcal{N} - 1$ , because  $\mathcal{N} = 0$  would lead to a droplet movement and  $\mathcal{N} = 1$  is associated with droplet expansion, which is not stable [73]. Hence, the first resonance mode is given for  $\mathcal{N} = 2$ . Figure 2.10 shows the first three characteristic modes of a sessile droplet under the influence of an electric field. The orientation of the electric field is tangentially aligned to the substrate.

## 2 Hydrodynamic and electrohydrodynamic phenomena

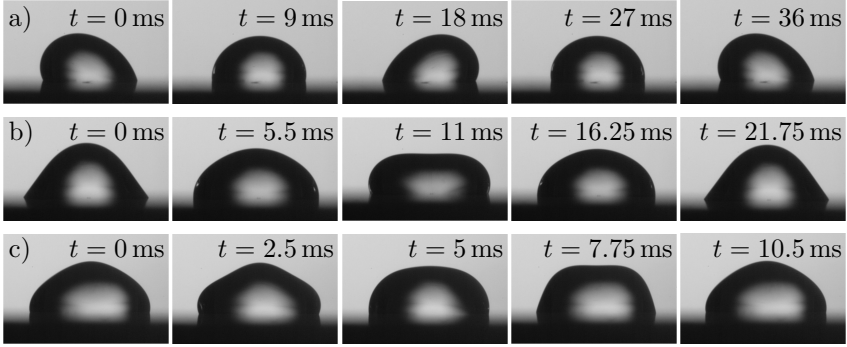


Figure 2.10: One cycle of the first three modes for  $\mathcal{N} = 2, 3, 4$  of uncharged droplets. a) Example of Mode 1 ( $\mathcal{N} = 2$ ) of a  $20 \mu\text{l}$  droplet at  $27 \text{ Hz}$  and  $\hat{E} = 3.81 \text{ kV/cm}$ , b) example of Mode 2 ( $\mathcal{N} = 3$ ) of a  $30 \mu\text{l}$  droplet at  $23 \text{ Hz}$  and  $\hat{E} = 4.67 \text{ kV/cm}$  and c) example of Mode 3 ( $\mathcal{N} = 4$ ) of a  $60 \mu\text{l}$  droplet at  $48 \text{ Hz}$  and  $\hat{E} = 7.37 \text{ kV/cm}$ . Reprinted figure (adapted) with permission from [156]. Copyright 2020 by the American Physical Society.

The first resonance mode shown in Fig. 2.10a is characterized by a principle motion parallel to the substrate and is often called *rocking* [52], *rachetlike* [194] or *bending motion* [164]. The droplet periodically leans sideways in the gap between the electrodes and changes its direction with a characteristic frequency while the three-phase contact line is still pinned. In contrast, the second mode has a principle direction perpendicular to the substrate as shown in Fig. 2.10b. Even if the undisturbed electric field is tangentially aligned to the substrate the droplet oscillates perpendicularly to the substrate. The motion is characterized by a periodically upsetting and stretching of the droplet. The third resonance mode is shown in Fig. 2.10c and is characterized by surface oscillations with a characteristic number of steady nodes on the surface. For  $\mathcal{N} = 3$  the number of steady nodes on the surface yields two. The oscillation of the droplets is characterized by a periodically bulging between the nodes. Modes of higher orders are characterized by a higher number of steady nodes on the surface. Accordingly, the behaviour of droplets oscillating in higher

## 2.4 Macroscopic interaction of sessile droplets and the electric field

orders are assumed to have a similar behaviour as droplets oscillating in third resonance mode.

The different oscillation modes induce periodic changes of the contact angle, which significantly influences the electric field distribution in that region. As already mentioned, the solution of the Laplace equation depends on the droplet shape, especially at the three-phase contact line, and theoretically has a singularity directly at the three-phase contact line [18]. Hence, the electric field strength should be infinite at this point according to theory. However, in reality the electric field strength cannot be infinite, so that the dielectric strength of the gas and the occurring partial discharges limit the electric field strength. Nevertheless, the local electric field directly at the three-phase contact line is enhanced so that the net charges of the droplet are concentrated in this region. From a macroscopic point of view the force caused by the electric field can be assumed to be concentrated at the three-phase contact line [18]. Using this macroscopic approach Young's equation (Eq. (2.2)) can be modified to take into account the impact of the electric field. The resulting equation is named Young-Lippmann equation because among others Lippmann [146] investigated the impact of electric field on the wetting of liquids. The Young-Lippmann equation modifies the interfacial tension between the substrate and the liquid

$$\gamma_{w,\ell,el} = \gamma_{w,\ell,0} - \gamma_{el}, \quad (2.53)$$

where  $\gamma_{w,\ell,el}$  is the modified interfacial tension between the substrate and the liquid. In addition,  $\gamma_{w,\ell,0}$  is the interfacial tension between the substrate and the liquid without an electric field and  $\gamma_{el}$  is the artificial interfacial tension resulting from the electric field. Inserting Eq. (2.53) in Eq. (2.2) results in

$$\gamma_{g,w} = \gamma_{w,\ell,el} + \gamma_{\ell,g} \cos(\theta_{el}), \quad (2.54)$$

where  $\theta_{el}$  is the resulting contact angle under the impact of the electric field. A comparison of Eqs. (2.2) and (2.54) expresses the contact angle under the impact of an electric field and the contact angle without an electric field [211]

$$\cos(\theta_{el}) = \cos(\theta) + \frac{\gamma_{el}}{\gamma_{\ell,g}}. \quad (2.55)$$

A more common representation of this equation is given by [115, 142]

$$\cos(\theta_{el}) = \cos(\theta) + \frac{CU^2}{2\gamma_{\ell,g}}, \quad (2.56)$$

## 2 Hydrodynamic and electrohydrodynamic phenomena

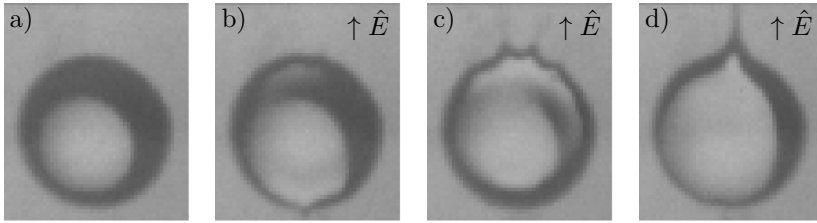


Figure 2.11: Formation of a Taylor cone by a sessile droplet ( $d_d \approx 1.00$  mm) under the impact of a switching impulse voltage with an electric field strength  $\hat{E} = 13.04$  kV/cm in top view. a) droplet in absence of an electric field, b)-c) formation of the Taylor cone and d) Taylor cone with jet (emission of droplets).

where  $C$  is the capacitance of dielectric layer (for the electrowetting on a dielectric [115]) and  $U$  is the applied voltage between the electrodes. Consequently, the presence of an electric field causes an altered contact angle, which is lower than the equilibrium contact angle in absence of an electric field. The electric field can be used to increase the wettability of a surface without changing the properties of the substrate, and thus is a reversible process. The active manipulation of the surface wetting is called *electrowetting* [183, 219]. Most applications like electrostatic lenses use the electric field to manipulate the contact angle or the curvature of the fluid in a desired manner. In contrast to the oscillations generated by the electric field strength, electrowetting is associated with a contact line movement. Generally, the state of electrowetting is achieved for high electric field strength, which results in a large change of the contact angle that exceeds the advancing contact angle.

In addition to the changed contact angle, the presence of an electric field provokes deformations of the droplet. The shape of the droplet is defined by the forces present at the interface of the droplet, namely gravity, surface tension and the force resulting from the electric field. Taylor [259] observed the formation of a conical shape and found that droplets exposed to high electric field strength can become unstable, similar to highly charged droplets. The conical shape of the droplet is called Taylor cone and is accompanied by the emission of tiny charged droplets [136].

## 2.4 Macroscopic interaction of sessile droplets and the electric field

A Taylor cone is characterized by a semi-vertical angle of  $49.3^\circ$  [259]. The formation of tiny droplets is associated with stresses tangentially aligned to the interface of the droplet [41] and results from the conical shape becoming unstable. Hence, the formation of small droplets generated by a Taylor cone can only be observed for dielectric or leaky-dielectric liquids. In case of a perfectly conducting liquid ( $\tau_{\text{el}}/\tau_{\text{char}} \ll 1$ ) the field inside the droplet and the tangential component of the electric stress on the droplet interface vanish, and consequently no Taylor cone is formed. However, even a droplet consisting of a conducting liquid can be deformed and can generate a conical shape [42]. The formation of the Taylor cone is not necessarily associated with electric charges [166, 195] but can also assist the formation of the Taylor cone especially for a droplet which is in contact with an electrode. An example for the formation of a Taylor cone by a sessile droplet is shown in Fig. 2.11. The droplet is clearly affected by the electric field and forms a cone. A liquid jet originates from the cone resulting in the formation of tiny droplets. Consequently, high electric fields precipitate the disintegration of the droplets similar to electric charges.

In summary, sessile droplets are significantly influenced by the presence of an electric field. The shape and motion of the droplet are mainly determined by the electric field strength and are assumed to be influenced by the presence of charges. In addition, the droplet interacts with the electric field and results in electrical critical points at the three-phase contact line. The interaction between the fluid dynamics of a sessile droplet and the associated electrical phenomena yields a complex system with various influencing factors. The individual influencing factors interact with each other, and all together determine the behaviour of the droplet under the impact of an electric field.



### 3 Ice nucleation

The freezing of liquid water is associated with a first-order phase transition, which is initiated by ice nucleation [117]. Ice nucleation can be defined as the first presence of a thermodynamically stable ice phase [266] and initiates the transition from a meta-stable to a thermodynamically stable state [117]. The meta-stable state, given by a locally unstable thermodynamic state of the liquid, is a necessary prerequisite for nucleation [71, 117, 216]. In case of ice nucleation the meta-stable state results from a liquid temperature below the melting temperature. The resulting temperature difference is called degree of *supercooling*. Hence, the supercooling is the thermodynamic driving force of the phase transition of the supercooled liquid to a lower-energy state [117]. Whether ice nucleation occurs is determined by the formation of an ice nucleus of a sufficient size to overcome the energy barrier of Gibbs free energy  $\Delta G$  [216]. The formation of a new phase inevitably results in the formation of a new interface between the liquid and the solid phase, which requires energy to form, because individual bonds between water molecules are broken and water-ice bonds are generated [216]. An ice nucleus originates from fluctuations in time and space of the temperature or density of the supercooled liquid [216] and is given by a spontaneous formation of a molecular cluster (germ) of sufficient size. This molecular cluster has similar properties as the new phase in terms of density [117]. The spontaneous formation of a germ mainly depends on the stochastic motion of the molecules, and consequently nucleation is a stochastic process [216, 266]. The stochastic nature of nucleation leads to time-consuming experiments, which necessitate numerous repetitions of the experiments to generate reliable data. Based on experimental data, several theories have been developed to describe and predict the nucleation behaviour. Amongst others, the *classical nucleation theory (CNT)* describes ice nucleation with respect to its stochastic nature.

In general, ice nucleation can be divided into *homogeneous* and *heterogeneous* ice nucleation. Homogeneous ice nucleation is characterized by ice nucleation inside a supercooled liquid without the influence of any foreign substances [266]. Thus, this type of nucleation only depends on the stochastic motion of the molecules. In contrast, heterogeneous ice nucleation is influenced by a foreign substance, which promotes ice nucleation [106, 266]. The foreign substance, often referred to as *ice nucleating*

### 3 Ice nucleation

*particle (INP)* [266], can be any particle like dust particles, volcanic ash, biomass or a substrate in contact with the supercooled liquid [114]. In general, the nucleation temperature is higher in case of heterogeneous compared to homogeneous ice nucleation (lower degree of supercooling), because the foreign substances reduce the necessary energy barrier for the phase transition, and thus promotes nucleation. Both homogeneous and heterogeneous ice nucleation are of great relevance for different research areas, because any kind of icing is initiated by ice nucleation. Both physical mechanisms are present in nature, but heterogeneous ice nucleation is more common in technical applications, because technical processes are not perfectly clean and often involve foreign substances or substrates.

## 3.1 Homogeneous ice nucleation

Homogeneous ice nucleation is only influenced by molecular motion of the liquid phase and not by other foreign substances. The energy barrier necessary for the transition from supercooled liquid to ice can be determined by the difference in Gibbs free energy of both thermodynamic states  $\Delta G = G_2 - G_1$ , where  $G_1$  and  $G_2$  are the Gibbs free energies before and after nucleation, respectively [213, 216]. The Gibbs free energy of pure supercooled liquid  $G_1$  is given by:

$$G_1 = VG_{V,\ell}, \quad (3.1)$$

where  $V$  is the liquid and total volume, because no ice is present, so that the liquid volume equals the total volume  $V = V_\ell$ . Furthermore,  $G_{V,\ell}$  is the Gibbs free energy of the liquid with respect to the volume. During nucleation a new interface is generated between the solid and the liquid phase. Hence, the Gibbs free energy after nucleation is given by

$$G_2 = V_\ell G_{V,\ell} + V_s G_{V,s} + A_{s,\ell} \gamma_{s,\ell}, \quad (3.2)$$

where  $\gamma_{s,\ell}$  is the interfacial tension between the solid and the liquid,  $A_{s,\ell}$  is the surface area of the solid in contact with the liquid, and  $V_\ell$  and  $V_s$  are the volume of the liquid and the solid phase, respectively. The index  $\ell$  labels properties of the liquid, whereas the index  $s$  indicates properties of the solid phase. The first term on the right-hand side of Eq. (3.2) defines the Gibbs free energy of the liquid volume. Similarly, the second term defines the Gibbs free energy of the solid volume. Note that after

### 3.1 Homogeneous ice nucleation

nucleation the bulk volume  $V$  is defined by  $V = V_s + V_\ell$ . The third term on the right-hand side defines the interfacial energy between the solid and liquid phase, which results from the generation of a new interface. Thus, the difference in energy  $\Delta G = G_2 - G_1$  is given by

$$\Delta G = -V_s \Delta G_V + A_{s,\ell} \gamma_{s,\ell}, \quad (3.3)$$

where  $\Delta G_V = G_{V,\ell} - G_{V,s}$ , which defines the change in Gibbs free energy with respect to the volume. Assuming a constant heat capacity of the solid and the liquid phase  $\Delta G_V$  can be approximated by [213]

$$\Delta G_V = \frac{L_V \Delta T}{T_m}, \quad (3.4)$$

where  $L_V$  is the latent heat of fusion per unit volume,  $\Delta T$  is the degree of supercooling and  $T_m$  is the melting temperature. The degree of supercooling is defined by the temperature difference between the melting temperature  $T_m$  and the current temperature  $T$ , which yields  $\Delta T = T_m - T$ . Assuming a spherical solid phase with a radius  $R$  and an isotropic interfacial tension  $\gamma_{s,\ell}$  the difference in energy can be expressed by [213]:

$$\Delta G = -\frac{4}{3}\pi R^3 \Delta G_V + 4\pi R^2 \gamma_{s,\ell}. \quad (3.5)$$

The first term on the right-hand side of Eq. (3.5) defines the release of the latent heat of fusion during the phase transition, and the second term defines the energy necessary to form a new interface between the solid and the liquid phase. Besides the properties of the liquid and the solid, both terms depend on the radius  $R$  of the (spherical) solid phase. The dependence of the energy barrier with respect to the radius  $R$  of the solid phase is shown in Fig. 3.1.

The two dashed lines show the dependence of the volume free energy and the interfacial energy on the radius  $R$ . While the volume free energy is proportional to  $-R^3$ , the interfacial energy is proportional to  $R^2$ . The resulting Gibbs free energy is given by the sum of both terms and is shown as a solid line. The formation of a new interface results in an increase of the Gibbs free energy, which leads to an energy barrier. In contrast, the release of latent heat of fusion during phase transition lowers the Gibbs free energy and results in a lower-energy state. The critical energy barrier  $\Delta G^*$  is defined by the maximum of the Gibbs energy and can be characterized by the critical radius  $R^*$ . To further minimize the Gibbs

### 3 Ice nucleation

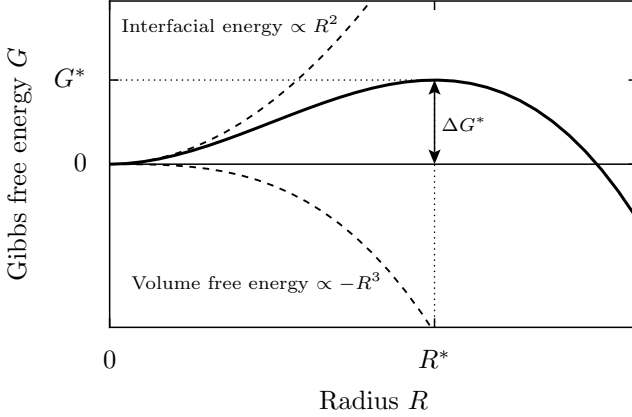


Figure 3.1: Gibbs free energy  $G$  depending on the radius  $R$ . The critical radius  $R^*$  defines the energy barrier  $\Delta G^*$  necessary to initiate the phase transition.

free energy and to reach a lower-energy state, the critical energy barrier  $\Delta G^*$  must be overcome, which strongly depends on the size of the solid phase. For  $R < R^*$  the unstable solid phase is named ice germ [269], because it vanishes over time. The phase transition between liquid and solid is not initiated, because reducing the size of an ice germ leads to a lower energy state, which is more favourable than increasing the size of the germ. Accordingly, the energy necessary to overcome the energy barrier is not present in this case. In contrast, a solid phase with size  $R \geq R^*$  will grow in size, because increasing the size will further minimize the Gibbs free energy as indicated by Fig. 3.1. In this case the solid phase is thermodynamically stable and will increase in size. Henceforth, the solid phase is called ice nucleus [213]. In consequence, only a nucleus with a certain size can initiate the phase transition between liquid and solid, which transfers the resulting phase into a lower-energy state.

The critical size  $R^*$  of a nucleus is defined by the maximum of  $\Delta G$  given by Eq. (3.5), which can be calculated by:

$$\frac{d(\Delta G)}{dR} = 0, \quad (3.6)$$

and leads to

$$R^* = \frac{2\gamma_{\text{s},\ell}T_{\text{m}}}{L_V\Delta T}. \quad (3.7)$$

The critical energy barrier  $\Delta G^*$  can be determined by inserting Eq. (3.7) into Eq. (3.5), which yields [213]

$$\Delta G^* = \frac{16\gamma_{s,\ell}^3 T_m^2}{3L_V^2 \Delta T^2}. \quad (3.8)$$

As indicated by Eq. (3.8) the critical energy barrier  $\Delta G^*$  depends amongst the properties of the liquid like  $L_V$  or  $T_m$  on the degree of supercooling  $\Delta T$ . The larger the degree of supercooling, the lower is the critical energy barrier to initiate the phase transition. Hence, the higher the degree of supercooling of a liquid, the more favourable is the formation of an ice nucleus of sufficient size  $R \geq R^*$ . In addition, the critical size of the ice nuclei also depends on the degree of supercooling, so that according to Eq. (3.7) the critical size decreases with increasing degree of supercooling. The decrease of the critical size depending on the degree of supercooling is shown in Fig. 3.2. The critical radius is calculated using an interfacial tension between ice and water of  $\gamma_{s,\ell} \approx 0.032 \text{ N/m}$  [100], a latent heat of fusion per volume of  $L_V \approx 333.12 \cdot 10^6 \text{ J/m}^3$  [50] (assuming a density of  $\rho = 999.84 \text{ kg/m}^3$  at  $0^\circ\text{C}$  [113]) and a melting temperature of  $T_m = 273.15 \text{ K}$ . Due to the fact that the formation of an ice nucleus depends on the molecular motion, the formation of small germs is much more favourable than the formation of large germs. Accordingly, the formation of an ice nucleus at low degrees of supercooling is less common than for large supercoolings, which is shown by the rapid increase of the critical radius for low degrees of supercooling in Fig. 3.2.

Homogeneous ice nucleation is often characterized by the *nucleation rate*, which defines the frequency of ice nucleation events per unit volume and unit time [269]. In consequence, the nucleation rate is inevitably connected to the formation of an ice nucleus of a certain size, which leads to the phase transition. A nucleation event is observed if an ice nucleus of sufficient size is present. Accordingly, the size distribution of ice germs inside the supercooled liquid is essential. The number of spherical clusters  $N_R$  with a radius of  $R$  in the supercooled liquid is given by a Boltzmann distribution [213]

$$N_R = N_0 \exp\left(-\frac{\Delta G_R}{k_b T}\right), \quad (3.9)$$

where  $N_0$  is the number of all atoms in the liquid,  $\Delta G_R$  is the free energy associated with a cluster of size  $R$  and  $k_b$  is the Boltzmann constant. Note that Eq. (3.9) is valid for all  $R$  if the temperature is higher than

### 3 Ice nucleation

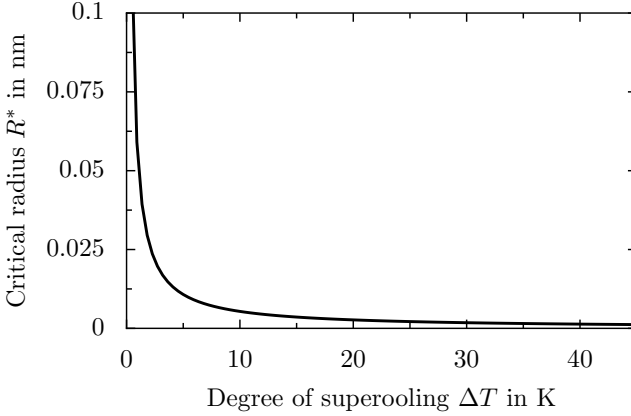


Figure 3.2: Critical radius of nucleus  $R^*$  depending on the degree of supercooling  $\Delta T$  according to Eq. (3.7).

the melting temperature  $T > T_m$ . In contrast, for temperatures  $T < T_m$  the equation is only valid for  $R < R^*$ , because ice germs larger than  $R^*$  are already solid ice particles and not part of the liquid any more [213]. Hence, a further increase of the size always leads to  $R > R^*$  and results in nucleation.

To determine the nucleation rate two physical phenomena have to be taken into account. First, the formation of an ice nucleus of sufficient size and second the attachment of atoms from the liquid bulk to the ice nucleus, which is associated with germ growth. The number of critical ice germs  $\mathcal{C}^*$  is obtained by inserting  $\Delta G^*$  into Eq. (3.9), which yields:

$$\mathcal{C}^* = \mathcal{C}_0 \exp\left(-\frac{\Delta G^*}{k_b T}\right), \quad (3.10)$$

where  $\mathcal{C}_0$  is the number of atoms per unit volume. Assuming that individual atoms are attaching to the cluster with a frequency of  $f_{0,c}$  the nucleation rate can be defined by [213]

$$\mathcal{J}_{\text{hom}} = f_{0,c} \mathcal{C}_0 \exp\left(-\frac{\Delta G^*}{k_b T}\right). \quad (3.11)$$

The frequency  $f_{0,c}$  is a complex function influenced by the vibration frequency of the atoms, the activation energy for diffusion in the liquid

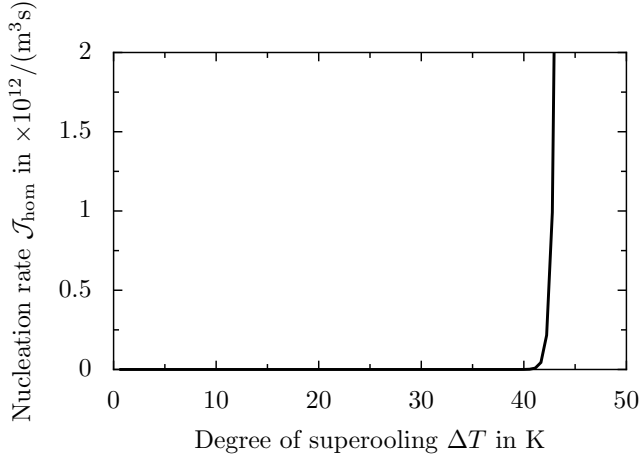


Figure 3.3: Homogeneous nucleation rate  $\mathcal{J}_{\text{hom}}$  depending on the degree of supercooling  $\Delta T$ .

and the surface area of the critical nucleus [213]. Inserting Eq. (3.8) in Eq. (3.11) results in the nucleation rate depending on the degree of supercooling

$$\mathcal{J}_{\text{hom}} = f_{0,c} \mathcal{C}_0 \exp\left(-\frac{16\gamma_{s,\ell}^3 T_m^2}{3k_b T L_V^2 (\Delta T)^2}\right), \quad (3.12)$$

which describes the number of nucleation events per unit volume and unit time. The unit of the nucleation rate is  $\text{m}^{-3}\text{s}^{-1}$ . The homogeneous nucleation rate  $\mathcal{J}_{\text{hom}}$  depending on the degree of supercooling  $\Delta T$  is shown in Fig. 3.3 and is calculated using the following parameters:  $f_{0,c} \approx 10^{11} \text{ Hz}$  (approximation based on the data for pure metal)[213, 235],  $\mathcal{C}_0 = N_A/18.02 \cdot 10^{-6} \text{ m}^3/\text{mol} = 3.35 \cdot 10^{28} \text{ m}^{-3}$  ( $N_A$  being the Avogadro constant  $N_A = 6.022 \cdot 10^{23} \text{ 1/mol}$ ),  $\gamma_{s,\ell} \approx 0.032 \text{ N/m}$  [100, 122],  $T_m = 273.15 \text{ K}$ ,  $k_b = 1.381 \cdot 10^{-23} \text{ m}^2 \text{ kg}/(\text{s}^2 \text{ K})$ ,  $L_V = 333.12 \cdot 10^6 \text{ J/m}^3$  [50] and  $T = T_m - \Delta T$ . As shown in Fig. 3.3, the nucleation rate is constant for a wide range of supercoolings and rapidly increases for  $\Delta T > 41 \text{ K}$ .

In general, the nucleation rate is calculated from experimental results, which contain the number of liquid and frozen droplets depending on the temperature. The exact number of atoms inside the droplets  $\mathcal{C}_0$  is

### 3 Ice nucleation

not known. Furthermore, Eq. (3.3) is defined for a unit volume, whereas experiments commonly use droplets of different sizes [216]. Hence, the nucleation rate should be determined using the individual nucleation events of a droplet ensemble. The droplet ensemble consists of  $N_0$  droplets with a volume of  $V_d$ . It is assumed that ice nucleation inside the droplets is not influenced by nearby droplets, so that each droplet defines a specific volume to investigate ice nucleation. Furthermore, it is presumed that the phase transition in each droplet is the result of a single nucleation event [216]. This assumption is valid for homogeneous nucleation, because the growth velocity of ice is very fast at high degrees of supercooling [216]. In consequence, the first nucleus already initiates the phase transition and causes the droplet to freeze. Furthermore, the latent heat of fusion released during the transition from supercooled liquid water to ice increases the temperature and reduces the probability of the formation of a second ice nucleus [216]. Due to the fact that each ice nucleus causes the droplet to freeze, the number of frozen droplets  $N_s$  produced during the time interval  $dt$  in the volume  $N_\ell V_d$  is given by [216]

$$dN_s = N_\ell V_d \mathcal{J}(T) dt. \quad (3.13)$$

Taking into account a constant number of droplets during an experiment leads to  $dN_s = -dN_\ell$ , because an increasing number of frozen droplets inevitably reduces the number of liquid droplets [216]. Replacing the frozen droplets  $N_s$  with the number of liquid droplets  $N_\ell$  results in

$$dN_\ell = -N_\ell V_d \mathcal{J}(T) dt. \quad (3.14)$$

Eq. (3.14) is a differential equation with respect to time. Integrating the equation using the number of droplets initially present in the ensemble  $N_0$  at  $t = 0$  and  $N_\ell$  as the number of liquid droplets at a specific time  $t$  yields [216]

$$N_\ell = N_0 \exp[-V_d \mathcal{J}(T)t]. \quad (3.15)$$

Consequently, the nucleation rate for a constant temperature is given by

$$\mathcal{J}(T) = -\frac{\ln(N_\ell/N_0)}{V_d t}, \quad (3.16)$$

which mainly depends on time. Instead of a constant temperature, the droplets are often exposed to a constant cooling rate  $\dot{T} = \partial T/\partial t$ , which leads to

$$\int_T^{T_0} \mathcal{J}(T) dT = -\frac{\ln(N_\ell/N_0) \dot{T}}{V_d}, \quad (3.17)$$

where  $T_0$  and  $T$  are the initial temperature (all droplets are still liquid) and the current temperature, respectively.

The same result could also be obtained by assuming that ice nucleation is a stochastic process and using Poisson distributed to describe the experimental data [216].

While homogeneous ice nucleation is important for ice particle formation in clouds [98], it is of secondary importance for many other technical applications, because the presence of foreign substances (like impurities or even the liquid container itself) inevitably results in heterogeneous nucleation. Accordingly, heterogeneous nucleation is much more relevant for technical applications.

## 3.2 Heterogeneous ice nucleation

Heterogeneous ice nucleation is influenced by the presence of a foreign substance, which promotes ice nucleation and results in a lower degree of supercooling necessary to initiate the phase transition [269]. The foreign substance can be any kind of particle immersed or in contact with the liquid as well as any substrate in case of sessile droplets. For simplification the ice nucleus is assumed to be a spherical cap (the influence of gravity is neglected) and is formed directly on a flat substrate or wall as shown in Fig. 3.4. Note that the principle shown in Fig. 3.4 is also valid for inclined substrates or vertical walls.

The solid nucleus surrounded by a supercooled liquid is in a thermodynamically stable state, and its shape can be described by the Young equation [291], which equates the interfacial tensions

$$\gamma_{w,\ell} = \gamma_{w,s} + \gamma_{s,\ell} \cos(\theta), \quad (3.18)$$

where  $\gamma_{w,\ell}$  is the interfacial tension between the liquid and the substrate/wall,  $\gamma_{w,s}$  is the interfacial tension between ice and substrate/wall and  $\gamma_{s,\ell}$  is the interfacial tension between ice and liquid. In addition,  $\theta$  denotes the static contact angle, which is defined by the angle between  $\gamma_{w,s}$  and  $\gamma_{s,\ell}$ . Similarly to homogeneous ice nucleation, heterogeneous ice nucleation also initiates a phase transition to a lower-energy state. The release of energy can be determined by equating the energy before and after nucleation, which yields  $\Delta G_{\text{het}} = G_2 - G_1$ . Taking into account

### 3 Ice nucleation

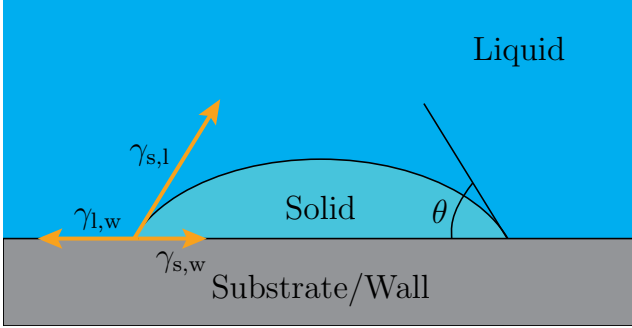


Figure 3.4: Schematic of a capped spherical ice nucleus on a substrate/wall surrounded by a liquid including the corresponding interfacial tensions  $\gamma$  and the contact angle  $\theta$ . Adapted figure, Copyright © 2009 from Phase Transformations in Metals and Alloys, Third Edition (Revised Reprint) by Porter et al. [213]. Reproduced by permission of Taylor and Francis Group, LLC, a division of Informa plc.

the different interfacial tensions as well as the volume free energy leads to [213]

$$\Delta G_{\text{het}} = -V_s \Delta G_V + A_{s,\ell} \gamma_{s,\ell} + A_{w,\ell} \gamma_{w,\ell} - A_{s,w} \gamma_{w,\ell}, \quad (3.19)$$

where the first two terms on the right-hand side are the difference in surface and volume free energy as already introduced for homogeneous nucleation, see Eq. (3.3). Note, that  $V_s$  and  $A_{s,\ell}$  describe the volume of the spherical capped ice and surface area of the liquid-solid interface, respectively. The two additional terms on the right-hand side take into account the interfacial energy due to the foreign substrate, where  $A_{w,\ell}$  is the surface area between the substrate/wall and liquid, and  $A_{s,w}$  is the surface between the substrate/wall and ice. Using the volume and surface area of the footprint of the spherical cap, the change in Gibbs free energy during the phase transition can be expressed depending on the radius  $R$  of the spherical cap as

$$\Delta G_{\text{het}} = \left[ -\frac{4}{3} \pi R^3 \Delta G_V + 4\pi R^2 \gamma_{s,\ell} \right] S(\theta), \quad (3.20)$$

### 3.2 Heterogeneous ice nucleation

where  $S(\theta)$  only depends on the contact angle  $\theta$  and is defined by

$$S(\theta) = \frac{[2 + \cos(\theta)][1 - \cos(\theta)]^2}{4}. \quad (3.21)$$

A comparison of Eq. (3.20) and Eq. (3.5) reveals that the change in Gibbs free energy for heterogeneous nucleation is given by an additional factor  $S(\theta)$  compared to homogeneous nucleation. Due to the fact that  $S(\theta)$  amounts only values in the interval  $[0, 1]$ , the change of Gibbs energy for heterogeneous nucleation is the same or lower compared to homogeneous ice nucleation. Hence, the change of the Gibbs free energy of heterogeneous ice nucleation can be expressed by

$$\Delta G_{\text{het}} = \Delta G_{\text{hom}} S(\theta). \quad (3.22)$$

The critical energy barrier and the associated cluster size to initiate ice nucleation is determined by the maximum of Eq. (3.20) with respect to the radius  $R$ , which can be calculated by

$$\frac{d(\Delta G_{\text{het}})}{dR} = 0. \quad (3.23)$$

Solving the equations yields the critical radius  $R^*$  of an ice nucleus to overcome the energy barrier and to initiate ice nucleation

$$R_{\text{het}}^* = \frac{2\gamma_{s,\ell} T_m}{L_V \Delta T}. \quad (3.24)$$

As shown by Eq. (3.24), the critical size of the nucleus does not depend on the contact angle, and therefore is independent of the wetting properties of the substrate. Thus, the critical radius is the same for homogeneous and heterogeneous nucleation. Inserting Eq. (3.24) into Eq. (3.20) results in the critical energy barrier  $\Delta G_{\text{het}}^*$  for the phase transition

$$\Delta G_{\text{het}}^* = \frac{16\gamma_{s,\ell}^3 T_m^2}{3L_V^2 \Delta T^2} S(\theta). \quad (3.25)$$

In contrast to the critical radius, the critical energy barrier  $\Delta G_{\text{het}}^*$  depends on the contact angle and is influenced by the surface properties. Usually, the contact angles in most applications and experiments are characterized by  $\theta \neq 180^\circ$  resulting in  $S(\theta) < 1$ , which always leads to smaller

### 3 Ice nucleation

nucleation temperatures compared to homogeneous nucleation. A comparison of the critical energy barrier for homogeneous and heterogeneous nucleation reveals that the critical energy barrier in case of heterogeneous nucleation is also lowered by the factor  $S(\theta)$

$$\Delta G_{\text{het}}^* = \Delta G_{\text{hom}}^* S(\theta). \quad (3.26)$$

Using the same approach as for homogeneous nucleation, the nucleation rate of heterogeneous ice nucleation  $\mathcal{J}_{\text{het}}$  can be determined by inserting Eq. (3.25) in Eq. (3.11), which yields the heterogeneous nucleation rate

$$\mathcal{J}_{\text{het}} = f_{0,c} \mathcal{C}_0 \exp\left(-\frac{\Delta G_{\text{het}}^*}{k_b T}\right). \quad (3.27)$$

A comparison of the homogeneous and the heterogeneous nucleation rate is shown in Fig. 3.5. The contact angle in case of heterogeneous nucleation is assumed to be  $\theta = 70^\circ$ , while the values of  $f_{0,c}$ ,  $\mathcal{C}_0$  and  $k_b$  are identical for homogeneous and heterogeneous ice nucleation (see Sec. 3.1 for further details). The lower energy barrier in case of heterogeneous nucleation

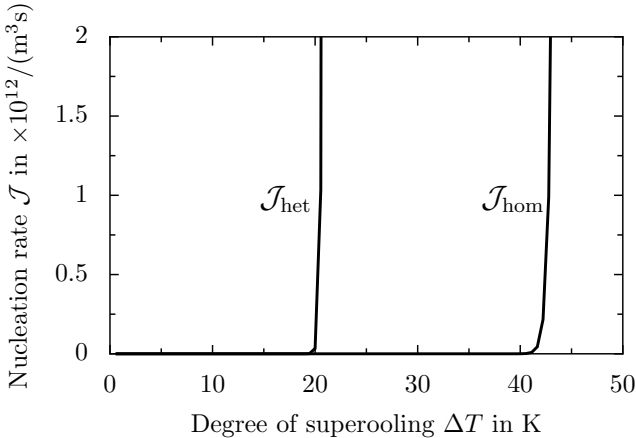


Figure 3.5: Comparison of homogeneous and heterogeneous nucleation rates  $\mathcal{J}$  depending on the degree of supercooling  $\Delta T$ . In case of heterogeneous nucleation the contact angle is defined by  $\theta = 70^\circ$ .

results in lower nucleation temperatures. Hence, the steep increase of the nucleation rate is observed at a lower degree of supercooling. The lower the contact angle (better surface wetting), the lower is the critical energy barrier and nucleation temperature. Finally, for  $\theta = 180^\circ$  (no wetting) homogeneous and heterogeneous ice nucleation have the same energy barrier.

As already mentioned for homogeneous ice nucleation, the ice nucleation rate is often determined by investigating ice nucleation of individual droplets of one ensemble. Thus, the nucleation rate has to be determined by the temporal evolution of the number of frozen and liquid droplets, which mainly depends on the droplet temperature. The correlation of the ratio of liquid and frozen droplets as well as the nucleation rate is described by several nucleation models, which mathematically model the nucleation behaviour and mainly originate from different observations during the experiments.

## 3.3 Ice nucleation models

Nucleation models are used to describe and predict the nucleation behaviour. Most nucleation theories were developed in the scope of nucleation of water droplets in supersaturated humid air and were later extended to additionally describe ice nucleation. The different nucleation theories can be categorized by phenomenological, kinetic and microscopic approaches [68, 116, 137]. The phenomenological approaches are based on the calculation of the Gibbs free energy for the cluster formation and the corresponding critical size of an ice germ using macroscopic properties like the surface tension [116]. In contrast, kinetic approaches use the molecular interaction to predict nucleation, and thus avoid using macroscopic properties like the surface tension. Furthermore, the kinetic theories do not calculate the energy necessary for cluster formation and do not use some of the strict assumptions of the classical nucleation theory [83]. The microscopic approaches use first-principle models and investigate the interaction between atoms to calculate the free energy for the cluster formation using functional density theories as well as molecular dynamics simulations [116]. In the scope of the present study, only selected phenomenological models, namely the classical nucleation theory, the singular model and extension of those, are discussed in detail due to their high relevance for interpreting experimental results. The partially

### 3 Ice nucleation

contrary approaches mainly originate from experimental observations and their interpretation. The main difference of these models is given by the different influencing parameters. This results in a controversial discussion if ice nucleation is a time or only temperature dependent process [266]. The various approaches and connections between them are subsequently presented.

#### 3.3.1 Classical (stochastic) nucleation model

The classical nucleation theory (CNT) originates amongst others from the work of Becker and Döring [12], Frenkel [71], Turnbull and Fisher [264], Volmer and Weber [272] and was developed to describe the nucleation of water droplets from vapour. Later the theory was adapted by Bigg [20, 21] and Carte [32, 33] to also describe ice nucleation, which nowadays is one of the most common theories taking into account the stochastic nature of nucleation and using a statistical approach to model ice nucleation.

The CNT assumes that nucleation is a stochastic process, and thus depends on time [265, 266, 269]. The two main assumptions of the CNT are that ice germs can be treated like liquid droplets and that the interaction between the solid and liquid phase is characterized by the contact angle [266].

Ice nucleation experiments are often performed using a specific volume of liquid, which is cooled to a specific temperature or at a specific cooling rate until nucleation occurs. This procedure is repeated several times with a fixed liquid volume under the same conditions or with multiple liquid droplets of the same size, which are exposed to the same conditions [216]. In case of multiple droplets, each individual droplet has to be isolated from the others so that the nucleation inside a droplet does not influence the neighbouring droplets [216]. The nucleation is assumed to be initiated by a single nucleation event inside the droplet [216]. Furthermore, the volume of the droplets has to be same [216]. Under these assumptions the various nucleation events can be compared and merged to a single data set, which comprises the ratio of liquid and frozen droplets depending on temperature or time. As a consequence, the experimental data can be used to determine the nucleation rate, which is often applied to characterize nucleation.

Taking into account the main assumption of the CNT that ice nucleation is a stochastic process implies that nucleation events are Poisson

distributed with respect to time [216]. Hence, the probability of nucleation of  $N_s$  droplets in the time interval  $[0, t_s]$  from a droplet ensemble with  $N_0$  droplets can be expressed by [216]

$$\mathcal{P}(N_s, t_s) = \frac{(V_d \mathcal{J}(T) t_s)^{N_s} \exp[-V_d \mathcal{J}(T) t_s]}{N_s!}, \quad (3.28)$$

where  $N_s$  is a positive integer in the interval  $[0, N_0]$ . The general formula given by Eq. (3.28) can be used to determine the probability that all droplets are still liquid ( $N_s = 0$ ) in the time interval  $[0, t_s]$ , which yields

$$\mathcal{P}(N_s = 0, t_s) = \frac{(V_d \mathcal{J}(T) t_s)^0 \exp[-V_d \mathcal{J}(T) t_s]}{0!} = \exp[-V_d \mathcal{J}(T) t_s]. \quad (3.29)$$

A comparison of Eq. (3.29) and Eq. (3.15) yields that  $\mathcal{P}(N_s = 0, t_s) = N_\ell/N_0$  and that the nucleation rate  $\mathcal{J}$  is given by

$$\mathcal{J}(T) = -\frac{\ln(N_\ell/N_0)}{V_d t}, \quad (3.30)$$

which is the same result as presented in Eq. (3.16). It characterizes the homogeneous nucleation rate depending on the liquid fraction of the droplet ensemble  $N_\ell/N_0$  and time  $t$ . For a constant cooling rate the nucleation rate is described by Eq. (3.17).

In case of heterogeneous ice nucleation the nucleation rate can be expressed by [102]

$$\mathcal{J}_{\text{het}}(T) = -\frac{\ln(N_\ell/N_0)}{V_d t}. \quad (3.31)$$

However, heterogeneous ice nucleation is affected by a foreign substance, which is in contact with the liquid in a meta-stable state, and thus can be characterized by the wetted area  $A_{\text{wet}}$ . Due to the fact that the critical energy barrier is lowered by the presence of a foreign substrate, which also influences the rate of nucleation, the nucleation rate is often defined with respect to the wetted area. Adapting the definition of Eq. (3.16), which defines the probability of nucleation events per unit volume and time, leads to

$$\mathcal{J}_{\text{het,surf}}(T) = -\frac{\ln(N_\ell/N_0)}{A_{\text{wet}} t}, \quad (3.32)$$

which defines the probability of freezing per unit surface area and time [266]. In this case the unit of the nucleation rate is  $\text{m}^{-2} \text{s}^{-1}$ .

### 3.3.2 Singular nucleation model

The singular nucleation model was developed among others by Levine [143] and Langham et al. [140] and assumes that nucleation is a time independent, but temperature dependent process [269]. The main assumption of the singular model is that all samples contain a certain spectrum of ice nucleating particles (INP) [269]. Each individual ice nucleating particle has a characteristic temperature at which the nucleation particle becomes active and initiates the phase change [266]. The INP with the highest characteristic temperature inside the sample determines the nucleation temperature. Therefore, in terms of a droplet ensemble, each droplet has a characteristic freezing temperature, which is associated with the INPs and their characteristic temperatures inside the droplets. Thus, nucleation is a time-independent, but temperature dependent process. Both the classical nucleation theory and the singular nucleation model are used to interpret experimental results, but there is an ongoing debate whether ice nucleation is a time-dependent or independent process.

Using the singular nucleation model, the ice nucleation is characterized by the nucleation site density. The nucleation site density is defined as the number of nucleation sites causing nucleation per unit surface area (of INP) [269]. Due to the fact that the singular nucleation model assumes that ice nucleation is initiated by INPs, the singular model is only valid for heterogeneous ice nucleation. The singular model assumes a spectrum of INPs inside a droplet volume. The number of INPs becoming active in the temperature interval  $[0, T]$  is defined by [102]

$$n_{\text{si}}(T) = n_0 \exp\left(\frac{T}{\mathcal{T}_0}\right), \quad (3.33)$$

where  $n_0$  and  $\mathcal{T}_0$  are constants with the dimensions of nucleation sites per surface area and Kelvin, respectively. Assuming that the droplet contains a random distribution of INPs, the probability of droplet freezing during cool-down is given by Poisson statistics [102]. Following the approach of Poisson statistics and defining the nucleation site density with respect to a characteristic surface  $A_{\text{surf}}$  the probability of  $N_s$  droplets freezing in the temperature interval  $[0, T]$  is given by [184]

$$\mathcal{P}(N_s, T) = 1 - N_\ell/N_0 = 1 - \exp[-n_{\text{si}}(T)A_{\text{surf}}]. \quad (3.34)$$

Hence, the nucleation site density can be determined using the liquid

fraction  $N_\ell/N_0$ , which leads to [184]

$$n_{\text{si}}(T) = \frac{-\ln(N_\ell/N_0)}{A_{\text{surf}}}. \quad (3.35)$$

The unit of the nucleation site density is  $\text{m}^{-2}$ .

### 3.3.3 Further nucleation models

Both the classical nucleation theory and the singular nucleation model are used to describe experimental data, even if the models are rather contrary. The different models are affirmed by different experiments and the resulting data. As an example, Durant [57], Shaw et al. [244], Zobrist et al. [296] or Seeley and Seidler [239] showed the stochastic nature of ice nucleation with different experiments. However, Connolly et al. [43], Möhler et al. [180] or Vali [265] revealed a singular nucleation and time independent nucleation behaviour. Neither the classical nucleation theory nor the singular nucleation model can describe all observations from experiments presented in the past. In consequence, several authors tried to adapt the existing models to reconcile both models, e.g. [193, 265, 268]. Subsequently, two models are exemplarily shown, namely the VS66 model and the Soccer ball model [193, 268].

The VS66 model, developed by Vali and Stansbury [268], combines the assumption of the stochastic and the singular model. It is assumed that ice nucleation can be characterized by a specific nucleation temperature  $T_{\text{nuc}}$ , which depends on the most active INP inside the droplet at a certain temperature. This characteristic temperature is defined by  $\mathcal{J}(T_{\text{nuc}}) = \text{const.}$ , where the nucleation rate is given by an arbitrary constant defining the characteristic temperature [266]. Furthermore, it is assumed that the nucleation temperature fluctuates around this characteristic temperature and nucleation is activated by the most active INP in the droplet. The characteristic temperature depends on the cooling rate and on chance [266]. The specific nucleation temperature  $T_{\text{nuc}}$  cannot be determined directly from the experiments, but can be approximated by them because of the rapid increase of the nucleation rate at  $T_{\text{nuc}}$  [266]. The VS66 model combines the observed phenomena and describes ice nucleation as a time and temperature dependent process.

The soccer-ball model was introduced by Niedermeier et al. [193] as an extension of the already existing conclusions of Marcolli et al. [170] and

### 3 Ice nucleation

Lüönd et al. [163]. The model is based on the assumption that nucleation is always initiated by random fluctuations of water molecules [193]. In consequence, the model takes into account the stochastic nature of nucleation. It is assumed that each water droplet contains numerous 'ice nucleus' particles of identical size [193]. The surface of each particle is subdivided into patches with different properties with respect to the surface wetting. The individual properties are determined by a probability function so that the contact angles are randomly distributed in the interval  $[0, \pi]$ . The transition between the stochastic and singular behaviour is affected by the distribution of wetting properties on the particle surface. A narrow range of contact angles causes a stochastic nature while a broader range of contact angles lead to a purely singular nature [193].

Both models try to combine the stochastic and singular behaviour of nucleation. Experiments revealed different properties of the nucleation behaviour, which can be described by different nucleation models. The combination of both models provided by Vali and Stansbury [268] or Niedermeier et al. [193] shows that the stochastic and singular nucleation model are not necessarily contrary to one another. As a consequence, the different properties of the models can be combined. However, the nucleation behaviour depends on the considered timescale, as stated by Niedermeier et al. [193], which might lead to a masking of the stochastic nature of nucleation. Generally, both the singular and the stochastic nature of ice nucleation are present simultaneously, so that ice nucleation is a time and temperature dependent process. However, one behaviour can be dominant depending on the boundary conditions.

## 3.4 Influence of electric fields on ice nucleation

The influence of electric fields on ice nucleation was already investigated experimentally [1, 45], theoretically [118, 119, 230] and numerically [22, 192, 253, 254, 287, 293] by several authors. However, the impact of electric fields is not completely understood, because the experimental results are not in complete agreement. Several authors already showed that electric fields have an impact on ice nucleation [24, 31, 127, 165, 168, 185, 197, 205, 215, 222, 227, 232, 251, 277, 283, 286, 290], while others could not observe any influence [47, 53, 167, 203, 214, 247, 279]. The contrary results are produced with various experimental setups under different conditions, which comprise homogeneous and heterogeneous nucleation, dif-

### 3.4 Influence of electric fields on ice nucleation

ferent temperature ranges, several fluids and different types of electric fields. Thus, a comparison of the results is rather difficult. The various boundary conditions such as the different investigated fluids or different kinds of electric fields with various field strengths increase the complexity of the physical mechanisms. Especially, the electric field and its properties as, for instance the type of electric field, namely constant, alternating or transient, the frequency of the electric field, the electric field strength or the orientation of the electric field adds a variety of new influences, which might have an impact on ice nucleation. As already mentioned, nucleation is very sensitive with respect to the boundary conditions so that some influences might be masked, e.g. by a wrongly selected timescale [193, 279]. Consequently, the impact of electric fields on ice nucleation has to be carefully investigated to determine even minor influences of the electric field on ice nucleation.

As shown in the previous sections, ice nucleation is initiated as soon as the critical energy barrier is reached and exceeded. The presented theories do not take into account the effect of an external electric field. Therefore, several authors have theoretically investigated the impact of electric fields on ice nucleation and have adapted the existing theories. Even though the analysis in Chap. 2 showed that the behaviour of water droplets is mainly determined by the electrical conductivity rather than the permittivity in low frequency fields, none of the existing models for ice nucleation under the influence of electric fields takes into account the electrical conductivity of ice. Instead, the influence of the electric field is assumed to originate from the different relative permittivities of water, ice and surrounding fluid, which is only valid for really small electrical conductivities of water and ice or high frequency fields ( $\tau_{\text{el}} \gg \tau_E$ ). However, for the sake of completeness, the existing models are reviewed. Among others, Kashchiev [118], Marand et al. [169], Orlowska et al. [197], Saban et al. [230] have adapted the phenomenological theory of ice nucleation to take into account the effect of constant electric fields. They have extended the change in Gibbs free energy  $\Delta G$ , shown in Eq. (3.5), by adding a term to take into account the energy associated with the electric field

$$\Delta G_E = 4\pi R^2 \gamma_{s,\ell} - \frac{4}{3}\pi R^3 (\Delta G_V + \Delta G_{V,E}), \quad (3.36)$$

where  $\Delta G_{V,E}$  is the additional term taking into account the effect of the electric field on the liquid volume. If  $\Delta G_{V,E} > 0$ , the electric field lowers the energy barrier, and thus promotes ice nucleation. In contrast, if

### 3 Ice nucleation

$\Delta G_{V,E} < 0$  ice nucleation is inhibited by increasing the energy barrier. Furthermore, a vanishing electric field leads to the already known energy barrier shown in Eq. (3.5). According to Kashchiev [118] and Saban et al. [230] the additional energy  $\Delta G_{V,E}$  is determined by the change of energy with respect to the electric field during the formation of an ice nucleus. Assuming a spherical droplet and a spherical nucleus with coinciding centres in the origin of a spherical polar coordinate system the impact of an electric field on the critical energy barrier can be analytically determined [230]. The energy of a liquid sphere in an external field is defined by [250]

$$G_{1,E} = \frac{1}{2} \int \vec{E}_\ell \cdot \vec{D}_\ell dV, \quad (3.37)$$

where  $\vec{E}_\ell$  and  $\vec{D}_\ell$  denotes the electric field and the electric displacement in the liquid, respectively. Using the correlation between the electric field and the electric displacement  $\vec{D} = \varepsilon \vec{E}$  leads to

$$G_{1,E} = \frac{1}{2} \varepsilon_\ell \int E_\ell^2 dV, \quad (3.38)$$

where  $\varepsilon_\ell = \varepsilon_{r,\ell} \varepsilon_0$  and is defined by the relative permittivity of the liquid  $\varepsilon_{r,\ell}$  and the vacuum permittivity  $\varepsilon_0$ . It is assumed that the liquid droplet has a constant permittivity  $\varepsilon_\ell$  and is surrounded by a fluid with a different permittivity  $\varepsilon_{\text{surr}}$  like oil or air. Furthermore, deformations of the droplet due to the electric field are neglected. The electric potential of the droplet  $\phi_\ell$  in spherical coordinates with  $r$  and  $\varphi$  being the coordinates in radial and azimuthal direction is given by

$$\phi_\ell = \frac{3\varepsilon_{\text{surr}}}{2\varepsilon_{\text{surr}} + \varepsilon_\ell} E_0 r \cos(\varphi), \quad (3.39)$$

where  $E_0$  is the norm of the external electric field strength and  $\varepsilon_{\text{surr}}$  as well as  $\varepsilon_\ell$  are the permittivity of oil and water, respectively. The resulting electric field strength inside the droplet is constant and is calculated by  $E = -\nabla\phi$ , which yields [230, 250]

$$E_\ell = \frac{3\varepsilon_{\text{surr}}}{2\varepsilon_{\text{surr}} + \varepsilon_\ell} E_0. \quad (3.40)$$

Inserting Eq. (3.40) in Eq. (3.38) and assuming a spherical droplet leads to the energy of the droplet inside an external electric field  $G_{1,E}$

$$G_{1,E} = 6\pi R_\ell^3 \frac{\varepsilon_\ell \varepsilon_{\text{surr}}^2}{(\varepsilon_\ell + 2\varepsilon_{\text{surr}})^2} E_0^2, \quad (3.41)$$

### 3.4 Influence of electric fields on ice nucleation

which depends on the permittivity of the liquid  $\varepsilon_\ell$  and the surrounding fluid  $\varepsilon_{\text{surr}}$  as well as the electric field strength  $E_0$ . Following the same approach as for the pure liquid state, the energy of a liquid sphere containing an ice nucleus can be determined by [230]

$$G_{2,E} = \frac{1}{2}\varepsilon_s \int E_s^2 dV_s + \frac{1}{2}\varepsilon_\ell \int E_\ell^2 dV_\ell. \quad (3.42)$$

It is assumed that the change of the permittivity of the liquid due to the formation of ice is negligible, and thus the permittivity of the liquid is used to calculate the free energy of the residual liquid phase. Following the same approach as before and using the following electric potentials for the ice nucleus and the residual water

$$\phi_s = \frac{9\varepsilon_{\text{surr}}\varepsilon_\ell}{(2\varepsilon_\ell + \varepsilon_s)(2\varepsilon_{\text{surr}} + \varepsilon_\ell)} E_0 r \cos(\varphi) \quad (3.43)$$

and

$$\phi_\ell = \frac{3\varepsilon_{\text{surr}}}{(2\varepsilon_{\text{surr}} + \varepsilon_\ell)} \left( r - \frac{\varepsilon_s - \varepsilon_\ell}{\varepsilon_s + 2\varepsilon_\ell} \frac{a^3}{r^3} \right) E_0 \cos(\varphi), \quad (3.44)$$

where  $a$  is the radius of the solid phase, the electric field and the corresponding Gibbs free energy can be determined. This yields the free energy after nucleation

$$G_{2,E} = \left[ \frac{2}{3}\pi\varepsilon_\ell(R_\ell^3 - a^3) + \frac{4\pi\varepsilon_\ell(\varepsilon_s - \varepsilon_\ell)^2 R_\ell^3}{3(\varepsilon_s + 2\varepsilon_\ell)^2} \left( 1 - \frac{a^3}{R_\ell^3} \right) + \frac{6\pi\varepsilon_s\varepsilon_\ell^2}{(\varepsilon_s + 2\varepsilon_\ell)^2} a^3 \right] \frac{3\varepsilon_{\text{surr}}E_0}{\varepsilon_\ell + 2\varepsilon_{\text{surr}}}. \quad (3.45)$$

The difference of the free energy  $\Delta G_E$  before and after nucleation characterizes the change of energy caused by the electric field, which is given by

$$\Delta G_E = -\frac{4}{3}\pi R^3 E_0^2 \underbrace{\frac{9\varepsilon_{\text{surr}}^2 \varepsilon_\ell (\varepsilon_s - \varepsilon_\ell)^2}{(\varepsilon_\ell + 2\varepsilon_{\text{surr}})^2 (\varepsilon_s - 2\varepsilon_\ell)^2}}_{\Psi}, \quad (3.46)$$

where  $\Psi$  is a constant which depends on the permittivities of the involved materials. The overall change in free energy  $\Delta G_{\text{tot}}$  is calculated by adding  $\Delta G_E$  to Eq. (3.5), which yields

$$\Delta G_{\text{tot}} = 4\pi R^2 \gamma_{s,\ell} - \frac{4}{3}\pi R^3 \left( L_V \frac{\Delta T}{T_m} + E_0^2 \Psi \right). \quad (3.47)$$

### 3 Ice nucleation

Comparing Eq. (3.5) and Eq. (3.47) reveals that the electric field influences the change of the free energy. Whether the free energy is increased or decreased is determined by the sign of  $\Psi$ , which is determined by the permittivities of the materials involved. The value of  $\Psi$  is always positive  $\Psi > 0$  (for the materials and liquids used in the present study) so that the total Gibbs energy is decreased and consequently ice nucleation is promoted. Following the same approach as for homogeneous and heterogeneous nucleation the critical energy barrier to initiate the phase transition is defined by

$$\frac{d(\Delta G_{\text{tot}})}{dR} = 0. \quad (3.48)$$

Solving Eq. (3.48) with respect to the radius results in the critical radius of an ice nucleus exposed to an external electric field to overcome the energy barrier, and yields

$$R_E^* = \frac{2\gamma_{s,\ell}}{L_V \Delta T / T_m + E_0^2 \Psi}. \quad (3.49)$$

Inserting the critical radius into Eq. (3.47) yields the energy barrier under the influence of an electric field

$$\Delta G_E^* = \frac{16\pi\gamma_{s,\ell}^3}{3 [L_V \Delta T / T_m + E_0^2 \Psi]^2}. \quad (3.50)$$

As already mentioned and shown by Eq. (3.50), the impact of the electric field mainly depends on the electric field strength  $E$  and the degree of supercooling  $\Delta T$ . Depending on the relative permittivities of the involved materials the electric field can inhibit or promote ice nucleation. Furthermore, a low electric field strength or  $\Psi$  close to zero leads to a vanishing influence of the electric field. One of the influencing factors might be dominant depending on the boundary conditions. Whether the temperature or the electric field is dominant is mainly characterized by the degree of supercooling and the electric field strength. Therefore, carefully performed experiments under well-defined conditions are necessary to determine the possibly minor influence of the electric field. The controversial results in literature might result from experiments not conducted carefully enough or the stochastic nature of nucleation itself, which can mask the impact of the electric field [279]. Note that the presented theory is only valid for constant electric fields and does not take into account alternating or transient electric fields. Furthermore, the influence of the electrical conductivity is neglected, even though it is important for low frequency or

### 3.4 Influence of electric fields on ice nucleation

constant electric fields as shown in Chap. 2. The electrical conductivity of ice can vary within several orders of magnitudes depending on the structure of ice and is reported to be in the order of  $\kappa_{\text{ice}} \approx 10^{-7}$  S/m to  $\kappa_{\text{ice}} \approx 10^{-10}$  S/m for constant electric fields [102]. Consequently, ice can also be characterized as a perfect conductor depending on the frequency of the electric field and the permittivity of ice. In case of  $\tau_{\text{ice}} \ll \tau_{\text{E}}$ , the physical mechanism is dominated by the ratio of the conductivities, and thus the presented model cannot describe the influence of the electric field on ice nucleation. Even the transition between both, the influence of electrical conductivity and permittivity, cannot be described accurately because the model does not take into account the electrical conductivities of ice and water. As a consequence, the presented model is only valid for  $\tau_{\text{ice}} \gg \tau_{\text{E}}$ . It is assumed that the experiments performed in this study cannot be accurately described by this theory. In fact, it is hypothesized that an adapted theoretical model is necessary to describe the influence of low frequency or constant electric fields on ice nucleation accurately. Hence, no general theoretical model to describe the influence of electric fields on ice nucleation is available at the moment.



**Part III**

**ELECTROHYDRODYNAMICS OF  
SESSILE DROPLETS**



## 4 Experimental details

---

---

The content of this chapter is partly based on the *Studienarbeit* of Duygu Cicekdagli [40] and the Master thesis of Jan Engelhardt [58], Franziska Zajonz [292] and Marvin Dietzmann-Kolbe [51], and has been partially published in the following publications and conference proceedings:

- [152] Löwe, J.-M., Secklehner, M., and Hinrichsen, V. Investigation of Surface Charges on Polymeric Insulators and the Influence of Sessile Water Droplets. In *2017 INSUCON - 13th International Electrical Insulation Conference (INSUCON)*, pages 1–7. IEEE, 2017. ISBN 978-1-9998-1569-1. doi:10.23919/INSUCON.2017.8097170
  - [153] Löwe, J.-M., Hinrichsen, V., and Tropea, C. Droplet Behavior Under the Impact of Lightning and Switching Impulse Voltage. In *2018 IEEE Electrical Insulation Conference (EIC)*, pages 443–447. IEEE, 2018. ISBN 978-1-5386-4178-1. doi:10.1109/EIC.2018.8480884
  - [150] Löwe, J.-M. and Hinrichsen, V. Experimental Investigation of the Influence of Electric Charge on the Behavior of Water Droplets in Electric Fields. In *2019 IEEE 20th International Conference on Dielectric Liquids (ICDL)*, pages 1–6. IEEE, 2019. ISBN 978-1-7281-1718-8. doi:10.1109/ICDL.2019.8796707
  - [156] Löwe, J.-M., Hinrichsen, V., Roisman, I. V., and Tropea, C. Behavior of Charged and Uncharged Drops in High Alternating Tangential Electric Fields. *Physical Review E*, 101(2):023102, 2020. doi:10.1103/PhysRevE.101.023102
  - [157] Löwe, J.-M., Hinrichsen, V., Roisman, I. V., and Tropea, C. Impact of Electric Charge and Motion of Water Drops on the Inception Field Strength of Partial Discharges. *Physical Review E*, 102(6):063101, 2020. doi:10.1103/PhysRevE.102.063101
- 
-

## 4.1 Experimental setup

The experimental setup aims to reproduce the conditions present in real-world applications while simultaneously generating well-defined conditions. For the investigation of sessile droplets under ambient conditions a generic insulator model as published e.g. by Nazemi and Hinrichsen [188] is used to investigate the behaviour under the impact of electric fields. The generic insulator serving as support for the single droplet consists of a dielectric material (silicone rubber or epoxy) and has a size of  $10\text{ cm} \times 10\text{ cm} \times 2\text{ cm}$  ( $l \times w \times h$ ). A schematic of the generic insulator is shown in Fig. 4.1. The properties of the dielectric materials are summarized in Table 4.2. To generate an electric field on the surface of the substrate two rod electrodes with a diameter of  $d_{\text{rod}} = 15\text{ mm}$  are embedded into the dielectric material with a separation of  $20\text{ mm}$ . The electrodes are off-centre in  $z$  direction so that the electrodes are closer to the substrate surface (resulting distance to surface:  $1\text{ mm}$ ). The specimen is produced in a casting mould with a fixed electrode position to ensure a repeatable production of the specimens. Each electrode made out of brass is pretreated with a primer prior to the casting process to ensure good adhesion between the brass and the dielectric material. The electrodes are inserted in the dielectric on opposite sides to increase the electric creeping distance between the electrodes. In addition, the dielectric material is degassed prior to the casting process to reduce the amount of air enclosed in the material in order to prevent the formation of cavities inside the specimen. Enclosed air in the specimen precipitate high electric field strength inside the cavity, and therefore might cause the generation of partial discharges, thus influencing the measurements. Depending on the

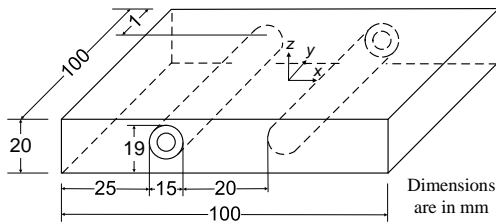


Figure 4.1: Schematic of the generic insulator with dimensions. Reprinted (adapted) with permission from [188], © 2013 IEEE.

Table 4.2: Overview of the dielectric properties of the used substrate materials.

Properties	Silicone rubber	Epoxy
Manufacturer	Wacker	Ciba
Name	Powersil 600 A/B	Araldit F/HY905
Mixing ratio by weight	90 % / 10 %	16 % / 16.5 %
Filler	None	Silbond W12 EST
Relative permittivity at 50 Hz	2.9	$\approx 4.6$
Specific Resistance	$10^{13} \Omega \text{ m}$	$\approx 10^{13} \Omega \text{ m}$
Breakdown field strength	23 kV/mm	$\approx 22 \text{ kV/mm}$
Advancing contact angle $\theta_{\text{adv}}$	$\approx 116^\circ \pm 4^\circ$	$\approx 89^\circ \pm 4^\circ$
Receding contact angle $\theta_{\text{rec}}$	$\approx 65^\circ \pm 2^\circ$	$\approx 20^\circ \pm 3^\circ$
Curing temperature	$\approx 20^\circ \text{C}$	$\approx 100^\circ \text{C}$

dielectric material, the specimen is cured at ambient conditions (silicone rubber) or is heat treated in an oven (epoxy) to ensure solidification of the material. The resulting specimen has a smooth surface similar to the weather sheds of high-voltage insulators. Both, the silicone rubber and the epoxy have a high breakdown field strength preventing an electrical breakdown inside the dielectric material (see Table 4.2), even under high electric field stress.

The electric field is generated by applying a high voltage between the electrodes. One of the electrodes is always grounded, whereas the other electrode is connected to a high-voltage source. The type of the electric field is defined by the high-voltage source. Three different types can be produced, namely constant, alternating and transient electric fields. A constant electric field is generated using a high precision constant voltage source (Heinzinger PNChp 20000) resulting in a maximum electric field strength of  $E = 7.4 \text{ kV/cm}$ . Alternating electric fields are generated using a function generator (GW Instek SFG 2104) supplying a sinusoidal signal with a frequency between  $f_{\text{AC}} = 10 \text{ Hz}$  and  $f_{\text{AC}} = 120 \text{ Hz}$  to a custom-made power amplifier. Subsequently, the signal is amplified by a high-

## 4 Experimental details

voltage transformer (MWB TEO 100/10) to generate a maximum electric field strength of  $\hat{E} \approx 7.4 \text{ kV/cm}$  for an applied voltage of  $\hat{U} = 20 \text{ kV}$ . This electric field strength is in the same order of magnitude as the maximum electric field strength tolerable on the surface of the weather sheds during operation ( $\hat{E} = 6.36 \text{ kV/cm}$ ) [209]. In the case of transient electric fields, one of the electrodes is connected to a two-stage Marx generator. Depending on the configuration, the Marx generator can supply different types of impulses such as standard lightning or standard switching impulse voltages. Both impulse voltage types are defined by the IEC 60060-1 standard with respect to the time to peak and the time to half value. The setup can produce an electric field strength  $\hat{E} \approx 18.4 \text{ kV/cm}$  for an applied voltage of  $\hat{U} = 50 \text{ kV}$ . Using the different kinds of electric fields the characteristic timescale of the electric field is changed. While this electric field strength is in the same order of magnitude as the electric field strength produced by overvoltages caused by switching operations (assuming an overvoltage three times higher than the nominal voltage as approximated by IEC 60071-2<sup>1</sup>), the electric field strengths produced by lightning strikes are much higher in reality (assuming an overvoltage five times higher than the nominal voltage. Note that even higher overvoltages were measured, e.g. by Eriksson et al. [61]).

The orientation of the electric field with respect to the substrate surface is defined by the geometrical arrangement of the electrodes. A setup as shown in Fig. 4.1 generates an electric field nearly tangentially aligned to the surface. In most applications a combination of tangential and normal electric fields is present. In terms of droplet motion and oscillation, an electric field tangentially aligned to the substrate has a higher impact compared to an electric field aligned perpendicular to the substrate [233] and recreates the typical electrical situation as present on the weather sheds of a high-voltage insulator. Thus, the present experimental setup generates well-defined boundary conditions with respect to the electric field and enables the investigations of applications with conditions in a simplified manner. However, the conditions present on the surface of an insulator are reproduced very accurately.

The applied voltage is measured with a universal high-voltage divider (Hilo HVT 40 RCR) for all configurations. The corresponding electric field strength is determined by a numerical calculation of the electric field

---

<sup>1</sup>In this context 'nominal voltage' refers to the 'highest voltage of equipment',  $U_m$ , as defined by IEC 60071-1.

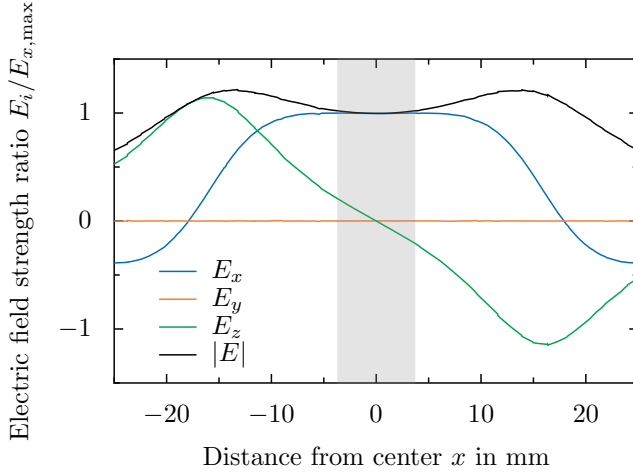


Figure 4.2: Dimensionless components of the electric field  $E_i/E_{x,\max}$  along the surface at the centre line ( $y = 0$  and  $z = 0$ , see Fig. 4.1) perpendicular to the electrodes. The data is related to the maximum field strength in  $x$  direction ( $E_{x,\max}$ ). The grey rectangle indicates the maximum width of a droplet with  $V = 100 \mu\text{l}$ .

performed with COMSOL Multiphysics<sup>®</sup>. As a reference the electric field strength in the centre of the substrate surface in absence of a droplet is used (see origin of coordinates in Fig. 4.1), because the electric field inside the droplet is significantly reduced due to the field displacement or even absent in case of a conductive droplet and cannot be directly measured. Furthermore, this position characterizes the electric field at the position of the droplet and can be compared to other experimental setups without any additional geometrical information. The distribution of the electric field strength on the substrate surface along the centre line ( $y = 0$  and  $z = 0$ ) perpendicular to the electrodes is shown in Fig. 4.2. Each component is presented in a dimensionless form with respect to the maximum electric field strength in  $x$  direction at a position of  $x = 0$ ,  $y = 0$  and  $z = 0$  (see Fig. 4.1). The  $x$  component of the electric field is tangentially aligned to the substrate and is almost constant for a distance of  $x = \pm 5$  mm. In contrast, the  $z$  component of the electric field changes almost linearly in this region. The maximum size of a hemispherical droplet with a volume

## 4 Experimental details

of  $V = 100 \mu\text{l}$  ( $d_d = 7.3 \text{ mm}$ ) is represented by the grey rectangle. The strength of the electric field at the droplet position is mainly defined by the  $x$  component of the electric field. In this region the electric field strength is almost constant, and the influence of the  $y$  component can be neglected. Hence, the generated electric field is almost perfectly tangentially aligned to the substrate surface. The electric field strength is directly proportional to the applied voltage. During the experiments the voltage level as well as the ambient conditions such as temperature or humidity are recorded using a data acquisition system (cDAQ-9174 with NI 9229 BNC, NI 9219 and NI 9401) from National Instruments<sup>TM</sup>.

### 4.1.1 Motion and oscillation of droplets

The behaviour of sessile droplets under the impact of an electric field is observed optically using a high speed camera. A schematic of the complete experimental setup comprising the specimen, specimen support, light source (LED) and a high-speed camera is shown in Fig. 4.3. Back-light shadowgraphy is used to capture the motion of the droplet under the influence of the electric field. Accordingly, the light source is directly pointed at the camera. To generate a uniform backlight an optical diffuser (PLEXIGLAS<sup>®</sup> Satinice with a transmission of 92%) is used. Two different high-speed cameras are used to capture the motion and oscillation of the droplet, namely the Phantom V12.1 from Vision Research or the Chronos 1.4 High Speed Camera from Kron Technologies. Each camera is operated at a minimum frame rate of 2000 fps to capture the motion of the droplet with a high temporal resolution. The individual frame rate was

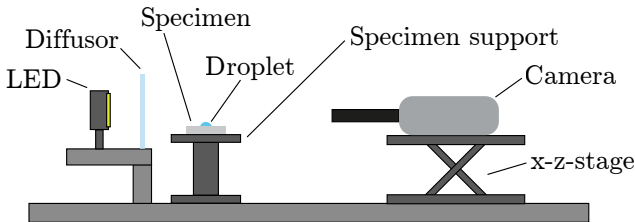


Figure 4.3: Principle of the experimental setup (not to scale). Reprinted figure (adapted) with permission from [156]. Copyright 2020 by the American Physical Society.

chosen according to the applied voltage type and the expected frequency of the droplet motion or oscillation. Hence, the record frequency was chosen to be at least ten times higher than the expected oscillation frequency of the droplet. Different magnification lenses are used to capture a close-up of the droplet and to generate a high spatial resolution.

### 4.1.2 Measurement of partial discharges

In addition to the droplet motion, the generation of electrical partial discharges (PDs) is investigated. For determining the location of the PDs the high-speed camera is replaced by a UV-camera (PCO pco.edge 4.2 bi UV) with a UV sensitive lens (UV-Nikkor 105 mm). The UV-camera is used to capture the location of the PDs in side view or in top view as shown in Fig. 4.4 and is operated at a maximum frame rate of 40 fps. To ensure a high quality of the UV-images all light sources are switched off and external light is prevented from entering the test chamber by black curtains. Besides the optical observation, the PDs are also measured electrically using a commercially available measurement system (Omicron MPD 600). The measurement system was added to the electrical circuit according to the IEC 60270 standard to guarantee an accurate measurement of the inception voltage for PDs. A schematic of the electrical circuit is shown in App. A. In addition, a calibrated coupling capacitor of  $C = 1200$  pC was used to accurately determine the (apparent) charge generated by the PDs. Prior to the experiments, the setup was calibrated using a defined charge of  $Q_{PD} = 1$  pC (Omicron CAL 542) as required, and the threshold for the PD detection was set to  $Q_{PD} = 5$  pC. During the experiment the PD

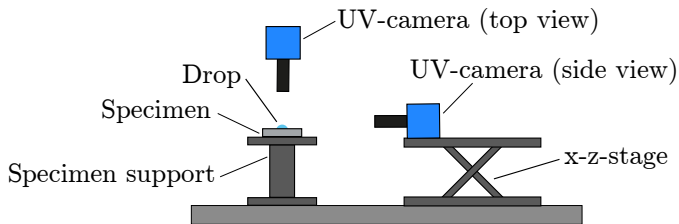


Figure 4.4: Principle of the experimental setup (not to scale). Reprinted figure with permission from [157]. Copyright 2020 by the American Physical Society.

## 4 Experimental details

activity is recorded using the MPD software from Omicron to determine the charge of each PD impulse and the corresponding voltage level. Furthermore, the experiments are performed inside a shielded and grounded test chamber to reduce the impact of external influences, resulting in a background noise level for the PD measurement of only  $Q_{\text{PD}} \approx 0.3 \text{ pC}$ . The PD inception field strength for the complete setup including the specimen but in absence of a droplet is  $\hat{E}_{\text{in}} \approx 9.2 \text{ kV/cm}$  and is not reached during the measurements.

### 4.2 Preparation

To ensure well-defined conditions the specimens have to be treated with caution. Especially, silicone rubber has a high affinity to accumulate negative charges on its surface by contact electrification [161, 298]. These unintentional charges influence the electric field distribution, the shape of the droplet or promote (enhanced) dust accumulation on the substrate surface. Hence, accumulated charges provoke unwanted or unknown boundary conditions. To ensure repeatable surface properties of the specimen, each substrate is carefully cleaned prior to an experiment with anti-static wipes soaked in isopropanol resulting in a dust-free surface. A comparison of different cleaning methods revealed that cleaning the specimen this way minimizes the surface charges [152]. Thus, the charge transfer between the sessile droplet and the substrate is also minimized. After the cleaning procedure any contact of the substrate surface was avoided to prevent accumulation of new charge.

The experimental setup and the procedure to determine the electric surface potential is described in detail in App. B. Note that the electric surface potential is directly correlated to the surface charge as indicated by Eq. (2.29). The difference in electric surface potential between an untreated and cleaned surface with the same scale is shown in Fig. 4.5. An untreated surface, which is directly measured after being taken from the storage, is shown in Fig. 4.5a. The electric surface potential is mostly negative with spots of high positive electric potential. Hence, the distribution is very inhomogeneous. Note that the scale is limited to  $\phi = \pm 1.5 \text{ kV}$  and that individual spots can have a higher positive or negative electric potential. The distribution itself is rather random and mainly depends on the storage conditions and handling of the substrate. In contrast, the cleaned surface shown in Fig. 4.5b has a very homogeneous electric surface po-

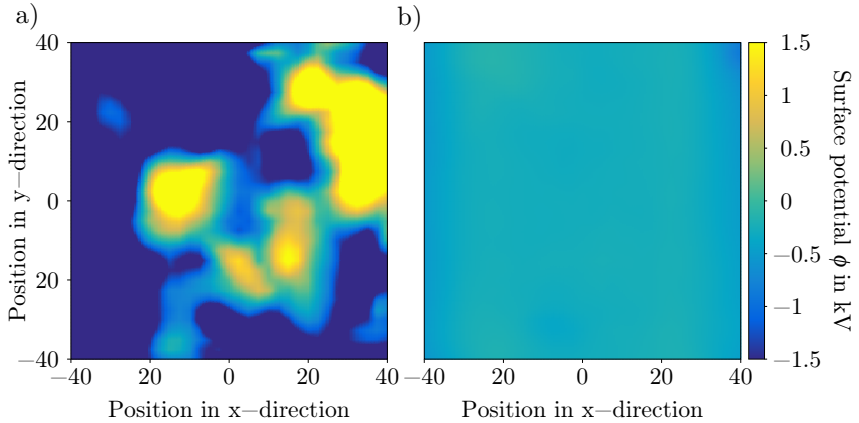


Figure 4.5: Measured electric surface potential  $\phi$  for a) an untreated surface directly taken from the storage (Reprinted (adapted) with permission from [152], © 2017 IEEE.) and b) a cleaned surface. The electric surface potential of the cleaned surface is determined by an average of ten measurements. Reprinted figure (adapted) with permission from [156]. Copyright 2020 by the American Physical Society.

tential, which is almost zero at any position of the substrate. The shown distribution of the electric surface potential was determined by the mean electric surface potential distribution of ten measurements. Especially, in the centre of the substrate the electric potential is very homogeneous. Both surface charge distributions with individual and adjusted scales can be found in App. C, see Figs. C.3 and C.4.

High surface charges can cause a charge transfer between the substrate and the droplet [152], which can significantly alter the outcome of the experiment. This is one possible reason for inconsistent results reported in literature. The effect of surface charges seems to have been neglected or at least underestimated in the past. The higher the charge difference between the substrate and the droplet, the higher is the affinity for the charge transfer. However, cleaning the substrate reduces the amount of charge on the substrate and leads to well-defined boundary conditions with respect to surface charges. Consequently, the charge accumulation

## 4 Experimental details

on the substrate can be neglected for a cleaned substrate.

In addition to the charges, any surface contamination on the substrate can influence the outcome of the experiment and cause an increased electric surface conductivity. Cleaning the substrate removes any visible surface contamination like e.g. dust and ensures a clean substrate.

Each substrate is used several times unless a visible change of the surface or their properties like the wetting behaviour was observed. Especially, before reusing the substrate each surface has to be cleaned carefully because electric charges transferred from a charged droplet to the substrate during the previous experiment might lead to unwanted surface charges [152]. Consequently, the substrate surface has to be cleaned carefully to ensure constant boundary conditions. In any doubt, the substrate was exchanged by a fresh one to ensure well-defined surface conditions.

### 4.3 Procedure

After cleaning the substrate to remove any surface contamination and accumulated charges on the specimen, the specimen is placed on the specimen support (see Figs. 4.3 and 4.4). Subsequently, a droplet is deposited on the substrate. The generation of charged and uncharged droplets as well as their positioning is described in detail hereinafter.

#### 4.3.1 Generation of charged and uncharged droplets

The generation of droplets with a well-defined charge or completely uncharged droplets is important to investigate the impact of charges on the behaviour of droplets under the influence of electric fields. Especially, the generation of droplets can lead to unwanted charges caused by the contact to a charged surface. Even commonly used techniques as for instance pipetting are associated with the generation of charges on the droplets [39]. Consequently, the generation of the droplet has to be performed with caution under well-defined conditions. Droplets with a volume between  $V_d = 10 \mu\text{l}$  and  $V_d = 100 \mu\text{l}$  are generated with a custom-built automated syringe. High purity water (Millipore Milli-Q Type I with an electrical conductivity of  $\kappa_{\text{el}} = 5.5 \cdot 10^{-6} \text{ S/m}$  at  $\vartheta = 25^\circ\text{C}$ ) is used to generate the droplets. The water is stored in carefully cleaned and gas-tight bottles under the absence of light to prevent any change of the properties. Each

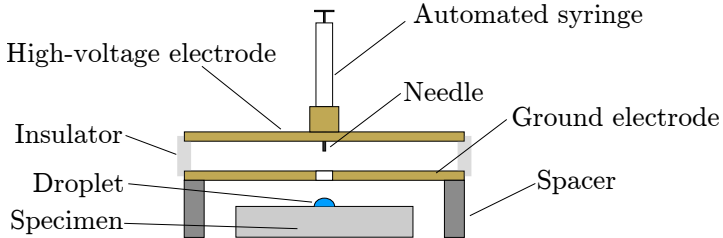


Figure 4.6: Schematic of the droplet charger in sectional view.

bottle is carefully cleaned with isopropanol and flushed several times with high purity water prior to the filling to prevent any contamination of the water. A gas-tight syringe (Hamilton 1710 RN - 100  $\mu\text{l}$ ) is used to meter the volume of the droplets and is automated by an Arduino (Arduino Uno, Adafruit Proto-Screwshield, Sparkfun EasyDriver v4.5) and a stepper motor (Nema 17 - 200 steps/rev). The Arduino controls the stepper motor, which drives a ball bearing spindle to draw up or release liquid from the syringe. Using this automated system the flow rate is controlled precisely and is always kept constant. In addition, the volume of the droplet can be precisely controlled with an error of  $\Delta V \approx 5\%$  of the desired volume. A metallic needle with an inner diameter of  $d = 0.5\text{ mm}$  or  $d = 0.7\text{ mm}$  is attached to the syringe. To generate uncharged droplets the needle is grounded. Charged droplets are generated using a droplet charger similar to [23], which is schematically shown in Fig. 4.6.

Two circular brass electrodes with a diameter of  $d = 110\text{ mm}$  are separated by an insulator at a distance of  $h = 5\text{ mm}$ . The upper electrode is connected to a voltage source (Heinzinger PNChp 20000), which applies a constant electric potential up to  $\phi = \pm 2\text{ kV}$  to the electrode. In contrast, the lower electrode is grounded resulting in almost homogeneous electric field between the electrodes. The metallic needle punctures the centre of the high-voltage electrode and is electrically connected to this electrode. Accordingly, the needle has the same electric potential as the upper electrode. To ensure a reliable detachment of the droplet and to prevent a wetting of the upper electrode, the tip of the needle is not flush with the electrode but enters the space between the plates ( $h \approx 2.5\text{ mm}$ ) as shown in Fig. 4.6. Thus, the liquid only contacts the needle and has no contact to the brass electrode. The lower electrode has a centred hole

#### 4 Experimental details

with a diameter of  $d = 5$  mm to enable the droplet to directly fall on the substrate without contacting the grounded electrode.

The high purity water is forced to flow through the needle with a constant flow rate by the automated syringe. The electric field between the electrodes causes a migration of charges, resulting in a charged droplet as soon as the droplet detaches from the needle. Hence, the droplet is charged by charge separation. After the droplet detaches from the needle, caused by the gravitational and electrical force higher than the surface tension between the droplet and the needle, the droplet directly leaves the droplet charger through the hole in the bottom electrodes and is directly placed in the centre of the substrate. Note that droplets with  $V > 10 \mu\text{l}$  generally do not detach as a single droplet but in multiple stages of smaller droplets. Consequently, the resulting charge of a droplet is given by the accumulated charge of the individual droplets. However, the volume of the resulting droplet can still be accurately determined. The reason for the detachment of smaller droplets is caused by the gravitational and electric force acting on the droplet. As a result the charge on the droplet might be higher than the Rayleigh limit due to the fact that the accumulated charge of smaller droplets is larger than the charge of a single droplet with the same volume of all small droplets. However, the droplets are not disintegrated because the droplets are interacting with the substrate, and thus are stable even if they are highly charged.

The actual charge on the droplet depends on the flow rate, the needle size, the droplet volume and the applied voltage between the electrodes of the droplet charger. Due to the fact that the charge of a droplet cannot be measured after the deposition because the droplet interacts with the substrate [152], the charge generation of the droplets is calibrated with respect to the already mentioned influencing factors. Note that the flow rate was kept constant for all experiments, and thus has no influence on the electric charge of the used droplets.

The charge of the droplets was measured using a Faraday cup similar to [23, 39]. The schematic of the Faraday cup is shown in Fig. 4.7. It consists of two concentric aluminium cups, both of them electrically insulated from each other to ensure an accurate measurement. The outer cup is grounded and serves as Faraday cage, which generates a field-free environment inside the cup. Thus, external influences are reduced and do not influence the measurement. The inner cup contains the droplet and is connected to an electrometer (Keithley 6514), which directly measures the charge. Prior

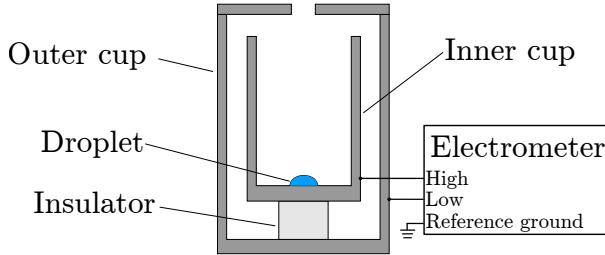


Figure 4.7: Schematic of the Faraday cup with connection diagram.

to the droplet deposition the electrometer is reset to ensure an accurate measurement of the actual charge on the droplet. The charge of the droplet is transferred to the aluminium cup by conduction (in case of direct contact) or induction (in case of no contact). Consequently, the charge of the droplet can be directly measured. Note that large droplets are produced by several smaller droplets, because the droplet prematurely detaches from the needle. In this case the charge of the final droplet is defined by the charge of the individual droplets produced by the droplet charger. Even though the droplet is produced by several small droplets or a single droplet, the charge is accurately determined because it represents the same procedure as used for the experiments.

The setup was calibrated prior to the measurements to determine the accuracy of the measurement. Instead of a droplet, a well-defined charge is applied to the inner cup using a charge calibrator (Kistler 5357 B). Charges in the range between  $Q = 1 \cdot 10^{-11} \text{ C}$  and  $Q = 7.5 \cdot 10^{-7} \text{ C}$  are directly applied to the inner cup and measured by the electrometer. More details about the calibration can be found in App. D. The calibration leads to an accurate measurement of the charge with a maximum error of  $\Delta Q = 5.5 \cdot 10^{-9} \text{ C}$  for the range used in this study. In addition, the resulting charge of the droplets is determined depending on the droplet volume and the applied voltage of the droplet charger. The resulting charge depending on the applied voltage for a needle with a diameter of  $d = 0.5 \text{ mm}$  is shown in Fig. 4.8.

Each measurement was repeated three times and averaged to determine the charge with high accuracy. The charge of a droplet increases with increasing applied voltage. For low voltages ( $U < 250 \text{ V}$ ) the increase

#### 4 Experimental details

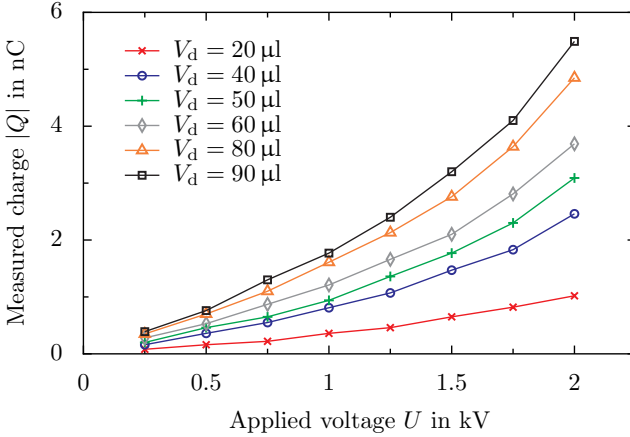


Figure 4.8: Resulting charge (norm)  $|Q|$  of a droplet depending on the droplet volume  $V_d$  and the applied voltage  $U$  between the electrodes of the droplet charger for a needle diameter of  $d = 0.5$  mm. Reprinted with permission from [150], © 2019 IEEE.

of charge is almost linear as shown by [23]<sup>2</sup>, but for higher voltages ( $U > 250$  V) the charge increases quadratically with the voltage as shown in Fig. 4.8. In addition, the higher the droplet volume, the higher is the resulting charge on the droplet. The corresponding data for a needle with a diameter of  $d = 0.7$  mm is shown in App. D. Generally, the smaller needle size was used to generate the droplet because the droplets detach much easier from the smaller needle (due to the lower force of surface tension) resulting in smaller residuals on the needle. Using the calibrated charge measurement and the determined correlation between the applied voltage of the droplet charger and the droplet volume for a fixed flow rate and needle size the amount of charge can be determined accurately without measuring the charge of the sessile droplet. To prevent charge accumulation on the substrate by contact, the droplet charger is directly placed above the substrate surface without touching the substrate. Furthermore, the position of the droplet charger is centred using fixed points to ensure that the droplet is placed in the centre of the substrate surface.

<sup>2</sup>The droplet size is almost constant (no influence of the electric field), so that besides the charge density, the charge is also linear correlated to the applied voltage.

### 4.3.2 Generation of inflexible gelatin droplets

Water droplets can be highly affected by electric fields, possibly resulting in droplet motion or oscillation. In fact, this motion or oscillation complicates the investigation of partial discharges because the geometry in the region of the three-phase contact line is continuously changed. Consequently, the generation of inflexible droplets would be beneficial to investigate the partial discharge inception. In this case however, the electrical properties of the inflexible droplet must match the electrical properties of water to accurately reproduce the given configuration. For this purpose inflexible droplets generated by a mixture of gelatin and water are used instead of pure water. High purity water (Millipore Milli-Q Type I) is mixed with gelatin (Sigma Aldrich G9391 - Bloom number  $\approx 225$ ) with a weight ratio of 25:1 (25 g of water and 1 g of dry gelatin powder). The mixture is continuously stirred for at least 5 min and simultaneously heated to a temperature of  $\vartheta \approx 70^\circ\text{C}$  to fully dissolve the gelatin powder in water. Afterwards, the liquid is placed on the specimen using an automated syringe to generate a droplet with precisely controlled volume. Then, the specimen comprising the liquid droplet is stored in a refrigerator at  $\vartheta \approx 7^\circ\text{C}$  for approximately one hour to cool down the mixture and to cause solidification. This procedure prevents the entrapment of air between the gelatin droplet and the substrate, which would produce significantly different results compared to liquid droplets with direct contact to the substrate.

Due to the fact that the gelatin droplets can evaporate, the experiments are performed shortly after the droplet is completely solid. Even long storage times in the refrigerator can lead to enormous droplet evaporation, i.e. a change of the droplet volume. One of the major advantages of gelatin droplets is that the fluid properties of the liquid mixture are similar to the fluid properties of water. Hence, the shape of a water droplet can be reproduced using the water-gelatin mixture as shown in Fig. 4.9. Even if the overall shape is reproduced very well, the static contact angle is lower in the case of the gelatin droplet. However, the behaviour of water and gelatin droplets under the impact of electric fields cannot be compared directly because of the motion of water droplets. Thus, the difference in contact angle is less important and has an almost negligible influence.

Besides the geometrical arrangement, the inflexible droplet has to have the same electrical properties in order to have the same mutual interaction on the electric field as a water droplet. A water droplet made out

## 4 Experimental details

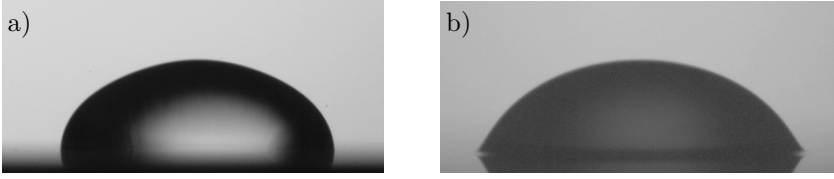


Figure 4.9: Comparison of the equilibrium shape of a water and gelatin droplet in absence of an electric field. Side view of a) water droplet and b) a gelatin droplet of the same volume of  $V = 100 \mu\text{l}$ .

of high purity water can be assumed to be a perfect conductor for low frequencies because of the charge relaxation time of  $\tau_{\text{el,wa}} = 1.3 \cdot 10^{-4} \text{ s}$  ( $\tau_{\text{el,wa}}/\tau_{\text{AC}} \ll 1$ , where  $\tau_{\text{AC}}$  is the characteristic time of the alternating electric field). To determine the charge relaxation time of the water-gelatin mixture the electrical conductivity and the relative permittivity of the solidified mixture was measured<sup>3</sup>. The measurement results can be found in App. F.

The electrical conductivity of gelatin decreases with decreasing frequency. In the low frequency range the electrical conductivity is similar to water so that the electrical conductivity of the mixture is assumed to be in the same order of magnitude ( $\kappa_{\text{gel}} \approx 10^{-5} \text{ S/m}$ ) as for water. Due to the fact that the relative permittivity of water is assumed to be constant for low frequencies ( $f < 1 \text{ GHz}$ ) even if the measured values are higher [5], the relative permittivity of the gelatin-water mixture is also assumed to be constant for the low frequency range. Thus, the relative permittivity of the mixture is determined at a frequency of  $f = 10^6 \text{ Hz}$ . A more detailed analysis of the measurement and the observed behaviour can be found in App. F. The relative permittivity of the gelatin-water mixture strongly depends on the temperature. The lower the temperature, the higher is the relative permittivity. For a conservative estimation a relative permittivity of  $\epsilon_r = 60$  is assumed, which leads to a charge relaxation time of  $\tau_{\text{el,gel}} \approx 5 \cdot 10^{-5} \text{ s}$ . Consequently, the water-gelatin mixture can also be assumed to be a perfect conductor for low frequencies (all frequencies of alternating electric fields investigated in the present study), because

<sup>3</sup>The dielectric measurement was performed in collaboration with Florian Pabst at the Institute for Condensed Matter Physics (TU Darmstadt).

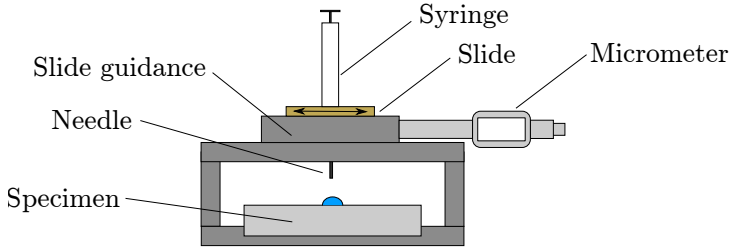


Figure 4.10: Schematic of the transverse for positioning multiple droplets on the substrate.

of  $\tau_{\text{el,gel}}/\tau_{\text{AC}} \ll 1$ , resulting in perfectly reproduced electrical boundary conditions.

### 4.3.3 Positioning of the droplets

In case of single droplets, the position of the droplets on the substrate is controlled by the position of the droplet charger above the substrate. The position of the droplet charger is fixed by edge guides mounted to the droplet charger to accurately and repeatably determine the position with respect to the substrate. Hence, the droplet is always placed directly at the centre of the substrate, which is located directly in the centre between the electrodes. The positioning of gelatin droplets or multiple droplets is performed with a traverse to precisely control the position of each droplet on the substrate and with respect to each other. A schematic of the traverse is shown in Fig. 4.10. The traverse is directly placed above the specimen. The position of the specimen below the traverse is fixed by a slot with the same size as the specimen. A digital micrometer is used to change the position of the needle in the  $x$  direction on the substrate surface (see Fig. 4.1). The micrometer moves a slide, which is directly connected to the needle and guided by the slide guidance to ensure that the position is only changed in the desired direction. Consequently, the position of each droplet can be precisely controlled with respect to the distance of the individual electrodes and the droplet-droplet separation.

The size of the droplet depends on the droplet volume so that the distance and position of the droplets must be adjusted for each droplet volume.

## 4 Experimental details



Figure 4.11: Different steps of image analysis with a) original image, b) black and white image of detected droplet after edge detection and morphological operations and c) detected contour and contact angles superimposed on the original image. Reprinted figure (adapted) with permission from [156]. Copyright 2020 by the American Physical Society.

Prior to the experiments, the position of the droplet is determined with preliminary tests to determine the necessary settings to generate the required droplet-droplet separation for a specific volume. For this purpose the droplet-droplet separation and the droplet size were determined using shadowgraphy for different settings. This method ensures that both droplets have the same distance from the electrodes and a fixed distance between each other. After deposition of the droplet the traverse was removed without moving the substrate or touching the sessile droplet and substrate.

In case of multiple droplets the needle was always grounded to minimize the generation of charges.

### 4.3.4 Analysis of the droplet motion experiments

The analysis of the experiments is performed with an in-house Matlab<sup>®</sup> code to analyse the data with respect to pre-defined criteria. For the analysis of the droplet motion the video data of the droplet is analysed frame by frame. The shape of the droplet is analysed in each frame. Therefore, the projected area of the droplet, centre of mass, deformation in height and width, curvature of the droplet surface as well as the contact angles are calculated using edge detection algorithms and morphological operations. An example of the image analysis for a single frame is shown in Fig. 4.11. The original image (grey scale image) is shown in Fig. 4.11a and is analysed by an edge detection to find the contour of the droplet. The

edge detection analyses the gradient of grey scale between the individual pixels in the image, and thus can distinguish the dark droplet from the much brighter background. The location of the substrate is determined semi-automatically by analysing the contact angles. The reflection of the droplet interface near the contact angles on the substrate virtually extends the droplet and produces a non-physical sharp kinks of the droplet interface (locally extreme changes of the curvature at the contact angles). The reflection of the contact angles is used to determine the interface between the substrate and the droplet, which is located in the axis of symmetry. Assuming a horizontal substrate the interface can be constructed by a straight line.

After performing several morphological operations to determine the shape of the droplet the image is converted into a black and white image as shown Fig. 4.11b. The black and white image is used to determine the contour of the droplet, the projected surface area, the width and height as well as the contact angles. The result of the analysis is shown in Fig. 4.11c, where the detected contour (red) and the contact angles (green) are superimposed on the original image. Due to the fact that this analysis is performed for each frame of a video all analysed quantities are time dependent. As an example, the evolution of the contact angles with respect to time is shown in Fig. 4.12. The figure shows the corresponding contact angle to the droplet presented in Fig. 4.11. Both, the contact angle on the right side of the droplet  $\theta_{\text{right}}$  and on the left side  $\theta_{\text{left}}$  are shown dependent on the time  $t$ . As indicated by the evolution of the signals, the droplet oscillates in the first resonance mode, which leads to large changes of the contact angle on both sides.

Besides the contact angle, the motion and oscillation can be analysed by several other time dependent quantities. To determine the oscillation frequency the time evolution of the quantities can be analysed using a fast Fourier transformation (FFT). As a result, the different frequencies of the individual signals are determined and can be correlated to the direction of motion and the applied electric field strength. An example of such a FFT is shown in Fig. 4.13. The single-sided amplitude spectrum of the signal is shown as a function of the frequency  $f$  in the range from  $f = 0$  Hz to  $f = 1000$  Hz. The data presented in this graph corresponds to the signal of  $\theta_{\text{right}}$  presented in Fig. 4.12. The main frequency of the signal is  $f = 27.99$  Hz, which is the same frequency as the applied voltage signal. Furthermore, several harmonics are present in the signal, as for example the doubled frequency of the voltage signal ( $f = 55.97$  Hz). To determine

#### 4 Experimental details

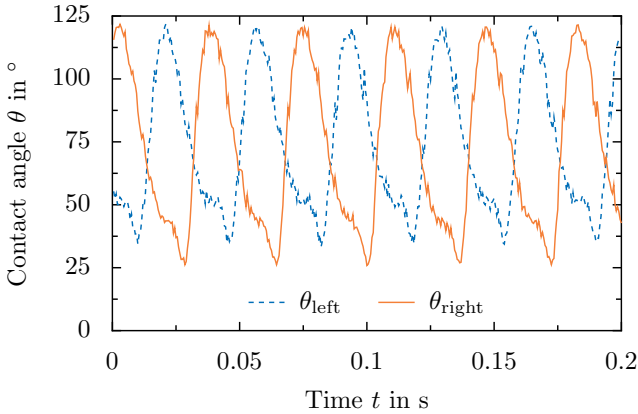


Figure 4.12: Time evolution of the contact angles  $\theta$  corresponding to the droplet shown in Fig. 4.11. Reprinted figure (adapted) with permission from [156]. Copyright 2020 by the American Physical Society.

the oscillation frequency of a droplet the frequencies of all signals are analysed and compared to each other. Finally, the oscillation frequency is determined with respect to the principle direction of motion and the most pronounced frequencies of the signals. However, the automatized detection of the oscillation frequency is sometimes not completely clear, because the analysis of the different time-dependent signals might lead to different results. As an example, the signals of the area or the contact angles of a droplet oscillating in the first resonance mode can lead to believe that the droplet oscillates with twice the frequency of the electric field (repeating signal after a half period) even if the video data shows that the droplet oscillates with the same frequency as the applied voltage. Especially, the first resonance mode is affected by this phenomenon.

Even if the droplet performs an asymmetric motion (by alternating leaning sideways) the projected area is almost equal in case of the largest amplitude/deformation, which yields a virtually increased frequency (compare the images shown in Fig. 2.10a). Consequently, the analysis of different signals possibly generate controversial results. Thus, well-defined criteria have to be defined to reliably determine the correct oscillation frequency.

For sessile droplets the motion of the centre of mass is always coupled

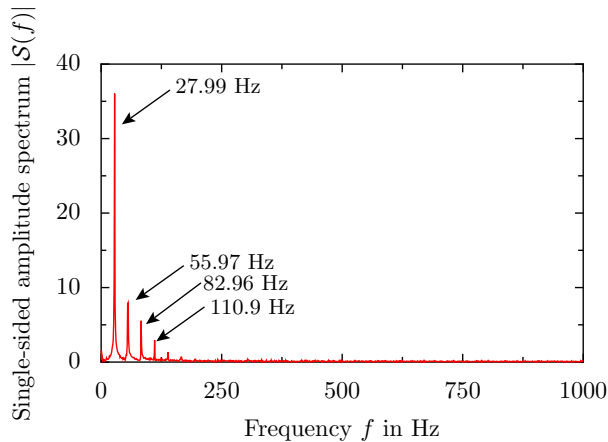


Figure 4.13: Single-sided amplitude spectrum  $\mathcal{S}(f)$  for  $\theta_{\text{right}}$  of the corresponding signal shown in Fig. 4.12. The droplet is excited with a frequency of  $f_{\text{AC}} = 27.99$  Hz. Reprinted figure (adapted) with permission from [156]. Copyright 2020 by the American Physical Society.

with the motion of the droplet [176] and can be used to determine the oscillation frequency of the droplet. Nevertheless, the motion with respect to different directions is not necessarily coupled so that still various frequencies can be observed. Hence, the frequency of the oscillation cannot be determined by the motion of the centre of mass alone.

In addition to the motion of the centre of mass, the principle direction of the motion has to be taken into account. Each oscillation mode has a principle direction of motion, which characterizes the oscillation. Furthermore, the general definition of an oscillation, which defines the period of the oscillation as the shortest time to repeat the exact and full motion, has to be taken into account to prevent a misinterpretation of the signals. In case of the first resonance mode, the principal motion is parallel to the substrate. In contrast, higher resonance modes have a principle motion perpendicular to the substrate. Analysing the motion of the centre of mass in the principal direction of motion leads to a more reliable determination of the resonance frequency. Especially, for the first resonance mode the different time-dependent signals have to be analysed with caution because the motion can be superimposed by other modes. In this case the

## 4 Experimental details

principal direction of motion is determined by theoretical principal motion defined by Eq. (2.51). Especially, for mixed motions (superposition of different oscillation modes) the result is carefully checked and repeated by hand to rule out any mistakes. A detailed analysis of accuracy of the method is examined in App. G.

### 4.3.5 Analysis of the partial discharge experiments

The analysis of the partial discharge experiments is twofold, because the partial discharge inception field strength is determined electrically and the location of partial discharges is captured by a UV-camera. During the experiment the applied, time-dependent voltage level is recorded with the MPD software from Omicron. Furthermore, the phase-resolved apparent charge of each individual partial discharge impulse is also recorded with respect to time. Both signals are synchronized using the time stamp and can be analysed in an automated way. An in-house Matlab<sup>®</sup> code determines the voltage level for the first appearance of a partial discharge impulse with an apparent charge of  $Q_{PD} = 5 \text{ pC}$ , which is defined as inception voltage. Afterwards, the inception voltage is used to calculate the inception field strength.

Due to the fact that the electric field is distorted by the droplet, which depends on the droplet position and the droplet size, the local electric field strength in presence of a droplet cannot be used as a reference. Instead, the electric field is calculated at the centre between the electrodes (see origin of the coordinate system in Fig. 4.1) in absence of a droplet depending on the applied voltage level. The calculation is based on a numerical simulation of the electric field performed with COMSOL Multiphysics<sup>®</sup>. The resulting electric field can be used as a reference and only depends on the geometrical arrangement and the applied voltage. Note that the actual electric field inside the droplet completely vanishes, because the droplet is assumed to be a perfect conductor for the investigated frequencies of the alternating electric field. Furthermore, the electric field strength directly at the three-phase contact line is higher than the reference value. However, using the same geometrical arrangement, the different experiments can be compared and different influencing factors can be determined by comparing the inception field strength.

In addition to the electrical measurement of the partial discharges the location of the partial discharges is determined using a UV-camera. To ac-

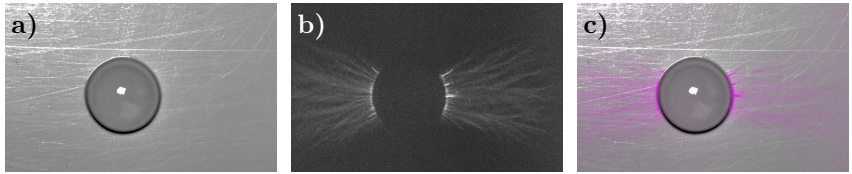


Figure 4.14: Different steps of optical analysis of partial discharges showing a) an original image, b) an image from camera and c) the superposition of the coloured UV image and original image. Reprinted figure (adapted) with permission from [157]. Copyright 2020 by the American Physical Society.

curately determine the location of the partial discharges the images of the UV-camera are superimposed to a reference image as shown in Fig. 4.14. Figure 4.14a shows the reference image of a sessile gelatin droplet. The captured UV-light produced by the partial discharges for the same droplet is shown in Fig. 4.14b. While the emitted UV light is captured with high resolution the shape of the droplet can only be approximated. Superimposing both images leads to an accurate determination of the location of the partial discharges. The combination of both images is shown in Fig. 4.14c. Note that the partial discharges are coloured to increase visibility. The colour strength corresponds to the intensity of the emitted UV light in Fig. 4.14b.



# 5 Motion of charged and uncharged sessile droplets

---

---

The content of this chapter is partly based on the Master thesis of Franziska Zajonz [292] and has already been partially published in the following publication and conference proceeding:

- [150] Löwe, J.-M. and Hinrichsen, V. Experimental Investigation of the Influence of Electric Charge on the Behavior of Water Droplets in Electric Fields. In *2019 IEEE 20th International Conference on Dielectric Liquids (ICDL)*, pages 1–6. IEEE, 2019. ISBN 978-1-7281-1718-8. doi:10.1109/ICDL.2019.8796707
- [156] Löwe, J.-M., Hinrichsen, V., Roisman, I. V., and Tropea, C. Behavior of Charged and Uncharged Drops in High Alternating Tangential Electric Fields. *Physical Review E*, 101(2):023102, 2020. doi:10.1103/PhysRevE.101.023102

---

---

## 5.1 General

The general behaviour of water droplets under the impact of constant and alternating electric fields was already investigated [13, 59, 196, 237]. However, the impact of electric charges on the behaviour of droplets is still not completely understood. Several theoretical models attempt to predict the behaviour of charged and uncharged droplets without quantifying the amount of charge necessary to influence the behaviour [75, 76]. Furthermore, the interaction between the electric field strength, the droplet volume and the charge has not been investigated in detail. Electric charges are ubiquitous, and already a small amount of charges can significantly influence the behaviour of droplets in electric fields. Droplets can be charged unintentionally by charge transfer between the substrate and the droplet [152], if the substrate surface contains a large amount of surface charges. In addition, the use of conventional pipettes is associated with the gen-

## 5 Motion of charged and uncharged sessile droplets

eration of unwanted charges on the generated droplet [39]. Consequently, a careful droplet handling is very crucial for well-defined conditions during the experiments. In addition, charged droplets are not only generated in the lab, but also occur in nature. These could be for instance charged rain drops which interact with technical systems such as high-voltage insulators or aircraft [91, 241, 246]. Measurements proved that droplets generated by collecting raindrops are generally charged. Consequently, sessile droplets generated by rain are also charged. The used measurement technique and a more detailed description of the investigation are presented in App. H. Thus, applications are also affected by charged droplets, which has been neglected in many investigations and this is one possible reason for the lack of accurate prediction models for the ageing of high-voltage insulators. Hence, experiments performed in the past (such as [66, 126, 187]) might have unintentionally used charged droplets with an unknown amount of charge. To determine the impact of electric charges on the behaviour of droplets under the impact of electric fields, experiments with well-defined boundary conditions are performed. The behaviour of the droplets is determined depending on the droplet volume, the electric field strength, the frequency of the electric field, the electric charge and the different oscillation modes of the droplet.

An overview of the tested parameters is shown in Table 5.2. Several combinations of these parameters are investigated to determine the behaviour of differently sized droplets under the impact of electric fields. The fre-

Table 5.2: Overview of tested parameters and their quantities. Reprinted (adapted) with permission from [156]. Copyright 2020 by the American Physical Society.

Parameter	Quantity
Droplet volume $V_d$ in $\mu\text{l}$	20, 40, 60, 80
Kinematic viscosity $\nu$ in $\text{m}^2/\text{s}$	$1.004 \cdot 10^{-6}$ , $1.88 \cdot 10^{-6}$
Electric field strength $\hat{E}$ in $\text{kV}/\text{cm}$	2.58, 4.42, 7.37
Frequency of electric field $f_{AC}$ in $\text{Hz}$	27.77, $\dots$ , 83.3
Electric charge $Q$ in $\text{nC}$	0, $\dots$ , 3.36

quency of the electric field was chosen with respect to the droplet volumes and the corresponding resonance frequencies of the droplet, see Eq. (2.51). In addition to pure water, a mixture of water and glycerol is used to study the impact of the viscosity on the behaviour of droplets under the impact of electric fields because of the similar properties of glycerol with respect to density ( $\rho_{\text{gly}} = 1260.8 \text{ kg/m}^3$ ) and surface tension ( $\gamma_{\text{gly}} = 63.4 \cdot 10^{-3} \text{ N/m}$ ) compared to water. A mixture with a volume fraction of 25 ml of glycerol and 100 ml of high purity water is used for the experiments. The kinematic viscosity of the mixture yields  $\nu_{\text{mix}} = 1.878 \cdot 10^{-6} \text{ m}^2/\text{s}$  at  $20^\circ\text{C}$ , and therefore is doubled compared to pure water.

Even though droplets with such a high viscosity do not appear in nature, the corresponding experiments are used to exceed the knowledge of the underlying physics and the impact of the viscosity on the motion of the droplets. Especially, for the generation of theoretical models a detailed knowledge of all influencing factors is crucial to accurately describe and predict the physics, i.e. the motion of the droplets.

Assuming that the behaviour of the droplet under the impact of an electric field is mainly influenced by the force generated by the electric field and the surface tension, the viscosity should have a negligible impact on the behaviour of the droplets. Consequently, doubling the viscosity should not affect the outcome of the experiments. The surface tension acts against the force of the electric field, which tries to deform the droplet. In addition, the surface tension tries to minimize the surface energy and shapes the droplet. However, depending on the size of the droplet also gravity can influence the shape of the droplet. In addition to these parameters, the wetting properties of the substrate influences the droplet shape.

To mathematically describe and characterize the behaviour of the droplets several dimensionless ratios are introduced. The Bond number

$$\text{Bo} = \frac{\rho g d_d}{\gamma} \hat{=} \frac{\text{Force of gravity}}{\text{Force of surface tension}}, \quad (5.1)$$

characterizes the ratio between the gravitational force and the surface tension, where  $\rho$  is the density of the fluid,  $g$  is the gravitational acceleration,  $d_d$  is the droplet diameter and  $\gamma$  is the surface tension. The droplets considered in this study have a Bond number in the order of unity so that the shape of the droplet in equilibrium is determined by surface tension and gravity. Any kind of external forces such as substrate vibrations or electric fields influence the shape of the droplet and promote droplet deformations.

## 5 Motion of charged and uncharged sessile droplets

As shown in Sec. 2.4 the electric field leads to a force, which in turn can generate droplet oscillations. The frequency of the droplet oscillation is mainly determined by the dominant force acting on the droplet. Generally both the Coulomb force and the dielectric/electrostrictive force are acting on the droplet because in reality almost every droplet contains net charges, even if they are very small. The strength of the individual components is characterized by the amount of charge on the droplet and the electric field strength. A characteristic ratio  $\xi$  is introduced to quantify the ratio between the Coulomb force and the dielectric/electrostrictive force. The dimensionless ratio is defined by

$$\xi = \frac{Q}{\varepsilon_0 \hat{E} d_d^2} \hat{=} \frac{\text{Coulomb force}}{\text{Dielectric/electrostrictive force}}. \quad (5.2)$$

For  $\xi \gg 1$  the Coulomb force is much stronger than the dielectric and electrostrictive force and determines the behaviour of the droplet. In case of an alternating electric field the droplet is then assumed to oscillate with the same frequency as the applied voltage. In contrast,  $\xi \ll 1$  leads to a dominant dielectric or electrostrictive force, which causes the droplet to oscillate with twice the frequency of the applied alternating voltage. A ratio  $\xi \approx 1$  indicates that both components of the resulting force are of the same order of magnitude.

It is assumed that the droplets oscillate with a frequency resulting from the superposition of the single and doubled frequency of the applied voltage. Accordingly, electric charges can significantly influence the oscillation behaviour of sessile droplets under the impact of alternating electric fields. To characterize whether the droplets behave like a charged or uncharged droplet, the oscillation frequency of the droplet  $f_d$  is compared to the frequency of the applied voltage signal  $f_{AC}$ . This dimensionless ratio is defined by

$$\frac{f_d}{f_{AC}} = \begin{cases} 1 & \text{- dominant Coulomb force} \\ 2 & \text{- dominant dielectric and electrostrictive force} \end{cases} \quad (5.3)$$

and mainly determines the behaviour of the droplet. Note that the definition in Eq. (5.3) is based on the observations that only distinct frequency ratios are present in the performed experiments.

The electric charge of the droplet can also be represented by a dimensionless quantity by using the Rayleigh charge as a reference. This results in the ratio  $Q/Q_{\max}$ , where  $Q_{\max}$  is defined by Eq. (2.4) and depends on

the droplet volume. The necessary charge to change the behaviour of the droplet that produces a dominant Coulomb is subsequently named the onset charge  $Q^*$ . It characterizes the minimum amount of electric charge to cause a droplet oscillation with the same frequency as the applied voltage. It is worth noting that the behaviour of a droplet is always defined by both the electric field and the electric charge so that the onset charge defines the minimum necessary charge for a corresponding electric field strength. Increasing the electric field always leads to a higher amount of charge necessary to reproduce the same behaviour.

The impact of charges on the behaviour of sessile water droplets is subsequently investigated for the first three resonance modes. Even higher resonance modes are assumed to have a comparable outcome due to the fact that increasing the resonance frequency only leads to the same general motion as for the third resonance mode but with an increased number of steady nodes on the droplet surface. High electric field strengths induce oscillations with large amplitudes, especially for a droplet oscillating in resonance. These oscillations produce periodical changes of the contact angle that can exceed the advancing contact angle, finally resulting in a droplet motion. Such behaviour is used for electrowetting applications, but is prevented by a limited electric field strength for the present experiments. Hence, only droplet oscillation with pinned contact line are investigated to determine the influence of electric charge on the frequency of droplet oscillation.

## 5.2 Motion of droplets in first resonance mode

The principal motion of a droplet oscillating in the first resonance mode ( $\mathcal{N} = 2$ ) is shown in Fig. 5.1a. This motion is often called rocking [52], ratchet-like [194] or bending motion [164] and is characterized by a motion mainly parallel to the substrate. The droplet periodically leans from left to right and vice versa. Accordingly, the motion is non-axisymmetric, which is the most important difference to higher oscillation modes, see Fig. 2.10. In case of Fig. 5.1a the motion of an uncharged droplet is shown with respect to time. The frequency of the droplet oscillation is the same as the frequency of the applied voltage, even if no charge is present. Comparing this behaviour to the motion of a charged droplet under the same conditions as shown in Fig. 5.1b reveals that the oscillation frequency is not changed by the presence of electric charges.

## 5 Motion of charged and uncharged sessile droplets

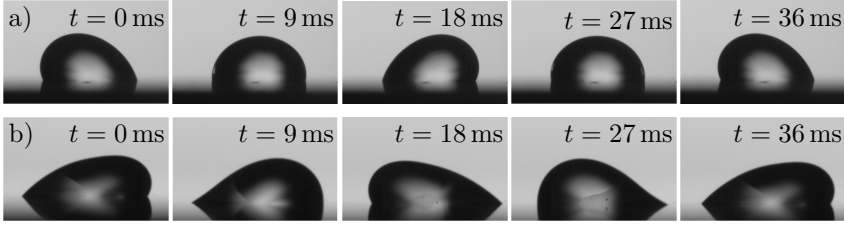


Figure 5.1: Comparison of one cycle of an uncharged and a charged droplet in first resonance mode. a) One cycle of an uncharged droplet with a volume of  $V_d = 20 \mu\text{l}$  and a voltage frequency of 27 Hz at an electric field strength of  $\hat{E} = 3.81 \text{ kV/cm}$  and b) one cycle of a charged droplet ( $Q = 0.646 \text{ nC}$ ) with a volume of  $V_d = 20 \mu\text{l}$  and a voltage frequency of 27 Hz at an electric field strength of  $\hat{E} = 4.42 \text{ kV/cm}$ . Reprinted figure (adapted) with permission from [156]. Copyright 2020 by the American Physical Society.

The droplet still oscillates with the same frequency as the applied voltage. However, the shape of the droplet is influenced by the presence of charges. Comparing the appearance of the droplet in Figs. 5.1a and b shows that the wetted area is increased due to the presence of electric charges. Consequently, the shape of the droplet is changed even if both droplets have the same volume. The increase in wetted area is caused by the presence of charges with the same polarity. These charges repel each other and act against the surface tension which tries to minimize the surface area. The new equilibrium shape is caused by a force balance between those two forces. Nevertheless, the principal motion is still the same and is independent of the amount of charge.

To investigate whether this behaviour is valid for different amounts of charge and electric field strengths, several droplet volumes were investigated under the impact of different electric field strengths and electric charges. As a result the frequency ratio  $f_d/f_{AC}$  depending on the characteristic ratio of the electric forces  $\xi$  is analysed for each droplet volume. An example for a droplet with a volume of  $V_d = 20 \mu\text{l}$  is shown in Fig. 5.2. The droplet always oscillates with the same frequency as the applied voltage, independent of the electric charge and the electric field

## 5.2 Motion of droplets in first resonance mode

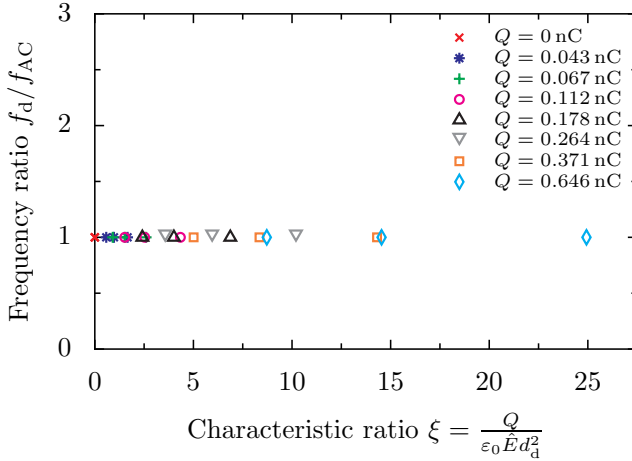


Figure 5.2: Dimensionless frequency ratio  $f_d/f_{AC}$  depending on the characteristic ratio  $\xi$  for a droplet oscillating in the first resonance mode with  $V_d = 20 \mu\text{l}$ . Reprinted figure (adapted) with permission from [156]. Copyright 2020 by the American Physical Society.

strength. Even in absence of electric charges the droplet oscillates with the same frequency as the applied voltage, which is contradictory to the presented theoretical model (Sec. 2.4). Note that the same result is obtained for all other droplet volumes so that a droplet oscillating in first resonance mode always oscillates with the same frequency as the applied voltage, and thus behaves like a charged droplet. Hence, no change of the oscillation frequency could be observed for the wide range of tested parameters. Nevertheless, an oscillation with the doubled frequency of the applied electric field was always recognized perpendicular to the principal direction of motion, i.e. perpendicular to the substrate.

The behaviour of a droplet in first resonance mode is independent of the electric charge, electric field strength and volume. Therefore, the behaviour in first resonance mode significantly differs from the behaviour of other resonance modes and an explanation for this behaviour is still missing. The charge relaxation time of water  $\tau_{el} \ll 1/f_d$  is much lower than the inverse of the applied frequencies so that net charges have always enough time to be oriented under the influence of the electric field. In

addition, the water molecules themselves are oriented by the electric field. However, the characteristic time of the electric field is also much lower than the time necessary for the alignment of water molecules in an electric field, because water molecules can follow frequencies up to the GHz range [242]. Consequently, the reason is not associated with the orientation of the water molecules or net charges but is assumed to be a result of the macroscopic non-axisymmetric motion of the droplet and has to be further investigated.

Depending on the position of the droplet in the electric field and the accuracy of droplet generation (droplet volume), a superposition of the first and second resonance mode could be observed. In this case both motions are superimposed and both frequencies, the single and the doubled frequency of the applied voltage, can be recognized. Hence, the resulting droplet motion is very sensitive to changes of the boundary conditions, and thus a careful and accurate handling is indispensable.

### 5.3 Motion of droplets in second resonance mode

In contrast to the first resonance mode, the second resonance mode ( $\mathcal{N} = 3$ ) causes a vertical droplet motion perpendicular to the substrate. The droplet is periodically compressed and stretched resulting in an axisymmetric motion as shown in Fig. 5.3. The principal oscillation behaviour of a droplet in the second resonance mode is shown for different boundary conditions. The motion of an uncharged droplet with a volume of  $V_d = 80 \mu\text{l}$  is shown in Fig. 5.3a. The frequency of the droplet oscillation is  $f_d \approx 54 \text{ Hz}$  and is twice the frequency of the applied voltage. Hence, the motion of the droplet is defined by a dominant dielectric force. A comparison of the observed behaviour and numerical simulations can be found in [198].

Increasing the amount of electric charge on the droplet causes a change of the behaviour as shown in Fig. 5.3b. An electric charge of  $Q = 2.76 \text{ nC}$  and an electric field strength of  $\hat{E} = 2.58 \text{ kV/cm}$  leads to a droplet oscillation with the same frequency as the applied voltage signal. The amount of charge present on the droplet provokes a dominant Coulomb force and a changed oscillation behaviour. Especially for low electric field strength

### 5.3 Motion of droplets in second resonance mode

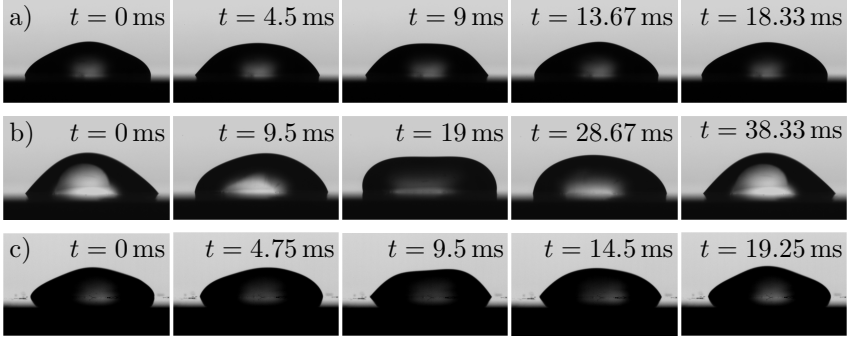


Figure 5.3: Comparison of one cycle for an uncharged and a charged droplet in second resonance mode. a) One cycle of an uncharged droplet with a volume of  $V_d = 80 \mu\text{l}$  and a voltage frequency of 26 Hz at an electric field strength of  $\hat{E} = 7.37 \text{ kV/cm}$ , b) One cycle of a charged droplet ( $Q = 2.76 \text{ nC}$ ) with a volume of  $V_d = 80 \mu\text{l}$  and a voltage frequency of 26 Hz at an electric field strength of  $\hat{E} = 2.58 \text{ kV/cm}$  and c) One cycle of a charged droplet ( $Q = 3.36 \text{ nC}$ ) with a volume of  $V_d = 80 \mu\text{l}$  and a voltage frequency of 26 Hz at an electric field strength of  $\hat{E} = 7.37 \text{ kV/cm}$ . Reprinted figure (adapted) with permission from [156]. Copyright 2020 by the American Physical Society.

and a sufficient amount of charge, the droplet is oscillating with the same frequency as the applied voltage signal.

A further increase of the electric field strength again induces a change of the behaviour as shown in Fig. 5.3c. Even for an increased amount of electric charge ( $Q = 3.36 \text{ nC}$ ) the droplet oscillates with twice the frequency of the applied voltage for the given electric field strength of  $\hat{E} = 7.37 \text{ kV/cm}$ . The higher the amount of charge, the higher is the electric field strength necessary to cause the change in oscillation behaviour. Consequently, the behaviour of the droplet is defined by the interaction of the electric charge and the electric field strength. This behaviour is well described by the theory presented in Sec. 2.4.

Due to the fact that the dielectric force is proportional to the squared

## 5 Motion of charged and uncharged sessile droplets

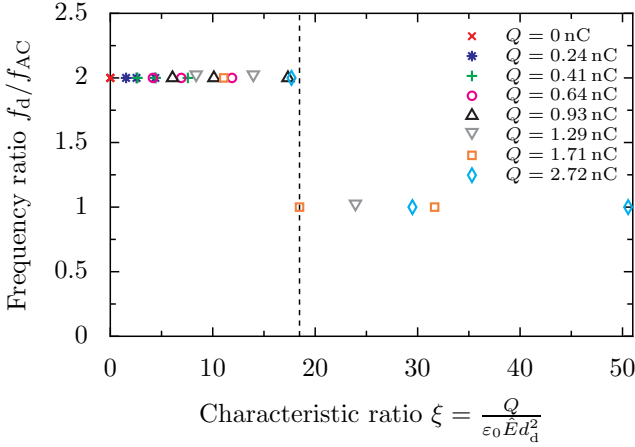


Figure 5.4: Dimensionless frequency ratio  $f_d/f_{AC}$  depending on the characteristic ratio  $\xi$  for a droplet oscillating in second resonance mode with  $V_d = 60 \mu\text{l}$ . The dashed line shows the critical characteristic ratio  $\xi^*$  for the change of the behaviour. Reprinted (adapted) with permission from [150], © 2019 IEEE.

electric field strength, increasing the electric field strength will always force the droplet to oscillate with twice the frequency of the applied voltage for a sufficiently high electric field. However, the presence of a large amount of charge, increases the electric field strength necessary to cause a change of the behaviour. Both, a large amount of charge and high electric field strength also influence the shape of the droplet, even if the three-phase contact line is pinned during the oscillation. An example is shown in Fig. 5.3c, where the wetted surface area is increased compared to the droplet shown in Figs. 5.3a and b. An even further increase of the electric field strength would lead to a motion of the three-phase contact line as observed for electrowetting.

The change of the oscillation behaviour depends on both the electric field strength and the electric charge. Hence, the change of the frequency can be analysed depending on the characteristic ratio of the electric forces as presented for a droplet with a volume  $V_d = 60 \mu\text{l}$  in Fig. 5.4. For  $\xi < 18.47$  the droplet oscillates with twice the frequency of the applied voltage. Hence, the amount of charge present on the droplet does not cause the droplet to oscillate with the same frequency as the applied

### 5.3 Motion of droplets in second resonance mode

voltage for the given electric field strength. Furthermore, in this case the electric field strength is high enough to suppress the change in behaviour. Increasing  $\xi$  to  $\xi^* = 18.47$  leads to a change of the behaviour, and for all  $\xi \geq \xi^*$  the frequency of the droplet oscillation is the same as the frequency of the applied voltage.

The same behaviour was observed for the other volumes and is in good agreement with the presented theory. Increasing the amount of charge for a fixed electric field strength can trigger a change of the behaviour. Accordingly, a specific amount of charge  $Q^*$  is necessary to cause a change of the oscillation behaviour. This minimum charge  $Q^*$  is determined by the electric field strength. Droplets with a charge  $Q < Q^*$  will behave like uncharged droplets for a specific electric field strength and oscillate with twice the frequency of the applied voltage. In contrast, a charge  $Q \geq Q^*$  cause the droplet to behave like a charged droplet, so that the droplet oscillates with the same frequency as the applied voltage. It is noteworthy that the  $\xi^*$  is not always a fixed value as shown in Fig. 5.4 but rather a transition region. This intermediate region appears if both oscillation frequencies can be observed for a fixed  $\xi$ .

The maximum amount of charge on a droplet is limited according to Eq. (2.4). Due to the fact that the charge is limited, increasing the electric field always provokes a droplet to oscillate with twice the frequency of the electric field for sufficiently high electric fields. Larger droplets are able to retain a larger amount of charge compared to smaller droplets. Hence, it is expected that the minimum charge  $Q^*$  also depends on the droplet volume. The dependence of the minimum onset charge  $Q^*$  on the droplet volume is shown in Fig. 5.5. The error bars show the variation of the data resulting from the charge measurement. An increasing droplet volume leads to an increasing minimum onset charge independent of the viscosity of the fluid. Two regimes, namely I and II, can be defined by the onset charge. Regime I describes the behaviour of charged droplets, where the droplets oscillate with the same frequency as the applied voltage. This regime is limited by the Rayleigh limit, which is represented as a solid line. Hence, the grey region defines non-physical conditions that cannot be reached in practice because the droplet would disintegrate under these conditions. Regime II characterizes the behaviour of uncharged droplets, which oscillate with twice the frequency of the applied voltage. The border between the two regimes is indicated by the dashed line, which is defined by a quadratic fit of the experimental data for water droplets. Consequently, the charge to mass ratio  $Q/m$  increases with increasing

## 5 Motion of charged and uncharged sessile droplets

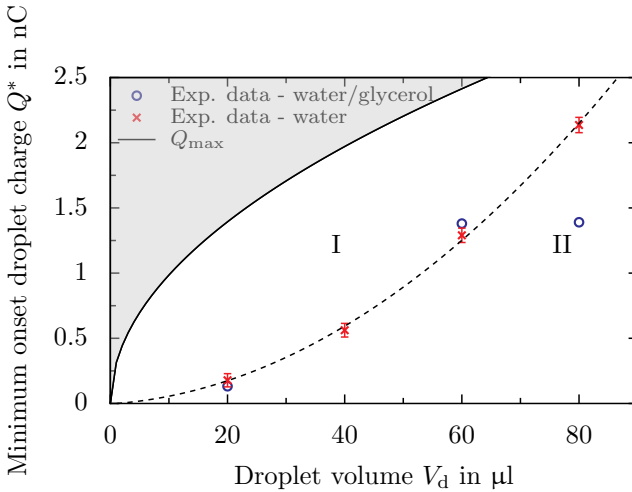


Figure 5.5: Minimum onset charge  $Q^*$  for a frequency change depending on the droplet volume  $V_d$  and  $Q_{\max}$  as defined by Eq. (2.4) for the second resonance mode and different viscosities. Data for pure water is taken from [154]. Regime I includes droplets with same frequency and regime II droplets with double the frequency of the applied voltage. The dashed line visualizes the two regimes. The solid line limits regime I due to the Rayleigh limit, therefore the grey area includes non-physical values. Reprinted figure (adapted) with permission from [156]. Copyright 2020 by the American Physical Society.

droplet volume and is not constant. For large droplet volumes the border between the two regimes and the solid line, indicating the Rayleigh limit, intersect. The intersection point is given for a volume of  $V_d^* \approx 97 \mu\text{l}$ , so that droplets with a volume  $V_d \geq V_d^*$  are not affected by electric charges and always behave like uncharged droplets, even if they contain a large amount of charge.

Furthermore, the influence of the viscosity is investigated using a water-glycerol mixture, which leads to an increased viscosity compared to water. The resulting viscosity is doubled compared to water, and thus should result in a significant change of the behaviour if the physical mechanism is influenced by this parameter. As already mentioned, glycerol was used

because of the similar fluid properties with respect to water. However, under the impact of electric fields, the behaviour of liquid droplets is also influenced by the electric properties of the liquid. Taking into account the mixing ratio the relative permittivity of the water-glycerol mixture and the electrical conductivity yields  $\varepsilon_{r,\text{mix}} \approx 73$  and  $\kappa_{\text{el}} \approx 13.8 \cdot 10^{-4} \text{ S/m}$ , respectively [84]. Calculating the charge relaxation time for the mixture reveals that  $\tau_{\text{el,mix}} \approx 4.70 \cdot 10^{-7} \text{ s} \ll \tau_{\text{AC}}$ , so that the water-glycerol mixture has to be assumed as a perfect conductor. Consequently, the mixture has the same electrical behaviour as pure water.

The comparison of the minimum onset charge of the water-glycerol mixture is also shown in Fig. 5.5. For droplet volumes  $V < 60 \mu\text{l}$  the onset charge does not depend on the viscosity of the droplet. The increased viscosity of the water-glycerol mixture has almost no impact on the minimum onset charge. In contrast, for larger droplets (e.g.,  $V = 80 \mu\text{l}$ ) the minimum onset charge of the water-glycerol mixture is lower compared to water. Hence, the viscosity has an effect on droplets with a large volume.

The minimum dimensionless onset charge depending on the Bond number is shown in Fig. 5.6. The error bars represent the measurement uncertainty of the net charge, the droplet volume and the applied voltage. The maximum charge defined by Eq. (2.4) is used as a scale for the minimum onset charge, and the Bond number is used to characterize the volume. A ratio of  $Q^*/Q_{\text{max}} = 1$  limits both regimes because it defines the maximum charge of a droplet. Similar to Fig. 5.5 two regimes can be identified. Regime I contains droplets with a sufficient charge to cause a droplet oscillation with the same frequency as the applied voltage. In contrast, regime II characterizes droplets, which oscillate with twice the frequency of the applied voltage. The dashed line is a linear fit of the experimental data for water and indicates the transition between both regimes.

The influence of the electric field is not directly shown in Fig. 5.6. Increasing the electric field strength leads to an increase of the minimum onset charge  $Q^*$ , and therefore changes the size of regime I. The higher the electric field strength, the higher is the charge necessary for a change of the behaviour. Hence, an increasing electric field strength shifts the boarder towards lower Bond numbers and reduces the size of regime I. For a sufficiently high electric field strength regime I vanishes because the charge necessary for the change in behaviour would exceed the Rayleigh charge, which is not achievable in practice. Furthermore, large droplet volumes, i.e. large Bond numbers, also cause regime I to vanish. For such

## 5 Motion of charged and uncharged sessile droplets

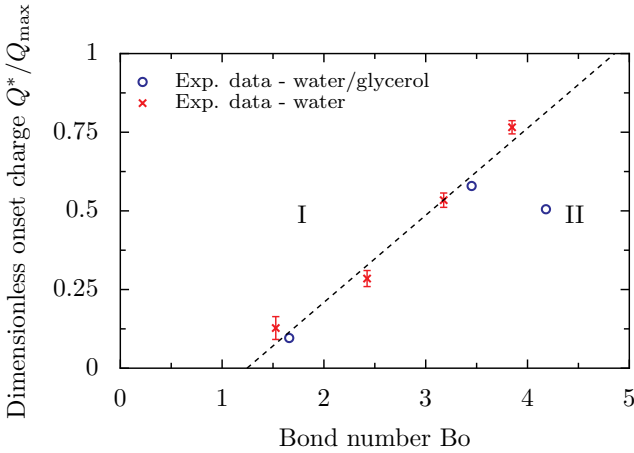


Figure 5.6: Dimensionless onset charge  $Q^*/Q_{\max}$  depending on the Bond number  $Bo$  for droplets oscillating in second resonance mode. Regime I includes droplets with same frequency and regime II droplet with double the frequency of the applied voltage. The dashed line visualizes the two regimes. Reprinted figure (adapted) with permission from [156]. Copyright 2020 by the American Physical Society.

large Bond numbers the charge necessary to change the behaviour of the droplet also exceeds the Rayleigh charge.

An increasing droplet volume causes an increasing dielectric and electrostatic force, as indicated by Eq. (2.50). However, the maximum possible charge does not increase in the same manner, because the influence of the surface tension decreases for an increasing droplet size. Consequently, large droplets are always acting as uncharged droplets independent of their net charge for sufficiently large Bond numbers. For the presented data all droplets with  $Bo > 4.9$  are not affected by net charges. Hence, the behaviour of small droplets is much more affected by electric charges than for larger droplets. Especially, for high electric field strengths only the behaviour of small droplets is affected by electric charges. The lower the volume, the lower is the minimum onset charge for the change of the oscillation behaviour compared to higher volumes. Droplets of very large volumes are assumed to be not affected by electric charges and always

oscillate with twice the frequency of the applied voltage even if they are highly charged.

The linear trend of the dimensionless onset charge and the Bond number can be observed for a wide range of Bond numbers. In case of pure water the linear trend is observed for all tested Bond numbers. In contrast, increasing the viscosity leads to a different tendency for large Bond numbers  $Bo > 4$ . For Bond numbers lower  $Bo < 4$  the linear trend of the dimensionless onset charge is also observed for an increased viscosity.

## 5.4 Motion of droplets in third resonance mode

Increasing the frequency of the applied voltage might promote the excitation of higher resonance modes. These modes are characterized by interface oscillations between steady nodes on the surface of the droplet. Increasing the resonance frequency increases the number of steady nodes on the interface of the droplet. In case of the third resonance mode two steady nodes are present on the interface of the droplet. The oscillation of a droplet in third resonance mode with and without charge is shown in Fig. 5.7. The principal motion of the droplet is perpendicular to the substrate, and the droplet periodically buckles between the steady nodes. An uncharged droplet oscillates with twice the frequency as the applied voltage as shown in Fig. 5.7a. Increasing the charge on the droplet causes a change in behaviour so that the droplet oscillates with the same frequency as the applied voltage. It is noteworthy that the electric field strength has to be sufficiently low to observe this behaviour. An example of such a behaviour is shown in Fig. 5.7b.

An increase of the electric field strength again induces a change of the behaviour, so that the droplet oscillates with twice the frequency of the applied voltage as shown in Fig. 5.7c. Even if the electric charge for Fig. 5.7c is lowered compared to Fig. 5.7b the change in oscillation frequency can be observed. Generally, the lower the electric charge, the lower is the electric field strength to cause the change in behaviour. Simultaneously, the higher electric field strength influences the footprint and the wetted area of the droplet. Also, the higher electric field strength stretches the droplet and increases the footprint of the droplet. In addition, increasing the electric field strength creates decreasing amplitudes of the oscillation, as shown in the comparison of the different time series. The reason for

## 5 Motion of charged and uncharged sessile droplets

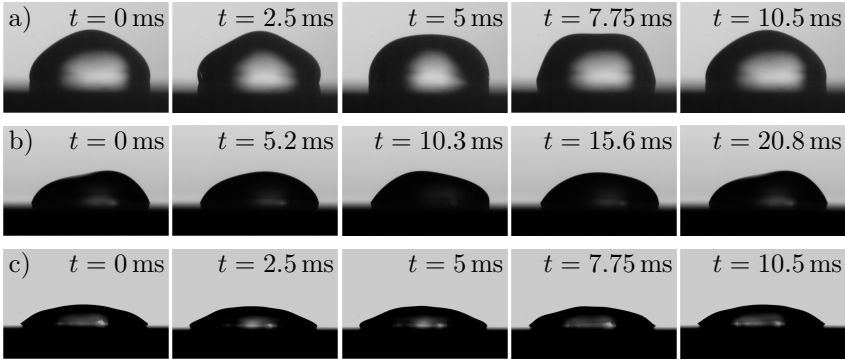


Figure 5.7: Comparison of one cycle for an uncharged and a charged droplet in third resonance mode. a) One cycle of an uncharged droplet with a volume of  $V_d = 60 \mu\text{l}$  and a voltage frequency of 48 Hz at an electric field strength of  $\hat{E} = 7.37 \text{ kV/cm}$ , b) one cycle of a charged droplet ( $Q = 3.69 \text{ nC}$ ) with a volume of  $V_d = 60 \mu\text{l}$  and a voltage frequency of 48 Hz at an electric field strength of  $\hat{E} = 2.58 \text{ kV/cm}$ . and c) one cycle of a charged droplet ( $Q = 2.72 \text{ nC}$ ) with a volume of  $V_d = 60 \mu\text{l}$  and a voltage frequency of 48 Hz at an electric field strength of  $\hat{E} = 7.37 \text{ kV/cm}$ . Reprinted figure (adapted) with permission from [156]. Copyright 2020 by the American Physical Society.

this behaviour is the increased surface area of the droplet, which leads to a larger influence of the surface tension limiting the deformation of the droplet interface. In general, the behaviour of a droplet oscillating in the third resonance mode is similar to the second resonance mode. Higher resonance frequencies are assumed to have a lower impact on the droplet due to the fact that the amplitude of the oscillation is decreased. Furthermore, the general behaviour is assumed to be the same as for the third resonance mode.

Besides the quantitative analysis of the droplet oscillation, the change of the behaviour depending on the electric charge and the electric field strength can be analysed using the dimensionless frequency ratio and the characteristic ratio of the electric forces, as presented exemplarily for a droplet with volume  $V_d = 20 \mu\text{l}$  in Fig. 5.8. A low amount of electric

## 5.4 Motion of droplets in third resonance mode

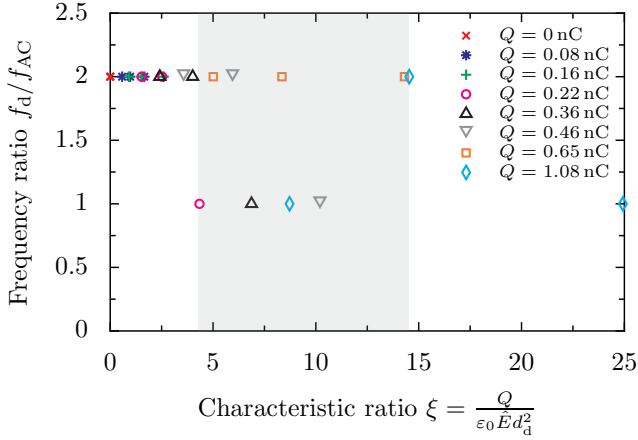


Figure 5.8: Dimensionless frequency ratio  $f_d/f_{AC}$  depending on the characteristic ratio  $\xi$  for a droplet oscillating in third resonance mode with a volume of  $V_d = 20 \mu\text{l}$ . The grey area shows the transition region. Reprinted figure (adapted) with permission from [156]. Copyright 2020 by the American Physical Society.

charge or high electric field strength lead to low characteristic ratios. For  $\xi < 4.34$  all droplets oscillate with twice the frequency of the applied voltage and behave like uncharged droplets. Increasing the characteristic ratio by increasing the electric charge on the droplet can cause a change of the oscillation frequency. The lowest characteristic ratio for a change of the behaviour is  $\xi^* = 4.34$ . Nevertheless, for larger  $\xi$  the presence of both frequencies can be observed. Hence, the transition between the oscillation frequencies is not given by a distinct characteristic ratio  $\xi$  but by a transition region.

The appearance of the transition region is observed to depend on the droplet volume and might be influenced by other boundary conditions like the droplet shape or the local charge on the substrate surface. For instance, for a droplet with a volume of  $V_d = 60 \mu\text{l}$  the transition is also given by a distinct characteristic ratio as seen for the second resonance mode. The corresponding figure can be found in App. E. An even further increase of the characteristic ratio is achieved by further decreasing the electric field strength and results in droplets oscillating only with the same frequency as the applied voltage. In case of these transition regions

## 5 Motion of charged and uncharged sessile droplets

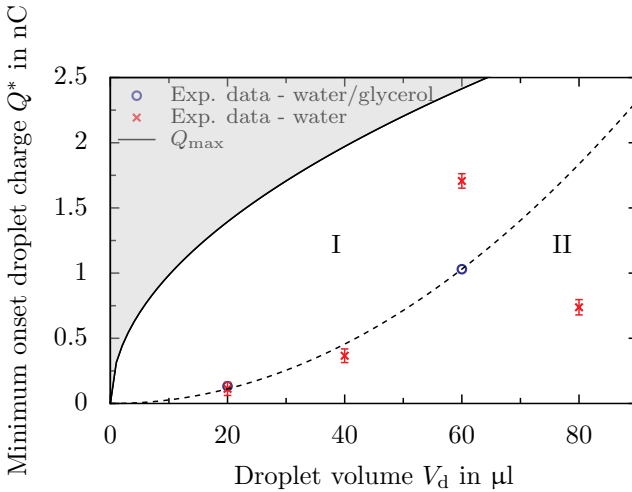


Figure 5.9: Minimum onset charge  $Q^*$  for a frequency change depending on the droplet volume  $V_d$  and  $Q_{\max}$  as defined by Eq. (2.4) for third resonance mode and different viscosities. Regime I includes droplets with same frequency and regime II droplets with double the frequency of the applied voltage. The dashed line visualizes the two regimes. The solid line limits regime I due to the Rayleigh limit, therefore the grey area includes non-physical values.

the onset charge for change of the behaviour is defined as the minimum charge to cause an oscillation with the same frequency as the applied voltage. For the data shown in Fig. 5.8 the minimum onset charge is given by  $Q^* = 0.22 \text{ nC}$  for characteristic ratio of  $\zeta^* = 4.34$ .

As already seen for the second resonance mode, the minimum onset charge to change the oscillation behaviour depends on the droplet volume. The dependence of the minimum onset charge  $Q^*$  on the droplet volume  $V_d$  for the third resonance mode is presented in Fig. 5.9. The error bars characterize the measurement uncertainty of the electric charge. Two regimes can be identified and characterized by the different behaviour of the droplets. Regime I contains droplets oscillating with the same frequency as the applied voltage, and thus characterizes the behaviour of charged droplets. This regime is limited by the Rayleigh limit, which de-

## 5.4 Motion of droplets in third resonance mode

defines the maximum possible amount of charge on a droplet and is shown by the solid line. Hence, the grey region defines non-physical values, which cannot be reached in practice because of droplet disintegration. The dashed line shows the estimate transition between both regimes and is given by a quadratic fit. For droplet volumes  $V_d < 60 \mu\text{l}$  both pure water and the water-glycerol mixture follow the same trend. An increasing volume precipitates an increasing minimum onset charge. In contrast, for higher droplet volumes  $V_d \geq 60 \mu\text{l}$  the data of pure water does not follow the trend any more. At first, the minimum onset charge significantly increases and subsequently decreases for even higher volumes. Accordingly, the behaviour is the same as for the second resonance mode but significantly differs for volumes  $V_d \geq 60 \mu\text{l}$ . The reason for the different behaviour is still unclear. However, the general behaviour is comparable to the second resonance mode.

The dimensionless onset charge depending on the Bond number is shown

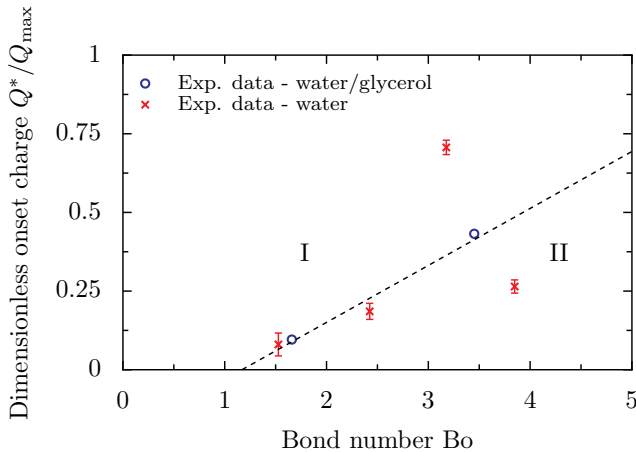


Figure 5.10: Dimensionless onset charge  $Q^*/Q_{\max}$  depending on the Bond number  $Bo$  for droplets oscillating in third resonance mode. Regime I includes droplets with same frequency and regime II droplets with doubled frequency of the applied voltage. The dashed line visualizes the two regimes. Reprinted figure (adapted) with permission from [156]. Copyright 2020 by the American Physical Society.

## 5 Motion of charged and uncharged sessile droplets

in Fig. 5.10. The data shown in Fig. 5.10 is shown in dimensionless form. The error bars represent the measurement uncertainty of the net charge, the droplet volume and the applied voltage. Similar to the second resonance mode, two characteristic regimes can be identified. However, for large Bond numbers the boundary between both regimes is not well-defined based on the experimental data. Regime I is limited by a ratio of  $Q^*/Q_{\max} = 1$ , which defines the maximum charge of a droplet. Note that the charge necessary for a change of the behaviour still depends on the electric field strength so that the size of the regime I depends on the electric field strength. The higher the electric field strength, the higher the necessary charge to induce an oscillation with the same frequency as the applied voltage, resulting in a shift of the border towards lower Bond numbers. The size of regime I decreases. Compared to resonance mode two, the slope of the linear border is lower for the third resonance mode. Thus, a lower amount of electric charge is necessary to change the behaviour of large droplets compared to the second resonance mode. The scatter of the experimental data for larger Bond numbers is significantly larger in case of the third resonance mode, but the tendency is still the same as for the second resonance mode. Hence, the theory is only valid for small droplet volumes. Larger droplet volumes are affected by additional influencing factors.

Comparing the values of  $Q^*/Q_{\max}$  for the second and third resonance mode reveals that the values are in the same order of magnitude. Similarly to the second resonance mode, droplets with small volumes are more affected than larger droplets, which is indicated by the variable size of regime I.

## 5.5 Conclusions

The behaviour of droplets under the influence of an alternating electric field is affected by net charges on the droplet depending on the volume, the electric field strength, the resonance mode and the amount of electric charge. Droplets oscillating in first resonance mode are not affected by electric charges independent of the droplet volume. The droplets always oscillate with the same frequency as the applied voltage, and thus act like charged droplets even if they are uncharged. Consequently, the change of the behaviour predicted by the theory presented in Sec. 2.4 is not observed for the first resonance mode. In contrast, the behaviour of droplets

oscillating in higher resonance modes is well described by the presented theory. The behaviour is mainly defined by the amount of charge present on the droplet and the electric field strength. Uncharged droplets oscillate with twice the frequency of the applied voltage because of the dominant dielectric and electrostrictive force.

Increasing the charge of the droplet changes the oscillation frequency depending on the electric field strength. For sufficiently high charges the droplet oscillates with the same frequency as the applied voltage, which results from the Coulomb force acting on the droplet. A further increase of the electric field strength leads to a second change of the behaviour, and the oscillation frequency of the droplet is doubled again. This behaviour is observed for the second and third resonance mode.

Furthermore, increasing the volume of a droplet requires a higher amount of charge to cause a change of the behaviour. Generally, smaller droplets are much more affected by electric charges than larger droplets. Sufficiently high droplet volumes will suppress the impact of electric charges so that large droplets always oscillate with twice the frequency of the applied voltage. The amount of charge to trigger a change of the oscillation frequency is generally low compared to the Rayleigh limit so that it is likely that droplets contain such an amount of charge in practice. The influence of the viscosity seems to be negligible for small droplet volumes but increases with increasing droplet volume.

A visual summary of the different cases is shown in Fig. 5.11. Note that the behaviour of the droplet always depends on the characteristic ratio  $\xi$ , which is not taken into account in the visual summary. As shown in Chap. 5, small droplets are prone to be affected by electric charges, which provoke an altered behaviour under the impact of electric fields. Such droplets should be handled with caution during laboratory experiments in order to ensure well-defined conditions, because the behaviour of such a droplet is very sensitive to the boundary conditions. Not only initially small droplets are affected by the electric field but also evaporating droplets. While the amount of charge is almost constant on an evaporating droplet, the volume continuously decreases finally resulting in changed behaviour. The oscillation in general influences the geometry near the three-phase contact line, and thus might also impact the generation of partial discharges. Especially, the frequency of the electric field can have a significant influence on the frequency and amount of generated partial discharges.

5 Motion of charged and uncharged sessile droplets

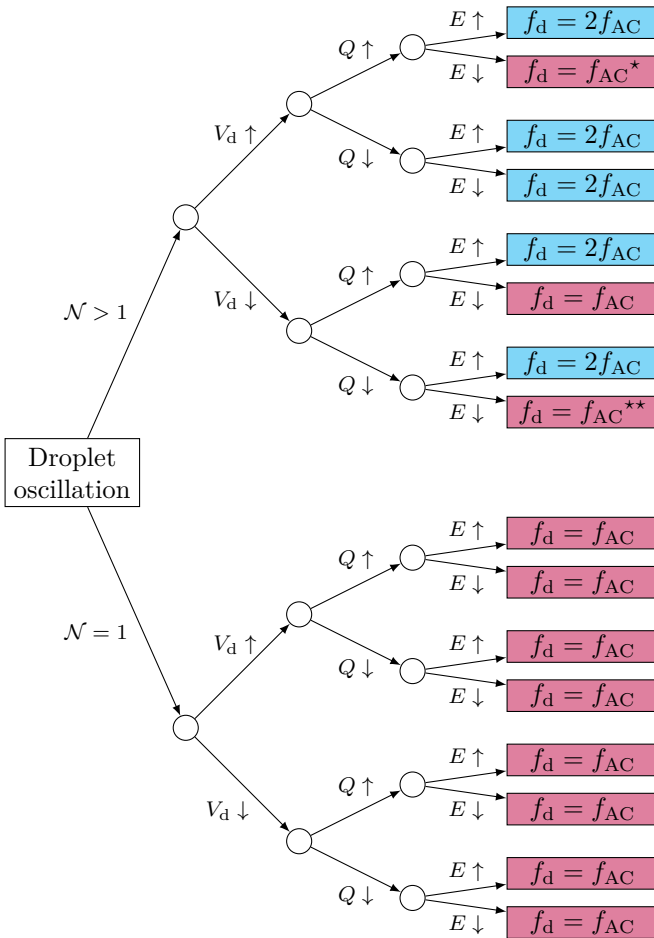


Figure 5.11: Visual summary of principle droplet behaviour depending on the mode number  $\mathcal{N}$ , droplet volume  $V_d$ , charge  $Q$  and electric field strength  $E$ . The symbols  $\uparrow$  and  $\downarrow$  indicate large and small quantities, respectively. The  $\star$  case is limited by the Rayleigh charge and might not be reachable in reality (volume dependent). The case indicated by  $\star\star$  can only be reached with sufficiently high charges and a low electric field strength. The red and blue colour indicate cases with a dominant Coulomb force and dominant dielectric force, respectively.

# 6 Partial discharges generated by sessile droplets

---

---

The content of this chapter has been partially published in the following publication:

- [157] Löwe, J.-M., Hinrichsen, V., Roisman, I. V., and Tropea, C. Impact of Electric Charge and Motion of Water Drops on the Inception Field Strength of Partial Discharges. *Physical Review E*, 102(6):063101, 2020. doi:10.1103/PhysRevE.102.063101
- 
- 

## 6.1 General

The presence of an electric field provokes a motion or oscillation of liquid droplets. This interaction between liquids and an electric field is commonly used for electrowetting applications [183, 190, 262] or for optical lenses [38, 144, 177]. Besides the impact of the electric field on the droplet motion and shape, the droplet also affects the electric field near the three-phase contact line. The shape of the droplet causes a field enhancement at the three-phase contact line, which results in the generation of electrical partial discharges (PD) for sufficiently high electric fields. These discharges affect the substrate and can alter the surface properties of the substrate as a result of the generated locally high temperatures or the emitted UV light [182, 231].

Especially, high-voltage insulators are exposed to PDs generated by sessile droplets on the weather sheds. The PDs accelerate the ageing of the insulator and affect their performance and lifetime [2, 81, 87]. Hence, a precise forecast of the lifetime is crucial for a reliable and efficient power transmission. However, to precisely predict the ageing of such surfaces, the physical mechanisms and the relevant influencing factors have to be determined to accurately model the impact of the PDs. Several studies have been performed to investigate the different influencing factors like droplet motion or surface contamination on the PD generation of a sin-

## 6 Partial discharges generated by sessile droplets

gle droplet [66, 149, 186, 207]. Furthermore, more application-oriented investigations were performed to determine the influence of the insulator geometry and the material properties by performing accelerated ageing tests [101, 179, 271]. In addition, many investigations focusing on electrowetting were already performed [19, 243, 262].

For the classical electrowetting setup, where the droplet is always in contact with one of the electrodes, the field enhancement at the three-phase contact line was theoretically investigated, and the occurrence of PDs was optically recorded [270]. In addition, the role of charge accumulation at the three-phase contact line was investigated in detail [56, 281]. However, the classical electrowetting setup differs from applications such as high-voltage insulators, because the sessile droplets present on the weather sheds are not in direct contact with one of the electrodes. The geometrical arrangements significantly differ, especially regarding the charge distribution. A droplet in direct contact to one electrode is at the same electric potential as the electrode, and charges are directly injected into the droplet. In contrast, a droplet resting on an insulator can only be charged by charge transfer from the surrounding fluid or the substrate in case of an alternating electric field as used in this investigation. This charge transfer is significantly slower compared to a droplet in direct contact with the electrode and is limited [152]. Hence, the experimental setup might significantly influence the outcome of the experiments.

Even though numerous theoretical and experimental investigations were performed in the past, the occurrence and the influencing parameters of PDs for droplets without contact to one of the electrodes is not completely understood yet. Thus, there are no reliable models for the forecast of the ageing of high-voltage insulators.

The occurrence of PDs is affected by several influencing factors and is superimposed on the droplet motion. To predict the generation of PDs, the coupled system of fluid motion and electric field distribution has to be solved simultaneously. This is rather difficult because the motion of the droplet is complex and influenced by several influencing factors as presented in the previous chapter. Furthermore, the electric field has a singularity at the three-phase contact line, which makes an accurate estimation very difficult [66, 270]. To reduce the complexity of the problem the generation of PDs is investigated with stationary droplets consisting of a yield stress fluid. The experiments serve as reference experiments for

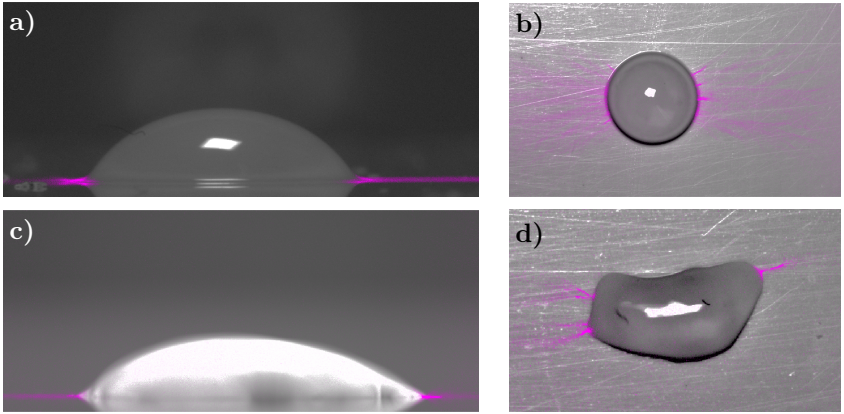


Figure 6.1: Exemplary images of gelatin and water droplets with superimposed image of UV-camera to visualize the partial discharges (coloured in magenta). a) Gelatin droplet with  $V_{d,gel} \approx 65 \mu\text{l}$  in side view for  $\hat{E} = 12.48 \text{ kV/cm}$  and b)  $V_{d,gel} \approx 130 \mu\text{l}$  in top view for  $\hat{E} = 10.27 \text{ kV/cm}$ . c) Water droplet with  $V_{d,wa} = 20 \mu\text{l}$  in side view for  $\hat{E} = 9.02 \text{ kV/cm}$  and d) in top view for  $\hat{E} = 9.63 \text{ kV/cm}$ . Reprinted figure (adapted) with permission from [157]. Copyright 2020 by the American Physical Society.

numerical simulations<sup>4</sup> which enable the development of simplified theoretical models and improve the understanding of the individual influencing factors on the generation of PDs. Especially, the influence of the droplet motion on the inception field strength for PDs is quantified and analysed to improve the accuracy of theoretical models.

Note that the investigation of inflexible droplets is only performed to improve the understanding of the physical mechanisms and does not occur in applications. For the generation of the stationary droplets a mixture of gelatin and water is used to reproduce the exact geometry of a sessile water droplet as well as the electrical properties of liquid water. As already shown in Subsec. 4.3.2, the gelatin droplets reproduce the electrical properties and the shape of a liquid water droplet almost perfectly. This

<sup>4</sup>The results of the corresponding numerical simulations can be found in [198].

## 6 Partial discharges generated by sessile droplets

can also be seen in the quantitative comparison of the water and gelatin droplets with respect to the generation of PDs shown in Fig. 6.1. The figure illustrates images of a gelatin and a water droplet in side and top view. To visualize the PDs the image of the UV-camera is superimposed to a regular image of the droplets as described in Subsec. 4.3.5. The intensity of the colour in the images corresponds to the strength of the PDs. Nevertheless, the intensity was adjusted for each image for better visualization, and thus cannot be compared between the individual images. The shape of a stationary gelatin droplet is shown in Figs. 6.1a and b. The droplet has a shape of a spherical cap, which is not influenced by the electric field. Consequently, no oscillation of the droplet is observable.

As indicated by the images, the PDs are generated directly at the three-phase contact line. The intensity is the highest directly at the three-phase contact line and decreases with increasing distance from this region. The PDs follow the direction of the electric field lines and only occur at locations with sufficiently high electric field strength. Note that the partial discharge pattern is affected by the geometrical arrangement, as indicated by the comparison of Fig. 6.1 and the results of Vallet et al. [270]. An exemplary electric field distribution (top view) including the electric field lines for the geometrical arrangement used in this study is shown in Fig. 6.2. The electric field distribution is calculated using COMSOL Multiphysics<sup>®</sup> assuming a hydrophilic substrate ( $\theta < 90^\circ$ ). The electric field strength was limited to  $\hat{E} = 35 \text{ kV/cm}$  for better visualization of the field distribution. A comparison between Figs. 6.1 and 6.2 confirms that the PDs are oriented along the electric field lines and at regions with high electric field strength.

The shape of a water droplet generating PDs is shown in Figs. 6.1c and d. A comparison of the side view between the gelatin and water droplet reveals no significant difference. In both cases the PDs are generated at the three-phase contact line. Furthermore, the PDs are only located at distinct sides of the droplets. However, the water droplets oscillate, which can be seen by the bright diffuse interface of the water droplet. Comparing the top view of the gelatin and the water droplet reveals the major difference between both droplets. While the shape of the gelatin droplet is not altered by the electric field, the water droplet is significantly deformed by the electric field. The force caused by the electric field induces a deformation and oscillation of the droplet, which results an irregular shape of the droplet. The shape of the water droplet is determined by the

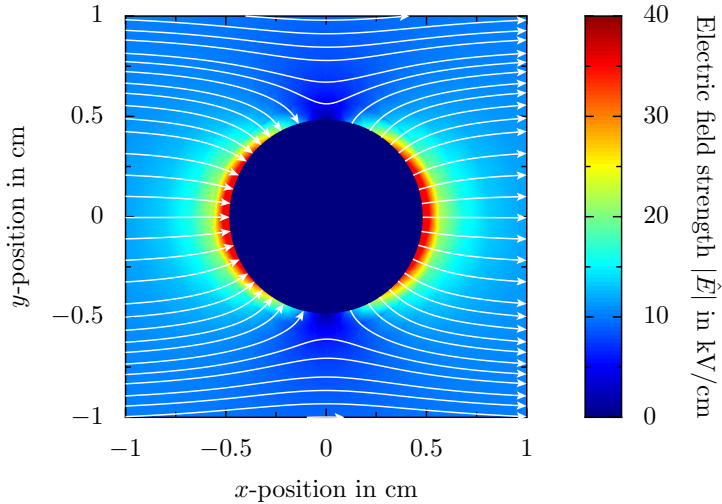


Figure 6.2: Top view of the electric field distribution around a sessile droplet with a volume of  $V = 150 \mu\text{l}$  including the electric field lines (white solid lines) at the surface of the insulator ( $z = 0 \text{ mm}$ ). The undistributed electric field strength is  $\hat{E}_0 = 10 \text{ kV/cm}$ .

wetting properties of the substrate as well as the electric field strength and cannot be approximated by a spherical cap any more.

The irregular shape of the droplet leads to a different PD distribution along the three-phase contact line. PDs are only observed at distinct locations of the three-phase contact line, which are oriented along the electric field lines similar to the gelatin droplet. The arising cones and edges at the three-phase contact line along the droplet as present on the right side of the droplet in Fig. 6.1d are more prone to generate PDs. The shape of the droplet significantly influences the field distribution around the droplet. Especially, the developed cones and edges generate high electric field strengths because the droplet is assumed as a perfect conductor and the curvature of the three-phase contact line is significantly altered compared to the gelatin droplet. The smaller the curvature of the interface, the higher is the electric field strength on the surface (as indicated by  $E \propto 1/R^2$ , where  $1/R^2$  is the curvature). This relation results from Eq. (2.16) under the assumption of a sphere with a constant charge in

## 6 Partial discharges generated by sessile droplets

free space, which is used as a first approximation). Hence, the cones and edges of the three-phase contact line locally increase the electric field strength resulting in the generation of PDs. Similar results were obtained by Feier-Iova [66] under the assumption of a dielectric droplet.

The irregular shape of the water droplet together with the droplet oscillations cause a complex arrangement, which is difficult to predict. Especially, the irregular shape of water droplets makes the prediction of PD more complex than originally presumed. The droplets cannot be assumed as spherical caps and are always deformed prior to the generation of PDs. Accordingly, the partial discharges can only be estimated by taking into account the deformation of the droplet as well as the droplet oscillations. To reduce the complexity single stationary droplets are investigated. Subsequently, the interaction of two neighbouring stationary droplets is examined. These results are extended by investigating charged and uncharged water droplets oscillating in different resonance modes to determine the impact of electric charges as well as the droplet oscillation on the PD behaviour. A summary of the tested quantities is presented in Table 6.2.

Table 6.2: Overview of tested parameters and their quantities to investigate the generation of PDs.

Parameter	Quantity
Droplet volume (water) $V_{d,wa}$ in $\mu\text{l}$	20, 40, 60, 80
Droplet volume (gelatin) $V_{d,gel}$ in $\mu\text{l}$	100, 150, 200, 250, 300
Droplet-droplet separation $h_{d-d}$ in mm	0.25, ..., 5.37
Electric field strength $\hat{E}$ in kV/cm	0, ..., 8.63
Frequency of electric field $f_{AC}$ in Hz	27.77, ..., 83.3
Electric charge $Q$ in nC	0, ..., 3.68

## 6.2 PD inception field strength of single inflexible droplets

The PD inception field strength  $\hat{E}_{\text{in}}$  of single gelatin droplets depending on the volume is shown in Fig. 6.3. Furthermore, the PD inception field strength is shown for different substrates, which have different wetting properties. Due to the fact that the droplets are produced by solidifying liquid droplets on the surface, the wetting properties of the substrate significantly influence the contact angles of the final inflexible droplet. A comparison of the PD inception field strength of the inflexible droplet with a volume of  $V_{\text{gel}} = 100, \dots, 300 \mu\text{l}$  and the PD inception field strength of water droplets ( $V_{\text{wa}} = 20, \dots, 100 \mu\text{l}$ ) from literature reveals that the PD inception field strength for gelatin droplets is in the same order of magnitude [149, 186, 207]. As already known, an increasing volume leads to a decreasing inception field strength [66, 187, 198], and thus the in-

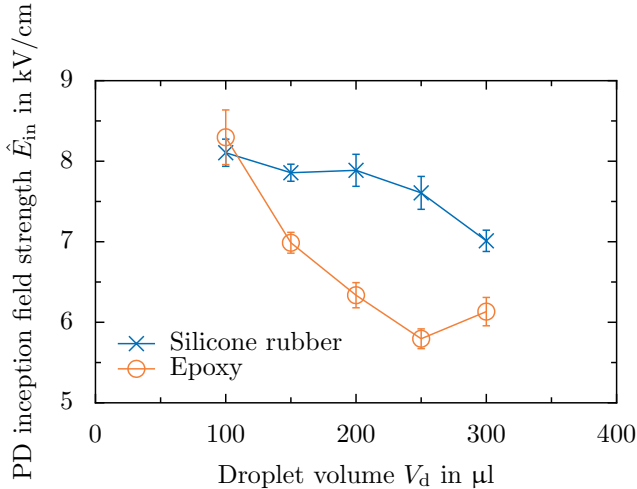


Figure 6.3: PD inception field strength  $\hat{E}_{\text{in}}$  ( $f = 50 \text{ Hz}$ ) for single gelatin drops depending on their volume  $V_d$  on silicone rubber and epoxy. The error bars show the standard deviation of the mean value. Reprinted figure (adapted) with permission from [157]. Copyright 2020 by the American Physical Society.

## 6 Partial discharges generated by sessile droplets

creased volume of the inflexible droplets compensates the influence of the droplet motion and finally results in a good agreement. Consequently, both the motion of the droplet and an increasing volume reduces the PD inception field strength. For droplets of the same volume, the inception field strength is lower for flexible compared to inflexible droplet because of the droplet motion. The PD inception field strength in the same order of magnitude again confirms the excellent reproduction of the electrical and geometrical arrangement by using larger gelatin droplets. The symbols in Fig. 6.3 show the mean value and the error bars represent the corresponding standard deviation of the mean value. The mean values are calculated with a minimum of 33 measurements in case of silicone rubber and a minimum of 9 measurements in case of epoxy. Generally, the PD inception field strength decreases with increasing droplet volume. The highest PD inception field strength is observed for a droplet volume of  $V_{d,gel} = 100 \mu\text{l}$ . For this volume the PD inception field strength is almost independent of the wetting properties, so that the PD inception field strength is almost identical for epoxy and silicone rubber. For an increasing droplet volume the PD inception field strength decreases, however the decrease is larger in case of epoxy compared to silicone rubber. This volume dependence was also observed for pure water [149, 207]. Hence, the inception field strength is lower for epoxy compared to silicone rubber, at least for  $V_{d,gel} > 100 \mu\text{l}$ .

The change of the PD inception field strength is caused by the change of the contact angle. For a droplet volume of  $V_{d,gel} = 100 \mu\text{l}$  the static contact angle is almost identical for epoxy and silicone rubber ( $\theta_{ep} \approx 65^\circ$  and  $\theta_{sil} \approx 64.2^\circ$ , respectively). In contrast, increasing the droplet volume leads to a larger difference between the contact angles. For a droplet with a volume of  $V_{d,gel} = 300 \mu\text{l}$  the contact angles are  $\theta_{sil} \approx 71.5^\circ$  and  $\theta_{ep} \approx 61.4^\circ$  for silicone rubber and epoxy, respectively. The influence of the wetting properties of different substrates was already investigated for water droplets and revealed lower inception field strengths in case of lower static contact angles [207]. Numerical simulations also confirmed the influence of the contact angle and the volume of the droplet [198].

Even though the influence of the droplet volume is counterintuitive, the behaviour can be explained by the motion of the droplets in case of water droplets. The smaller the droplet volume the smaller the curvature of the interface, and therefore the PD inception field strength should be reduced. Simultaneously, the influence of the surface tension is more dominant in case of smaller water droplets, so that smaller water droplets are less deformed by the forces generated by the electric field. As shown

### 6.3 PD inception field strength of two adjacent inflexible droplets

by Ouedraogo [198], the influence of the contact angle is much larger than the impact of the droplet volume for flexible droplets. Hence, the PD inception field strength is decreased for larger water droplets due to the larger oscillations and the corresponding changes of the contact angle. In case of inflexible droplets the impact of the droplet oscillation cannot explain the decreasing PD inception field strength for larger droplets. However, for larger droplet volumes a decreased contact angle is observed. As already stated, the impact of a changed contact angle is much larger than the impact of the volume, so that the decreasing contact angle (for an increasing volume) is accompanied by a decreasing PD inception field strength for inflexible droplets.

Due to the fact that the PD inception field strength mainly depends on the electric field distribution, the change of the substrate relative permittivity might have an influence on the PD inception field strength. As already presented in Table 4.2 both substrates have different relative permittivities. However, the change in relative permittivity is rather small ( $\Delta\varepsilon_r \approx 1.7$ ), and for a volume of  $V_{d, \text{gel}} = 100 \mu\text{l}$  no difference in the PD inception field strength could be observed. This suggests that the influence of a changed relative permittivity of the substrate can be neglected. In addition, numerical simulations confirmed that lower contact angles cause lower inception field strengths and that the relative permittivity of the substrate has only a negligible influence for the present range of permittivities [198]. Thus, the better the wettability of the substrate, the lower is the inception field strength for partial discharges. Furthermore, the simulations showed that large droplets are more prone to generate partial discharges than smaller droplets [198].

## 6.3 PD inception field strength of two adjacent inflexible droplets

In applications such as high-voltage insulators not only single droplets are present on the weather sheds but rather several droplets. The droplets might interact with each other, which possibly produces different results as for single droplets. Thus, several authors have already investigated the behaviour of multiple water droplets with respect to partial discharges [149, 229, 284]. The presence of additional droplets can decrease the PD inception field strength as reported by Lopes et al. [149] for two neigh-

## 6 Partial discharges generated by sessile droplets

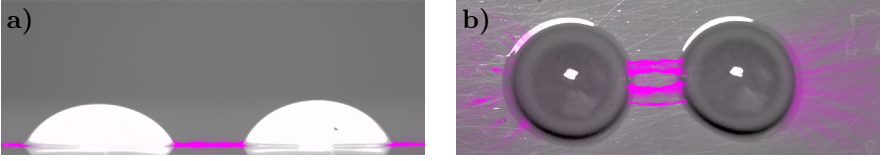


Figure 6.4: Exemplary images of two gelatin droplets a)  $V_{d,\text{gel}} \approx 60 \mu\text{l}$  and b)  $V_{d,\text{gel}} \approx 150 \mu\text{l}$  with superimposed image of UV-camera to visualize the partial discharges (coloured in magenta) in a) side view for  $\hat{E} \approx 9.9 \text{ kV/cm}$  and b) top view for  $\hat{E} \approx 10.1 \text{ kV/cm}$ . Reprinted figure (adapted) with permission from [157]. Copyright 2020 by the American Physical Society.

bouring droplets. Even though several investigations have already been performed, the influence of the droplet motion on the separation between the droplets is only investigated superficially [187]. To investigate the influence of the droplet-droplet separation decoupled from the motion or oscillation, which might significantly influence the droplet-droplet separation, stationary droplets are used. The droplets with the same volume are carefully placed on the substrate within a well-defined separation to investigate whether the droplets influence each other or not.

An exemplary partial discharge pattern generated by two neighbouring droplets is shown in Fig. 6.4. Similar to previous images, the image of the UV-camera is superimposed on a regular daylight image of the droplets. The observed pattern is similar to the pattern observed for single droplets. Partial discharges are generated at the three-phase contact line of both droplets and only occur at distinct regions, because the PDs are oriented along the electric field lines. As shown by the intensity of the colour the strongest partial discharges are located between the droplets. Hence, the neighbouring droplets interact with each other.

The measured PD inception field strength  $\hat{E}_{\text{in}}$  depending on the droplet-droplet separation  $h_{d-d}$  for different droplet volumes  $V_d$  is shown in Fig. 6.5. Droplets at large separations do not interact with each other, so that the inception voltage for a large droplet-droplet separation is similar to the inception voltage of a single droplet. A comparison of the inception field strengths for single droplets and two droplets with the largest separation is presented in Table 6.3. Decreasing the separation between the

### 6.3 PD inception field strength of two adjacent inflexible droplets

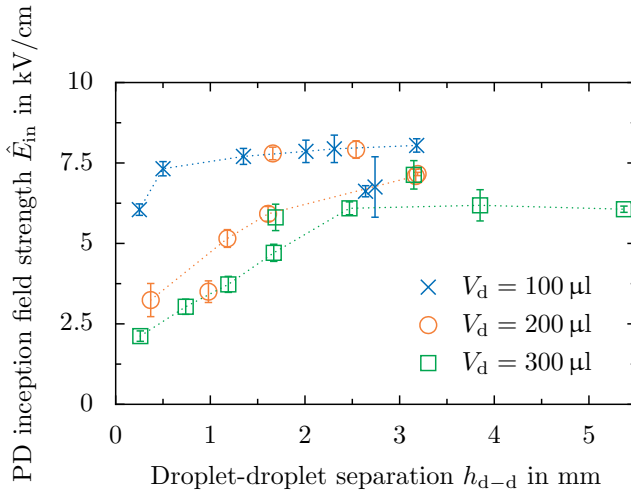


Figure 6.5: PD inception field strength  $\hat{E}_{in}$  of two gelatin droplets depending on the separation  $h_{d-d}$  for different volumes  $V_d$ . The error bars show the standard deviation of the mean value and the dotted lines visualize the trend of the data. Reprinted figure (adapted) with permission from [157]. Copyright 2020 by the American Physical Society.

droplets lowers the PD inception field strength. The smaller the droplet-droplet separation, the lower is the PD inception field strength. A typical droplet-droplet separation can be defined, which leads to an interaction between the droplets, and thus a decrease of the electric field strength. This typical separation increases with increasing droplet volume. Hence, larger droplets interact with each other over larger distances compared to smaller droplets. The distortion of the electric field is larger in case of larger droplets, and so the droplets affect each other over a larger separation compared to smaller droplets.

Consequently, neighbouring droplets can interact with each other depending on the droplet volume and the droplet-droplet separation. Generally, larger droplets are more prone to generated PDs and to interact with adjacent droplets. The presence of multiple droplets significantly reduces the PD inception field strength compared to single sessile droplets. Due to the properties of the gelatin droplets a movement of the droplets is

Table 6.3: Mean PD inception field strength for single gelatin drops  $\hat{E}_{\text{in, single}}$  compared to the PD inception field strength of a droplet pair  $\hat{E}_{\text{in, two}}$  on silicone rubber depending on the volume. For  $\hat{E}_{\text{in, two}}$  the converging limit value for large separations is taken into account. Single outliers are neglected. Reprinted (adapted) with permission from [157]. Copyright 2020 by the American Physical Society.

Volume $V$ in $\mu\text{l}$	100	200	300
Single droplet: $\hat{E}_{\text{in, single}}$ in kV/cm	8.11	7.89	7.01
Droplet pair: $\hat{E}_{\text{in, two}}$ in kV/cm	8.04	7.15	6.18

not observed independently of the electric field strength. Hence, coalescence of the droplets is not possible. However, water droplets are likely to coalesce, especially for small droplet-droplet separations or high electric field strengths. In case of a high-voltage insulator, this would lead to the formation of larger droplets, which further decrease the PD inception field strength and increase the amount of partial discharges. Consequently, the coalescence of small droplets accelerate the surface ageing but is almost not avoidable because the size and the distribution of the droplets cannot be actively influenced during operation.

## 6.4 PD inception field strength for charged and uncharged water droplets

As shown in Chap. 5, the presence of electric charges can significantly change the behaviour of sessile droplets under the influence of electric fields. The frequency of the droplet oscillation is determined by the electric charge, the volume and the electric field strength. The region near the three-phase contact line is the most critical one, because the electric field is enhanced in this region. The droplet oscillation influences the geometry of the droplet by periodically changing the contact angles. In the previous subsections it was shown that a change of the contact angle

## 6.4 PD inception field strength for charged and uncharged water droplets

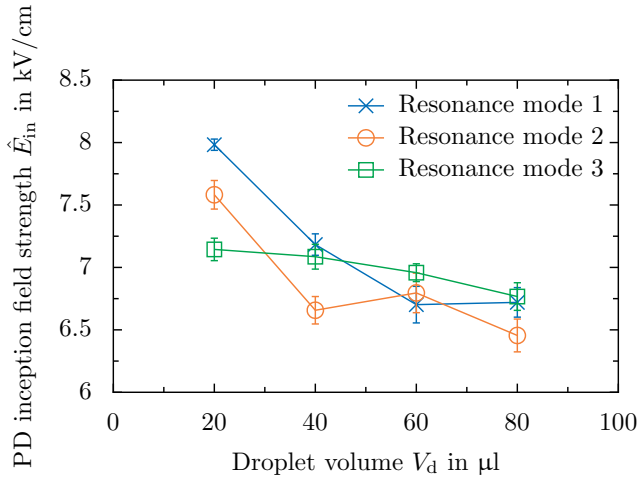


Figure 6.6: PD inception field strength  $\hat{E}_{in}$  of single uncharged water droplets depending on the volume  $V_d$  and resonance mode. Reprinted figure (adapted) with permission from [157]. Copyright 2020 by the American Physical Society.

can lead to a decreased PD inception field strength. Consequently, the motion of droplets can significantly affect the PD inception field strength. While the influence of the wetting properties and the droplet volume was already investigated for (assumedly) uncharged droplets [186, 207], the effect of the droplet motion, the different oscillation modes and the electric charge was not investigated in detail. Depending on the resonance mode, the shape of the droplet is significantly changed during one cycle. Furthermore, this provokes severe changes of the static contact angle, and thus might affect the generation of partial discharges.

Electric charges influence the oscillation frequency of the droplet, which influence the occurrence of critical (low) contact angles. The more frequently these critical contact angles appear, the higher the number of generated partial discharges. Consequently, the PD inception field strength and the impact of electric charges have to be determined for the different resonance modes. The PD inception field strength  $\hat{E}_{in}$  depends on the droplet volume  $V_d$  for uncharged water droplets oscillating in the first three resonance modes as shown in Fig. 6.6. The symbols represent the

## 6 Partial discharges generated by sessile droplets

mean value, and the error bars quantify the standard deviation of the mean value. Each value is based on a minimum of four measurements. Generally, an increasing droplet volume decreases the PD inception field strength as already observed for single gelatin droplets and as reported in literature. Qualitatively the decrease of the PD inception field strength is independent of the resonance mode. However, the volume dependent decrease of the PD inception field strength depends on the resonance mode. The higher the resonance mode, the lower is the impact of the volume on the inception field strength.

Each resonance mode is characterized by a different oscillation pattern as shown in Fig. 2.10. The first resonance mode induces large changes of the contact angle. Hence, very high and low contact angles are possible. Furthermore, the frequency of an uncharged droplet oscillating in first resonance mode is lower compared to higher resonance modes because the droplet always behaves like a charged droplet and oscillates with the same frequency as the applied voltage. In contrast, the change of the contact angle is lower for higher resonance modes because of the changed motion. However, low contact angles can also be observed in case of the second resonance mode.

The oscillation frequency of an uncharged droplet is higher compared to the first resonance mode because an uncharged droplet always oscillates with twice the frequency of the applied voltage. Thus, small contact angles are more frequently observed for the second than for the first resonance mode. This might be a reason for the decrease of the PD inception field strength. Consequently, the inception field strength of PDs is influenced by the resonance mode. Higher resonance modes are more prone to generate PDs compared to lower modes. The larger the droplet volume, the lower is the difference of the PD inception field strength between the different modes. Comparing these results to already existing measurements reveals that the inception field strength is in the same order of magnitude [149, 186, 188, 207]. The small differences might originate from unwanted charges or different wetting properties of the used substrates.

Especially, electric charges influence the behaviour of sessile water droplets under the impact of electric fields. The behaviour is determined by the droplet volume, the electric charge and the electric field strength. To investigate whether electric charges influence the PD inception field strength, various droplets with well-defined volume and electric charge are investigated. The influence of the electric charge can only be deter-

## 6.4 PD inception field strength for charged and uncharged water droplets

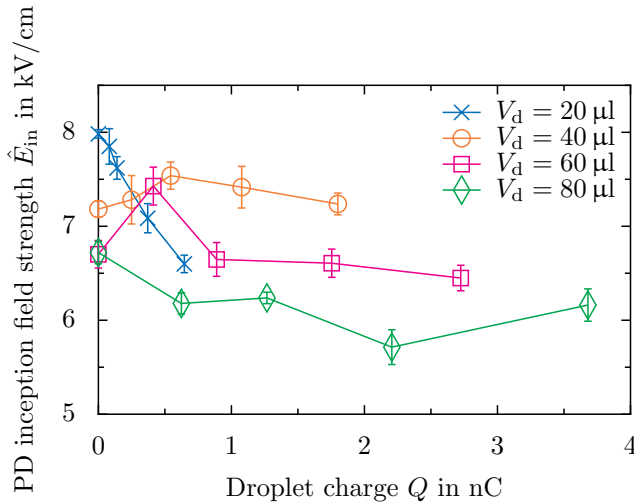


Figure 6.7: PD inception field strength  $\hat{E}_{in}$  of single water droplets depending on the volume  $V_d$  and electric charge  $Q$  for the first resonance mode. The error bars show the standard deviation of the mean value. Reprinted figure (adapted) with permission from [157]. Copyright 2020 by the American Physical Society.

mined if all other boundary conditions are kept constant including the resonance mode and the oscillation frequency of the droplet. Due to the fact that the behaviour of the droplet is mainly influenced by the electric field strength and the charge, the boundary conditions have to be chosen accordingly. During the experiments the electric charge on the droplet is constant, but the electric field strength is increased until the PD inception field strength is reached. For low electric field strengths and large amount of charges the droplet oscillates with the same frequency as the applied voltage. However, increasing the electric field strength causes a changed behaviour so that the droplet oscillates with twice the frequency of the applied voltage. Such changes can significantly impact the outcome of the experiments.

In Sec. 5.2 the first resonance mode was identified to have a constant oscillation frequency for a fixed droplet volume independent of the net charge and the electric field strength. Hence, the first resonance mode is used to determine the influence of electric charges on the inception field

## 6 Partial discharges generated by sessile droplets

strength of PDs. The PD inception field strength for charged and uncharged droplets oscillating in first resonance mode for different droplet volumes is shown in Fig. 6.7. All experiments are performed on silicone rubber substrates. Each measurement was repeated at least four times. Increasing the net charge of the droplet decreases the inception field strength for PDs independent of the droplet volume. Especially, for a droplet volume of  $V_d = 20 \mu\text{l}$  the decrease of the PD inception field strength with increasing electric charge is clearly observable. Nevertheless, the trend is not so clear for larger droplet volumes. In case of a droplet volume of  $V_d = 40 \mu\text{l}$  or  $V_d = 60 \mu\text{l}$  the increase of the electric charge initially induces an increase of the PD inception field strength. Consequently, smaller droplets are much more affected by the presence of charges not only with respect to the droplet motion but also with respect to the generation of partial discharges. The net charge on the droplet affects the electric field around the droplet. For smaller droplets this effect is larger with respect to the volume compared to larger droplets. Note that the maximum electric charge on the droplets depends on the droplet volume. Accordingly, small droplets cannot contain the same amount of electric charge as large droplets without disintegrating.

The comparison of the PD inception field strengths for different modes reveals whether the change of the oscillation frequency has an impact on the inception field strength of PDs. In contrast to the first resonance mode, droplet oscillating in second resonance mode oscillates with different frequencies depending on the electric field strength and the charge of the droplet. While the charge is fixed for each experiment, the electric field strength is continuously increased to determine the PD inception field strength. Due to the fact that the oscillation behaviour is determined by both, the electric charge and the electric field strength, the droplet frequency is not constant for different volumes. Hence, droplets oscillating with different frequencies are compared with each other, which distort the outcome of the experiments. Droplets oscillating with a different frequency might cause a different number of PD impulses and additionally affect the strength of each discharge. To compare droplets oscillating at different frequencies the electric field strength and the charge has to be kept constant. Unfortunately, this is not possible in this case because applying electric charge to the droplet always leads to a reduction of the PD inception field strength, and thus changes the boundary conditions. Accordingly, it is not possible to directly compare the different oscillation frequencies. But even though it is not possible to hold the oscillation fre-

## 6.4 PD inception field strength for charged and uncharged water droplets

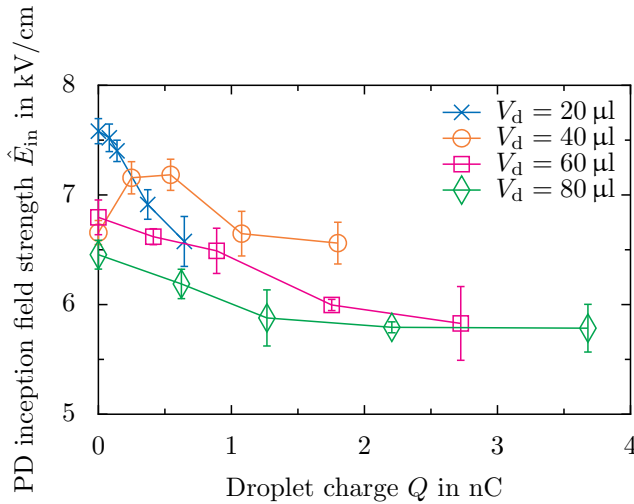


Figure 6.8: PD inception field strength  $\hat{E}_{in}$  of single water droplets depending on the volume  $V_d$  and electric charge  $Q$  for second resonance mode. The error bars show the standard deviation of the mean value. Reprinted figure (adapted) with permission from [157]. Copyright 2020 by the American Physical Society.

quency constant for all experiments, the overall behaviour for the second resonance mode can be investigated.

The PD inception field strength for charged and uncharged water droplets oscillating in the second resonance mode is shown in Fig. 6.8. Each experiment was repeated at least four times. Similar to the first resonance mode, increasing the electric charge results in a decreasing PD inception field strength. In addition, the smaller the droplet volume, the higher is the PD inception field strength. Thus, the PD inception field strength depends on the droplet volume and is larger for small droplet volumes. Large droplet volumes are less affected by this effect. Comparing the PD inception field strength of droplets oscillating in the first and second resonance mode reveals that the PD inception field strength is generally lower for the second resonance mode. The behaviour of droplets oscillating in higher resonance modes is assumed to be the same as for the second resonance mode, because the principle direction of motion is the same and the amplitude of the oscillation is reduced. Furthermore, the volume de-

pendence of the partial discharge inception as shown in Fig. 6.6 was lower for the third resonance mode compared to lower resonance modes. Thus, this impact is assumed to be lower also for charged droplets.

### 6.5 Conclusions

Stationary droplets made out of gelatin was proven to replicate the electrical boundary conditions while not being affected by the electric field with respect to oscillations. Hence, the inception field strength for partial discharges could be determined for non-moving droplets. The PD inception field strength is in the same order of magnitude as for water and depends on the wetting properties of the substrate as well as the droplet volume. The higher the droplet volume, the lower is the inception field strength for PDs. In addition, a better wettability of the substrate also reduces the inception field strength.

Neighbouring droplets can interact with each other depending on the droplet volume and the droplet-droplet separation. For large separations no interaction of the droplets could be observed. The PD inception field strength is the same as for single droplets. Decreasing the droplet-droplet separation and reaching a characteristic separation, the droplets interact with each other, and the PD inception field strength is decreased. The lower the separation between the droplets, the lower is the PD inception field strength. The typical separation for an interaction of the droplets depends on the volume. Larger droplets affect each other over a larger distance. Consequently, the presence of multiple droplets on a substrate significantly change the overall partial discharge behaviour.

The presence of net charges strongly influences the motion of droplets under the impact of an electric field and might also have an impact on the generation of partial discharges. To investigate the influence of the resonance modes and the influence of net charges, the PD inception field strength is analysed for different configurations. The PD inception field strength depends on the resonance mode and the droplet volume. Increasing the volume leads to a decreasing inception field strength. Furthermore, for small droplets the PD inception field strength is the highest for the first resonance mode and decreases with higher resonance modes. In addition to the resonance mode, the partial discharge inception clearly depends

Table 6.4: Summary of principal influence of different parameters on PD inception field strength  $\hat{E}_{\text{in}}$ .

Parameter	$\hat{E}_{\text{in}}$
Volume $V \uparrow$	$\downarrow$
Volume $V \downarrow$	$\uparrow$
Charge $Q \uparrow$	$\downarrow$
Charge $Q \downarrow$	$\uparrow$
Static contact angle $\theta \uparrow$	$\uparrow$
Static contact angle $\theta \downarrow$	$\downarrow$
Mode number $\mathcal{N} \uparrow$	$\downarrow$
Mode number $\mathcal{N} \downarrow$	$\uparrow$
Droplet-droplet separation $h_{\text{d-d}} \uparrow$	$\uparrow$
Droplet-droplet separation $h_{\text{d-d}} \downarrow$	$\downarrow$

on the net charge of the droplet. Increasing the net charge of a droplet decreases the PD inception field strength especially for small droplets.

Consequently, the generation of partial discharges is very sensitive to different boundary conditions like the droplet volume, droplet charge, oscillation mode or the presence of nearby droplets. The interaction of these influencing factors generates a complex system with multiple interactions. The impact of the individual parameters is summarized in Table 6.4.

Especially, high-voltage insulators containing sessile droplets are affected by these factors. The interaction of neighbouring droplets determines the size of each droplet and the droplet distribution on the weather sheds. Particularly, the droplet size and the droplet distribution can result in a reduction of the PD inception field strength, and thus promote the generation of partial discharges. These experimental results improve the understanding of the partial discharge behaviour of single and multiple droplets and might help to develop reliable ageing models for high-voltage insulators.



# 7 Droplets under the impact of transient electric fields

---

---

The content of this chapter is partly based on the Master thesis of Marvin Dietzmann-Kolbe [51], and has been partially published in the following conference proceeding:

- [153] Löwe, J.-M., Hinrichsen, V., and Tropea, C. Droplet Behavior Under the Impact of Lightning and Switching Impulse Voltage. In *2018 IEEE Electrical Insulation Conference (EIC)*, pages 443–447. IEEE, 2018. ISBN 978-1-5386-4178-1. doi:10.1109/EIC.2018.8480884

---

---

## 7.1 General

The behaviour of single and multiple droplets under quasi-static electric fields was described in the previous chapters. In this chapter the impact of transient electric fields on the behaviour of single and multiple droplets is investigated. While the impact of switching on and off of a constant electric field or instantly changing the electric field strength was already investigated [14, 107, 252], the effect of transient electric fields generated by standard lightning and standard switching impulse voltage on sessile droplets has not yet been investigated in detail. Hence, the behaviour of droplets under the impact of transient electric fields is not completely understood, because the influence of impulse length and frequency as well as the corresponding electric field strength is still unknown. The transient electric fields used in the present experiments are characterized by a short duration, commonly in the order of several micro- or milliseconds, with a steep increase of the electric field strength followed by a slower decrease. For the present investigation standard lightning and switching impulse voltages are used to generate the transient electric field. Both impulse voltages are double exponential impulses and are defined by the IEC 60060-1 standard, which specifies the time to peak and half value.

## 7 Droplets under the impact of transient electric fields

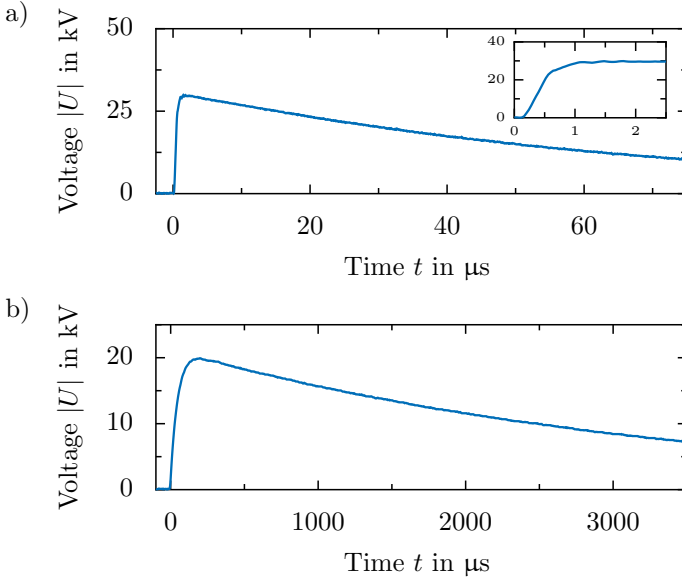


Figure 7.1: Exemplary measured temporal evolution of the voltage  $U$  generated by the impulse generator. a) Standard lightning impulse voltage (1.2/50  $\mu\text{s}$ ), the insert shows the course to peak more detailed and b) standard switching impulse voltage (250/2500  $\mu\text{s}$ ).

A standard lightning impulse (LI) is defined as 1.2/50 impulse, where the first number indirectly defines the time to peak ( $t = 1.2 \mu\text{s}$ ) and the second number defines the time to half value ( $t = 50 \mu\text{s}$ ). Accordingly, the standard switching impulse (SI) is defined as 250/2500 impulse (time to peak  $t = 250 \text{ ms}$ , time to half value  $t = 2500 \text{ ms}$ ). An example of both impulse voltages obtained from measurements is shown in Fig. 7.1. Hereinafter, standard lightning impulse voltage and standard switching impulse voltage are referred to as LI and SI voltage for simplification purposes. These impulse voltages are commonly used to test high-voltage equipment and to reproduce overvoltages generated by lightning strikes or switching operations [133]. While it was already shown that time variant electric fields are able to actively manipulate the behaviour of single

droplets [211], transient electric fields are also capable to cause coalescence of droplets [162, 174, 284]. To increase the understanding of the underlying physical mechanisms, the behaviour of single sessile droplets under the impact of transient electric fields is investigated. Subsequently, the behaviour of two neighbouring droplets is investigated to determine under which conditions transient electric fields induce electro-coalescence.

## 7.2 Single droplet behaviour

Single sessile droplets are not only affected by a quasi-static electric field but also by transient electric fields. The overall behaviour of the droplet mainly depends on two influencing factors, namely the impulse type, including the duration and the steepness, and the electric field strength. Generally, the higher the electric field strength, the higher is the force acting on the droplet, which promotes a deformation or oscillation of the droplet. In addition, the shorter the duration of the impulse, the lower is the impact on the droplet, because the electric force acts only for a short time on the droplet and cannot significantly accelerate the fluid. A characteristic time series for a sessile droplet under the impact of a SI voltage is shown in Fig. 7.2. The equilibrium shape of a droplet with a volume of  $V_d = 90 \mu\text{l}$  is shown in Fig. 7.2a. The applied electric field with an electric field strength of  $\hat{E} = 18.4 \text{ kV/cm}$  causes a force acting on the droplet. The force is mainly concentrated at the three-phase contact line and initiates a movement of the three-phase contact line as shown in Fig. 7.2b. In case of an electric field tangentially aligned to the substrate

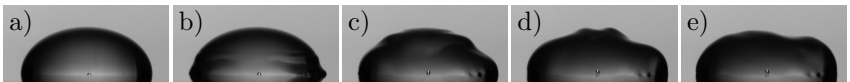


Figure 7.2: Time series for a single droplet with a volume of  $V_d = 90 \mu\text{l}$  under the impact of a SI voltage ( $\hat{E} = 18.4 \text{ kV/cm}$ ). a) undisturbed droplet ( $t = 0 \text{ s}$ ), b) droplet with moving contact line ( $t = 1.11 \text{ ms}$ ), c) surface waves propagating on the interface of the droplet ( $t = 4.44 \text{ ms}$ ), d) interaction of the surface waves at the top of the droplet ( $t = 7.77 \text{ ms}$ ) and e) oscillating droplet ( $t = 11.11 \text{ ms}$ ).

## 7 Droplets under the impact of transient electric fields

as given in the present study, the force of the electric field is not homogeneously distributed along the three-phase contact line but only acts at regions orientated in the same direction as the electric field lines. Hence, the resulting force stretches the droplet and results in an increase of the wetted area on the substrate while the bulk of the droplet is still at rest. The contact line movement is the reason for disturbances resulting in surface (capillary) waves travelling from both sides of the droplet towards the top of the droplet, as shown in Fig. 7.2c. As soon as the surface waves reach the top of the droplet, they interact and trigger macroscopic droplet oscillations, see Figs. 7.2d and e. The resulting oscillation is continuously damped by the viscosity of the liquid until the droplet comes to rest, which can take up to the order of seconds. Note that the shape of the droplet at  $t = 250 \mu\text{s}$  and  $t = 2500 \mu\text{s}$  is characterized by the oscillation, similar to Figs. 7.2e.

The impact of the electric field on the movement seems negligible after initiating the surface waves. Depending on the wetting properties of the substrate the three-phase contact line can move to its initial position or stay at the new position after the electric field has decayed, resulting in a permanently increased wetted area. In addition, the increase of the wetted area can change the static contact angle of the droplet due to a different equilibrium shape of the droplet and the contact angle hysteresis.

While the SI voltage causes large macroscopic oscillations and an increase of the wetted area, the impact of LI voltage is lower for the same electric field strength. A time series of a water droplet with the same volume as shown in Fig. 7.2 is presented in Fig. 7.3. The maximum electric field strength of the impulse is kept constant and amounts  $\hat{E} = 18.4 \text{ kV/cm}$ . The undisturbed droplet at rest is shown in Fig. 7.3a. Applying an electric field also causes a force on the droplet and results in a similar behaviour of the droplet as already described. However, the impact of the LI voltage is much smaller compared to SI voltages. The initial movement of the three-phase contact line is also present but hardly to observe.

To visualize the small movement of the contact line and the generated surface waves, the difference between the actual image and the initial state shown in Fig. 7.3a is presented in Figs. 7.3b-e. Thereby, the region close to the left three-phase contact line is magnified and the difference between the images is brightly coloured for better visibility. Even if the change of shape is difficult to observe in the time series, the movement of the three-phase contact line and the resulting surface waves can be clearly

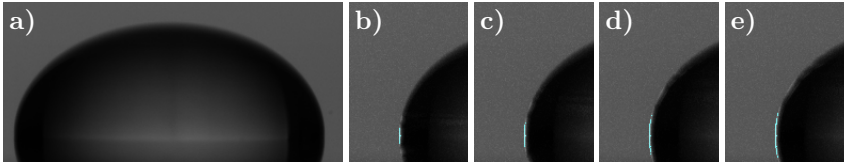


Figure 7.3: Time series for a single droplet with a volume of  $V_d = 90 \mu\text{l}$  under the impact of a LI voltage ( $\hat{E} = 18.4 \text{ kV/cm}$ ). a) undisturbed droplet ( $t = 0 \text{ s}$ ), b) detailed view of initial deformation of the contact line on the left side of the droplet ( $t = 0.44 \text{ ms}$ ), c)-e) detailed view of the expanding surface wave on the interface of the droplet ( $t = 0.88 \text{ ms}$ ,  $t = 1.33 \text{ ms}$  and  $t = 1.78 \text{ ms}$ , respectively). The bright colour in image b)-e) indicates the change to image a).

identified using the high-speed video. The general behaviour of a droplet under the impact of a LI voltage is the same as for a SI voltage, but with a smaller contact line motion and smaller amplitudes of the generated surface waves. Consequently, the size of the droplet is hardly increased and no significant macroscopic oscillations are visible.

Besides the impulse type, the electric field strength significantly influences the behaviour of the droplets. Increasing the electric field strength induces a larger force acting on the droplet, which causes a larger movement of the three-phase contact line and larger disturbances. Nevertheless, the impact of SI voltages is larger than for LI voltages at the same electric field strength. Even if the maximum electric field strength is kept constant for both impulse types, the duration of electric field application is significantly longer for SI voltages. Due to the different time constants of LI and SI voltages, not only the duration varies but also the average electric field strength which is applied to the droplet. Hence, the maximum electric field strength is applied for a much longer time. Especially, the duration and the characteristic time scales significantly influence the physical behaviour. For low frequencies, as present for alternating electric fields, the droplet can be assumed to be a perfect conductor, so that the behaviour is mainly affected by the electrical conductivity of water. In case of transient electric fields the frequencies of the applied electric field are much higher compared to the investigated alternating electric fields.

## 7 Droplets under the impact of transient electric fields

Table 7.2: Approximated order of magnitude for the characteristic time scales for water (charge relaxation time) and the different impulse voltages. The values are calculated taking into account IEC 60060 and the approximation given by [133].

Description	Characteristic timescale
Charge relaxation time constant	$\tau_{\text{el}} = \frac{\varepsilon_r \varepsilon_0}{\kappa_{\text{el}}} \approx 10^{-4} \text{ s}$
Time to peak (LI)	$\tau_{1,\text{LI}} \approx 10^{-7} \text{ s}$
Time to half value (LI)	$\tau_{2,\text{LI}} \approx 10^{-5} \text{ s}$
Time to peak (SI)	$\tau_{1,\text{SI}} \approx 10^{-4} \text{ s}$
Time to half value (SI)	$\tau_{2,\text{SI}} \approx 10^{-3} \text{ s}$

To investigate whether the droplet behaves as a perfect conductor or a leaky dielectric under the impact of transient electric fields, the characteristic time scales of the impulse voltage and the charge relaxation time constant of water have to be compared.

Both impulse voltages are defined by two characteristic times, one for the time to peak and one for the time to half value. The approximated characteristic time scales for standard lightning and switching impulse voltages for the given experimental setup are summarized in Table 7.2. Comparing the different time scales reveals that the characteristic times of LI voltages are generally smaller than the charge relaxation time constant of water. The assumption of a perfectly conducting droplet is only valid for  $\tau_{\text{el}} \ll \tau_E$ , where  $\tau_E$  is the characteristic time of the applied electric field. In this context  $\gg$  and  $\ll$  represents at least a factor of ten, so that one time constant is significant larger/lower than the other. For LI voltages both time scales are significantly smaller than the charge relaxation time of water ( $\tau_{\text{el}} \gg \tau_{1,\text{LI}}$  and  $\tau_{\text{el}} \gg \tau_{2,\text{LI}}$ ) so that the behaviour of the droplet is characterized by the relative permittivity and an electrostatic field. In case of SI voltages the characteristic time scales are higher compared to LI voltages. The characteristic time for the time to peak is in the same order of magnitude than the charge relaxation time of water ( $\tau_{\text{el}} \approx \tau_{1,\text{SI}}$ ). Hence, the behaviour of the droplet during the time to peak is characterized by a combination of an electrostatic and electric flow field.

During the time to half value the behaviour of the droplet is characterized as perfect conductor (electric flow field), because  $\tau_{el} \ll \tau_{1,SI}$ . Consequently, the electric field inside the droplet and the electric field stress tangentially to the interface of the droplet vanish during this time. Therefore, the force generated by the electric field only has a component perpendicular to the interface of the droplet. During a SI voltage a transition from an electric flow field to an electrostatic field is observed. This transition leads to a superposition of both physical mechanisms, so that the behaviour of the droplet is defined by the relative permittivity and the electrical conductivity. In this case the force generated by the electric field has a component parallel and perpendicular to the interface of the droplet. Thus, the impulse type does not only change the macroscopic behaviour of the droplet but also the physical interaction of the droplet and the electric field.

Even though the SI voltage is associated with a transition of the physical mechanism with respect to the description of the electric field, the observed behaviour is almost the same for both impulse types, which suggests the assumption that the overall behaviour is characterized by a dielectric behaviour. The much larger timescale of the SI voltage results in a higher impact on the behaviour and causes larger amplitudes, because a higher electric field strength is applied for a longer time. Accordingly, the forces resulting from the electric field are applied for a longer time.

Principally, sessile droplets are affected by transient electric fields, which initiate oscillations and movement of the droplets. The movement of the three-phase contact line does not only change the wetted area of the droplet but might also cause an interaction with nearby droplets. In case of a high-voltage insulator the occurring LI and SI voltages can influence the surface distribution of sessile droplets and might increase the wetted area on the silicone rubber surface. Especially, the change of the contact angle and the size of the droplet can be critical for the generation of partial discharges, as already presented in the previous chapter.

## 7.3 Coalescence of neighbouring droplets

Single sessile droplets are significantly affected by transient electric fields. The resulting droplet oscillation and movement provoke an interaction of neighbouring droplets and might finally result in coalescence of the

## 7 Droplets under the impact of transient electric fields

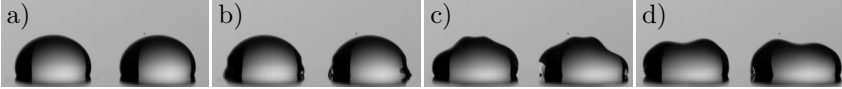


Figure 7.4: Time series of two neighbouring droplets with a volume of  $V_d = 40 \mu\text{l}$  and a separation of  $h_{d-d} = 2 \text{ mm}$  under the impact of a SI voltage. a) Undisturbed droplets ( $t = 0 \text{ ms}$ ), b) moving three-phase contact line and propagating surface waves ( $t = 1.45 \text{ ms}$ ) and c)-d) oscillating droplets with pinned three-phase contact lines ( $t = 5.5 \text{ ms}$  and  $t = 9.5 \text{ ms}$ , respectively).

droplets. Thereby, the wetted area on the substrate is changed as well as the resulting droplet volume. Both influencing parameters are crucial for the generation of partial discharges. Hence, the coalescence of neighbouring droplets and the corresponding influencing factors is investigated in detail. The behaviour of neighbouring droplets under the impact of a transient electric field can be characterized by the resulting motion of the droplets. Three principal behaviours were observed during the experiments. For low electric field strengths the disturbances initiated at the three-phase contact line of the droplets are hardly recognizable, and therefore no macroscopic motion is observable. Apparently, the droplets are not affected by the electric field. This is the case for very low electric field strengths and for all LI voltages independent of the electric field strength. If the electric field strength is increased, the individual droplets are affected by the electric field and the same behaviour as for single droplets is observable. Both droplets are affected by the electric field, which increases the wetting area of both droplets so that the droplet-droplet separation is reduced. Subsequently, the disturbances initiated at the three-phase contact line produce droplet oscillations. In case of a large droplet-droplet separation, the distance between the droplets is not covered by the three-phase contact line motion or the oscillations of the droplets so that no coalescence is observable.

A time series of two neighbouring droplets behaving like single droplets is shown in Fig. 7.4. The increase of the wetting area permanently reduces the separation between the droplets. However, the movement of the three-phase contact line is generally not large enough to cause coalescence and only results in small reduction of the droplet-droplet separation, as shown

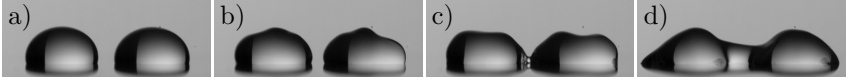


Figure 7.5: Time series of droplet coalescence under the impact of a SI voltage. The initial separation between the droplets with a volume of  $V_d = 40 \mu\text{l}$  is  $h_{d-d} = 1 \text{ mm}$ . a) Undisturbed droplets ( $t = 0 \text{ ms}$ ), b) propagation surface waves on both droplets resulting in a decreasing droplet-droplet separation ( $t = 8.06 \text{ ms}$ ), c) formation of a liquid bridge (caused by droplet oscillations) between the droplets ( $t = 10.0 \text{ ms}$ ) and d) complete coalescence of both droplets ( $t = 16.5 \text{ ms}$ ). Reprinted (adapted) with permission from [153], © 2018 IEEE.

in Fig. 7.4b. In contrast, the amplitude of the droplet oscillations are much larger and might cover the droplet-droplet separation. Both droplets perform almost identical motions. The motion is symmetric with respect to the centre plane between the droplets perpendicular to the substrate. Consequently, the shaped nodes on the droplet surface partially cover the droplet-droplet separation at the same time resulting in a significantly reduced separation between the droplets. However, for large droplet-droplet separations no coalescence is observed, as shown in Figs. 7.4c and d. Nevertheless, the resulting shape of the individual droplets is significantly influenced in terms of wetted area and contact angle. The behaviour of the individual droplets is comparable to the single droplet motion, and no interaction between the droplets is visible.

Further decreasing the separation between the droplets or increasing the electric field strength induces coalescence of the droplets. A time series of droplet coalescence is shown in Fig. 7.5. For comparison reasons the same droplet volume was used in Fig. 7.4 and Fig. 7.5, however, the droplet-droplet separation was reduced from  $h_{d-d} = 2 \text{ mm}$  to  $h_{d-d} = 1 \text{ mm}$  to cause droplet coalescence. The general behaviour of the droplets is the same as already discussed. The applied electric field causes a motion of the three-phase contact line and an increase of the wetted area, as shown in Fig. 7.5b. The droplet-droplet separation is decreased, but the motion of the contact line cannot initiate coalescence because the motion only covers a small distance of the complete droplet-droplet separation.

## 7 Droplets under the impact of transient electric fields

Only for very small droplet-droplet separations the contact line motion results in coalescence of the droplets. However, the initiated droplet oscillation forces the droplets to turn towards each other, resulting in the formation of a liquid bridge between the droplets, as shown in Fig. 7.5c. Generally, the liquid bridge is not formed directly at the substrate but at the closest distance between the droplets, which mainly depends on the wetting properties. For hydrophilic substrates the closest distance between the droplets is the distance between the three-phase contact lines directly at the substrate. In contrast, for a hydrophobic substrate the smallest distance between the droplets is given at approximately half of the droplet height. This first connection between the droplets initiates the full coalescence of the droplets, which covers the complete droplet-droplet separation and finally results in the formation of a single droplet as shown in Fig. 7.5d. The merging of the droplets provokes large oscillations of the final droplet, which result in a further motion of the three-phase contact line. As a consequence, the shape of the final droplet is significantly changed with respect to the contact angles and the wetted area, as seen by comparing Figs. 7.5a and d.

The presented behaviour of the droplets is influenced by different parameters like the droplet-droplet separation, the electric field strength, the droplet volume and the impulse type. To categorize the behaviour of the droplets three different regimes are used, namely no movement, vibration or movement of the individual droplets without and with coalescence of the droplets.

The large number of influencing parameters requires numerous experiments to determine the influence of each parameter. To mathematically characterize the behaviour, dimensionless quantities are more convenient. Hence, the electrical Bond number is used to characterize the behaviour of the droplets, which is defined as

$$\text{Bo}_{\text{el}} = \frac{\varepsilon_0 U^2}{\gamma h_{\text{d-d}}} \hat{=} \frac{\text{Force of electric field}}{\text{Force of surface tension}}, \quad (7.1)$$

where  $h_{\text{d-d}}$  is the shortest droplet-droplet separation. Note that the voltage  $U$  is directly proportional to the electric field applied to the droplet and is used for dimensional reasons. The droplet-droplet separation characterizes the deformation of the droplet necessary to cause coalescence. The deformation is caused by the electric field and the resulting force. In addition, the surface tension counteracts the deformation and tries to minimize the surface area of the droplet. Hence, the electrical Bond number

Table 7.3: Experimental parameters to investigate the coalescence of neighbouring droplets under the impact of LI and SI voltages.

Variable	Quantity
Droplet volume $V_d$ in $\mu\text{l}$	20, 40, 60, 80, 100
Droplet-droplet separation $h_{d-d}$ in mm	1, 2, 3, 4, 5
Applied voltage $U$ in kV	20, 30, 40, 50
Electric field strength <sup>5</sup> $\hat{E}$ in kV/cm	7.4, 11.1, 14.7, 18.4

characterizes the important physical mechanisms to describe the coalescence of neighbouring droplets. To obtain the data shown in the following sections, the droplet volume  $V_d$ , the applied voltage  $U$  and the droplet-droplet separation  $h_{d-d}$  are varied. The ranges of these parameters are shown in Table 7.3.

### 7.3.1 Standard lightning impulse voltage

The results of the experiments performed with LI voltages are presented in Fig. 7.6. The electrical Bond number  $\text{Bo}_{\text{el}}$  depending on the droplet volume  $V_d$  is shown, where each symbol corresponds to a single experiment. Three different regimes can be identified, which are numbered with Roman numerals. Generally, for low Bond numbers ( $\text{Bo}_{\text{el}} < 45$ ) no interaction of the droplets and the electric field is observed, independent of the droplet volume. Accordingly, the droplets are at rest, and no visible motion or disturbance can be recognized. Thus, the applied electric field of  $\hat{E} = 7.4 \text{ kV/cm}$  does not affect the droplets even for a droplet-droplet separation of  $h_{d-d} = 1 \text{ mm}$ , independent of the droplet volume. The resulting regime is the no interaction regime and is labelled as 'III'. For small droplet volumes ( $V_d < 40 \mu\text{l}$ ) no interaction between the droplets and the electric field can be observed up to a Bond number of  $\text{Bo}_{\text{el}} \approx 200$ . Hence, larger droplets are already affected by lower electric field strengths, while small droplets are not affected by the same electric field strength.

<sup>5</sup>Electric field strength corresponding to the applied voltage.

## 7 Droplets under the impact of transient electric fields

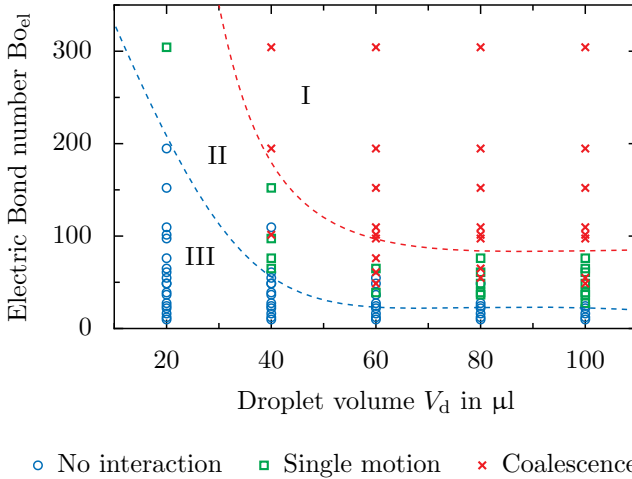


Figure 7.6: Regime map characterizing the behaviour of neighbouring droplets using the electrical Bond number  $Bo_{el}$  and the droplet volume  $V_d$  under the impact of LI voltages. The dashed lines indicate the transition between the different regimes. Reprinted (adapted) with permission from [153], © 2018 IEEE.

A reason for this behaviour is the increased influence of surface tension for small droplets compared to larger ones.

Increasing the electrical Bond number by reducing the droplet-droplet separation or increasing the electric field strength leads to the transition to the single motion regime, which is indicated by the green squares. Note that the transition between the regimes is continuous. The dashed borders are defined by the experimental data and are shown for better visibility of the different regimes. In this intermediate regime the individual droplets are affected by the applied electric field. Each droplet is excited by the electric field and starts to oscillate. However, the droplets do not interact with each other and behave like single droplets. For a droplet volume of  $V_d = 20 \mu l$  no interaction between the droplets is observable even for the shortest droplet-droplet separation and the highest electric field strength. Consequently, droplets with a volume  $V_d \leq 20 \mu l$  are almost not affected by LI voltages. In contrast, higher droplet volumes are clearly affected for electrical Bond numbers  $Bo_{el} > 45$ .

The intermediate regime (labelled with 'II') is characterized by the appearance of different behaviours including no interaction and coalescence. Increasing the Bond number further causes coalescence of the droplets (regime labelled with 'I'). In this regime the applied electric field forces the droplets to merge, which finally results in a single droplet. While the onset of this regime increases for droplet volumes  $V_d \leq 60 \mu\text{l}$ , the onset at higher droplet volumes is almost constant ( $\text{Bo}_{\text{el}} \approx 100$ ). Larger droplets are affected by smaller electric field strengths and interact for even larger separations. The increased volume and the decreased influence of the surface tension induces larger oscillations of the droplet, which cover a larger droplet-droplet separation. The larger the droplets, the more likely is an interaction with neighbouring droplets. For large Bond numbers  $\text{Bo}_{\text{el}} > 100$  and large droplets  $V_d \geq 60 \mu\text{l}$  only coalescence of the droplets was observed. Hence, small droplet-droplet separations and large electric field strengths always evokes droplet coalescence. However, increasing the separation between the droplets significantly influences the interaction of the droplets and can avoid the droplet-droplet interaction and coalescence.

#### 7.3.2 Standard switching impulse voltage

To determine the influence of the different types of impulse voltages additional experiments with SI voltages are performed similar to the experiments with LI voltages. The experimental results are shown in Fig. 7.7. The electrical Bond number depending on the droplet volume is presented for the same parameters as for LI voltages (see Table 7.3). In contrast to LI voltages, SI voltages also affect droplets with small volumes. For  $\text{Bo}_{\text{el}} < 55$  no interaction of the droplets and the electric field is observed. The behaviour for such low electrical Bond numbers is independent of the droplet volume. Furthermore, the critical electrical Bond number for the transition between the 'no interaction' (III) and the 'intermediate' (II) regime is almost the same for large droplets  $55 < \text{Bo}_{\text{el}} < 175$  compared to LI voltages. Increasing the electrical Bond number by increasing the electric field strength or decreasing the droplet-droplet separation provokes an interaction of the droplets and the electric field.

While droplets with a volume of  $V_d = 20 \mu\text{l}$  are not affected by LI voltages, SI voltages cause an interaction of the electric field and the droplets for sufficiently high electrical Bond numbers independent of the droplet volume. Comparing the range of the intermediate regime between LI and

## 7 Droplets under the impact of transient electric fields

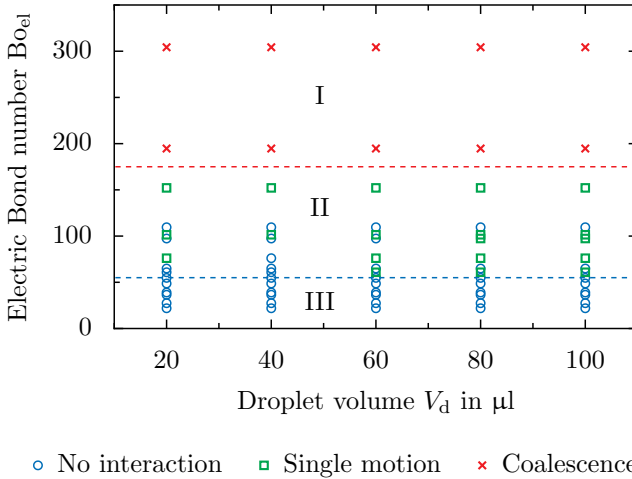


Figure 7.7: Regime map characterizing the behaviour of neighbouring droplets using the electrical Bond number  $B_{o_{el}}$  and the droplet volume  $V_d$  under the impact of SI voltages. The dashed lines indicate the transition between the different regimes. Reprinted (adapted) with permission from [153], © 2018 IEEE.

SI voltages reveals that the intermediate regime is larger in case of SI voltages. Although no coalescence of droplets with a volume of  $V_d = 20 \mu\text{l}$  was observed for LI voltages, Bond numbers  $B_{o_{el}} > 175$  always result in coalescence of the droplets, independent of the droplet volume, in case of SI voltage. However, the onset electrical Bond number for large droplet volumes is lower in case of LI voltage compared to SI voltages. Generally, the same behaviour of the droplets is observable for both impulse types. Increasing the electric field strength or decreasing the droplet-droplet separation increases the impact of the electric field on the behaviour of the droplets. For low separations and high electric fields, neighbouring droplets can always be forced to coalesce, independent of the droplet volume. In contrast to LI voltages, the effect of droplet size is not observable for SI voltages. The onset value of the electrical Bond number is almost constant for the entire range of droplet volumes, so that increasing the droplet volume does not lower the critical electrical Bond numbers for the transition of the different regimes.

## 7.4 Conclusions

Single sessile droplets and multiple neighbouring droplets are affected by transient electric fields. The behaviour of the droplets is influenced by several parameters, namely the droplet-droplet separation, the droplet volume and the applied voltage (the electric field strength and the impulse type, respectively). Both tested impulse types influence the behaviour of single sessile droplets, but the impact on the droplet behaviour is generally higher for SI voltages compared to LI voltages for the same electric field strength. The transient electric field produces a movement of the three-phase contact line, which initiates disturbances and causes surface waves on the droplets interface, finally resulting in a macroscopic droplet oscillation. This macroscopic motion might cause an interaction of neighbouring droplets. Especially, the macroscopic droplet oscillation initiates droplet coalescence similar to the numerical simulations of droplets oscillating in resonance presented in [198].

Generally, increasing the applied voltage and the electric field strength, respectively, causes larger electrical Bond numbers and promotes the interaction of the droplets. Low electrical Bond numbers corresponding to low voltages, do not initiate a droplet movement or oscillation. At such conditions the droplet is not affected by the electric field.

In addition, the droplet-droplet separation has a significant influence on the behaviour of the droplets. Decreasing the droplet-droplet separation also increases the electrical Bond number and reduces the voltage necessary for droplet coalescence. In contrast, increasing the separation between droplets makes the interaction between the droplets less likely.

The droplet volume may have an impact on the interaction of the droplets. While the droplet behaviour under the impact of SI voltages is almost independent of the droplet volume, the droplet behaviour under the impact of LI voltage is significantly influenced by the droplet volume. The smaller the droplet volume, the smaller is the impact of the electric field. Hence, small droplets ( $V_d = 20 \mu\text{l}$ ) are not affected by the transient electric field resulting from LI voltages.

Furthermore, the droplet interaction and behaviour is influenced by the impulse type. Switching impulse voltages also affects droplets with small volumes and have an almost constant onset electrical Bond number for the coalescence regime. In contrast, the onset electrical Bond number

## *7 Droplets under the impact of transient electric fields*

for the coalescence regime is lower in case of high droplet volumes and LI voltages compared to SI voltages.

Therefore, transient electric fields can significantly influence the single droplet behaviour and the interaction of neighbouring droplets.

**Part IV**

**ICE NUCLEATION OF SUPERCOOLED  
DROPLETS**



## 8 Experimental details

---

---

The content of this chapter is partly based on the *Advanced Design Project* of Tim Dorau, Moritz Hülsebrock, Patrick Weis and Julia Wenzel [54], and has been published in the following publication and conference proceedings:

- [151] Löwe, J.-M., Hinrichsen, V., Schremb, M., Dorau, T., and Tropea, C. Experimental Investigation of Electro-freezing of Supercooled Droplets. In *9th World Conference on Experimental Heat Transfer, Fluid Mechanics and Thermodynamics*, Foz do Iguacu, Brasilien, 2017
- [154] Löwe, J.-M., Schremb, M., Hinrichsen, V., and Tropea, C. Ice Nucleation in the Presence of Electric Fields: An Experimental Study. In SAE International, editor, *International Conference on Icing of Aircraft, Engines, and Structures*, SAE Technical Paper Series. SAE International400 Commonwealth Drive, Warrendale, PA, United States, 2019. doi:10.4271/2019-01-2020
- [160] Löwe, J.-M., Schremb, M., Hinrichsen, V., and Tropea, C. Experimental Methodology and Procedure for SAPPHIRE: a Semi-automatic APParatus for High-voltage Ice nucleation REsearch. *Atmospheric Measurement Techniques*, 14(1):223–238, 2021. doi:10.5194/amt-14-223-2021

---

---

### 8.1 Experimental setup

The experimental setup called **SAPPHIRE**: a **S**emi-automatic **APP**aratus for **H**igh-voltage **I**ce nucleation **RE**search is used to investigate the impact of electric fields on ice nucleation. A schematic of the experimental setup, which is capable of investigating ice nucleation of sessile and emulsified droplets, is shown in Fig. 8.1. The ceramic body made out of SHAPAL<sup>TM</sup> Hi-M soft serves as a specimen holder and defines the po-

## 8 Experimental details

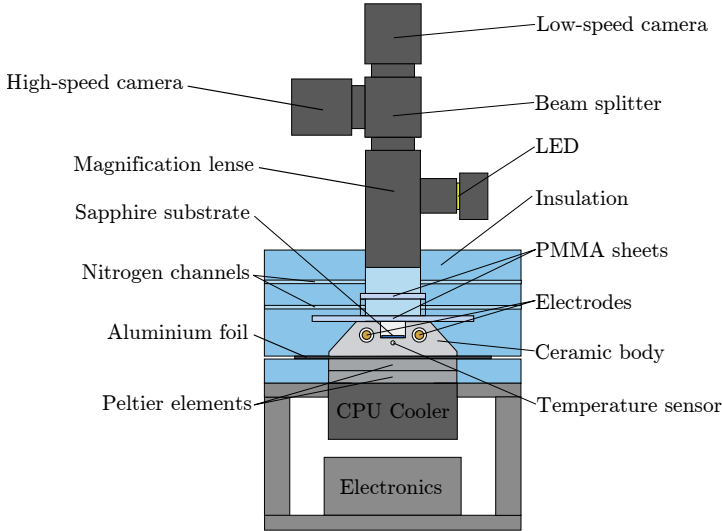


Figure 8.1: Schematic of the experimental setup used for the examination of ice nucleation in a droplet ensemble exposed to an electric field. Reprinted with permission from [160], under the Creative Common License - Attribution 4.0 International (CC BY 4).

sition of the droplets within the electric field. The ceramic has a high heat conductivity of  $\lambda_{\text{cer}} = 92 \text{ W}/(\text{m}\cdot\text{K})$  at  $25^\circ\text{C}$  and approximately  $\lambda_{\text{cer}} = 95 \text{ W}/(\text{m}\cdot\text{K})$  at  $-25^\circ\text{C}$ , which ensures a homogeneous, fast and accurately controlled temperature of the droplets. In addition to the excellent thermal properties, the ceramic material has a low electrical conductivity of  $\kappa_{\text{cer}} = 1 \cdot 10^{-13} \text{ S}/\text{m}$  and a high dielectric strength of  $E_{\text{max,cer}} = 65 \text{ kV}/\text{mm}$ . Thus, the chosen material is the best compromise with respect to a good thermal conductivity and being an electric non-conductive material. A sapphire glass sheet with a high heat conductivity of  $\lambda_{\text{gla}} = 40 \text{ W}/(\text{m}\cdot\text{K})$  at  $25^\circ\text{C}$  and  $\lambda_{\text{gla}} = 80 \text{ W}/(\text{m}\cdot\text{K})$  at  $-40^\circ\text{C}$  is used as sample holder. Similar to the ceramic material, the sapphire has a low electrical conductivity of  $\kappa_{\text{gla}} = 10^{-14} \text{ S}/\text{m}$  at  $25^\circ\text{C}$  and a high dielectric strength of  $E_{\text{max}} = 48 \text{ kV}/\text{mm}$ . Thus, the sample holder has a heat conductivity, which ensures a homogeneous temperature distribution throughout the substrate. The experimental setup is enclosed in Styro-

foam to minimize the heat conduction from the surroundings. PMMA (polymethylmethacrylat) sheets embedded into the Styrofoam enable the optical access during the experiment. A PMMA sheet directly above the ceramic body is used to hold the ceramic in position. Furthermore, the PMMA sheet applies pressure on the ceramic body and the Peltier elements below to ensure a good heat conductivity between the components. During the experiments the complete setup is placed inside a climate chamber (Weiss WK340) operated at a constant temperature of  $\vartheta = 10^\circ\text{C}$  to ensure well-defined conditions with respect to the surrounding temperature and to reach lower temperatures.

### 8.1.1 Temperature control

The high heat conductivity of the ceramic body ensures an accurate and fast control of the droplet temperature. The temperature of the ceramic, i.e. of the droplets, is controlled using two stacked Peltier elements below the ceramic body. A commercially available Peltier controller (Meerstetter TEC-1090-HV) runs the Peltier elements, which are operated in parallel. A feedback control system given by the Peltier controller and the temperature measurement is used to accurately control the temperature. The heat generated by and transferred through the Peltier elements is dissipated by a custom designed, but commercially available CPU water cooling system (Enermax Liqmax II 240/Alphacool Eisblock XPX 1U, Eisstation DDC, NexXoS UT60 Full Copper 240 mm Radiator). Thus, the generated heat is transferred to the surrounding air by forced convection using a radiator. The temperature of the surrounding air is kept constant at  $\vartheta = 10^\circ\text{C}$ . Using the Peltier elements to control the temperature enables an accurate and dynamic control of the droplet temperature. Any kind of temporally variable temperature profile including constant temperatures, transient temperature profiles or fixed cooling rates can be realized with the experimental setup.

To ensure good thermal conductivity throughout the experimental setup, thermally conductive but electrically non-conductive thermal paste (Thermal Grizzly Kryonaut with a heat conductivity of  $\lambda = 12.5\text{ W}/(\text{m}\cdot\text{K})$ ) is used to minimize the heat transmission resistance between the different components, namely, the ceramic, the Peltier elements and the CPU cooler. Thereby, the experimental setup is able to reach a droplet temperature as low as  $\vartheta_d = -40^\circ\text{C}$  at a constant cooling rate of  $\dot{T} = 5\text{ K}/\text{min}$

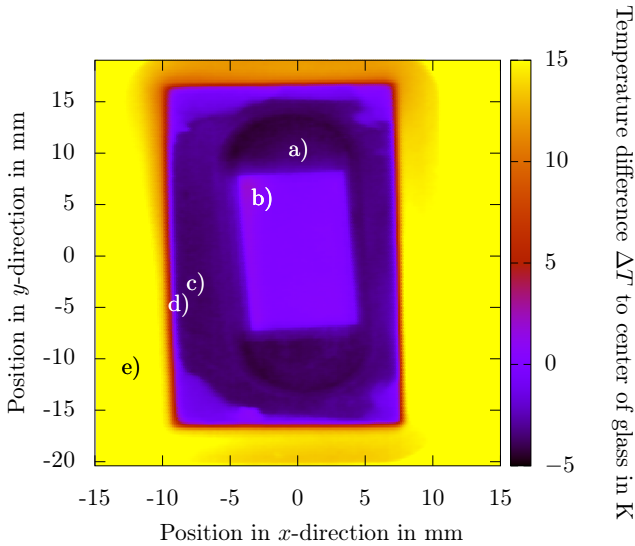


Figure 8.2: Infrared thermography image of the sapphire substrate placed inside the ceramic during the cool-down phase at a cooling rate of  $\dot{T} = 5 \text{ K/min}$ . The data represents the temperature difference at each position with respect to the temperature of the sapphire substrate in the image centre (0,0). Note the homogeneous temperature distribution in all parts, which are a) bottom of the ceramic groove ( $\Delta T \approx -3.8 \text{ K}$ ), b) sapphire substrate ( $\Delta T \approx 0 \text{ K}$ ), c) top surface of the ceramic ( $\Delta T \approx -3.7 \text{ K}$ ), d) sealing between PMMA cover sheet and ceramic body ( $\Delta T \approx 5 \text{ K}$ ), and e) PMMA cover sheet ( $\Delta T \approx 19 \text{ K}$ ). Reprinted (adapted) with permission from [160], under the Creative Common License - Attribution 4.0 International (CC BY 4).

with high accuracy. This temperature range covers the relevant temperatures to observe homogeneous and heterogeneous ice nucleation [70, 140]. The minimum temperature reachable depends on the cooling rate and is higher the lower the cooling rate. The Peltier elements and the ceramic body are separated by a grounded aluminium foil to shield the Peltier

elements from the electric field. Thus, the electronics below the ceramic body are also protected from electromagnetic interference resulting from the electric field.

The temperature distribution on the sapphire glass sheet without droplets and not covered by silicone oil during cooling at a constant rate of  $\dot{T} = 5 \text{ K/min}$  is shown in Fig. 8.2. The local surface temperature of the sapphire glass placed in the groove in the ceramic body is measured by an IR camera (VarioCam hr Head HiRes 640). The emission coefficients of the different materials, namely sapphire glass, ceramic and PMMA are defined for each section in the image and were obtained by a calibration for each material, but still has to be assumed to be an approximation of the true emission coefficients. Hence, the measured temperature distribution is not a quantitative reference but simply shows the homogeneous temperature distribution on the sapphire substrate and the other components like the ceramic. The temperature is presented as a temperature difference between the centre of the sapphire substrate at the origin of the coordinate system and the local temperature. Especially, the temperature distribution on the sapphire substrate, labelled with b) in Fig. 8.2, is very homogeneous. The temperature difference on the sapphire substrate yields  $\Delta T \approx 0 \text{ K}$  according to the temperature sensor being used.

The bottom of the groove inside the ceramic, labelled with a), has a slightly lower temperature than the sapphire ( $\Delta T \approx -3.9 \text{ K}$ ). However, the temperature is still very homogeneous for the entire groove. The sections label with c) and d) correspond to the top of the ceramic and the sealing between the PMMA sheet and the ceramic, respectively. They also exhibit a constant temperature slightly lower than the sapphire. Only the temperature of the PMMA sheet significantly differs from the temperature of the sapphire ( $\Delta T \approx 19 \text{ K}$ ). However, this does not influence the droplet temperature, and thus is not relevant for the experiments.

### 8.1.2 Temperature measurement

The temperature measurement is essential for an accurate control of the droplet temperature, because the measured temperature is used as an input signal for the Peltier controller and is part of the feedback control loop. Nevertheless, the actual temperature of the individual droplets cannot be measured during the experiments because the temperature sensor would affect the temperature field or ice nucleation itself. Furthermore, the tem-

## 8 Experimental details

perature measurement would be affected by the electric field, depending on the sensor type. Therefore, the temperature is continuously measured inside the ceramic. The temperature sensor is embedded into thermal paste and is placed in a hole approximately 1 mm below the bottom of the groove in the ceramic body. An appropriate calibration of the temperature at the droplet position and the temperature inside the ceramic body enables an indirect temperature measurement of the droplet temperature during the experiments with high accuracy. To ensure an interference free temperature measurement, a fibre optical temperature sensor (Fiso FOTL-SD) is used. The electric potential free measurement of the temperature eliminates any interaction between the electric field and the temperature measurement and ensures an accurate measurement. Any other electrical measurement of the temperature like thermocouples or resistor based temperature measurement might not work correctly under the influence of strong electric fields. The temperature accuracy of the sensor is limited and yields  $\delta T = \pm 1 \text{ K}$  in the temperature range from  $\vartheta = -40^\circ \text{C}$  to  $\vartheta = 300^\circ \text{C}$ . In addition, the temperature measurement inside the ceramic body is non-invasive with respect to the electric field distribution at the droplet position. Note that the local electric field strength strongly depends on the involved materials and their position, so that the electric field can be locally suppressed or enhanced based on the properties of the materials.

To determine the difference between the droplet temperature and the temperature inside the ceramic, both temperatures are measured during calibration. A thermocouple (type K) is attached to the sapphire glass sheet using Kapton tape to accurately measure the temperature at the droplet position in absence of any external electric field. The Kapton tape secures the temperature sensor on the sapphire glass and is expected to have only a small influence on the temperature distribution because of the very thin height (0.1 mm) and the good thermal properties. To reproduce the exact conditions during the experiments, the groove is filled with silicone oil as done for the experiments. The temperature difference between the ceramic and the droplet position is measured for different cooling rates to determine the dependence of the temperature difference on the actual temperature inside the ceramic. The temperature inside the ceramic body  $\vartheta_{\text{hole}}$  is controlled by the Peltier controller and is continuously decreased with a constant cooling rate. Simultaneously, the temperature at the droplet position  $\vartheta_{\text{gro}}$  is continuously measured to determine its de-

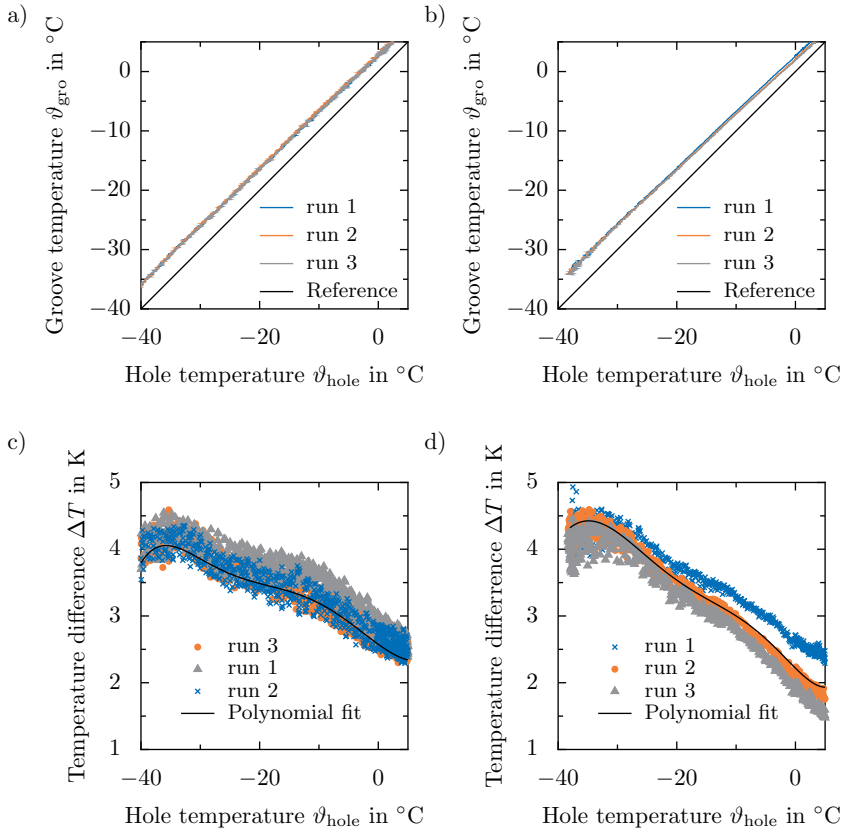


Figure 8.3: Example data obtained during temperature calibration. a) and b) Sapphire substrate temperature  $\vartheta_{gro}$  as a function of the ceramic temperature  $\vartheta_{hole}$  for  $\dot{T} = 3\text{ K/min}$  and  $\dot{T} = 5\text{ K/min}$ . c) and d) Difference  $\Delta T$  between the sapphire substrate temperature  $\vartheta_{gro}$  and the ceramic temperature  $\vartheta_{hole}$  depending on the latter for  $\dot{T} = 3\text{ K/min}$  and  $\dot{T} = 5\text{ K/min}$ . Reprinted (adapted) with permission from [160], under the Creative Common License - Attribution 4.0 International (CC BY 4).

## 8 Experimental details

pendence on the actual temperature and the cooling rate. Two different cooling rates are tested, namely  $\dot{T} = 3 \text{ K/min}$  and  $\dot{T} = 5 \text{ K/min}$ .

Each calibration is repeated at least three times to increase the statistical significance of the data and to ensure a high repeatability. The same test procedure as for the experiments with droplets is used for the calibration to ensure that the calibration is performed under the same boundary conditions. Thus, the temperature of the experimental setup is kept constant for at least 5 min prior to the experiment in order to achieve constant thermal conditions. Typical calibration data for sessile droplets cooled at a constant rate of  $\dot{T} = 3 \text{ K/min}$  and  $\dot{T} = 5 \text{ K/min}$  are shown in Fig. 8.3. The temperature inside the ceramic body  $\vartheta_{\text{hole}}$  depending on the temperature at the droplet position  $\vartheta_{\text{gro}}$  is presented in Figs. 8.3a and b. Comparing the two temperatures reveals that the temperature inside the ceramic is always lower than the droplet temperature, independent of the cooling rate as indicated by the difference of the individual runs and the solid black line. The temperature of the ceramic body should always be lower, because otherwise a cooling of the sapphire would not be possible.

The temperature difference between both temperatures,  $\Delta T = \vartheta_{\text{hole}} - \vartheta_{\text{gro}}$ , for the different cooling rates is shown in Figs. 8.3c and d. The temperature difference  $\Delta T$  increases with decreasing temperature of the ceramic. This is mainly caused by the thermal inertia of the system. Comparing Figs. 8.3c and d reveals that the temperature difference between the droplet temperature and the temperature of the ceramic body only slightly depends on the cooling rate. Increasing the cooling rate slightly increases the temperature difference. The temperature difference mainly depends on the thermal properties of the ceramic, the sapphire glass and the thermal connection between the different components. Thus, the better the thermal connection and the thermal properties, the lower is the difference in temperature. Due to the fact that the increase in temperature difference for the different cooling rates is very small, the thermal connection between the components is considered to be good.

In addition to the measured and calculated temperature difference, a polynomial fit of the data is calculated and shown as solid line, see Fig. 8.3c and d. The polynomial function describes the difference in temperature between the ceramic body and the droplet position, depending on the actual temperature in the ceramic body, and is used to estimate the droplet temperature based on the measurement inside the ceramic body. Even

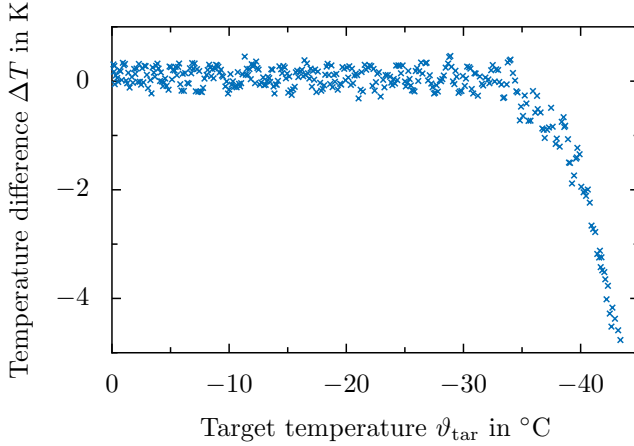


Figure 8.4: Example data obtained during temperature calibration. Test of the temperature calibration with  $\dot{T} = 5 \text{ K/min}$ . Difference  $\Delta T$  between the indirectly measured sapphire substrate temperature  $\vartheta_{\text{hole}}$  and the target temperature  $\vartheta_{\text{tar}}$  prescribed by the Peltier controller in order to follow the temperature ramp, depending on the target temperature itself. Reprinted (adapted) with permission from [160], under the Creative Commons License - Attribution 4.0 International (CC BY 4).

though the data of a single calibration run fluctuates and varies for the different calibration runs with a constant cooling rate, the trend is described with good accuracy by a polynomial of sixth order. Consequently, the droplet temperature is indirectly measured through the temperature inside the ceramic body during the experiments, but actively controlled by the Peltier controller. To verify the accuracy of the calibration, the measured temperature at the droplet position and the corrected temperature of the ceramic body are compared. The resulting temperature difference  $\Delta T$ , depending on the desired target temperature  $\vartheta_{\text{tar}}$  for a constant cooling rate of  $\dot{T} = 5 \text{ K/min}$ , is shown in Fig. 8.4. The target temperature is defined by the temperature ramp prescribed by the Peltier controller and the desired droplet temperature. The temperature difference of the estimated and the measured temperature at the droplet position fluctuates slightly but is almost constant, exhibiting only little deviation, as shown in Fig. 8.4. Hence, the correction of the temperature inside the ceramic

## 8 Experimental details

via the polynomial fit results in an excellent control of the sapphire substrate temperature. Consequently, the droplet temperature is measured accurately and reliably during the experiments, even though it is only measured indirectly.

The maximum temperature difference for target temperatures down to  $\vartheta_{\text{tar}} \approx -34^\circ\text{C}$  is only  $\Delta\vartheta \approx 0.46\text{ K}$ . In contrast, a further decrease of the target temperature leads to a larger deviation of  $\Delta\vartheta \approx 1.94\text{ K}$  for a target temperature of  $\vartheta_{\text{tar}} = -40^\circ\text{C}$ . For such low temperatures the Peltier controller and elements are not able to cool the ceramic body with the prescribed cooling rate, so that the temperature at the droplet position cannot follow the desired cooling rate. Thus, the temperature can be controlled very precisely down to temperatures of  $\vartheta_{\text{d}} \approx -34^\circ\text{C}$ . Taking into account that ice nucleation in sessile droplets is mostly observed at a mean temperature of  $\vartheta_{\text{d}} \approx -25^\circ\text{C}$ , ice nucleation of sessile droplets can be investigated with a high accuracy. The total temperature uncertainty arising from the temperature calibration and the measurement accuracy of the temperature sensor amounts to  $\Delta T = 1.46\text{ K}$  for a target temperature of  $\vartheta_{\text{tar}} = -34^\circ\text{C}$ . Note that for emulsified droplets a similar calibration was performed with an adapted geometry. The corresponding calibration data and further details can be found in App. L.

### 8.1.3 Observation system

Ice nucleation is observed from above using a low-speed (Basler A631fc) or high-speed camera (Photron Fastcam MC2.1-10K) and a high magnification lens with co-axial illumination (Navitar 12x Zoom Lens). The use of an optical beam splitter enables the simultaneous use of both cameras, but with reduced brightness of both images. Hence, generally only one camera is used to record the nucleation events. The selection of the camera mainly depends on the expected timescale of ice nucleation. For very fast processes like ice nucleation under the impact of transient electric fields or to record the different stages of ice nucleation in detail, the high-speed camera is used. In contrast, for slower process like ice nucleation under the impact of constant or alternating electric fields, the low-speed camera is used. Optical access is ensured by PMMA sheets embedded into the Styrofoam housing of the experimental setup. In addition to the optical access, the PMMA sheets thermally insulate the camera and lens from the specimen. The inside of the Styrofoam housing is flooded with gaseous

nitrogen to prevent condensation of water at the PMMA sheets during the cooling process. This would disturb the optical access, and therefore should be avoided. Surrounding the region near the ceramic body with gaseous nitrogen instead of air ensures optical access for all temperatures.

The wide zoom range of the lens, the beam splitter and the different cameras offer a large variability of the experimental setup. Thus, not only ice nucleation inside individual droplets can be observed with high magnification to locate the position of ice nucleation, but also the nucleation behaviour of a complete droplet ensemble. Using both cameras ensures that the different processes during the experiments can be captured very accurately. Hence, slow and fast processes can be investigated with a high temporal resolution. During the experiments different phases of the freezing process are observed on significantly different timescales, for example the cool-down phase (slow), ice nucleation and supercooled freezing (extremely fast), and subsequent thawing (slow).

The measured temperature is correlated to the video data during the experiment. Accordingly, the thermal resolution of the droplet temperature mainly depends on the frames per second rate of the camera and the actual cooling rate. For both, the low-speed and high-speed camera, the minimum resolution for a constant cooling rate of  $\dot{T} = 5 \text{ K/min}$  is determined and amounts  $\approx 15 \cdot 10^{-3} \text{ K/frame}$  at 10 fps and  $\approx 4 \cdot 10^{-5} \text{ K/frame}$  at 2000 fps. Consequently, the developed observation system is capable to capture the relevant processes during ice nucleation under the impact of electric fields.

### 8.1.4 Electric field generation

The electric field is generated by two rod electrodes made out of brass embedded into the ceramic body. The electrodes with a diameter of 4 mm and a length of 39 mm are embedded parallel to each other and in alignment with the sapphire substrate. Before inserting the electrodes using electrically conductive adhesive, the holes inside the ceramic body are covered with conductive silver paint. Thus, the electric potential within the hole inside the ceramic is constant and is defined by the applied electric potential. Hence, the electrode size is well-defined and given by the size of the hole inside the ceramic body. This prevents the generation of partial discharges caused by cavities inside the adhesive. The electrodes are mounted from opposite sides to increase the creeping distance between

## 8 Experimental details

the electrodes and to prevent surface discharges originating from the electrodes. A high-voltage cable is connected to each of the electrodes and the connection between the electrode and the cable is encased in epoxy to prevent electrical discharges between the electrodes and the grounded aluminium foil placed below the ceramic body.

The generated electric field is tangentially aligned to the sapphire substrate, which represents one of the major stresses of a sessile droplet on the surface of a high-voltage insulator. In comparison to an electric field perpendicular to the substrate, a tangentially aligned electric field has a significantly larger impact on the macroscopic behaviour of sessile droplet [233] and has a larger impact on ice nucleation [192]. The electric components below the ceramic body including the Peltier elements and the measurement and control electronics have to be protected from the electric field. Therefore, the electronics are shielded by a grounded aluminium foil placed below the ceramic body. This grounded foil affects the field distribution inside the ceramic body and necessitates the electric field to be generated by two individual high-voltage sources with opposite polarities. Only with two high-voltage sources a well-defined and homogeneous electric field is generated.

The resulting electric field distribution using two high-voltage sources with opposite polarity is illustrated in Fig. 8.5a. The results are obtained from numerical simulations of the field distribution using COMSOL Multiphysics<sup>®</sup>. The resulting electric field distribution is very homogeneous at the surface of the sapphire substrate, i.e. at the position of the droplets. As shown in Fig. 8.5b only the component tangentially aligned to the sapphire substrate is non-zero in the centre of the groove in the ceramic body. The total width of the groove is 9 mm. Only in close distance to the walls of the groove, the electric field strength in  $y$  direction increases. However, the field distribution is almost perfectly tangentially aligned to the substrate surface and very homogeneous at the position of the droplets. Nevertheless, using only a single high-voltage source to generate the electric field and grounding the other electrode leads to a distortion of the electric field. The field distribution for this case is shown in App. J. Due to the fact that one of the electrodes and the aluminium foil have the same electric potential the generated electric field is distorted and is neither tangentially aligned to the sapphire substrate nor homogeneously distributed. Only a symmetrical supply of the electrodes ensures a well-defined and homogeneous electric field at the position of the droplets.

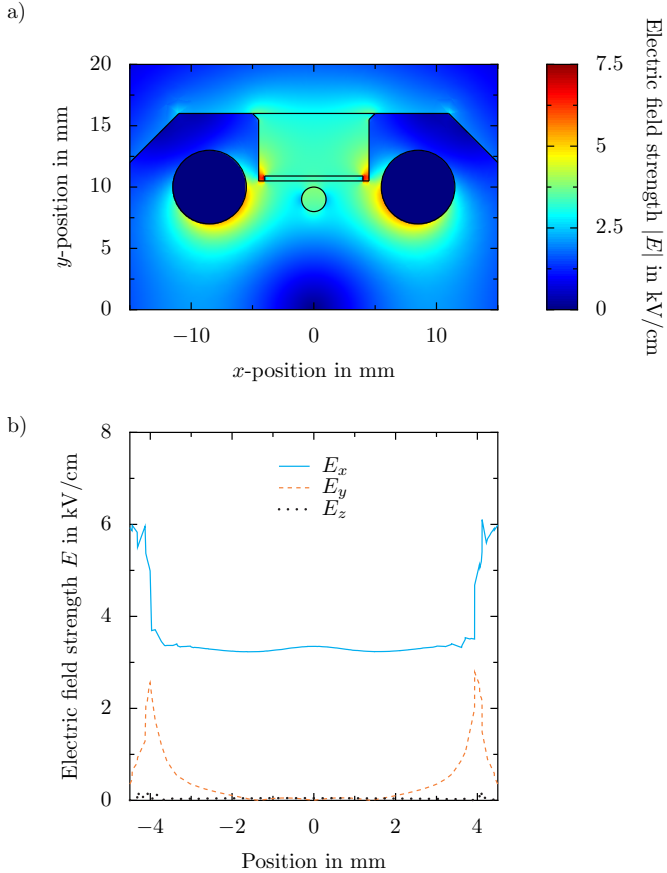


Figure 8.5: Numerical results of the electric field distribution in the  $x - y$  plane of the ceramic without droplets in a), and the different components of the electric field strength  $E_i$  along the  $x$  direction in the centre of the ceramic at the sapphire substrate surface in b). The electric field is calculated for a voltage of  $\hat{U} = \pm 2.0$  kV applied to each electrode. Note that the field distribution is qualitatively the same for other types of electric fields. Reprinted (adapted) with permission from [160], under the Creative Common License - Attribution 4.0 International (CC BY 4).

## 8 Experimental details

Note that the electric field is only tangentially aligned to the sapphire substrate in absence of droplets. Droplets of high purity water have a charge relaxation time which is much smaller than the characteristic timescale of the tested electric fields. Hence, the droplets are assumed to be perfect conductors and the electric field inside the droplets completely vanishes. As a result, the surface of the droplet is an equipotential surface and the electric field lines are always perpendicular to that surface.

The experimental setup is very variable with respect to the generated electric field. Different types of electric fields, namely constant, alternating and transient electric fields, are generated to investigate the impact of electric fields on ice nucleation. The generation of each type is performed with different high-voltage sources.

### 8.1.4.1 Constant electric fields

Constant electric fields are generated using two identical high-precision, high-voltage power sources (Heinzinger PNChp 30000-2 ump) with a maximum (electric) output potential of  $\phi = \pm 30$  kV. One high-voltage source is connected to each electrode and both high-voltage sources are operated individually with opposite polarity. The maximum applicable voltage is limited by the dielectric strength between the electrodes embedded into the ceramic and the grounded aluminium foil. Due to the fact that the distance between the different electric potentials is very small, the region is prone to surface flash-overs. Hence, the maximum electric potential is limited to  $\phi_{\max} = \pm 8$  kV for each electrode, which leads to maximum electric field strength at the droplet positions of  $E_{\max} = 11.61$  kV/cm.

### 8.1.4.2 Alternating electric fields

The generation of an alternating electric field is more complex than the generation of a constant electric field. Similar to the generation of a constant electric field, two high-voltage sources with opposite polarity are necessary to generate the electric field. A function generator (BK Precision 4052) generates a sinusoidal signal with small amplitude ( $\hat{U}_{\max} = 10$  V - peak to peak) and a frequency between  $f = 10$  Hz and  $f = 500$  Hz, which is amplified by a power amplifier (Thomann TA2400 MK-X). The amplified signal is used as input signal for two identical high-voltage transformers (Wirges EUVE 30K). Due to the alternating signal, the input signals

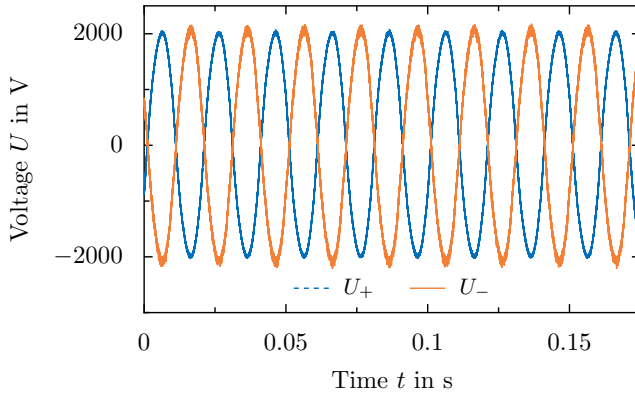


Figure 8.6: Exemplary measured temporal evolution of the alternating voltage signals  $U$  (frequency  $f = 50$  Hz) supplied to the electrodes. The signals are almost perfectly shifted by  $180^\circ$ .

of the high-voltage transformers have to be shifted by  $180^\circ$  to achieve signals with different polarity. Both high-voltage transformers are connected to the output of the same power amplifier but with shifted phases. This leads to a perfect shift of both signals of  $180^\circ$ . The voltage supplied to each electrode is continuously measured by two custom-made, high-voltage dividers connected to a computer using a data acquisition device (National Instruments<sup>TM</sup> BNC-2110). An in-house Labview<sup>TM</sup> program is used to control the voltage level during the experiment and to measure the voltage level. Similar to the constant electric field the maximum applicable electric potential for alternating voltages is limited and yields  $\phi_{\max} = \pm 4.24$  V for each electrode. This leads to a maximum electric field strength of  $\hat{E}_{\max} = 7.16$  kV/cm.

An exemplary temporal evolution of the perfectly shifted alternating voltages supplied to the electrodes is shown in Fig. 8.6.

#### 8.1.4.3 Transient electric fields

Two single stage impulse generators are used to generate transient electric fields [133]. Each impulse generator supplies a maximum electric potential of  $\phi_{\max} = \pm 25$  kV to one of the electrodes but with opposite polarity. Both impulse generators are triggered at the same time using a custom-

## 8 Experimental details

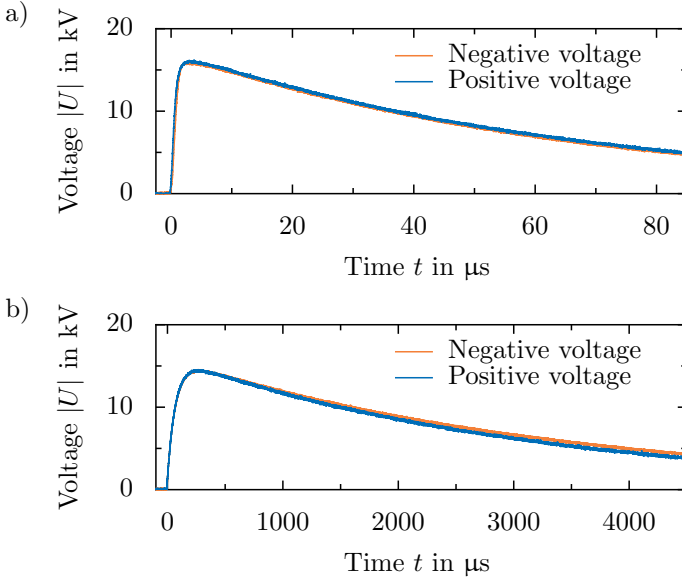


Figure 8.7: Exemplary measured temporal evolution of the voltage  $U$  generated by the impulse generator. a) Standard lightning impulse voltage (1.2/50  $\mu\text{s}$ ) and b) standard switching impulse voltage (250/2500  $\mu\text{s}$ ). Each curve shows the norm of the supplied voltage signal of one electrode. Reprinted (adapted) with permission from [159], under the Creative Common License - Attribution 4.0 International (CC BY 4).

made Thyristor switch. To change the polarity of the impulse generator anti-parallel diodes are used. The characteristics of the impulse voltage supplied to the electrodes is adjusted by the damping and discharge resistors of the impulse generator. Thus, two different types, namely standard lightning and standard switching impulse voltages, are generated. These types of impulse voltages are commonly used in high-voltage engineering to test high-voltage equipment and are defined by IEC 60060-1. In case of a transient electric field the maximum applied voltage to each electrode is  $\phi_{\max} = \pm 12 \text{ kV}$ , which results in maximum electric field strength of  $\hat{E}_{\max} = 22.82 \text{ kV/cm}$ .

An exemplary temporal evolution of the two synchronous standard lighting and switching impulse voltages supplied to the electrodes is shown in Fig. 8.7. Both signals are triggered almost perfectly at the same time. Furthermore, the course of the two signals are almost perfectly identical with respect to the maximum amplitude and the temporal evolution. Hence, the synchronized impulse generators are able to repeatedly generate a homogeneous transient electric field.

#### 8.1.4.4 Electric field strengths present in applications

The electric field strength present in high-voltage systems mainly depends on the components of the system. Each component is designed for a specific voltage level (and the associated electric field strength), so that the maximum electric field strength at the surface is limited. In case of a high-voltage insulator operated under alternating voltage, the maximum field strength on the surface is given by  $\hat{E}_{\max,AC} = 6.36 \text{ kV/cm}$  [209]. Hence, the electric field strengths for alternating electric fields generated by the experimental setup are in the same order of magnitude. However, e.g. the situation on the surface of an overhead conductor line cannot be reproduced by the experimental setup because the electric field is perpendicularly aligned to the surface of the conductor and the maximum electric field strength is much higher  $\hat{E}_{\max,AC} = 17 \text{ kV/cm}$  [145].

Overvoltages generated by lightning and switching impulse voltages generally result in higher electric field strengths as the presented maximum electric field strength for alternating electric fields. Switching impulse voltages can generate overvoltages of up to three times larger than the nominal line voltage as stated by IEC 60071-2. The overvoltages generated by lightning impulse voltages is assumed to be even higher (more than five times the nominal line voltage as measured by Eriksson et al. [61]). This results in an electric field strength of  $\hat{E}_{\max,SI} \approx 19 \text{ kV/cm}$  and  $\hat{E}_{\max,LI} \approx 31 \text{ kV/cm}$  for switching and lightning impulse voltage (based on the maximum electric field strength of  $\hat{E}_{\max,AC} = 6.36 \text{ kV/cm}$ ), respectively. While the overvoltages generated by switching impulse voltages can be reproduced with the experimental setup very well, the overvoltages produced by lightning impulse voltages are generally higher in reality. Even though the conditions present on the conductor line cannot be reproduced by the experimental setup, the conditions on the weather shed of a composite insulator can be reproduced very accurately.

### 8.1.5 **Boundary conditions**

Ice nucleation is affected on different length scales by the electric fields ranging from the nano-scale, including the orientation of water molecules [289], to the macro-scale, including macroscopic oscillation of droplets [224, 237]. Accordingly, the experiments have to be performed under well-defined and precisely controlled boundary conditions. Changing the boundary conditions can have a significant effect on the outcome of the experiments because ice nucleation is an extremely sensitive physical process depending on several influencing factors. However, laboratory experiments might exhibit boundary conditions deviating from those of the applications. One example is the use of silicone oil to prevent the evaporation of the droplets, which is in contact with the droplet interfaces and result in different wetting properties. Such adaptations possibly influence the nucleation behaviour. Therefore, the different influences are analysed in detail to determine their impact on ice nucleation.

#### 8.1.5.1 **Surrounding fluid**

Generally, droplets are surrounded by air, especially in the scope of high-voltage insulators affected by ice accretion. In contrast, the droplets are surrounded by oil in the laboratory experiments in order to prevent the interaction of neighbouring droplets and to reduce the evaporation of the droplets. Even though the change of the surrounding fluid affects the surface tension, the droplet shape is almost not affected in the present experiments. However, the changed fluid properties might significantly influence ice nucleation. Droplets are significantly influenced by the presence of electric fields, which induces droplet oscillations or movement. This macroscopic motion is influenced by the surrounding fluid because of a changed viscosity or an increased density. In addition, the oil has different dielectric properties compared to air, which also have an impact on the electric field distribution or on the ice nucleation behaviour.

The behaviour of sessile droplets is significantly affected by external electric fields. As already presented in Part III, the electric field generates droplet oscillations which are mainly affected by the electric field strength, frequency of the electric field, droplet charge and droplet volume. The oscillation of the droplet is very sensitive to changes of the boundary conditions such as the electric charge or the frequency. A change of these parameters promotes different oscillation modes. In turn, this can affect

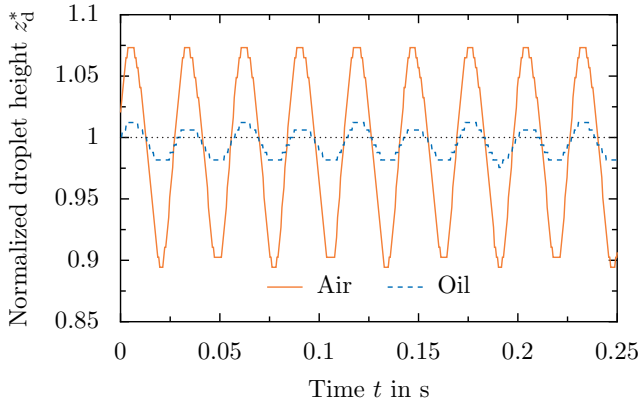


Figure 8.8: Comparison of droplet oscillation for different surrounding fluids by means of the temporal variation of the normalized droplet height  $z_d^*$ . Reprinted (adapted) with permission from [160], under the Creative Common License - Attribution 4.0 International (CC BY 4).

ice nucleation because the interaction of the droplet and the substrate is changed. This is the case, especially at the contact area of the fluid and the substrate, where ice nucleation is expected to take place. Using oil instead of air significantly increases the viscosity of the surrounding fluid ( $\eta_{\text{oil}}/\eta_{\text{air}} \approx 252$ ). Hence, the motion of the droplet surrounded by oil is significantly damped compared to air. Furthermore, the amplitude of the oscillation is lowered in case of oil as surrounding fluid.

For comparison reasons the motion of a droplet oscillating in the second resonance mode is analysed for different surrounding fluids. The result is shown in Fig. 8.8. Both droplets are exposed to the same electric field strength of  $\vec{E} = 3.59$  kV/cm ( $f = 17.56$  Hz) and have the same volume of  $V = 50$   $\mu\text{l}$ . The principle motion of the droplet is independent of the surrounding fluid. An example of the principal motion is shown in Fig. 2.10b. The motion of the droplet is analysed by using the dimensionless height of the droplet  $z_d^* = z_d(t)/z_{0,d}$ , where  $z_d(t)$  is the time-dependent droplet height and  $z_{0,d}$  is the droplet height in equilibrium without an electric field. As shown by the data, the oscillation of the droplet is not influenced in terms of frequency by the surrounding fluid. However, the amplitude of the oscillation is significantly reduced in oil compared to water

## 8 Experimental details

( $z_{d,\text{air}}^*/z_{d,\text{oil}}^* = 5.35$ ). Accordingly, the oscillation of the droplet is drastically damped as a result of the increased viscosity of the surrounding fluid.

As shown by Eq. (2.52), the resonance frequency of the droplet depends on the surrounding fluid. For air the influence of the surrounding fluid is negligible because the density of air is much lower than the density of water. However, this is not the case for oil as surrounding fluid. Taking into account the fluid properties of oil and air, namely the density ( $\rho_{\text{oil}} = 920 \text{ kg/m}^3$  and  $\rho_{\text{air}} = 1.204 \text{ kg/m}^3$  at a temperature of  $\vartheta = 25^\circ \text{C}$ ) and the surface tension ( $\gamma_{\text{wa-oil}} \approx 35.9 \cdot 10^{-3} \text{ N/m}$  [204] and  $\gamma_{\text{wa-air}} \approx 72.75 \cdot 10^{-3} \text{ N/m}$ ), reveals that the resonance frequency is significantly changed, e.g. for the first resonance mode:  $f_{\text{oil}} = 0.55 f_{\text{air}}$ . The resonance frequency is almost reduced in half. However, Eq. (2.52) is only valid for free or sessile droplets on a hydrophobic substrate. The static contact angle of a sessile droplet on sapphire surrounded by oil exhibits  $\theta = 78^\circ \pm 7^\circ$ , and is thus hydrophilic. Hence, the results have a limited validity for this case. Even though the result is not fully applicable to droplets surrounded by oil, it is expected that the qualitative influence is still transferable to the present case. The resonance frequency is lower in case of oil compared to air. However, the principal motion and the different resonance modes are not affected by a change of the surrounding fluid.

Despite the fact that the resonance frequencies of the droplet are shifted to lower frequencies, the motion of a droplet surrounded by oil is not affected as shown in Fig. 8.8. The frequency of the droplet only depends on the frequency of the applied electric field. The surrounding fluid does not have an impact on the frequency but only on the amplitude of the oscillation.

Shear (flow) inside a droplet resulting from droplet oscillation caused by the presence of an electric field can affect ice nucleation [22, 224]. Consequently, changing the surrounding fluid results in a changed motion of the droplet which indirectly has an impact on ice nucleation. Increasing the electric field strength leads to a larger amplitude of the droplet oscillation, so that a droplet surrounded by oil performs the same motion as a droplet surrounded by air but at higher electric field strength. Consequently, droplets surrounded by oil have the same behaviour as droplets surrounded by air.

Besides the impact on the motion of the droplets, the surrounding fluid

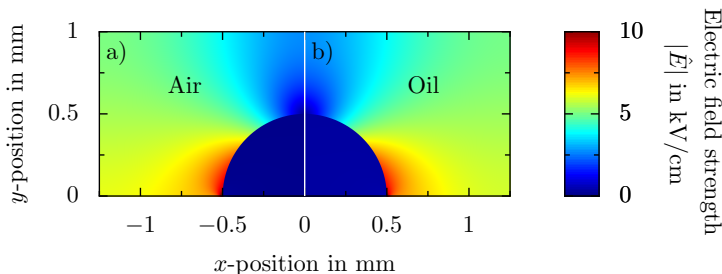


Figure 8.9: Comparison of the electric field distribution for a droplet deposited onto a rigid substrate between two plate electrodes for a) air and b) oil as the surrounding fluid. An alternating voltage of  $\hat{U} = 10 \text{ kV}$  ( $f = 50 \text{ Hz}$ ) is applied between the electrodes, resulting in an electric field strength of  $\hat{E} = 4 \text{ kV/cm}$ . Reprinted (adapted) with permission from [160], under the Creative Common License - Attribution 4.0 International (CC BY 4).

might also impact the electric field distribution because of the changed dielectric properties compared to air. The distribution of the electric field mainly depends on the relative permittivity and electrical conductivity of the involved materials. For low frequencies the droplet can be assumed to be a perfect conductor so that the electric field inside the droplet vanishes. In contrast, the electric field strength directly at the three-phase contact line is enhanced and depends on the relative permittivity of the surrounding fluid. While air has a relative permittivity of  $\varepsilon_{r,\text{air}} = 1$ , the relative permittivity of oil is higher ( $\varepsilon_{r,\text{oil}} \approx 2.8$ ). This might significantly impact the electric field distribution around the droplets. A comparison of the field distribution around the droplets for the different surrounding fluids is shown in Fig. 8.9. The electric field distribution has been obtained for the same boundary conditions with respect to the droplet position and the electric field strength. The droplet is placed in the centre between two plate electrodes separated by 2.5 mm. A symmetrical voltage is applied to the electrodes resulting in an electric potential difference of  $\hat{U} = 10 \text{ kV}$ . This results in an electric field strength of  $\hat{E} = 4 \text{ kV/cm}$  in absence of the droplet. The resulting electric field lines are in parallel to the  $x$  axis. Hence, this setup reproduces the electrical situation in the ceramic directly at the position of the droplets very well. The droplet is

## 8 Experimental details

modelled as a hemisphere and is assumed to be stationary. Thus, the fluid motion caused by the electric field is not taken into account. Only the Laplace equation to determine the electric field distribution is solved for the given geometry using COMSOL Multiphysics<sup>®</sup>. The resulting electric field distribution is almost not affected by the surrounding fluid. The electric field inside the droplet vanishes and the interface of the droplet forms an equipotential surface.

The highest electric field strength occurs in the region close to the three-phase contact line for both cases. Due to the fact that  $\varepsilon_{r,\text{air}} < \varepsilon_{r,\text{oil}}$  the maximum field strength is generally higher in air compared to oil. However, the small difference in relative permittivity of the different fluids leads to almost the same electric field distribution. It is worth noting that the electric field strength shown in Fig. 8.9 is limited to  $\hat{E} = 10 \text{ kV/cm}$  for a better visualization. However, the field strength inside the air is slightly higher than in oil. Even for higher frequencies, the electric field inside the droplet would almost vanish, because the relative permittivity of water is much higher than the relative permittivity of oil or air.

As shown in Part III the region near the three-phase contact line is prone to generate partial discharges due to the enhanced electric field strength. The occurrence of partial discharges mainly depends on the breakdown strength of the surrounding fluid, which is higher in case of oil compared to air. Thus, the formation of partial discharges possibly influences ice nucleation, but is suppressed by using oil instead of air as surrounding fluid. In contrast, the field distribution inside the droplet is not affected by the surrounding fluid.

In conclusion, using oil as surrounding fluid instead of air neither changes the principal influence on the general behaviour of droplets under the impact of electric field nor the electric field distribution around the droplet. However, oil decreases the maximum electric field strength and significantly damps the motion of the droplet. Consequently, the impact of the electric field on ice nucleation might be underestimated while using oil compared to air.

### 8.1.5.2 Electric charges on the droplet and the substrate

Electric charges were proven to have an impact on the macroscopic behaviour of water droplets under the impact of electric fields. Not only the oscillation of droplets is affected but also the generation of partial dis-

charges. In addition to this dynamic behaviour, electric charges affect the equilibrium shape of a static droplet caused by an inhomogeneous surface charge distribution on the substrate or a significant net charge on the droplet. The charges might originate from droplet generation [39] or sample preparation. Accumulated charges on the substrate can be transferred to the sessile droplet [152] and can affect the oscillation behaviour. A change of the oscillation behaviour with respect to the frequency impacts the fluid motion, and so electric charges indirectly affect ice nucleation.

The charge of the droplets and the substrate is not actively controlled during the experiment. Hence, the electric charge is only a boundary condition for the present experiments. The droplets and the sample are prepared with extreme caution to prevent charge accumulation during the preparation. Especially, the sapphire glass is rinsed several times with isopropanol and direct contact to the substrate is prevented to minimize the generation of surface charges. Thus, the sample preparation aims to reduce the charges on the droplets and the substrate. Even if the charge of the individual droplets may vary by an inhomogeneous surface charge distribution, droplets generated on a different day or from a different source of water, the impact of electric charges is presumably negligible for the present experiments. Using the same droplet ensemble to investigate one influencing parameter leads to an almost constant charge for the individual droplets. Due to the fact that the charge transfer between the droplets and the substrate is assumed to take a long time [152], the charge is constant during the experiments. Although, the electric charge is not actively controlled during the experiments, an unknown essential impact on the ice nucleation behaviour can be essentially ruled out due to the fact that the same droplets are used for the experiments.

Besides charged, also uncharged droplets are significantly affected by the electric field. High electric field strengths generate large droplet deformations, which might finally result in the formation of a Taylor cone accompanied by the formation of small, highly charged satellite droplets [166, 261]. The ejection of small droplets leads to a decrease of the droplet volume, possibly resulting in a reduced wetted area. Especially, heterogeneous nucleation depends on the properties of the wetted surface. Reducing the size of the wetted area generally reduces the droplet freezing rate. However, if the formation of a Taylor cone is observed during the experiments, the corresponding droplet is not taken into account during the analysis. Generally, only large droplet deformations and oscillations are observed during the experiments.

The careful handling of the droplets and the sample during preparation aims to reduce the accumulated charges and leads to well-controlled boundary conditions. The use of the same droplet ensemble during a set of experiments ensures a high level of accuracy and reproducibility.

## 8.2 Preparation and Procedure

Careful sample preparation is necessary to generate accurate and repeatable results, because ice nucleation inside water droplets is affected by several influencing factors like the droplet size [20, 97], the proximity of neighbouring droplets [249], any contamination or impurities on the substrate surface [30, 103] or inside the droplet [106] which possibly promotes ice nucleation.

Prior to the experiments, the groove inside the ceramic body is carefully cleaned with isopropanol and is dried using a bellows. In addition, the sapphire sample holder, which is stored in isopropanol, is rinsed with fresh isopropanol to remove any contamination or residual oil on the substrate. To avoid the generation of electric charges or a new contamination of the substrate, any direct contact to the surface is avoided by using tweezers. Once the sample holder was carefully rinsed with isopropanol, the surface is dried using a bellows. After each experiment the sapphire sample holder is intensively cleaned in an ultrasonic bath of isopropanol to remove any residual oil on the surface and to ensure well-defined surface conditions. Subsequently, the sample holder is stored in a Petri dish filled with isopropanol to prevent any contamination of the substrate.

### 8.2.1 Generation of sessile droplets

The sessile droplets to investigate heterogeneous ice nucleation are generated from high purity water (Millipore Milli-Q Type 1, electrical conductivity of  $\kappa_{\text{el}} = 5.5 \cdot 10^{-6} \text{ S/m}$ ). A piezo-driven, droplet-on-demand droplet generator, similar to [93], is used to deposit the individual droplets with a well-defined size on a sample holder. The size of the droplets can generally be adjusted by the nozzle size and the impulse characteristics applied to the piezo-element. However, for the present experiments the droplet size is not varied, but is kept constant at  $d_{\text{d}} \approx 0.73 \text{ mm}$ . Prior to the droplet generation, the closed loop system of the droplet generator is purged sev-

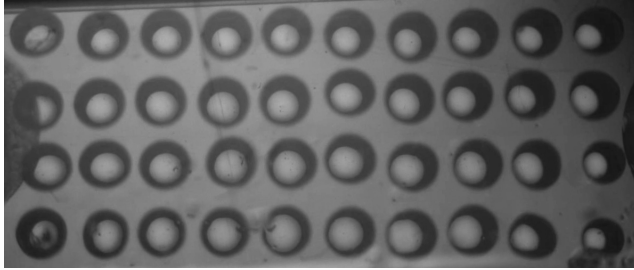


Figure 8.10: Top-view images showing a droplet matrix consisting of droplets with a mean size of  $\bar{d}_d = 1.04\text{mm}$  placed on the sapphire substrate. Reprinted figure (adapted) with permission from [158]. Copyright 2021 by the American Physical Society.

eral times with high purity water to minimize the contamination of the droplets. Afterwards, fresh and degassed high purity water is filled in the closed-loop system and sealed to prevent any contamination. The water is vacuum degassed at a pressure of  $p \leq 1\text{ mbar}$  for at least 30 min.

The droplets are positioned in an equidistant matrix on the sapphire substrate. Two linear stages controlled and synchronized with the droplet generator are operated by an Arduino to adjust the position of the substrate below the droplet generator to generate the equidistant droplet matrix. An example of such a droplet matrix is shown in Fig. 8.10. The sapphire glass is placed in the groove inside the ceramic and is subsequently covered by silicone oil ( $\nu = 5\text{ cSt}$ ) to prevent the droplet evaporation and to minimize the interaction of the neighbouring droplets, similar to [30]. Covering the droplets with silicone oil avoids mutual influences on the droplets during the experimental procedure (cool-down), e.g. via the Wegener-Bergeron-Findeisen process [67, 249]. The contact angle of sessile water droplets on the sapphire glass surrounded by oil is  $\theta \approx 78^\circ$ . The generated droplets with a size of  $d_d \approx 0.78\text{ mm}$  are associated with a diameter of the wetted area of  $d_{\text{wet}} \approx 1\text{ mm}$ . In case of heterogeneous ice nucleation, this diameter is used to characterize the droplets. Generally, 40 droplets are placed on the sapphire glass with a surface area of  $8 \times 15\text{ mm}^2$ .

Even though the droplet-on-demand generator repeatedly produced droplets with an almost constant volume, the size of the sessile droplets

## 8 Experimental details

varies as shown in Fig. 8.10. To ensure that only droplets with the same size are taken into account during the analysis of the experiments, droplets which vary in size more than 10 % from the mean diameter are sorted out. Comparing this size variation to the size variation in already existing literature reveals that the values are in the same order of magnitude, for example the deviation is given by 4 – 10 % of the volume by Zhang et al. [294], up to 40 % of the diameter by Atkinson et al. [7], approximately 13 % of the diameter by Atkinson et al. [6] or 3 % of the volume by Budke and Koop [28].

### 8.2.2 Generation of emulsified droplets

Emulsified water droplets are used in this study to investigate the influence of the electric field in absence of a substrate. Water droplets made from high purity water (Millipore Milli-Q Type 1) are stabilized in oil (Novec<sup>TM</sup> 7500) to generate free floating droplets which are only in contact with oil and no additional surface or medium. A commercially available bio-compatible surfactant (Sphere Fluidics Pico-Surf<sup>TM</sup> 1) pre-dissolved in Novec<sup>TM</sup> 7500 oil is used to prevent coalescence of the droplets. The mixture has a weight ratio of 5 % Pico-Surf<sup>TM</sup> and 95 % Novec<sup>TM</sup> 7500 oil and is used without further dilution. The emulsion is generated using a T-junction (Upchurch Scientific MicroTee P-890) with an inner diameter of 0.15 mm and constant flow rates of oil and water. Mainly, the inner diameter of the T-junction as well as the ratio of flow rates between water and oil determine the final size of the emulsified droplets [79]. An automated syringe pump (KD Scientific KDS-100-CE) with a constant volumetric flow rate is used to convey both fluids to the T-junction. The volume rate of the oil and water is adjusted by the used syringe size (diameter). A 1 ml (inner diameter  $d = 4.69$  mm) and a 2 ml (inner diameter  $d = 9.75$  mm) syringe are used for water and oil, respectively. Accordingly, the flow rate of oil is about four times larger than the flow rate of water. Both fluids are supplied to an individual port of the T-junction using PEEK (Polyetheretherketone) tubing, which have a high chemical resistance to prevent any contamination of the fluids by dispersion through the tubing. The third port directly supplies the emulsion to the sample holder made out of sapphire.

A custom-made sample holder was designed and produced to investigate only a single layer of droplets which is exposed to well-defined conditions



Figure 8.11: Image of the sample holder made out of sapphire. The two-part design forms a liquid channel to contain the emulsified droplets.

in terms of temperature and electric field. Furthermore, the movement of individual droplets during the experiment should be inhibited, because it complicates the analysis. A two-part design was used to produce a fluid channel with a height of 0.45 mm. The top and bottom part of the channel are made out of the same material as the specimen holder of the sessile droplets, namely sapphire glass, due to its high thermal conductivity and low electrical conductivity. Both parts are joined by using an adhesive. An image of the CAD (computer aided design) model of the sample holder is shown in Fig. 8.11. Prior to the experiment the channel is carefully cleaned by flooding the channel with isopropanol and high purity water. The emulsified droplets are supplied into the channel through the holes in the cover. The channel is completely filled with the emulsion to minimize the movement of the droplets inside the channel. The density of the water droplets is lower than the density of the oil, so that the droplets float on top of the oil, as already reported in [258]. Due to the cover and the small height of the channel, the droplets are completely surrounded by oil and the contact between droplets and sapphire glass is minimized. The sample holder comprising the emulsified droplets is placed inside the groove of the ceramic body. Subsequently, the air gap between the sample holder and the boundary of the groove is filled with oil (Novec<sup>TM</sup> 7500) to improve the heat transfer between the ceramic and the sample holder.

The emulsified droplets have a mean size of  $\bar{d}_d = 124.8 \mu\text{m}$ . An exem-

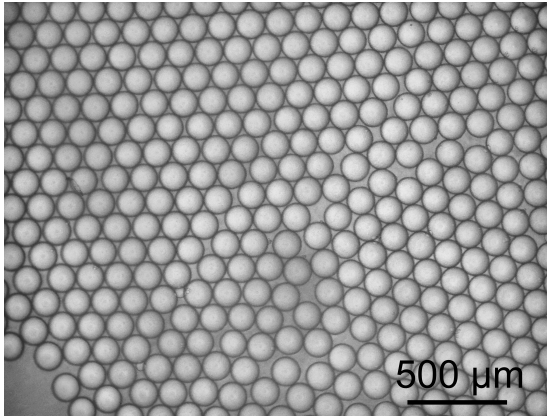


Figure 8.12: Microscopic image of emulsified droplets.

plary image of the generated emulsion taken by a microscope is shown in Fig. 8.12. As illustrated in the image, the size of the individual droplets is almost identical and they are closely packed without coalescing. The size variation of the droplets allowed during the analysis is  $\pm 15\%$  with respect to the mean diameter. Droplets with a smaller or larger size are automatically sorted out during the analysis. Using the given combination of surfactant and water results in an emulsion, which can be stabilized for several hours and days, as already reported in [105, 258]. For each experiment a fresh ensemble is used due to the fact that the droplets coalesce after a freezing and thawing cycle, similar to [258].

### 8.2.3 Experimental procedure

After careful cleaning of the experimental setup including the sample holders and completed droplet generation, the sample holder containing the sessile or emulsified droplets is placed in the groove in the ceramic body. In case of emulsified droplets, the space between the sample holder and the wall of the groove is filled with heat transfer fluid to improve the heat transfer from the ceramic to the sample holder. Sessile droplets are also covered with oil to prevent the interaction of nearby droplets. Subsequently, the groove is sealed by a cover with embedded PMMA sheet to protect the experimental space from any external influences. Further-

more, the experimental space is flooded with gaseous nitrogen to avoid condensation of water during the cooling process.

The experiment is fully automated for a single run and is started by the in-house Labview<sup>TM</sup> program. After starting the experimental procedure, the temperature is held constant at  $\vartheta = 14\text{ }^{\circ}\text{C}$  for at least 5 min to ensure well-defined and repeatable thermal conditions for each run. At the end of the 5 min the cooling process starts automatically and the electric field is switched on manually. The temperature is constantly lowered at the desired rate. The temperature and the video data are captured during the experiment. As soon as a temperature of about  $\vartheta_d = -40\text{ }^{\circ}\text{C}$  is reached the procedure is stopped and the temperature is increased to initiate the thawing of the droplets.

For the investigation of the impact of transient electric fields on ice nucleation the procedure is slightly adapted. Instead of cooling at a constant rate, the temperature is decreased to a specific temperature at a constant rate ( $\dot{T} = 5\text{ K/min}$ ) and is then kept constant for at least 2 min to ensure a homogeneous temperature distribution. After this time, the transient electric field is applied to the droplet ensemble. Finally, the video and temperature data are saved and the next experimental run can be started.

In case of sessile droplets, the experiments investigating one parameter are performed with the same droplet ensemble to rule out any influence of freshly generated droplets. Comparing the ice nucleation behaviour of different ensembles and the ice nucleation behaviour of a single ensemble for multiple freezing and thawing cycles reveals that the change of the droplets can have a significant influence on the nucleation behaviour.

An exemplary comparison is shown in Fig. 8.13. The data is presented as droplet survival curves. The liquid fraction  $N_\ell/N_0$ , where  $N_\ell$  is the number of liquid droplets for a specific temperature and  $N_0$  is the number of initially liquid droplets, is shown in dependence on the droplet temperature  $\vartheta_d$ . Hence, the figure illustrates the decay of liquid droplets for a decreasing temperature. Both experiments are performed under the same conditions. Droplets of an almost identical size are cooled at a constant cooling rate of  $\dot{T} = 5\text{ K/min}$  until all droplets are frozen. The data shown in Fig. 8.13a are generated by repeating the experiment four times with freshly generated droplets for each experiment. The general shape of survival curves is represented by the typical 'S'-shape and is similar for all experiments. However, the nucleation temperature of the droplets

## 8 Experimental details

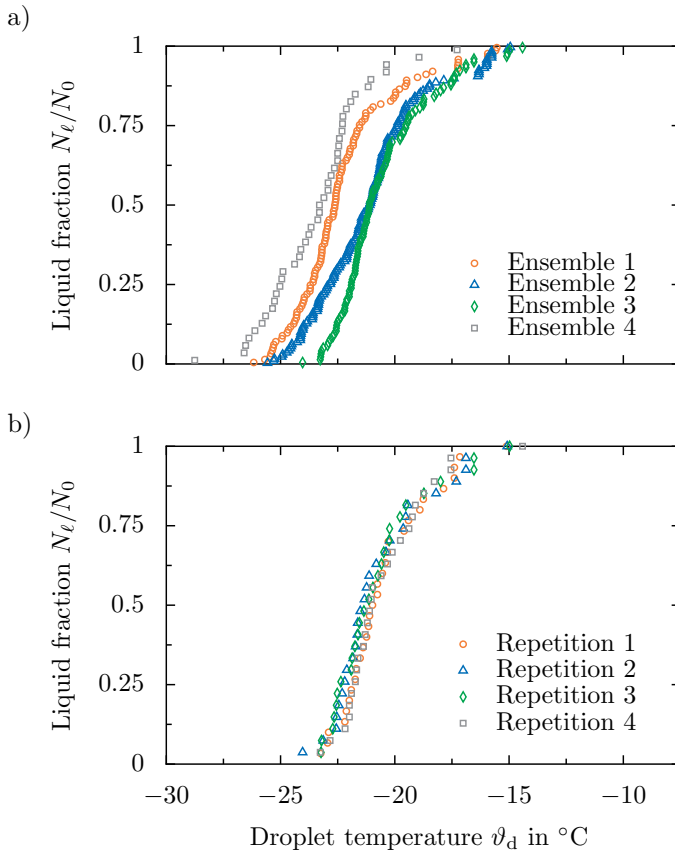


Figure 8.13: Comparison of the effect of re-using the same droplets, or generating fresh ones for each experiment on the observed nucleation behaviour without an electric field. The data is presented by the liquid fraction  $N_\ell/N_0$  depending on the droplet temperature  $\vartheta_d$ . a) Droplet survival curves obtained using fresh droplets for each of the shown experiments. b) Droplet survival curves obtained using the same droplets for each of the shown repetitions. Republished (adapted) with permission of [154]; permission conveyed through Copyright Clearance Center, Inc..

varies even for constant boundary conditions. Even though, the experiment is carefully prepared and conducted under well-defined conditions, the repeatability of the experiments is limited.

The variation can be quantified by comparing the mean nucleation temperatures  $\vartheta_{0.5}$  for the different experiments. The mean nucleation temperature corresponds to  $N_\ell/N_0 = 0.5$  and defines the temperature, where half of the ensemble is frozen. Using freshly generated droplets for each experiment leads to a large deviation of the mean freezing temperature between the different runs of  $\Delta\vartheta_{0.5} \approx 2.2$  K. Assuming a singular ice nucleation model, heterogeneous ice nucleation is assumed to take place at a specific temperature for each droplet. The nucleation temperature of each droplet depends on the characteristic temperature of the most active nucleation site inside the droplet [266]. However, ice nucleation is still a stochastic process, even for perfectly constant conditions [193, 268]. Whether the stochastic nature of ice nucleation is observable or not is influenced by the timescale, as reported by [193], and thus might be masked. In spite of the careful preparation of the droplets and the careful cleaning of the substrate, a contamination of the droplets cannot be completely ruled out. Furthermore, the position of the droplets on the substrate vary, and so the local wetting properties. Consequently, changing the droplets always leads to changed nucleation temperatures of the droplets because the ice nucleation particle (INP) spectrum inside the droplet is changed. Hence, the most active nucleation site is different in each droplet.

Due to the fact that the effect of electric fields on ice nucleation is controversially discussed and only observed in specific experiments, the influence of the electric field on ice nucleation might be very small. Accordingly, the large variations in temperature between the different runs with freshly generated droplets might mask the influence of the electric field. Using freshly generated droplets for the experiment would necessitate numerous experiments to determine a statistical significant influence of the electric field. To rule out the influence of freshly generated droplets and the changed INP spectrum, the same droplet ensemble is used to investigate a specific parameter such as the electric field strength or the frequency. As shown in Fig. 8.13b the variation of the nucleation temperature can be clearly attributed to the sample preparation. Using the same droplet ensemble for multiple experiment results in an almost perfect agreement between the individual repetitions. The almost perfect agreement of the survival curves yields a difference of the mean nucleation temperature of  $\Delta\vartheta_{0.5} \approx 0.35$  K, which is significantly lower compared to the freshly gen-

## 8 Experimental details

erated droplets. Furthermore, this supports the assumption of a singular nucleation behaviour. The remaining scatter results from the stochastic nature of ice nucleation. Consequently, repeating the same experiment with the same droplet ensemble can increase the number of freezing events exposed to the same conditions, which clearly increases the statistical significance of the results. Usually, the data of the individual droplet survival curves for fixed boundary conditions are combined to one data set containing all freezing events. Thus, it is ensured that a sufficient number of freezing events is analysed for each boundary conditions.

For emulsified droplets it was not possible to re-use the same droplets because the freezing and thawing cycle always led to droplet coalescence. However, the number of detected freezing events is much larger compared to sessile droplets so that the individual experiments do not have to be repeated.

### 8.2.4 Analysis of the experiments

The analysis of the video data is performed with an in-house MATLAB<sup>®</sup> code to ensure a repeatable and accurate analysis of the videos. At first the video data including the temperatures is imported into MATLAB<sup>®</sup> and the user has to input additional information about the start and end frame for the analysis as well as the temperatures for the corresponding frames. Based on this information the cooling rate is determined and the video is analysed. Afterwards, the pixel to meter ratio is calculated based on a reference length identified by the user in the image. Thus, the original size of the droplet and the wetted area can be determined accurately.

The contact angles of the droplets on the sapphire glass surrounded by oil were measured to be  $\theta \approx 78.8^\circ$ . Hence, the projected area captured by the video camera equals the wetted area on the substrate and can be determined by measuring the size of the droplet. The size variation of the droplets can be defined by the user, so that only droplets with a specific range of size are taken into account during the analysis. Each frame of the video within the defined range is analysed in sequence and compared to the previous frame to detect any change. The freezing of sessile droplets is detected by the vanishing glare point of the individual droplets. In case of emulsified droplets, the grey scale change of the droplet (from transparent to dark), caused by the different light refraction of water and ice, is used

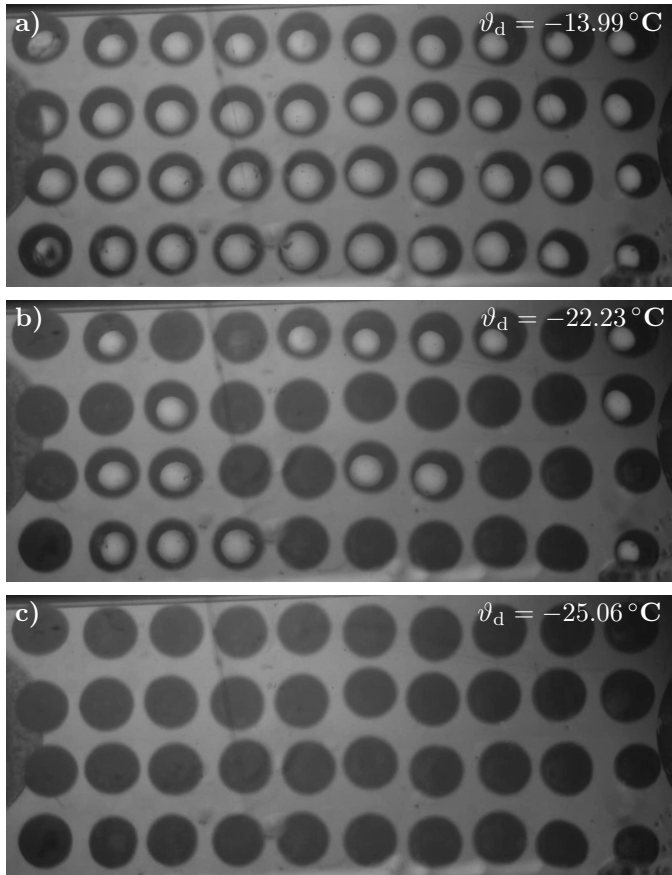


Figure 8.14: Top-view images showing a droplet matrix consisting of droplets with a mean size of  $\bar{d}_d = 1.04\text{mm}$  placed on the sapphire substrate. The droplet matrix is shown at different moments during a nucleation experiment, illustrating the gradual decay of the ratio of liquid droplets in the ensemble. a) Unfrozen droplet ensemble at  $\vartheta_d = -13.99^\circ\text{C}$ , b) partially frozen ensemble at  $\vartheta_d = -22.23^\circ\text{C}$ , and c) completely frozen ensemble at  $\vartheta_d = -25.06^\circ\text{C}$ . Reprinted figure (adapted) with permission from [158]. Copyright 2021 by the American Physical Society.

## 8 *Experimental details*

to detect the nucleation event. For each freezing event the location of the vanishing glare point is detected. Afterwards, the detected freezing event is assigned to a specific droplet. An example for the vanishing glare point is illustrated in Fig. 8.14, which shows the droplet ensemble at different temperatures. The liquid droplets can be clearly identified by the bright glare point, while the frozen droplets are characterized by completely dark circles. Decreasing the temperature leads to an increasing number of frozen droplets.

Each droplet in the equidistant matrix has a specific identification number (ID) according to the position inside the matrix. The numbering of the droplets starts from the upper left corner and proceeds row by row. As soon as all frames are analysed the result of the automated analysis is shown to the user. The detected droplets are highlighted on the image and numbered according to the freezing order. The user can check the result of the analysis and sort out droplets by hand, e.g. in case of a false detection. Finally, the data of each freezing event is saved including the specific time, temperature, size of the droplet, droplet position, freezing order and the liquid fraction. This information can be used to further analyse the data.

This semi-automated procedure ensures that the analysis of the video is performed with fixed criteria and results in an accurate analysis of the experiments.

## 9 Results using supercooled sessile droplets

---

---

The content of this chapter is partly based on the Bachelor thesis of David Zöllner [297], and has been partially published in the following publications and conference proceedings:

- [151] Löwe, J.-M., Hinrichsen, V., Schremb, M., Dorau, T., and Tropea, C. Experimental Investigation of Electro-freezing of Supercooled Droplets. In *9th World Conference on Experimental Heat Transfer, Fluid Mechanics and Thermodynamics*, Foz do Iguacu, Brasilien, 2017
  - [154] Löwe, J.-M., Schremb, M., Hinrichsen, V., and Tropea, C. Ice Nucleation in the Presence of Electric Fields: An Experimental Study. In SAE International, editor, *International Conference on Icing of Aircraft, Engines, and Structures*, SAE Technical Paper Series. SAE International400 Commonwealth Drive, Warrendale, PA, United States, 2019. doi:10.4271/2019-01-2020
  - [160] Löwe, J.-M., Schremb, M., Hinrichsen, V., and Tropea, C. Experimental Methodology and Procedure for SAPPHIRE: a Semi-automatic APParatus for High-voltage Ice nucleation REsearch. *Atmospheric Measurement Techniques*, 14(1):223–238, 2021. doi:10.5194/amt-14-223-2021
  - [158] Löwe, J.-M., Hinrichsen, V., Schremb, M., and Tropea, C. Ice Nucleation in High Alternating Electric Fields: Effect of Electric Field Strength and Frequency. *Physical Review E*, 103(1): 012801, 2021. doi:10.1103/PhysRevE.103.012801
  - [159] Löwe, J.-M., Hinrichsen, V., Schremb, M., and Tropea, C. Ice nucleation forced by transient electric fields. *Physical Review E*, 104(6):064801, 2021. doi:10.1103/PhysRevE.104.064801
- 
-

## 9.1 Four stages of ice nucleation experiments

During the experiments the water droplets undergo numerous freezing and thawing cycles. This cycle can be divided into different stages, depending on the underlying mechanism active at these stages. The four stages are namely, first and second freezing stage, thawing stage and dissolving (of residual gas bubbles) stage. Each individual stage is investigated using a high-speed camera to determine the time resolved behaviour of the droplets. The first freezing stage is illustrated in Fig. 9.1. Initially, the

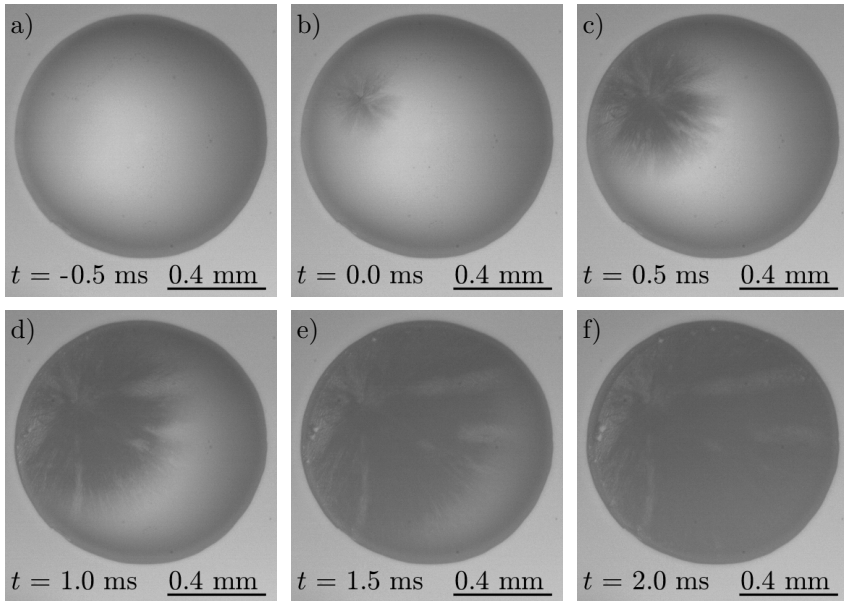


Figure 9.1: Stages of the freezing process of a supercooled water droplet. a) Initially liquid droplet at a temperature below  $\vartheta = 0^\circ\text{C}$ , b) nucleation inside the droplet at a temperature of  $\vartheta = -22.65^\circ\text{C}$ , c)-e) dendritic growth and freezing of the droplet, f) end of dendritic growth. Reprinted (adapted) with permission from [160], under the Creative Common License - Attribution 4.0 International (CC BY 4).

## 9.1 Four stages of ice nucleation experiments

sessile droplets are liquid, as shown in Fig. 9.1a. As soon as the temperature of the droplet is lower than the melting temperature the liquid is supercooled but still liquid. Further decreasing the temperature increases the degree of supercooling and promotes ice nucleation inside the droplet, as shown in Fig. 9.1b. In the presented case ice nucleation is observed at a liquid temperature of  $\vartheta = -22.65^\circ\text{C}$ . The location of ice nucleation inside the droplet is located on an arbitrary point and is mainly determined by the position of the most active nucleation germ at the given temperature (assuming a singular nucleation behaviour). Furthermore, ice nucleation is not located at the three-phase contact line and is only caused by the decreasing temperature because the droplet is at rest. Due to the fact that the liquid is in direct contact with the substrate and the observed nucleation temperatures are rather higher compared to the theoretical nucleation temperature of homogeneous ice nucleation, most probably heterogeneous ice nucleation at the substrate is observed. In addition, the substrate and the liquid layer at the substrate have a slightly lower temperature than the bulk of the liquid, because the substrate is cooled from below. Hence, heterogeneous ice nucleation is more favourable than homogeneous ice nucleation, because of the lowered temperature directly at the substrate.

After the initial ice nucleation, a dendritic growth of the ice phase can be observed, as shown in Fig. 9.1c-e. As soon as the complete droplet volume is pervaded by the dendritic ice structure the first phase of solidification has been completed as shown in Fig. 9.1f [236]. During the dendritic growth the mixture of solid ice and supercooled liquid water is warmed up to the equilibrium freezing temperature, because of the release of latent heat of fusion during the phase transition [236]. Accordingly, the droplet consists of a mixture of liquid water and ice in local thermodynamical equilibrium. The residual portion of liquid in between the dendritic ice is determined by the degree of supercooling [236].

The first stage of freezing is completed on a small timescale as shown in Fig. 9.1, where the process only takes about  $t \approx 2$  ms. Due to the fact that the dendritic growth is a fast process, the solidification of the droplet is only initialized by ice nucleation at a specific location and not multiple locations as assumed for homogeneous nucleation [216].

At this stage the mixture of water and ice is in local thermal equilibrium at the melting temperature [235]. A further extraction of heat will lead to the freezing of the residual liquid water, which is also called second

## 9 Results using supercooled sessile droplets

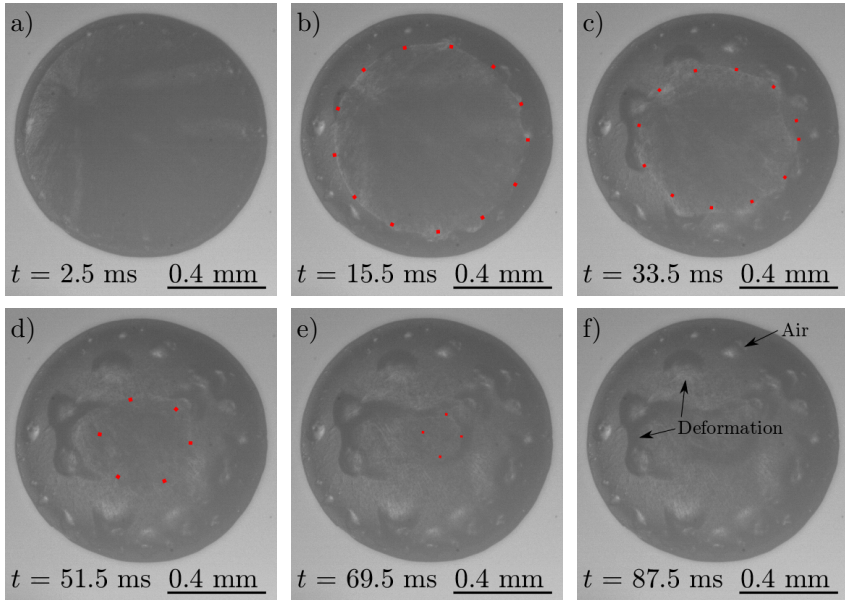


Figure 9.2: Time series of the second freezing stage. a)-e) Freezing of the residual water in between the dendritic structure observed from above resulting in a fully frozen droplet. The images show the propagation of the boarder (red dotted circle) for the different stages from a partially frozen to a completely frozen droplet in top view. f) shows a completely frozen droplet with entrapped air (bright regions) and deformations of droplet surface (dark contours), caused by the volume expansion during freezing.

stage of freezing [235]. A time series of the second freezing stage is shown in Fig. 9.2. The second freezing stage directly follows the first freezing stage so that the initial phase of the second freezing stage is similar to the last phase of first freezing stage (Fig. 9.1f) as shown in Fig. 9.2a. Due to the constant cooling of the substrate the residual water in between the dendritic structure freezes starting at the substrate surface [236]. The resulting freezing front propagates perpendicular to the substrate surface and has to fulfil the boundary conditions on the interface of the droplet

## 9.1 Four stages of ice nucleation experiments

[236]. Hence, the freezing front has a curved shape, because it has to be perpendicular to the interface of the droplet [236].

The top view of the droplet containing the propagating freezing front is shown in Fig. 9.2b-e. The propagating freezing front cannot be seen directly from above because of the first freezing stage. However, the position of the freezing front can be observed on the interface of the droplet, which is indicated by the dotted circles in the images. Outside these circles the droplet is completely frozen while the portion inside the circles represents the capped sphere of water-ice mixture. As soon as the freezing front reaches the top of the droplet the second freezing stage is completed and the droplet is completely frozen. The final phase of the second freezing stage is shown in Fig. 9.2f.

Comparing the duration of the first and second freezing stage reveals that the duration of the second freezing stage is much longer than the first and is in the order of tens of milliseconds. Even if the droplet appears to have the same shape in the top view, the shape of the droplet is altered because of the volume expansion during freezing [236]. In side view the droplet has a cusp shape [236]. However, the contour of the deformations can be observed even in top view as presented and marked in Fig. 9.2f. In addition to the deformation of the droplet, entrapped air can be observed by bright regions inside the droplet (see Fig. 9.2f). The solubility of air in water is higher than in ice so that air bubbles are encapsulated during freezing [34] and subsequently entrapped in the ice. Even if the water was degassed prior to the experiments the water still contains resolved gasses.

Once all droplets of an ensemble are frozen and a temperature of about  $\vartheta \approx -45^\circ\text{C}$  is reached, the temperature is increased to cause thawing of the frozen droplets. A time series of the thawing stage is shown in Fig. 9.3. The temperature of the droplet has to be increased to be higher than the melting temperature. The start of the melting process is shown in Fig. 9.3a, which shows a completely frozen droplet. Heat is supplied from below so that melting is initiated at the substrate. As shown in Fig. 9.3b the first liquid water can be observed near the contact line and appears as a ring in top view. Note that even if the liquid water is only visible near the three-phase contact line the substrate might be complete or at least partially wetted by liquid water. A further increase of the temperature leads to a decreasing fraction of ice inside the droplet as shown in Figs. 9.3c-e. Due to the fact that the density of ice is lower than

## 9 Results using supercooled sessile droplets

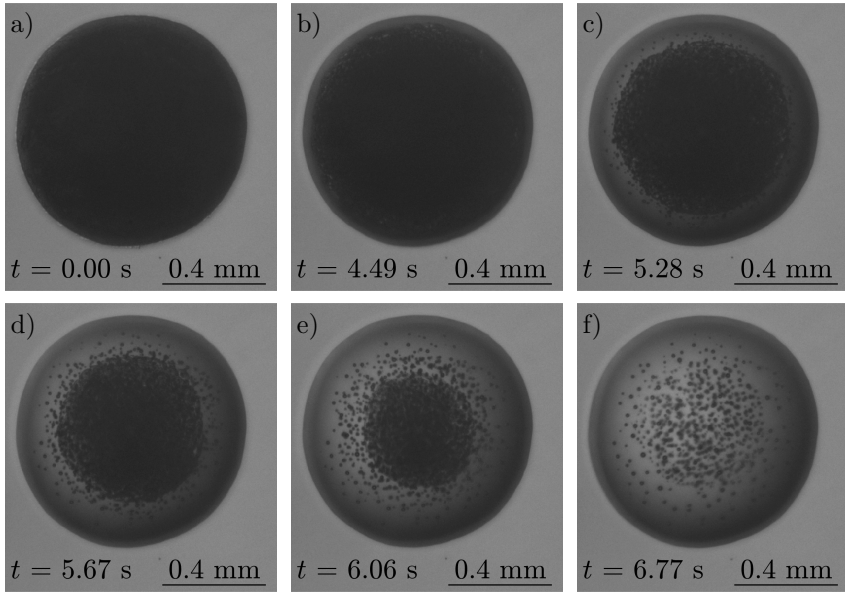


Figure 9.3: Melting of a completely frozen droplet. a) Start of the melting process ( $\vartheta = 0.09^\circ\text{C}$ ), b)-e) melting of the ice inside the droplet starting at the substrate and continually decreasing the fraction of ice while releasing entrapped air bubbles (Temperatures: b)  $\vartheta = 1.71^\circ\text{C}$ , c)  $\vartheta = 1.74^\circ\text{C}$ , d)  $\vartheta = 1.83^\circ\text{C}$ , e)  $\vartheta = 2.24^\circ\text{C}$ ), f) liquid droplet at a temperature of  $\vartheta = 2.47^\circ\text{C}$  with air bubbles.

the density of water the residual ice floats on top of a liquid layer and is in contact with the droplet interface. Figure 9.3e shows the floating ice residual inside the liquid. With increasing temperature the amount of ice decreases until the droplet is completely liquid again as shown in Fig. 9.3f. In this example the droplet is already liquid at a temperature of  $\vartheta = 2.47^\circ\text{C}$ . The thawing stage is completed as soon as the droplet is completely liquid. In comparison to the first and second freezing stage the thawing stage takes even longer and is in the order of several seconds.

During thawing, entrapped air bubbles in the ice are released, which are

### 9.1 Four stages of ice nucleation experiments

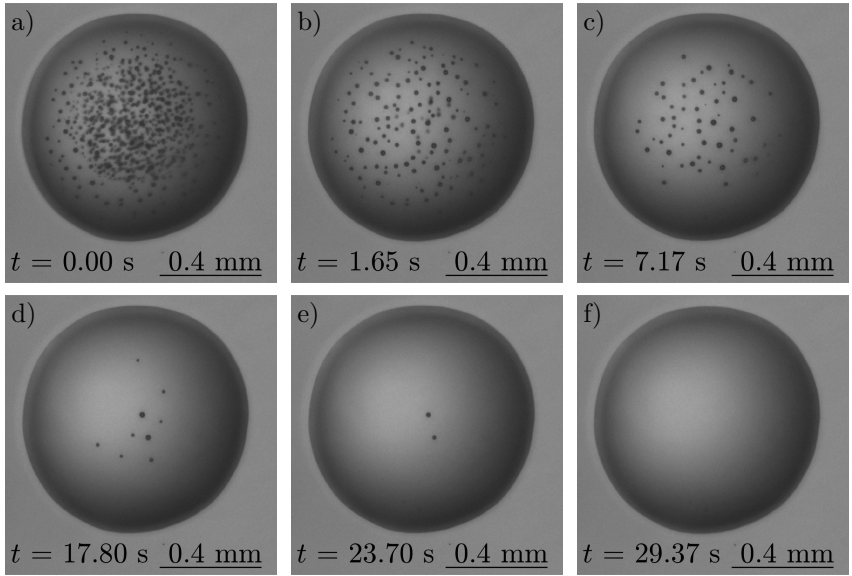


Figure 9.4: Time series of a droplet with entrapped air. a) Just melted droplet with entrapped bubbles at a temperature of  $\vartheta = 2.24\text{ }^{\circ}\text{C}$ , b)-e) dissolving of bubbles into the water, f) liquid droplet without air bubbles.

observable inside the liquid phase. The individual air bubbles are randomly distributed in the droplet as shown in Fig. 9.3f. In spite of the lower density of air bubbles compared to water, no movement of the air bubbles towards the interface is observable.

In the fourth and final stage air bubbles dissolve into the water, as shown in Fig. 9.4. While Fig. 9.4a shows the last phase of the previous stage (Fig. 9.3f), the Figs. 9.4b-f show the reduction and dissolving of the gas bubbles over time. The liquid water generated by melting of ice is undersaturated in terms of gas so that the air bubbles inside the liquid can dissolve. The driving force for this process is the gradient of dissolved gas. Each individual bubble becomes smaller with evolving time until it completely vanishes, as shown in Fig. 9.4f. The lifetime of the bubbles can be estimated by the Epstein-Plesset theory as  $t_{\text{life}} \approx R_{\text{bub}}\rho_{\text{air}}/(3Dc_{\text{air}})$

## 9 Results using supercooled sessile droplets

[60, 147], where  $R_{\text{bub}}$  is the radius of the bubble,  $\rho_{\text{air}}$  is the density of air,  $\mathcal{D}$  is the diffusion coefficient of air in water and  $c_{\text{air}}$  is the solubility of air in water. Assuming a bubble radius of  $R_{\text{bub}} \approx 5 \mu\text{m}$ , a density of  $\rho_{\text{air}} \approx 1.2 \text{ kg/m}^3$ , a diffusion coefficient of  $\mathcal{D} \approx 2 \cdot 10^{-9} \text{ m}^2/\text{s}$  [11] and a solubility of air in water of  $c_{\text{air}} \approx 3.7 \cdot 10^{-2} \text{ kg/m}^3$  at  $\vartheta = 0^\circ\text{C}$  [275] the lifetime yields  $t_{\text{life}} \approx 135 \text{ ms}$ . However, the timescale for the dissolving of the bubbles is in the order of tens of seconds up to several minutes, and thus takes much longer than the other stages. The discrepancy of the observed and the estimated lifetime is supported by Lohse and Zhang [147], who also reported significantly longer lifetimes for very small bubbles compared to the estimate lifetime  $t_{\text{life}}$ .

The final stage is completed as soon as all bubbles inside the liquid are vanished. As soon as the dissolving stage is completed, the droplet ensemble is ready for a new freezing and thawing cycle. However, to guarantee well-defined and repeatable conditions for each run the droplet ensemble is heated to a temperature of  $\vartheta = 14^\circ\text{C}$  and the temperature is held constant for 5 min before starting a new cycle. Thus, the influence of air bubbles present in the liquid on ice nucleation can be neglected and each run is performed under the same boundary conditions.

## 9.2 Constant electric fields

Even though several theoretical [118, 230] and experimental investigations [31, 47, 53, 197, 217, 222, 227, 277, 279] as well as molecular dynamics simulations [192, 287–289, 293] are performed to determine the influence of constant electric fields on ice nucleation, the outcome of the different investigations are rather contradictory. An overview of the different investigations and parameters reported in literature can be found in App. K. While some studies report a clear influence of the electric field on ice nucleation such as [197, 217, 277], other studies [53, 279] did not observe any effect of a constant electric field. The different outcomes might result from the different experimental setups and boundary conditions. Wilson et al. [279] assume that the effect of the electric field is very small, and thus might be masked by the stochastic nature of ice nucleation. This is one possible reason why several authors have not observed any influence of the electric field on ice nucleation. In addition, ice nucleation is very sensitive with respect to the boundary conditions, as for instance by the presence of contamination on the substrate or in the droplet. Con-

Table 9.2: Overview of tested parameters and their quantities to investigate the influence of constant electric fields on heterogeneous ice nucleation.

Parameter	Quantity
Mean droplet diameter $\bar{d}_d$ in mm	$1.1 \pm 0.19$
Electric field strength $E$ in kV/cm	0, . . . , 9.76
Cooling rate $\dot{T}$ in K/min	5

sequently, careful sample preparation is necessary to ensure well-defined boundary conditions to determine even small effects of the external electric fields and to be able to distinguish the effect of the electric field from the stochastic scattering of the data. A summary of the experimental conditions is shown in Table 9.2.

### 9.2.1 Impact of the electric field strength

The results of the experiments using constant electric fields are presented as droplet survival curves as shown in Fig. 9.5. Each survival curve comprises a minimum of four repetitions for the same conditions, which results in a minimum of 70 nucleation events for each survival curve. The typical 'S'-shape of the survival curves is preserved independent of the applied electric field strength, which is also an indicator for well-defined boundary conditions. Increasing the electric field strength slightly affects the nucleation temperature of the first nucleation event of the droplet ensemble. Only for the two highest electric field strength the nucleation temperature of the first freezing event is increased. In addition, for  $E = 9.76$  kV/cm a horizontal shift of the droplet survival curve in comparison to the survival curve without the influence of an electric field is recognizable. Nevertheless, for an electric field strength of  $E < 9.76$  kV/cm the electric field only slightly affects ice nucleation and no significant difference between the experiments with and without electric field can be recognized. In this case, the effect of the electric field might be masked by the stochastic nature of ice nucleation [279]. In contrast, an electric field strength of

## 9 Results using supercooled sessile droplets

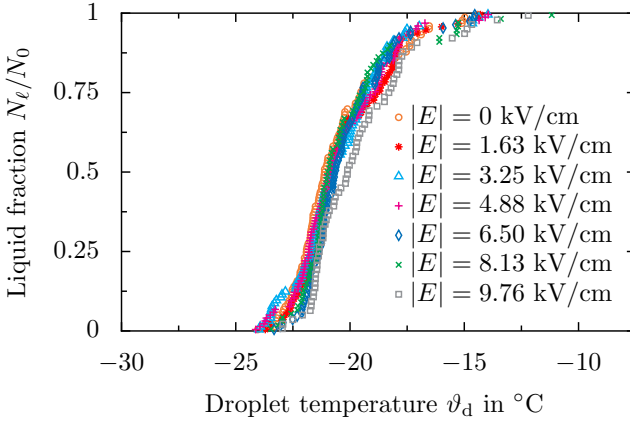


Figure 9.5: Droplet survival curves for varying electric field strength obtained with the same ensemble of droplets for all experiments. Ratio of current number of liquid droplets  $N_\ell$  to the initial number of liquid droplets  $N_0$ , depending on the ensemble temperature  $\vartheta_d$  and the electric field strength  $|E|$ . Republished (adapted) with permission of [154]; permission conveyed through Copyright Clearance Center, Inc..

$E = 9.76 \text{ kV/cm}$  results in a significant shift of the survival curves to higher temperatures.

The electric field influences all droplets of the ensemble in an almost constant manner, because shifting the nucleation curve to higher temperatures, leads to higher nucleation temperatures for all droplets. The theoretical model of Saban et al. [230] predicts such a constant influence of the electric field, which results from the reduction of the critical energy barrier for ice nucleation by the electric field. However, comparing the order of magnitude for the influence of the latent heat of fusion  $L_V \Delta T / T_m$  and the electric field  $E_0 \Psi$  reveals that  $L_V \Delta T / T_m \gg E_0 \Psi$  even for the highest electric field strength tested. The highest electric field strength of  $E = 9.76 \text{ kV/cm}$  leads to  $E_0^2 \Psi \approx 1.25 \text{ J/m}^3$  assuming a relative permittivity of  $\varepsilon_{r,s} \approx 3.2$  for ice (see App. I, [102]),  $\varepsilon_{r,\ell} = 81$  for water and  $\varepsilon_{r,\text{surr}} \approx 2.5$  for oil. In comparison, the term for the latent heat of fusion is given by  $L_V \Delta T / T_m \approx 1.2 \cdot 10^5 \Delta T \text{ J/(m}^3 \text{K)}$  (for  $L_V = 333.12 \cdot 10^6 \text{ J/m}^3$  [50]) and is always larger than  $E_0^2 \Psi$  for relevant supercoolings  $\Delta T$ .

It can be assumed that the critical energy barrier is slightly reduced by the electric field in comparison to the experiments without an electric field, but the model of Saban et al. [230] cannot completely describe the observed behaviour. One possible reason is that the model was developed for homogeneous ice nucleation, and thus does not take into account the possible interaction of the electric field and the substrate. Especially, the geometry and the dielectric properties of the substrate and the corresponding INPs significantly influence the local electric field strength, which might influence ice nucleation. In addition, the model of Saban et al. [230] does not take into account that the droplets have to be assumed as a perfect conductor for constant electric fields. Instead, the model only takes into account the ratio of the permittivities, which is not valid for the given boundary conditions. Hence, the underlying physics in the experiment might differ from the theory. However, to determine the exact reason further investigations and adaptations of the theoretical model are necessary.

The experimental data can be further analysed with respect to singu-

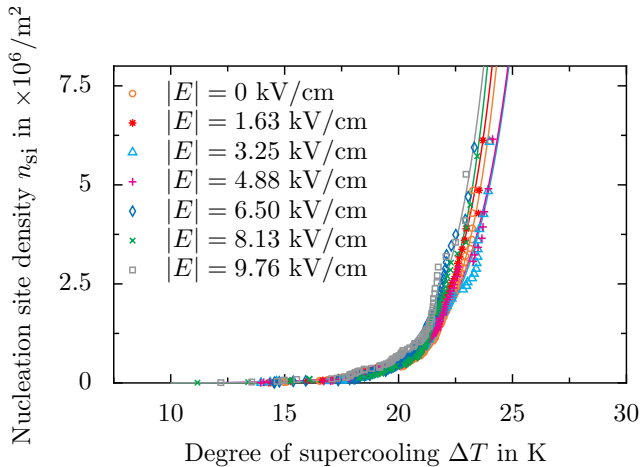


Figure 9.6: Nucleation site density  $n_{\text{si}}$  of corresponding data as a function of the degree of supercooling  $\Delta T$  depending on the electric field strength  $|E|$ . Republished (adapted) with permission of [154]; permission conveyed through Copyright Clearance Center, Inc..

## 9 Results using supercooled sessile droplets

lar nature of ice nucleation. For this purpose the nucleation site density  $n_{\text{si}}$  depending on the degree of supercooling  $\Delta T$  is shown in Fig. 9.6. The presented data corresponds to the data shown in Fig. 9.5. In addition, to the data points representing the individual nucleation events, the best fit of Eq. (3.33) for each electric field strength is shown as solid lines. As indicated by the good agreement, the experimental data can be described with the singular nucleation model with good accuracy. Generally, the nucleation site density increases exponentially with increasing degree of supercooling. Similar to the droplet survival curves, the electric field strength shifts the individual curves to lower degrees of supercooling. The higher the electric field strength, the higher is the nucleation site density for a fixed degree of supercooling. While the change is hardly observable for low electric field strengths, high electric field strengths significantly increase the nucleation site density compared to smaller electric field strengths or in absence of the electric field.

The impact of the electric field is even more obvious when analysing the characteristic temperatures  $\vartheta_i$ , where  $i$  corresponds to the liquid fraction defined as  $N_\ell/N_0 = i$ , depending on the electric field strength as shown in Fig. 9.7. Each temperature  $\vartheta_i$  corresponds to a specific liquid fraction, e.g.  $\vartheta_{0.25}$  corresponds to  $N_\ell/N_0 = 0.25$  and characterizes the nucleation temperature necessary to cause 25 % of the droplet ensemble to be already frozen at this temperature.

Analysing the dependence of the characteristic temperatures on the electric field strength reveals whether the electric field influences all droplets of one ensemble in the same manner or not. The characteristic temperatures derived from the experimental data are represented by symbols. For better visualization of the trend, the data points are connected by solid lines. As already seen for the droplet survival curves and the nucleation site density, the influence of the electric field is almost negligible for low electric field strength. For these low electric field strengths the characteristic temperature is almost constant. However, increasing the electric field strength leads to an increase of the characteristic temperatures. For the mean nucleation temperature  $\vartheta_{0.5}$  the maximum change between the highest electric field strength and the reference without electric field yields  $\Delta\vartheta_{0.5} \approx 1 \text{ K}$  and increases with an increasing liquid fraction. In spite of  $\vartheta_1$ , the increase of the characteristic temperature follows a linear trend. Comparing this temperature increase to the temperature variation between different repetitions without an electric field ( $\Delta\vartheta_{0.5} \approx 0.5 \text{ K}$ , an example is shown in Fig. 8.13) reveals that the change of the character-

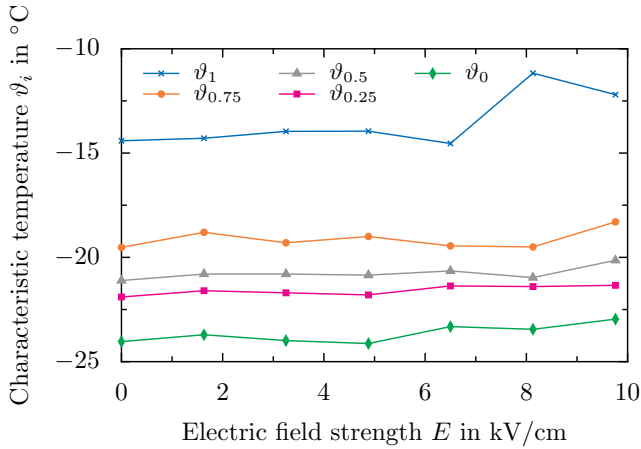


Figure 9.7: Characteristic temperatures  $\vartheta_i$  for the decay of a droplet ensemble depending on the electric field strength  $E$ . The present data corresponds to the experimental series already shown in Fig. 9.5. The temperature  $\vartheta_i$  of an ensemble represents the temperature, where  $N_\ell/N_0 = i$ .

istic temperatures is still significant and not masked by the stochastic nature of ice nucleation. However, the change is in the same order of magnitude as the accuracy of the temperature sensor ( $\Delta\vartheta_{0.5} = \pm 1$  K). Since, the electric field increases the temperature even more for high liquid fractions, an influence of a constant electric field on ice nucleation is still observable. For  $\vartheta_1$  the change of the nucleation temperature almost yields  $\Delta\vartheta_1 \approx 5$  K. The influence of a contamination in the droplet can be completely ruled out due to the fact that the same droplets are used for all experiments investigating a single parameter. Consequently, constant electric fields can affect ice nucleation depending on the electric field strength, even though the influence is very weak.

### 9.2.2 Singular behaviour of ice nucleation

The singular nature of the present experiments becomes even more obvious by comparing the nucleation temperature of each droplet for the different repetitions as shown in Figs. 9.8 and 9.9. Figure 9.8 shows the

## 9 Results using supercooled sessile droplets

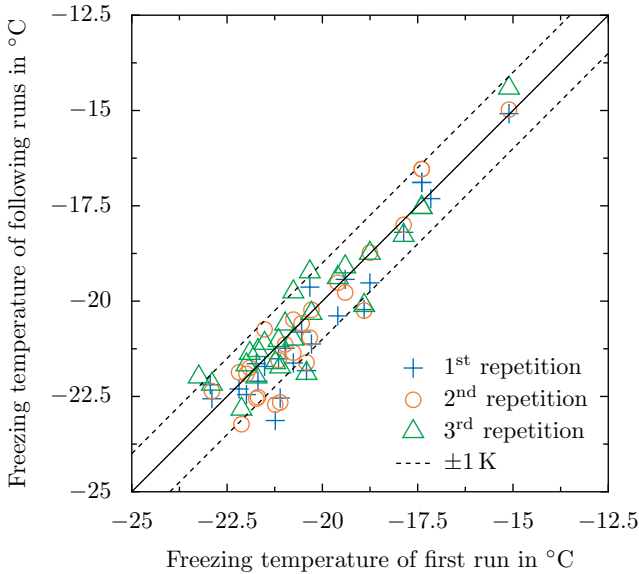


Figure 9.8: Variation of the nucleation temperature of the individual droplets of a typical droplet ensemble obtained with the electric field turned off. Nucleation temperature of a droplet measured in three further repetitions of the experiment shown as a function of the nucleation temperature obtained in the first experiment.

correlation of the nucleation temperature of the individual droplets in absence of an electric field. Thus, the general nucleation behaviour without the impact of an electric field can be analysed with respect to the singular nature of ice nucleation. Each symbol corresponds to a single nucleation event. The solid line shows the perfect correlation, i.e. identical nucleation temperatures for the first run and the following repetitions. As shown by the figure, the deviation from the solid line is rather small and yields  $\Delta T \approx 1$  K for most of the data points. Hence, the nucleation temperature of each droplet is almost constant and independent of the number of repetitions. The remaining variation of the data is caused by the stochastic nature of ice nucleation, which is still present. However, the nucleation temperature is mainly influenced by the most active nucleation site in contact with the droplet and its characteristic temperature. This

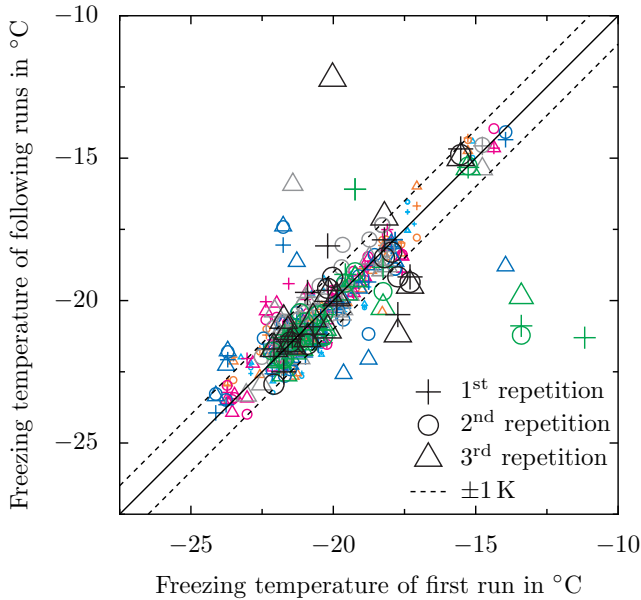


Figure 9.9: Variation of the nucleation temperature of the individual droplets of a typical droplet ensemble obtained with a constant electric field. Nucleation temperature of a droplet measured in three further repetitions of the experiment shown as a function of the nucleation temperature obtained in the first experiment. The plus signs indicate the first, the circles the second and the triangle the third repetitions. The colour and size of the individual symbols correspond to the electric field strength between  $E = 0$  kV/cm and  $E = 9.76$  kV/cm.

characteristic temperature is different for each droplet and ranges from about  $\vartheta_d \approx -15^\circ\text{C}$  to  $\vartheta_d \approx -22.5^\circ\text{C}$ . In general, the singular effect of ice nucleation is much more dominant compared to the stochastic effects involved in ice nucleation for droplets in absence of an electric field. To determine whether this effect is also observable when an electric field is applied, the nucleation temperatures obtained by the different repetitions have to be analysed for all electric field strength. The result is shown in Fig. 9.9. The nucleation temperature of each individual droplet observed in the repetitions of the experiments is compared to the first experiments

## 9 Results using supercooled sessile droplets

performed with the same boundary conditions, i.e. the same electric field strength. Each symbol corresponds to a single nucleation event. The size of the symbols correspond to the electric field strength, the larger the symbol the larger is the electric field strength applied during the experiment. Again, the solid line represents the perfect correlation. In comparison to Fig. 9.8, the data shown in Fig. 9.9 exhibits larger scatter. However, most of the symbols are located close to the perfect correlation. Generally, the scatter of the data is still lower than  $\Delta T = 1$  K, but individual droplets have significantly different nucleation temperatures compared to the previous runs. These droplets are clearly affected by the presence of the electric field, which is indicated by large deviations from the perfect correlation. The assumption of a singular nucleation behaviour is generally valid for the present data, revealing an almost constant nucleation temperature for each droplet. However, both the singular and the stochastic nature of ice nucleation can be observed in the present data.

### 9.2.3 Droplet hydrodynamics in electric fields

Besides ice nucleation, the hydrodynamic behaviour of the droplets is influenced by the electric field. Even though the force generated by the electric field is constant, droplet oscillations can be observed for high electric field strengths like  $E = 9.76$  kV/cm. An exemplary visualization of the droplet deformation is shown in Fig. 9.10. The figure shows the shape of the droplet in absence of an electric field (Fig. 9.10a) and the conical deformation of the droplet as well as the increasing size of the released satellite droplets nearby the droplet (Figs. 9.10b-c). Under the influence of high electric field strengths the formation of a sharp cone can be observed, which is accompanied by the release of small satellite droplets. The developed cone is called Taylor cone [259] and is well-known by other applications such as electro-spinning. Theoretically the Taylor cone is characterized by a half angle of  $49.3^\circ$ , which is in good agreement with the measured half-angle of approximately  $48.5^\circ$  and  $50^\circ$  on the left and right side (in Fig. 9.10c), respectively.

The general physical mechanism of the formation of a Taylor cone is already widely investigated and is mainly caused by stresses on the interface of the droplet [41, 42, 136, 259]. The formation and the accompanied release of small satellite droplets are repeatably observed. As soon as the presumably charged satellite droplets [41] are released, the primary

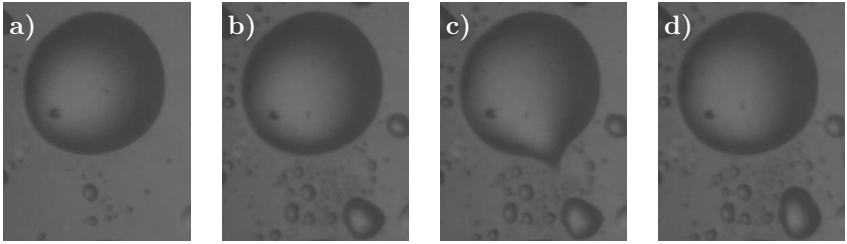


Figure 9.10: Formation of a Taylor cone during the experiments with constant electric field ( $E = 9.76 \text{ kV/cm}$ ). a) Droplet in absence of an electric field, b) Primary droplet and satellite droplets after applying the electric field, c) Formation of a Taylor cone and d) increased size of satellite droplet nearby the primary droplet. Republished (adapted) with permission of [154]; permission conveyed through Copyright Clearance Center, Inc..

droplet adopts a more hemispherical shape again. The repeated formation of a Taylor cone and deformation of the droplets leads to an oscillation of the droplet, which can be observed during the experiment.

The ejected satellite droplets reside in the space between the individual droplets. Consequently, the volume of the droplet decreases with an increasing number of experiments. However, the size of the droplets is continuously controlled during the analysis and individual droplets are sorted out if the size is too small. Note that droplets which are highly deformed are not taken into account during the analysis, because the macroscopic motion of the droplet might also affect ice nucleation. The oscillation of the droplet might result in a shear flow inside the droplet which possibly impact ice nucleation [22, 224]. Also, the release of small droplets impact ice nucleation because large changes of the volume causes a change of the wetted surface area, and thus leads to a decreasing freezing probability. Nevertheless, the change of the volume is very small in the present experiments so that the influence of the changed volume is negligible.

## 9.2.4 Conclusions

Constant electric fields can influence ice nucleation depending on the electric field strength. While low electric field strengths  $E < 9.76$  kV/cm are identified to have an almost negligible influence on ice nucleation, an electric field strength of  $E = 9.76$  kV/cm can promote ice nucleation. Generally, the nucleation temperatures are increased for increasing electric field strengths, and thus the electric field promotes ice nucleation. The characteristic freezing temperatures are used to determine the increase of the nucleation temperatures and revealed a difference of several degrees depending on the specific liquid fractions. In addition, the nucleation behaviour of the droplets was identified to be predominately of singular nature rather than stochastic. However, both the singular and the stochastic behaviour of ice nucleation can be observed by the present data. In addition to the influence of the electric field on ice nucleation, the electric field also affects the hydrodynamics of the droplets. For large electric field strengths the formation of a Taylor cone can be observed, which is accompanied by the formation of presumably charged satellite droplets. The periodical formation of the Taylor cone results in droplet oscillations even for a constant electric field, which might also influence ice nucleation.

Hence, constant electric fields and the resulting motion of the droplet can promote ice nucleation.

## 9.3 Alternating electric fields

The influence of constant electric fields has been extensively investigated in the past and resulted in controversial results. In the previous section, it was shown that a constant electric field can have an influence on ice nucleation. In addition to constant electric fields, alternating electric fields are commonly used in applications such as conventional power distribution and transmission [109]. Several experimental investigations have already been performed to determine the influence of alternating electric fields on ice nucleation [127, 165, 232, 247, 251, 286]. An overview of the different experimental parameters can be found in App. K. Even though many investigations were already performed, only a few investigations have been conducted with pure water. Primarily, the different investigations focus on various different liquids and solutions. In addition, all

experiments are associated with different boundary conditions, such as the applied electric field strength, frequency of the electric field, degree of supercooling, physical mechanism of ice nucleation (homogeneous or heterogeneous ice nucleation) or the use of different liquids. The summary of the experimental parameters shown in App. K reveals that most of the investigations are performed for frequencies  $f > 1 \cdot 10^3$  Hz, which are significantly higher than the relevant frequencies for power transmission and distribution (50 Hz for the European power transmission and distribution [109]). Consequently, there is a lack of knowledge of the impact of electric fields with low frequencies on ice nucleation. This influence is subsequently investigated with respect to the electric field strength, the electric history of the droplets, the frequency of the applied electric field, the singular nature of the electric field and the temperature. The experimental parameters for the present experiments are summarized in Table 9.3. The experiments are performed under well-defined boundary conditions with respect to the electric field and the temperature. Each individual influencing parameter, as for instance the electric field strength or the frequency of the electric field, is investigated with the same droplet ensemble to rule out any influence of the droplet contamination on the outcome of the experiments. Each combination of electric field strength and frequency is repeated at least three times, which generally results in a minimum of 78 nucleation events for each boundary condition. Only a single set of repetitions, namely the reference ( $\hat{E} = 0$  kV/cm) for a decreasing field strength has a decreased number of droplets (55 droplets).

Table 9.3: Overview of tested parameters and their quantities to investigate the influence of alternating electric fields on heterogeneous ice nucleation.

Parameter	Quantity
Mean droplet diameter $\bar{d}_d$ in mm	0.95, ..., 1.09
Electric field strength $\hat{E}$ in kV/cm	0, ..., 7.16
Frequency $f$ in Hz	10, ..., 110
Cooling rate $\dot{T}$ in K/min	5

## 9 Results using supercooled sessile droplets

The reduced number results from the disintegration of individual droplets and an accompanied size reduction of the droplets. Hence, the droplet size is significantly changed so that some droplets are sorted out during the analysis to ensure a constant droplet size. All experiments were performed with a constant cooling rate of  $\dot{T} = 5 \text{ K/min}$ .

### 9.3.1 Influence of the electric field strength

The droplet ensemble with a mean size of  $\bar{d}_d = 1.04 \text{ mm}$  is exposed to an electric field with a constant frequency of  $f = 50 \text{ Hz}$  and variable electric field strength. The electric field strength is increased step-wise after a minimum of three repetitions at the same electric field strength. Prior to the runs with increasing electric field strength, the reference experiment without an electric field is performed.

The results of the experiments are shown in Fig. 9.11, where the change in nucleation temperature for each droplet  $\Delta\vartheta_{\text{nuc}}$  depending on the electric field strength  $\hat{E}$  is illustrated. The change of the nucleation temperature is defined as the difference between the nucleation temperature with and without an electric field  $\Delta\vartheta = \vartheta_{\text{nuc}}|_{\hat{E}>0} - \vartheta_{\text{nuc}}|_{\hat{E}=0}$ . The reference temperature  $\vartheta_{\text{nuc}}|_{\hat{E}=0}$  indicated by the dashed line is determined by the mean freezing temperature of all three repetitions in absence of the electric field. In contrast, the data for  $\hat{E} > 0$  is not averaged and each nucleation event is represented as a single symbol. Due to the fact that the experiments are repeated at least three times, each individual droplet corresponds to three symbols for constant conditions. The repetitions of the experiments are performed to increase the number of nucleation events which results in an increased statistical significance of the data.

As shown in Fig. 9.11 the nucleation temperatures vary even in the absence of the electric field. The variation of the nucleation temperature results from the stochastic nature of ice nucleation and the different nucleation temperatures for each droplet. For an electric field strength  $\hat{E} \leq 2.86 \text{ kV/cm}$  the change of the nucleation temperature  $\Delta\vartheta_{\text{nuc}}$  is almost constant. The maximum variation is  $\Delta\vartheta_{\text{nuc}} = \pm 4.55 \text{ K}$ , which is indicated by the dotted lines in Fig. 9.11. The grey area visualizes the change of the behaviour. For low electric field strengths no significant influence of the electric field on ice nucleation can be observed. Even if the electric field has an impact on ice nucleation for such small electric field strength, the influence is masked by the stochastic nature of ice nucleation.

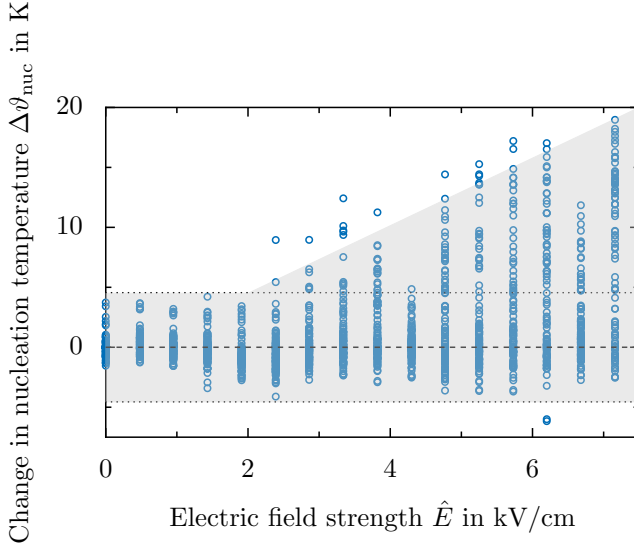


Figure 9.11: Change of the nucleation temperature due to the electric field  $\hat{E}$ ,  $\Delta\vartheta_{\text{nuc}} = \vartheta_{\text{nuc}}|_{\hat{E}>0} - \vartheta_{\text{nuc}}|_{\hat{E}=0}$ , shown for all droplets in the present experiments.  $\vartheta_{\text{nuc}}|_{\hat{E}>0}$  and  $\vartheta_{\text{nuc}}|_{\hat{E}=0}$  denote the nucleation temperature of a droplet observed with and without an electric field. The horizontal dotted lines illustrate the temperature band of  $\pm 4.55$  K around 0 K, which corresponds to the maximum deviation of the droplet nucleation temperature for low electric field strength. Reprinted figure (adapted) with permission from [158]. Copyright 2021 by the American Physical Society.

In contrast, increasing the electric field strength leads to significant changes of the nucleation temperature. Generally, the nucleation temperature is increased  $\Delta\vartheta_{\text{nuc}} > 0$  for increasing electric field strength. As a consequence, ice nucleation is observed at higher temperatures for specific droplets. The maximum increase of the nucleation temperature is observed for an electric field strength of  $\hat{E} = 7.16$  kV/cm and is  $\Delta\vartheta_{\text{nuc}} \approx 20$  K. While the upper limit of the change in nucleation temperature increases for an increasing electric field strength, the lower limit is almost constant for the entire range of electric field strengths. Thus,

## 9 Results using supercooled sessile droplets

the electric field does not decrease the nucleation temperature of the individual droplets ( $\Delta\vartheta_{\text{nuc}} < 0$ ).

Due to the stochastic nature of the ice nucleation, the significance of a droplet-wise analysis is limited. In fact, numerous nucleation events are necessary to quantify the effect of the electric field. The large number of experiments presented in Fig. 9.11 clearly reveals that ice nucleation is promoted by an alternating electric field depending on the electric field strength. The higher the electric field strength, the larger is the increase in nucleation temperature.

A droplet-wise analysis of the data has a limited significance, which can be increased by an ensemble-wise analysis. Instead of comparing the nucleation temperature of each individual droplet to the reference temperature of the individual droplet in absence of the electric field, the general behaviour of the ensemble is investigated using the droplet survival curves. The droplet survival curves depend on the electric field strength as shown in Fig. 9.12a. As already shown in Fig. 9.11, low electric field strengths  $\hat{E} \leq 2.86 \text{ kV/cm}$  do not affect the ice nucleation behaviour of the droplets. The nucleation curves, represented by the typical 'S'-shaped trend, are virtually not affected and almost identical. A very small and negligible variance is observable, which results from the stochastic nature of ice nucleation. Hence, for low electric field strengths the result of the ensemble- and droplet-wise analysis is the same.

Increasing the electric field strength  $\hat{E} > 2.86 \text{ kV/cm}$  leads to a more significant impact of the electric field on ice nucleation. The effect of the electric field turns out to be twofold. First, the shape of the survival curves is significantly altered from the typical 'S'-shape and second, the temperature range  $|\vartheta_0 - \vartheta_1|$ , where  $\vartheta_0$  and  $\vartheta_1$  correspond to a liquid fraction of  $N_\ell/N_0 = 0$  and  $N_\ell/N_0 = 1$ , significantly increases. While the lowest temperature  $\vartheta_0$  is almost unaffected by the electric field, the temperature  $\vartheta_1$  increases for an increasing electric field strength. Hence, ice nucleation inside the individual droplets is observed at higher temperatures, so that the electric field promotes ice nucleation.

The corresponding nucleation site density, defined by Eq. (3.35), is shown in Fig. 9.12b and describes the number of active nucleation sites per unit area for a specific temperature. The nucleation site density directly correlates with the droplet freezing rate. The higher the number of active nucleation sites, the higher is the droplet freezing rate. A decreasing temperature, i.e. increasing degree of supercooling, leads to an increasing

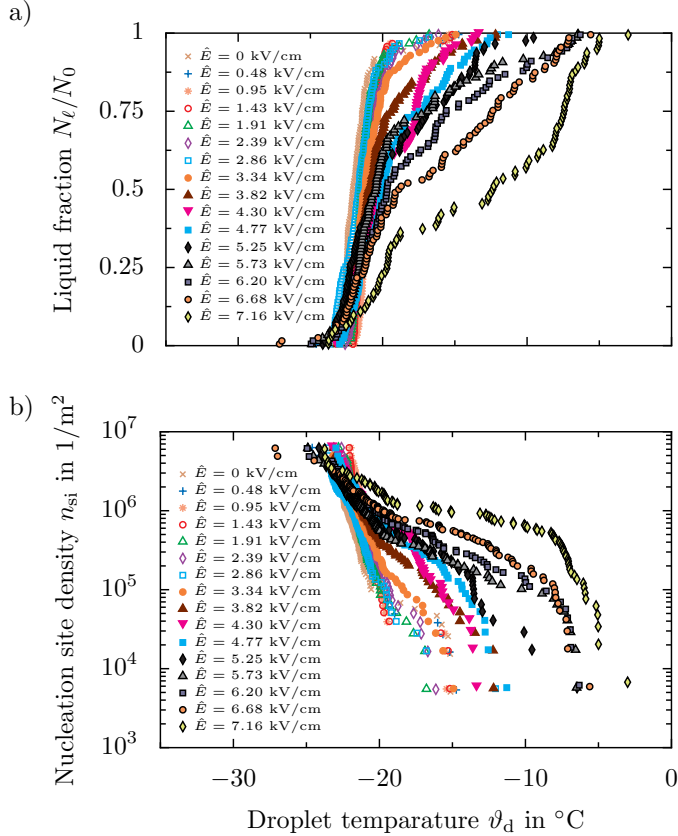


Figure 9.12: a) Droplet survival curves for varying electric field strength obtained with the same ensemble of droplets for all experiments. Ratio of current number of liquid droplets  $N_\ell$  to the initial number of liquid droplets  $N_0$ , depending on the ensemble temperature  $\vartheta_d$ . b) Nucleation site density  $n_{si}$  of corresponding data as a function of droplet temperature  $\vartheta_d$ . The electric field strength  $\hat{E}$  is gradually increased after each experimental run, starting with  $\hat{E} = 0$ . The frequency of the electric field is  $f = 50$  Hz and the mean diameter of the droplets amounts  $\bar{d}_d = 1.04$  mm. Reprinted figure (adapted) with permission from [158]. Copyright 2021 by the American Physical Society.

## 9 Results using supercooled sessile droplets

nucleation site density. Similar to the droplet survival curves, the trend of the nucleation site density is not affected by the electric field for low electric field strengths ( $\hat{E} < 3.34 \text{ kV/cm}$ ). On a logarithmic scaled ordinate, the data points follow a constant slope which is almost independent of the electric field strength in this range ( $\hat{E} < 3.34 \text{ kV/cm}$ ). Such a constant slope characterizes a stochastic nucleation behaviour [193]. For the given droplet size, i.e. the given wetted area, the maximum nucleation site density yields  $n_{\text{si}} \approx 6 \cdot 10^6 \text{ m}^{-2}$ . Note that the maximum and minimum nucleation site density also depends on the liquid fraction  $N_\ell/N_0$  and its resolution, which is defined by the number of droplets analysed. The lower the temperature of the droplet  $\vartheta_d$ , the smaller is the impact of the electric field on the nucleation site density. For low temperatures ( $\vartheta_d \leq -22^\circ\text{C}$ ) the influence of the temperature is more dominant than the impact of the electric field, resulting in an almost constant nucleation site density for low temperatures independent of the applied electric field strength.

As indicated by the shape of the droplet survival curves, the electric field has a much larger impact on ice nucleation at higher temperatures  $\vartheta_d > -20^\circ\text{C}$ . The higher the electric field strength, the lower is the degree of supercooling necessary to yield a nucleation site density of  $n_{\text{si}} \approx 5 \cdot 10^3 \text{ m}^{-2}$ , which is the lowest nucleation site density for the given wetted area and resolution of the liquid fraction for the given data. In contrast to low electric field strengths ( $\hat{E} < 3.34 \text{ kV/cm}$ ), the trend of the nucleation site density is clearly affected by high electric field strengths. Instead of a constant gradient (on a logarithmic scaled ordinate), the gradient decreases with increasing degree of supercooling. Initially, the nucleation site density for large electric field strengths increases rapidly and is significantly decreased for temperatures  $\vartheta_d < -10^\circ\text{C}$ . The higher the electric field strength, the higher is the initial increase of the nucleation site density. According to Niedermeier et al. [193] a changed slope indicates the transition of pure stochastic to a more singular nucleation behaviour. Hence, the twofold influence observed by analysing the droplet survival curves is also observable for the nucleation site density.

The electric field strength significantly impacts the behaviour of individual droplets and promotes ice nucleation. High electric field strength forces individual droplets to freeze earlier, while low electric fields have no effect on ice nucleation. Besides the boundary conditions such as the droplet size, ice nucleation is clearly affected by two main factors, namely the temperature and the electric field strength.

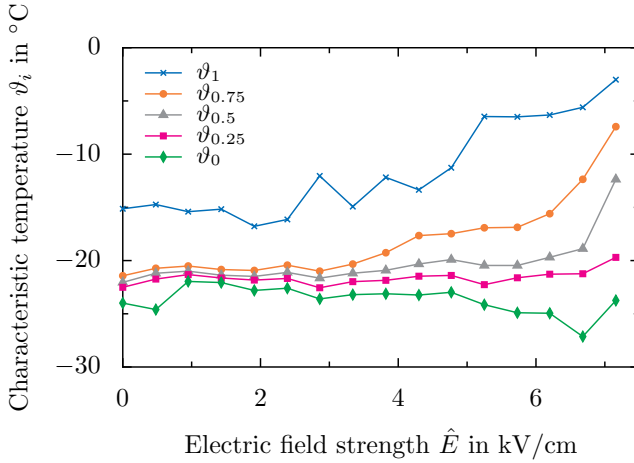


Figure 9.13: Characteristic temperatures  $\vartheta_i$  for the decay of a droplet ensemble depending on the electric field strength  $\hat{E}$ . The present data corresponds to the experimental series already shown in Fig. 9.12. The temperature  $\vartheta_i$  of an ensemble represents the temperature, where  $N_\ell/N_0 = i$ . Reprinted figure (adapted) with permission from [158]. Copyright 2021 by the American Physical Society.

To quantify the impact of the electric field and the forced freezing at higher temperatures, the characteristic temperatures  $\vartheta_i$  are analysed. The characteristic temperatures  $\vartheta_i$  correspond to a liquid ratio of  $N_\ell/N_0 = i$  and can be determined depending on the electric field strength as shown in Fig. 9.13. As indicated by the data, the lowest freezing temperature  $\vartheta_0$  is almost constant ( $\vartheta_0 \approx -24^\circ\text{C}$ ) and does not depend on the electric field strength. In contrast, the temperature of the first nucleation event  $\vartheta_1$  is significantly affected by the electric field. An increasing electric field strength leads to higher nucleation temperatures. While the first droplet nucleates at a temperature of  $\vartheta_1 \approx -15^\circ\text{C}$  in absence of an electric field, the first nucleation event is observed at a temperature of  $\vartheta_1 \approx -3^\circ\text{C}$  for an electric field strength of  $\hat{E} = 7.16\text{ kV/cm}$ . All characteristic temperatures  $\vartheta_i$  with  $0.25 < i \leq 1$  increase with increasing electric field strength.

The largest change of the nucleation temperature is always observed for an electric field strength of  $\hat{E} = 7.16\text{ kV/cm}$ . However, the trend is not

## 9 Results using supercooled sessile droplets

observable for  $i < 0.25$ . Especially, for  $\vartheta_0$  and  $\vartheta_{0.25}$  the change of the temperature depending on the electric field strength is negligibly small and only slightly increases in case of  $\vartheta_{0.25}$ , but slightly decreases for  $\vartheta_0$ . The number of droplets affected by the electric field increases with increasing electric field strength, which is indicated by the characteristic nucleation temperatures. The mean nucleation temperature  $\vartheta_{0.5}$  is affected for  $\hat{E} \geq 6.5$  kV/cm, the temperature  $\vartheta_{0.75}$  is already influenced for  $\hat{E} \geq 3.82$  kV/cm and  $\vartheta_1$  increases already for  $\hat{E} \geq 2.86$  kV/cm. Consequently, the effect of the electric field increases with increasing electric field strength. Furthermore, for a constant electric field strength, the influence of the electric field on  $\vartheta_i$  increases with increasing  $i$ .

### 9.3.2 Time effects regarding the electric field strength

Using the same set of droplets for all experiments (to investigate the influence of one parameter) rules out any influence of the contamination of the individual droplets. However, each droplet is exposed to various electric field strengths. An alternating electric field leads to an oscillation of the droplet at which the amplitude is mainly influenced by the electric field strength. A continuously increasing electric field strength affects the droplets not only by a decreasing droplet volume caused by the oscillation and the release of tiny droplets, but also affects the droplets with respect to the electric history of the droplets. To investigate whether the impact of the electric field is caused by the continuous increasing electric field strength or is independent of the electric history of the droplets, the experiments presented in the previous subsection are repeated. The experiments are performed with an inverse order compared to Subsec. 9.3.1, starting with an electric field strength of  $\hat{E} = 6.68$  kV/cm, which is then step-wise decreased. Hence, it can be determined if the exposure of an electric field strength on the droplets affects subsequent runs with respect to the number of droplets freezing or the range of nucleation temperatures.

For these experiments a fresh ensemble with a mean droplet diameter of  $\bar{d}_d = 1.09$  mm is used. In addition, the experiments can be used to determine the sensitivity of the experimental outcome with respect to the use of a fresh droplet ensemble, i.e. a changed INP spectrum of the droplets. The comparison of experimental results of Subsec. 9.3.1 and the experimental data obtained by decreasing the electric field strength are shown in Fig. 9.14. The data is presented as droplet survival curves.

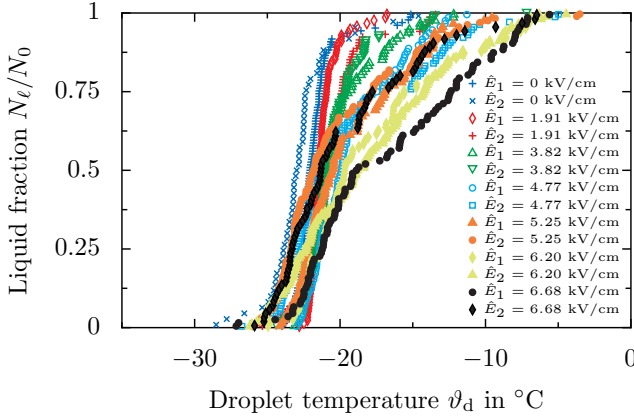


Figure 9.14: Droplet survival curves for two different sets of droplets serving to examine the influence of previous exposure to electric field strength  $\hat{E}$  on ice nucleation. The index of  $\hat{E}$  designates the droplet set. Data with index 1 was obtained by starting with a low electric field strength, which was then continuously raised. The data with index 2 started with the highest electric field strength, which was then step-wise lowered. The frequency of the electric field was kept constant at  $f = 50$  Hz. Reprinted figure (adapted) with permission from [158]. Copyright 2021 by the American Physical Society.

Similar to the experiments with increasing electric field strength, each of the present experiments is repeated at least three times with constant boundary conditions and afterwards the electric field strength is lowered. The different repetitions are used to generate a larger number of nucleation events to increase the statistical significance of the data. The experiments are still performed for a constant frequency of  $f = 50$  Hz. The index  $i$  of  $\hat{E}_i$  indicates the different sets and the boundary conditions. The index  $i = 1$  is used for a set exposed to a continuously increasing electric field strength and index  $i = 2$  indicates the set which is initially exposed to the highest electric field strength, which is subsequently lowered.

The corresponding runs which are exposed to the same electric field strength are coloured identically in Fig. 9.14. As shown in the figure, the agreement among the different experiments is very high. Especially,

## 9 Results using supercooled sessile droplets

for low electric field strengths the data coincide almost perfectly. Note that slight variations of the different experiments are unavoidable and result from the stochastic nature of ice nucleation as well as the changed set of droplets, i.e. different nucleation sites inside the droplets and slightly different droplet volumes. Only for an electric field strength of  $\hat{E} = 6.68 \text{ kV/cm}$  a larger deviation between the droplet survival curves is observable. However, the trend is still the same and the survival curves representing the experiments with decreasing electric field strength is shifted to lower temperatures. In this case the effect of an increasing electric field strength is higher than for the decreasing electric field. For the decreasing electric field strength the impact of an electric field with  $\hat{E} = 6.2 \text{ kV/cm}$  is higher than for  $\hat{E} = 6.68 \text{ kV/cm}$ , which is an unusual behaviour compared to the other electric field strengths and leads to the deviation between both sets. Generally, both experiments show the same impact of the electric field on ice nucleation. Increasing the electric field strength increases the influence of the electric field on ice nucleation. In addition, the higher the electric field strength, the more droplets are affected by the electric field.

The presence of the electric field evokes an earlier freezing of individual droplets, which is shown by the changed slopes of the droplet survival curves. Consequently, the electric history of the droplets in terms of previous applied electric field strength does not have an impact on ice nucleation during subsequent runs. The experimental results are highly reproducible even with a changed droplet ensemble under different conditions. Hence, the impact of a changed droplet ensemble, i.e. changed nucleation sites inside the droplets and a slightly varying droplet diameter, have an almost negligible influence on ice nucleation. Especially for high electric field strength and moderate droplet temperatures  $\vartheta_d > -20 \text{ }^\circ\text{C}$ , electric fields have a larger influence on ice nucleation compared to the temperature.

The nucleation behaviour of a droplet ensemble previously exposed to an electric field with various different field strengths is almost the same as for an ensemble of freshly generated droplets. Only slight variations are observable for an electric field strength of  $\hat{E} = 6.68 \text{ kV/cm}$ , which are rather insignificant and do not disprove the general behaviour. Note that even if previously applied electric field strengths do not have a direct influence on ice nucleation, ice nucleation might be indirectly affected by the disintegration of the droplet or a continuous release of tiny droplet caused by the droplet oscillations under the impact of high electric fields. However, the

effect seems to be negligible because of the very good agreement among the droplet survival curves of the different experimental sets.

Due to the fact that previously applied electric fields do not have a direct impact on ice nucleation leads to the result that the electric fields only influence ice nucleation on a small timescale. As a consequence, ice nucleation is only determined by the boundary conditions, mainly the degree of supercooling and the electric field strength present at the moment of ice nucleation. While large electric field strengths can promote ice nucleation at moderate temperatures ( $\vartheta_d > -20^\circ\text{C}$ ), ice nucleation at temperatures lower than  $\vartheta_d < -20^\circ\text{C}$  are almost not affected by the electric field independent of the electric field strength. The outcome of the experiments is independent of the number of repetitions, i.e. freezing and thawing cycles or higher electric field strengths previously exposed to the droplets. A similar time-dependent behaviour of ice nucleation with respect to the singular and stochastic nature of ice nucleation was already observed by Niedermeier et al. [193], who mentioned that the observed behaviour is affected by the considered timescale. Consequently, the considered timescale is important in the analysis of ice nucleation experiments. As a result of the electric field influencing ice nucleation on rather small timescales, probably in the order of the timescale of ice nucleation itself, external influences like charge accumulation or a previously applied electric field, have a rather insignificant influence on the experimental results. Especially, charge accumulation is associated with a significantly longer timescale compared to ice nucleation. The amount of charges is always conserved, and thus electric charges can only be transferred from the substrate or through the oil to the droplet. Assuming an almost perfectly clean sapphire substrate, the surface charge on the substrate is almost negligible. Hence, the charges can only originate from the oil or charge injected to the oil. The charge relaxation time of silicone oil  $\tau_{\text{oil}} \approx 2.3 \cdot 10^3 \text{ s}$  is much larger than the characteristic timescale of ice nucleation so that the influence is negligible.

These results are also supported by analysing the characteristic temperatures  $\vartheta_i$  of the experiments with decreasing electric field strengths, as shown in Fig. 9.15. Comparing the results to the characteristic temperatures shown in Fig. 9.13 reveals that the lowest nucleation temperature  $\vartheta_0$  is lower for an ensemble exposed to decreasing electric field strength compared to increasing electric field strength. However, in principle the tendency is the same. An increasing electric field strength leads to increasing characteristic temperatures. The characteristic temperatures correspond-

## 9 Results using supercooled sessile droplets

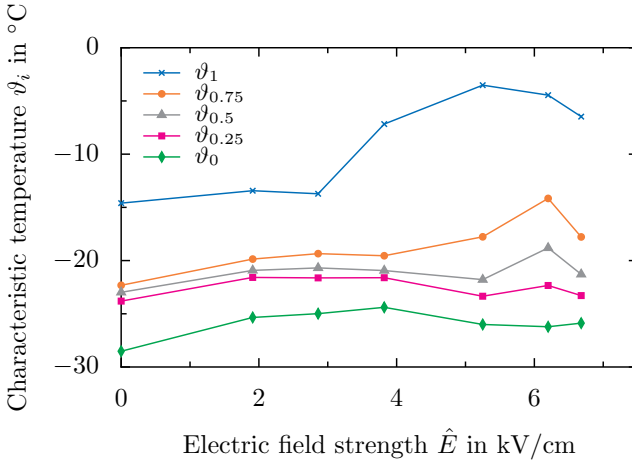


Figure 9.15: Characteristic temperatures  $\vartheta_i$  for the decay of a droplet ensemble depending on the electric field strength  $\hat{E}$ . The ensemble is initially exposed to the highest electric field strength, which is then continuously lowered after a minimum of three repetitions. The data corresponds to the experimental series already shown in Fig. 9.14. The temperature  $\vartheta_i$  of an ensemble represents the temperature, where  $N_\ell/N_0 = i$ . Reprinted figure (adapted) with permission from [158]. Copyright 2021 by the American Physical Society.

ing to higher liquid fractions  $i > 0.5$  are generally more affected by the electric field than the characteristic temperatures of lower liquid fractions. The higher the liquid fraction, the lower is the electric field strength necessary to affect the characteristic temperature. The most significant difference between the experiments with increasing and decreasing electric field strengths is observable for the high electric field strengths. While the characteristic temperature continuously increases with increasing electric field strength, a continuously decreasing electric field strength causes decreasing characteristic temperatures for the highest electric field strength, as already seen for the droplet survival curves, and corresponds to the shifted survival curves.

### 9.3.3 Singular ice nucleation

The analysis of the data presented in the previous subsection only takes into account the stochastic nature of ice nucleation, even though it is well known that ice nucleation can have a singular behaviour with respect to the temperature. Both the stochastic and the singular nucleation behaviour are present in all nucleation experiments but might be masked by the boundary conditions, such as the observed timescale [193, 266]. Hence, the experimental data has to be analysed in more detail to investigate whether the influence of the temperature and/or the influence of the electric field has a singular impact on ice nucleation. A singular nucleation behaviour is associated with the presence of nucleation sites in the droplet, so that nucleation is triggered by the most active nucleation site becoming active the earliest at a characteristic temperature [216]. Thus, each nucleation event is characterized by a droplet specific temperature, so that the nucleation of the droplet mainly depends on the temperature rather than time. During the experiments the same droplet ensemble performs several freezing and thawing cycles. According to the singular nucleation model, the nucleation temperature of each droplet should be reproducible, almost constant and independent of the number of repetitions. The active nucleation site originates from the water or substrate not being perfectly clean and summarized under the term INP.

The careful sample preparation aims to minimize these external influences and to prevent a contamination of the substrate and the droplets. However, the influence of contamination inside the water or on the substrate cannot be completely eliminated. Each droplet of an ensemble has a specific INP spectrum [266], which is assumed to be the same, even though the INP spectrum of individual droplets generated from the same bulk can differ [267]. This assumption is mainly supported by the high repeatability of the 'S'-shaped droplet survival curves, indicating a carefully controlled experiment and an almost identical INP spectrum for all droplets.

To further investigate the presumably singular nucleation behaviour of the data, Fig. 9.16 shows the nucleation temperature of the individual droplets of one ensemble depending on the different repetitions in absence of an electric field. Using the nucleation temperature of each individual droplet  $\vartheta_{\text{nuc}}$  observed in the first run as a reference and comparing the nucleation temperature of the individual droplets in the subsequent runs, reveals whether the nucleation temperature of each individual droplet of

## 9 Results using supercooled sessile droplets

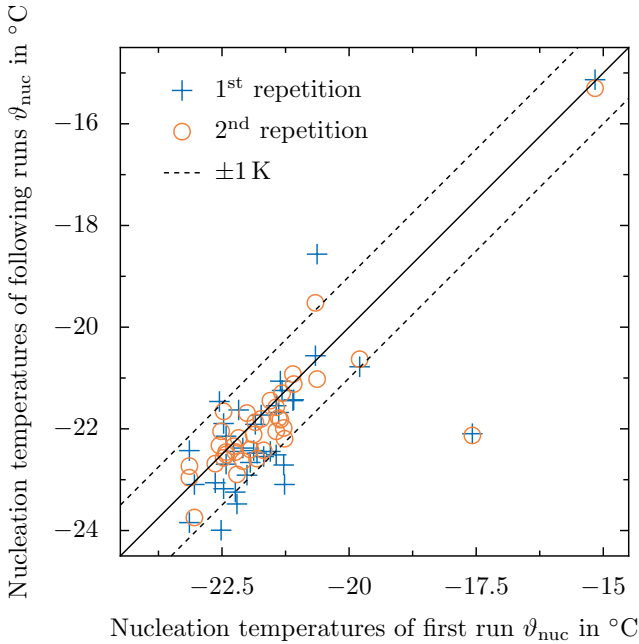


Figure 9.16: Variation of the nucleation temperature of the individual droplets of a typical droplet ensemble obtained with the electric field turned off. Nucleation temperature of a droplet measured in two further repetitions of the experiment shown as a function of the nucleation temperature obtained in the first experiment. Reprinted figure (adapted) with permission from [158]. Copyright 2021 by the American Physical Society.

the ensemble is constant or not. For better visualization, the deviation of  $\Delta T = \pm 1$  K from the perfect correlation is illustrated by the dashed lines. The nucleation events represented by the symbols are located closely to the perfect correlation and only vary slightly.

Excluding a few outliers, all droplets have an almost fixed nucleation temperature, varying only by approximately  $\Delta T = \pm 1$  K. The almost constant nucleation temperature of the individual droplets supports the assumption of a singular nucleation behaviour with respect to the tem-

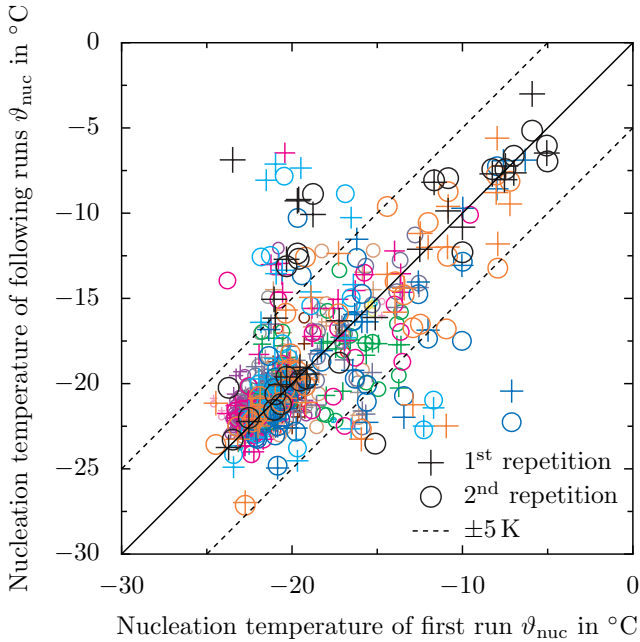


Figure 9.17: Variation of the nucleation temperature of the individual droplets of a typical droplet ensemble obtained with the electric field of a constant frequency  $f = 50$  Hz. Nucleation temperature of a droplet measured in two further repetitions of the experiment shown as a function of the nucleation temperature obtained in the first experiment. The plus signs indicate the first and the circles the second repetitions, respectively. The colour and size of the individual symbols correspond to the electric field strength between  $\hat{E} = 0$  kV/cm and  $\hat{E} = 7.16$  kV/cm. Reprinted figure (adapted) with permission from [158]. Copyright 2021 by the American Physical Society.

perature. However, the slight variation of the nucleation temperature, i.e. the scatter of the data, and the outliers indicate that ice nucleation is still a stochastic process. While ice nucleation in absence of the electric field is more a singular rather than a stochastic process, the electric field have a stochastic influence at least for low electric field strength

## 9 Results using supercooled sessile droplets

( $\hat{E} < 2.86$  kV/cm). Comparing the temperature variation for such low electric fields ( $\Delta T = \pm 4.55$  K), with the variation of the nucleation temperature in absence of the electric field shown in Fig. 9.16, proves that low electric field strengths impact ice nucleation even though no clear trend can be observed. Consequently, the impact of the electric field appears to be stochastic. Nevertheless, the nucleation events under the impact of an electric field are analysed in the same manner as without an electric field in order to investigate whether the electric field has a stochastic influence or not.

The nucleation temperature of each individual droplet measured in the initial run for specific boundary conditions is compared to the nucleation temperature of the same droplet and under the same conditions for the subsequent in Fig. 9.17. Each nucleation event is represented by a single symbol. The size of the symbol correlates with the applied electric field strength. Hence, the higher the electric field strength, the larger is the symbol. The different kinds of symbols represent the different repetitions under the same conditions, so the plus signs and the circles indicate the first and second repetitions, respectively. A perfect correlation between the temperatures, i.e. a constant nucleation temperature, is indicated by the solid line. In addition, a deviation of  $\Delta T = \pm 5$  K from the perfect correlation is indicated by the dashed line.

While most of the data points are located close to the solid line, which indicates a constant nucleation temperature for constant conditions, the general variation of the nucleation temperature is much larger ( $\Delta T = \pm 5$  K, ignoring outliers) compared to the data represented in Fig. 9.16. As already observed in Subsec. 9.3.1, the variation in nucleation temperature is given by  $\Delta T = \pm 4.55$  K for low electric field strengths, and thus is about five times higher compared to experiments without an electric field. Consequently, even low electric field strengths have an impact on ice nucleation. Although the impact of the electric field appears to be stochastic, ice nucleation is observed to be still singular even with an applied electric field. The individual droplets of the ensemble have an almost constant nucleation temperature independent of the electric field strength. The influence of the stochastic behaviour increases when an electric field is applied. Consequently, the data presented include both singular and stochastic ice nucleation behaviour with respect to the temperature and the electric field.

In addition, the electric field does not affect all droplets of the ensemble in

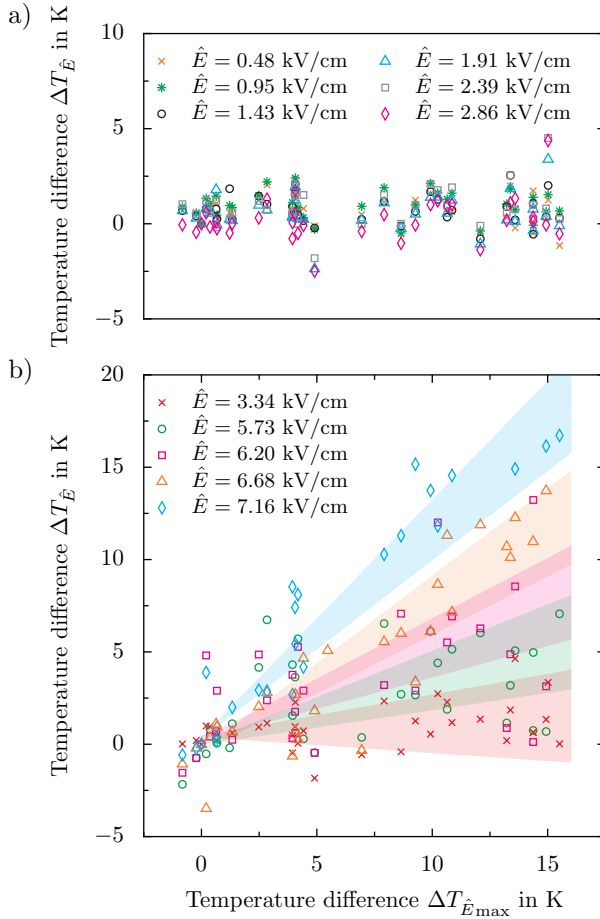


Figure 9.18: Change of the mean freezing temperature for varying field strength,  $\Delta T_{\hat{E}} = \bar{T}_{\hat{E}} - \bar{T}_0$ , depending on the temperature difference corresponding to the highest field strengths,  $\Delta T_{\hat{E}_{\max}} = \bar{T}_{\hat{E}_{\max}} - \bar{T}_0$ . Each symbol corresponds to a specific droplet. The symbol type and colour refer to the electric field strength under consideration. The coloured regions indicate the trends for the varying electric field strength. Reprinted figure (adapted) with permission from [158]. Copyright 2021 by the American Physical Society.

## 9 Results using supercooled sessile droplets

the same manner, so that the impact of the electric field is also singular. As shown in Fig. 9.12 the number of droplets affected by the electric field increases with increasing electric field strength. However, ice nucleation at low temperatures does not appear to be affected by the electric field independent of the electric field strength. The impact of the electric field appears to be mainly present at high temperatures.

Therefore, the data is investigated in more detail to determine whether the impact of the electric field on ice nucleation is of singular or stochastic nature with respect to the individual droplets. For this purpose the change of the mean nucleation temperature is analysed. The mean nucleation temperature is defined as  $\Delta T_{\hat{E}} = \bar{T}_{\hat{E}} - \bar{T}_0$ , where  $\bar{T}_{\hat{E}}$  is the mean nucleation temperature for the droplets exposed to an electric field with a specific field strength and  $\bar{T}_0$  is the mean nucleation temperature of the individual droplets in absence of an electric field. The individual mean nucleation temperatures are calculated for each individual droplet using the repetitions under the same conditions. This temperature difference  $\Delta T_{\hat{E}}$  characterizes the mean impact of the electric field for each individual droplet with respect to the reference experiment without an electric field. The mean change in freezing temperature  $\Delta T_{\hat{E}}$  as a function of the change in freezing temperature for the individual droplet for the highest electric field strength  $\Delta T_{\hat{E}_{\max}}$  is shown in Fig. 9.18. Note that  $\Delta T_{\hat{E}_{\max}}$  is defined as  $\Delta T_{\hat{E}_{\max}} = \bar{T}_{\hat{E}_{\max}} - \bar{T}_0$ , where  $\bar{T}_{\hat{E}_{\max}}$  is the mean nucleation temperature of the individual droplets with respect to the two highest electric field strengths, namely  $\hat{E} = 6.20 \text{ kV/cm}$  and  $\hat{E} = 7.16 \text{ kV/cm}$ . This definition was chosen to take into account the stochastic nature of ice nucleation. Using this definition sorts the droplets along the abscissa according to the impact of the electric field on the nucleation temperature. The higher the impact, the higher is  $\Delta T_{\hat{E}_{\max}}$ . Furthermore, a drop-wise analysis is appropriate to determine whether the electric field influences only the same droplets of one ensemble or not. The same data as shown in Fig. 9.12 is shown in Fig. 9.18 but separated by electric field strength for better visibility.

As observed in the previous subsections, an electric field strength  $\hat{E} < 3.34 \text{ kV/cm}$  does not influence the nucleation behaviour, as shown in Fig. 9.18a. In contrast, the data for higher electric field strengths  $\hat{E} \geq 3.34 \text{ kV/cm}$  is shown in Fig. 9.18b. Each symbol of one kind represents the mean nucleation temperature of a specific droplet of the ensemble.

Increasing the electric field strength leads to a significant influence of the electric field on ice nucleation as already observed in the analysis of the droplet survival curves in Subsec. 9.3.1. The corresponding data for the droplet-wise analysis is shown in Fig. 9.18b. Note that not the complete data set is shown for better visualization. However, the trend of the missing data set is the same as for the presented data points. The coloured regions illustrate the trend of the data for the corresponding field strength, showing a maximum deviation of  $\Delta T_{\hat{E}} = \pm 2.5 \text{ K}$  at  $\Delta T_{\hat{E}_{\max}} \approx 16 \text{ K}$ , which is constant for all electric field strength.

The representation of the data shown in Fig. 9.18b reveals the singular impact of the electric field on ice nucleation. The number of droplets affected by the electric field strength increases with increasing electric field strength. In addition, the effect of the electric field on ice nucleation on the individual droplets which are affected by the electric field increases with increasing electric field strength. However, not all droplets are affected by the electric field. Even for the highest electric field strength some droplets freeze at almost the same temperature. Due to the stochastic nature of ice nucleation the data for a constant electric field strength has a significant scatter, which is not completely encompassed by the coloured regions. However,  $\Delta T_{\hat{E}}$  clearly increases with increasing  $\Delta T_{\hat{E}_{\max}}$ , which indicates that droplets which are significantly affected by high electric field strengths (indicated by large values of  $\Delta T_{\hat{E}_{\max}}$ ) are also significantly influenced by lower electric field strengths (indicated by large values of  $\Delta T_{\hat{E}}$ ) and vice versa. For a purely stochastic behaviour of ice nucleation with respect to the electric field, the impact of the electric field on ice nucleation would be the same for all droplets of the ensemble, resulting in no consistent trend in Fig. 9.18. Consequently, the impact of the electric field is more singular than statistical in nature, because only specific droplets in the ensemble are affected by the electric field.

The increasing number of droplets affected by the electric field for an increasing electric field strength, and the fact that low electric field strengths do not affect ice nucleation at all, leads to the assumption that ice nucleation of the individual droplets is not only characterized by a characteristic temperature, but also by a characteristic critical electric field strength necessary to affect ice nucleation. The characteristic electric field strength appears to depend on the individual droplets of the ensemble. Only, if the characteristic critical electric field strength is reached, the individual droplet is affected by the electric field. Furthermore, the characteristic field strength is associated with the general proneness for ice nucleation

## 9 Results using supercooled sessile droplets

of the individual droplets, and thus is associated with the nucleation sites in the droplet. Droplets which are highly prone to nucleate due to their nucleation sites are also more prone to be affected by the electric field. This can be clearly observed by the fact that the nucleation temperature is significantly increased for droplets freezing at a high temperature in absence of the electric field.

The existing theoretical model presented in Sec. 3.4 cannot describe the observed behaviour because the model intends to describe the impact of constant electric fields and only takes into account the stochastic nature of ice nucleation. The assumption of a general reduction of the critical Gibbs free energy is not valid, because some droplets are not affected by the electric field strength. Consequently, existing models, as for instance [118, 230], cannot describe the singular impact of the electric field on ice nucleation. Thus, the physical mechanism is more complex.

Similar to the characteristic temperature of each droplet for ice nucleation as defined by singular nucleation model, the electric field exhibits a singular behaviour on ice nucleation. Currently, only a hypothesis can be formulated about the physical mechanism which has to be investigated in more detail.

The ice nucleation behaviour in absence of an electric field is mainly defined by the ice nucleation particles present in the droplets. The more active the INP with respect to the temperature, the higher is the nucleation temperature observed in the experiment. As observed in the experiments, droplets which are already prone to nucleate at high temperatures, nucleate at even higher temperatures under the influence of an electric field. Hence, the INP become even more active under the influence of an electric field. Thus, the influence of the electric field is associated with the INP present in the droplet, i.e. the wetted surface of the droplet in case of heterogeneous ice nucleation. Generally, the electric field distribution strongly depends on the involved materials and their geometry, e.g. small curvatures of surfaces produce large electric field strengths or a high relative permittivity induces a significant field displacement. Especially, the curvature of the INP, i.e. the size of the INP, is also known to have a major effect on the ice nucleation temperature. Thus, the impact of the electric field significantly depends on the geometrical and electrical properties of the INPs present in the individual droplets.

For each droplet a necessary critical electric field strength to influence ice nucleation can be defined. This hypothesis might be an explanation for the

significant influence of the electric field, but cannot explain the significant impact of the frequency on the behaviour. It is very unlikely that the electrical properties of the involved INPs are strongly dependent on the frequency of the electric field, especially for the given range of frequencies. In such a case, not only specific frequencies would promote ice nucleation but the influence of the frequency would continuously increase.

Consequently, it is assumed that the macroscopic oscillation of the droplet has also a significant influence on ice nucleation. Shear is already known to possibly affect ice nucleation [22, 224] and is generated by the droplet motion. The effect of shear might depend on the oscillation frequency as well as the properties of the INP immersed in the liquid or in contact with the liquid. Especially, for an INP completely immersed in the liquid, the size impacts the flow around the particle. The smaller the particle, the faster is the motion of the particle. In contrast, large droplets are exposed to significant slip velocities due to their inertia, which leads to increased shear. Nevertheless, the physical mechanism behind the impact of the electric field on ice nucleation is still not completely understood and needs further investigations.

#### 9.3.4 Influence of the frequency of the electric field

Besides the electric field strength, the frequency of the electric field might have a significant influence on ice nucleation. The summary of the already performed investigations (App. K) shows that various different frequencies were already tested. While frequencies up to the kHz-range promote ice nucleation, higher frequencies (MHz or GHz-range) prevent ice nucleation by heating the water [257]. Accordingly, the influence of the electric field on ice nucleation significantly depends on the frequency of the applied electric field. In addition to the influence of high frequency electric fields on the microscopic level, electric fields cause an oscillation of the droplet depending on the electric field strength, frequency of the electric field, the droplet volume and the charge of the droplet as shown in Chap. 5. The resulting fluid motion inside the droplet might lead to shear which possibly affects ice nucleation [22, 224]. During the experiments the oscillation of the droplets was clearly observable. The amplitude of the oscillation mainly depends on the frequency of the electric field as well as the droplet volume and is the largest for a droplet oscillating in resonance. The larger

## 9 Results using supercooled sessile droplets

the fluid motion, the larger might be the occurring shear flow, which possibly impacts ice nucleation.

Therefore, the impact of different frequencies on ice nucleation is investigated for a fixed droplet size of  $\bar{d}_d = 0.95$  mm. Changing the frequency at a constant electric field strength of  $\hat{E} = 2.26$  kV/cm should influence the droplet motion, and thus possibly affect ice nucleation. The results are represented as droplet survival curves and nucleation site density, which are shown in Fig. 9.19. In Fig. 9.19a the droplet survival curves are shown for different frequencies of the electric field. For comparison purposes a reference without an electric field and a constant electric field ( $f = 0$  Hz) are also shown.

Comparing the different droplet survival curves shows that electric fields with frequencies  $f < 90$  Hz have almost no influence on ice nucleation for the given electric field strength. The shape of the droplet survival curves follow the typical 'S'-shape. The observed variance between the survival curves can be attributed to the stochastic nature of ice nucleation. Note that the influence of the electric field is significantly influenced by the electric field strength, and thus a higher electric field strength can also influence ice nucleation under the impact of low frequency fields. Even though the general behaviour is the same for such low frequencies, the nucleation temperature of the first nucleation event  $\vartheta_1$  increases with increasing frequency. The droplet comprising the most active nucleation sites is slightly affected by the change of the frequency and becomes active at even higher temperatures. Similar to the effect of the electric field strength, increasing the frequency leads to a significantly changed droplet survival curve, which does not follow the classical 'S'-shaped trend. However, the largest impact is not observed for the highest frequency, but for a frequency of  $f = 100$  Hz. A further increase of the frequency again reduces the influence of the electric field. In addition, to the changed trend of the survival curve, the temperature range of nucleation  $|\vartheta_1 - \vartheta_0|$  increases with increasing frequency and is affected the most for the frequencies  $f = 100$  Hz and  $f = 110$  Hz.

The nucleation site density, corresponding to the droplet survival curves, is shown in Fig. 9.19b. For large degrees of supercooling the impact of the electric field and the different frequencies becomes negligibly small. At such low temperatures,  $\vartheta_d < -22^\circ\text{C}$  the temperature is the predominant influencing factor, similar in magnitude to the impact of the electric field strength as shown before. Hence, the nucleation site density is represented

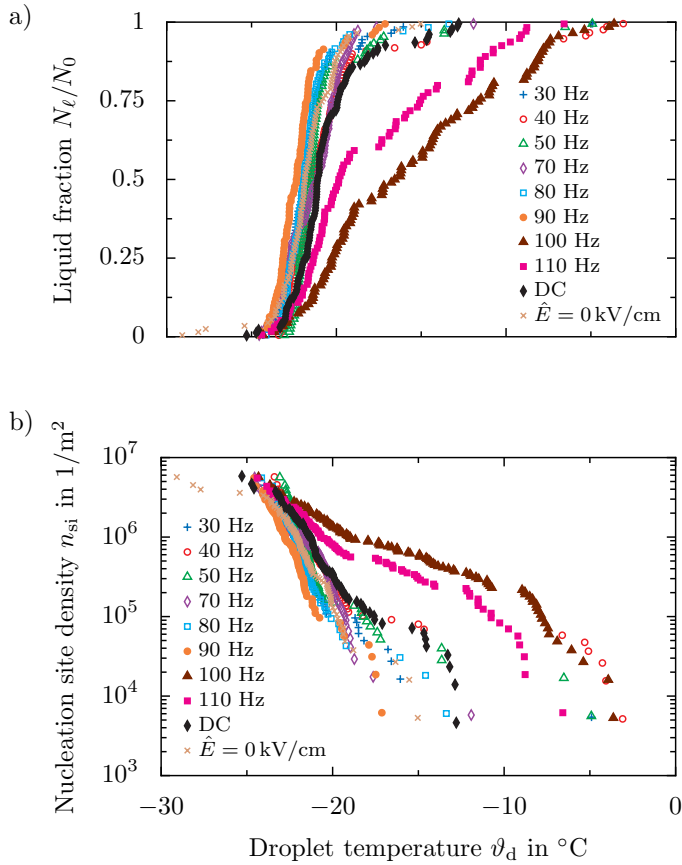


Figure 9.19: a) Droplet survival curves for a constant electric field strength of  $\hat{E} = 2.26 \text{ kV/cm}$  and varying frequency depending on the droplet temperature  $\vartheta_d$ , and b) corresponding nucleation site density  $n_{si}$ . The mean diameter of the used droplets is  $\bar{d}_d = 1.09 \text{ mm}$ . Reprinted figure (adapted) with permission from [158]. Copyright 2021 by the American Physical Society.

## 9 Results using supercooled sessile droplets

by an almost constant slope. In addition, an electric field with a frequency of  $f \leq 90$  Hz does not influence ice nucleation, which is indicated by the almost constant gradient of the nucleation site density for the entire range of temperatures. The influence of the frequency of the electric field is only observable for frequencies  $f > 90$  Hz and for temperatures  $\vartheta_d > -22^\circ\text{C}$ . Similar to the influence of the electric field strength, the nucleation site density rapidly increases at low degrees of supercooling and has a changing gradient depending on the temperature. The influence of the frequency of the electric field is assumed to be associated with the macroscopic oscillation of the droplet, because the microscopic orientation of the water molecules is much faster and can follow external electric fields with frequencies of up to the GHz range [242]. Consequently, it is assumed that the impact is mainly caused by the droplet oscillation. Note that the oscillation of the droplets is mainly influenced by the droplet volume, so that the frequency with the highest impact on ice nucleation varies with the droplet volume.

The largest oscillation of the droplets is associated with the droplet resonance, and so it is assumed that one resonance frequency of the droplet with a mean diameter of  $\bar{d}_d = 1.09$  mm is close to a frequency of  $f = 100$  Hz. However, the observation from above does not allow determining the frequency of the droplet oscillation. Furthermore, the theoretical oscillation frequency presented by Eq. (2.51) is only valid for free droplets or sessile droplets on a hydrophobic substrate, and thus the equation is not valid for sapphire which is hydrophilic. Consequently, it can only be assumed that the droplets are excited close to a resonance frequency, but most probably not perfectly in resonance, which leads to the significant impact of the electric field.

Even though the volume dependence of the frequency and the actual resonance frequency was not further investigated, it was shown that the frequency of the electric field can have a significant influence on ice nucleation. Due to the fact that the experiments concerning the impact of the frequency of the electric field are performed in the same manner as the experiments concerning the electric field strength, it is assumed that the same assumptions with respect to the repeatability and the accuracy of the experiments are still valid for the experiments investigating the influence of the frequency of the electric field.

The observed results are also confirmed by analysing the characteristic temperatures  $\vartheta_i$  which are illustrated in Fig. 9.20. As already observed,

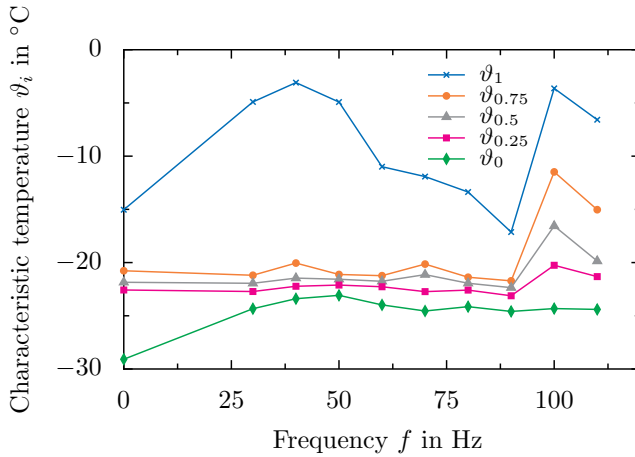


Figure 9.20: Characteristic temperatures  $\vartheta_i$  for the decay of a droplet ensemble depending on the frequency  $f$  of the electric field exposed with a constant electric field strength of  $\hat{E} = 2.26$  kV/cm. The present data corresponds to the experimental series shown in Fig. 9.19. The temperature  $\vartheta_i$  of an ensemble represents the temperature, where  $N_\ell/N_0 = i$ . Reprinted figure (adapted) with permission from [158]. Copyright 2021 by the American Physical Society.

the characteristic temperature  $\vartheta_1$  corresponding to the first nucleation event significantly depends on the frequency of the electric field. A significant impact is observable for the frequencies  $f = 40$  Hz and  $f = 100$  Hz, which leads to the highest nucleation temperatures. While the characteristic temperature  $\vartheta_0$  is significantly increased by applying an electric field compared to the reference without an electric field, the characteristic temperatures  $\vartheta_i$  with  $0 \leq i < 1$  are almost constant for frequencies  $f \leq 90$  Hz. At a frequency of  $f = 100$  Hz the characteristic temperature  $\vartheta_i$  is increased, while the impact decreases with decreasing liquid fraction. The lowest nucleation temperatures are only affected by applying an electric field, but not by changing the frequency of the electric field. Hence, the temperature is the more dominant influencing factor compared to the frequency of the electric field for large degrees of supercooling, which is similar to the effect of the electric field strength. Even though the effect of the changed frequency is not as significant as the impact of the electric

field strength, an influence of the frequency on ice nucleation was clearly observed.

### 9.3.5 Conclusions

While constant electric fields have an almost negligible influence on ice nucleation, alternating electric fields significantly promote ice nucleation depending on the boundary conditions. Electric fields with an electric field strength  $\hat{E} < 2.86 \text{ kV/cm}$  do not influence ice nucleation. However, increasing the electric field strength leads to a significant impact of the electric field on ice nucleation, as indicated by the droplet survival curves and the nucleation site density. The impact of the electric field increases with increasing electric field strength. An increasing electric field strength increases the characteristic temperature such as the mean nucleation temperature. Thus, increasing the electric field strength promotes ice nucleation. Nevertheless, the lowest nucleation temperature is almost not affected by the electric field, so that not all droplets of the ensemble are affected in the same manner. Droplets which are already prone to nucleate at high temperatures are even more prone to nucleate under the influence of an electric field. The number of droplets affected by the electric field increases with increasing electric field strength. In addition, it could be shown that the impact of the electric field is of singular nature rather than stochastic. Each droplet is associated with a critical electric field strength necessary to affect ice nucleation. Consequently, only specific droplets of the ensemble are affected, which appear to be the same for the different electric field strengths. Accordingly, the nucleation behaviour is not only singular with respect to the temperature, but also with respect to the electric field strength. However, the experimental data shows also the presence of the stochastic nature of ice nucleation.

Although the droplet ensemble is exposed to different electric field strengths, the previously exposed electric field strengths do not have any influence on ice nucleation. Therefore, an electric field can only influence ice nucleation on a small timescale. Ice nucleation is mainly influenced by the boundary conditions directly at the moment of nucleation.

Besides the electric field strength, the frequency of the electric field was identified to have a significant influence on ice nucleation. Especially for a frequency of  $f = 100 \text{ Hz}$ , ice nucleation was significantly promoted. The

impact of the frequency of the electric field is assumed to originate from the fluid motion and the associated shear.

In summary, alternating electric fields can significantly promote ice nucleation and increase the nucleation temperature depending on the frequency and the electric field strength. Existing theoretical models cannot describe the observed behaviour, so that further investigations are necessary to reveal the physical mechanism behind the observations and to prove or falsify the presented hypothesis.

## **9.4 Transient electric fields**

As shown in the previous section, a quasi-static but time-variant electric field has a larger impact on ice nucleation compared to a time-invariant, static electric field. The time dependence and the type of the electric field have a significant influence on the outcome of the experiments. To extend the investigation of the influence of different types of electric fields on ice nucleation, transient electric fields are investigated. The impact of transient electric fields has only been rarely investigated [24, 167, 205, 290] in comparison to alternating or constant electric fields. Even though a variety of experiments have already been performed in the past, the impact of transient electric fields on sessile droplets, which are not in contact to one of the electrodes, is still unknown. Several experimental setups, like the classical electrowetting setup using single droplets [290] or a completely enclosed bulk of water [24, 205], are used to investigate the impact of transient electric fields on ice nucleation. These experimental setups recreate conditions useful for example for food preservation, but cannot emulate the conditions present for supercooled sessile droplets only in contact with dielectrics, which are affected by transient electric fields. Such conditions are present at the weather sheds of high-voltage insulators under the impact of lightning or switching impulse voltages, which are generated by a lightning strike on an overhead line or a switching operation inside the power transmission and distribution system [133]. Although alternating electric fields vary in time, these kinds of electric fields are often assumed to be quasi-static because of the low frequencies [238]. In contrast, transient electric fields are generally characterized by a fast increase and a slower decrease of the electric field strength. The use of the standardized lightning and switching impulse voltages ensure a well-defined electric field with respect to time and an accurate reproduction of

## 9 Results using supercooled sessile droplets

Table 9.4: Overview of tested parameters and their quantities to investigate the influence of transient electric fields on heterogeneous ice nucleation.

Parameter	Quantity
Mean droplet diameter $\bar{d}_d$ in mm	0.96, . . . , 1.07
Electric field strength $\hat{E}$ in kV/cm	0, . . . , 22.82
Temperatures $\vartheta$ in °C	-5.9, . . . , -21
Impulse type (IEC 60060-1) in $\mu$ s	1.2/50, 250/2500

the boundary conditions present in power transmission and distribution systems.

Due to the time-variance of the electric fields, the experimental procedure is changed compared to constant or alternating electric fields. The experiments are not performed using a constant cooling rate but a constant temperature. The experimental procedure was described in Subsec. 8.2.3. An overview of the tested parameters is shown in Table 9.4. In addition to the calibration procedure shown in Subsec. 8.1.2, the evolution of the temperature is determined for each temperature level prior to the experiment to ensure that the temperature at the droplet position is accurately determined during the experiment. Due to the fact that the calibration was performed for a constant cooling rate, it may be that the temperature is changing over time for a constant temperature. To avoid a false calculation of the droplet temperature, the calibration data is used to determine the actual droplet temperature at the moment the electric field is applied. This ensures well-defined boundary conditions with respect to the temperature.

The duration and the rate of change is much faster for transient electric fields compared to constant or alternating electric fields. To capture all relevant physical mechanisms, a high-speed camera is used to investigate the nucleation behaviour of the sessile droplets. The use of the high-speed camera limits the recording time because of the limited memory of the camera. For the maximum frame rate of the camera (4000 fps) the maximum recording time is  $t = 1.5$  s. It might be possible that individual

droplets freeze after the recording is already finished. Those nucleation events are not taken into account because they cannot be clearly correlated to the applied electric field.

As already presented in the previous section, the impact of electric fields on ice nucleation depends on different influencing factors like the electric field strength or the frequency, i.e. the time. Due to the fact that ice nucleation is a time-dependent process it is assumed that the duration of an impulse has a significant impact on the outcome of an experiment. Thus, two impulse voltages, namely standard lightning and standard switching impulse voltage, are used. The different impulses cover different time scales, which enables the investigation of the role of time. Besides that, the general influence of high-voltage impulses on ice nucleation is investigated. Each measurement is repeated at least four times under constant conditions (a specific impulse type and temperature) to generate numerous nucleation events and ensure reliable results.

### 9.4.1 Impact of standard lightning impulse voltages

The standard lightning impulse voltage is defined by IEC 60060-1 as 1.2/50 impulse and is subsequently called lightning impulse voltage. The first number of the definition is related to the time to peak, which is  $t = 1.2 \mu\text{s}$  and the second number characterizes the time to half value, which is  $t = 50 \mu\text{s}$ . Thus, the electric field strength has a fast and steep increase followed by a slower decrease. The characteristic time scales of a lightning impulse voltage (compare Table 7.2) are much lower than the general resonance frequencies of a liquid droplet, which are in the order of tens to a hundred milliseconds. This leads to the assumption that the influence of time/duration of presence of an electric field is more important for transient compared to constant or alternating electric fields.

The nucleation behaviour is analysed using the frozen fraction  $N_s/N_0$  after a constant time of  $t = 1.5 \text{ s}$ . The resulting frozen fraction depending on the electric field strength and the degree of supercooling is shown in Fig. 9.21. Note that these results were obtained by the low-speed camera.

After recognizing that nucleation of the individual droplets takes place in a very short time, the following experiments are performed with the high-speed camera to obtain a higher temporal resolution of the experimental data. Nevertheless, the data of the present figure is evaluated after  $t = 1.5 \text{ s}$  for comparison purposes. The amplitude of the electric

## 9 Results using supercooled sessile droplets

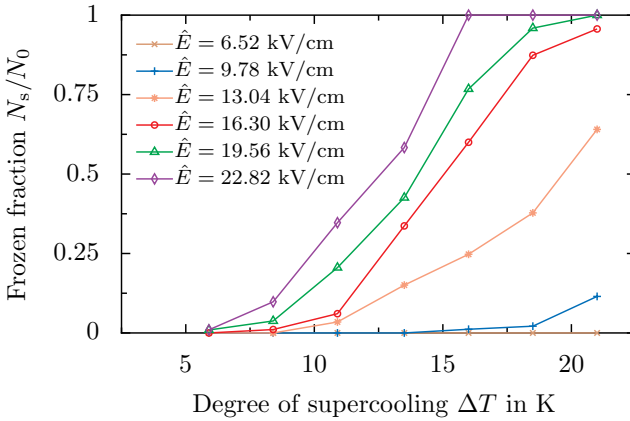


Figure 9.21: Final frozen fraction  $N_s/N_0$  measured long times after applying the impulse voltage, depending on the ensemble supercooling  $\Delta T$  for lightning impulse voltages of varying peak electric field strength  $\hat{E}$ . Reprinted (adapted) with permission from [159], under the Creative Common License - Attribution 4.0 International (CC BY 4).

field strength  $\hat{E}$  corresponds to the highest amplitude of the electric field during the impulse voltage is applied and characterizes the highest electric field strength exposed to the droplets. Similar to the liquid fraction, the frozen fraction is defined as the ratio of the number of frozen droplets  $N_s$  and the number of initially liquid droplet  $N_0$ . It characterizes the impact of a specific electric field strength at a given temperature. For lightning impulse voltages a minimum of 95 nucleation events for a specific combination of temperature and electric field strength is investigated to determine the behaviour. The results are presented in Fig. 9.21.

Both the temperature and the electric field have a significant influence on ice nucleation. Increasing the electric field strength leads to an increasing impact on ice nucleation, and thus to a larger frozen fraction for a constant degree of supercooling. Furthermore, the impact of the electric field increases with increasing degree of supercooling. While low electric field strengths  $\hat{E} < 9.78$  kV/cm have no impact on ice nucleation, independent of the degree of supercooling, larger electric field strengths significantly promote ice nucleation. For  $\hat{E} \leq 6.52$  kV/cm none of the

droplets freeze under the influence of the transient electric field, independent of the degree of supercooling. In contrast, electric field strengths  $6.52 \text{ kV/cm} < \hat{E} < 19.56 \text{ kV/cm}$  cause an increasing number of frozen droplets. However, the electric field strength does not cause all droplets to freeze ( $N_s/N_0 = 1$ ) even for the highest degree of supercooling  $\Delta T = 21 \text{ K}$ . The higher the electric field strength, the lower is the necessary degree of supercooling to cause an effect of the electric field on ice nucleation. Increasing the electric field strength even more ( $\hat{E} > 16.30 \text{ kV/cm}$ ) results in a completely frozen ensemble for a sufficiently high degree of supercooling. For an electric field strength of  $\hat{E} = 19.56 \text{ kV/cm}$  a ratio of  $N_s/N_0 = 1$  is reached for a supercooling of  $\Delta T = 21 \text{ K}$ . Larger electric field strength results in an already completely frozen ensemble at lower supercoolings. For the highest electric field strength  $\hat{E} = 22.82 \text{ kV/cm}$  a completely frozen ensemble is already observed for a supercooling of  $\Delta T = 16 \text{ K}$ .

To quantify the increasing impact of the electric field strength, the mean freezing temperature  $\vartheta_{0.5}$ , which corresponds to  $N_s/N_0 = 0.5$ , is analysed depending on the electric field strength. Due to the fact that the experimental data is only given for specific frozen fractions, the mean freezing temperature is approximated by the available experimental data. A linear approximation of the two frozen fractions the closest to  $N_s/N_0 = 0.5$

Table 9.5: Approximated mean nucleation temperature  $\vartheta_{0.5}$  depending on the electric field strength  $\hat{E}$  for lightning impulse voltage. The mean nucleation temperature correlates to  $N_s/N_0 = 0.5$  and characterizes the electric field strength to freeze half of the ensemble. Reprinted with permission from [159], under the Creative Common License - Attribution 4.0 International (CC BY 4).

$\hat{E}$ in kV/cm	$\vartheta_{0.5}$ in °C
13.04	-19.66
16.30	-15.05
19.56	-14.04
22.82	-12.58

## 9 Results using supercooled sessile droplets

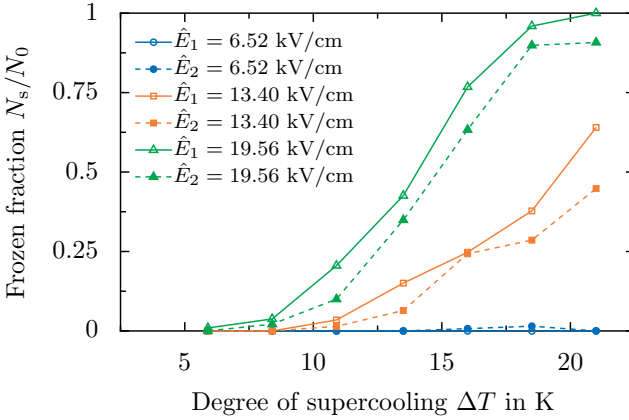


Figure 9.22: Frozen fraction  $N_s/N_0$  for two different droplet ensembles depending on supercooling  $\Delta T$  and the electric field strength  $\hat{E}$ . Both ensembles are exposed to lightning impulse voltages. The data shown in Fig. 9.21 is indicated by the index 1 and is compared to the data obtained with a fresh ensemble (index 2). Reprinted (adapted) with permission from [159], under the Creative Common License - Attribution 4.0 International (CC BY 4).

is used to calculate the mean freezing temperature for each electric field strength. The result is summarized in Table 9.5.

The mean freezing temperature  $\vartheta_{0.5}$  is significantly affected by the electric field and decreases with increasing electric field strength. Note that for  $\hat{E} < 13.04$  kV/cm no mean freezing temperature is calculated due to the fact that less than the half of the ensemble is frozen after  $t = 1.5$  s. Increasing the electric field strength from  $\hat{E} = 13.04$  kV/cm to  $\hat{E} = 22.82$  kV/cm results in an increase of the mean freezing temperature of  $\Delta\vartheta_{0.5} \approx 7$  K.

The experiments are performed with the same set of droplets to rule out any influence associated with the droplet position or contamination of the droplets. However, a second set of droplets is used to investigate the repeatability and sensitivity of the results with respect to a changed droplet ensemble. The resulting frozen fractions of the different ensembles are compared in Fig. 9.22, depending on the electric field strength  $\hat{E}$  and the degree of supercooling  $\Delta T$ . The hollow symbols and the solid lines

correspond to the data presented in Fig. 9.21, which are labelled with the index 1. The filled symbols and dashed lines represent the data of the new ensemble and are labelled with the index 2. Identical colours correspond to the same electric field strength.

As shown by the data, the agreement of the different ensembles is very good. For low electric field strengths ( $\hat{E} = 6.52 \text{ kV/cm}$ ) almost no deviation between the sets is observable. The electric field does not cause any droplet to freeze, independent of the degree of supercooling. For larger electric field strengths only slight variations are observable, but the trend is still the same. An increasing electric field strength leads to an increasing frozen fraction. For supercoolings of  $\Delta T > 10 \text{ K}$  the resulting frozen fraction of the second ensemble is generally lower than the first ensemble. The difference between the ensembles is most likely caused by the change of the droplets, which is associated with a changed INP spectrum inside the droplets affecting the nucleation temperature. Furthermore, the mean droplet size of the ensemble varies slightly, which also has an impact. However, the change of the INP spectrum seems to have an insignificant influence compared to the impact of the electric field.

### 9.4.2 Impact of standard switching impulse voltages

To investigate the impact of the impulse duration and a change of the characteristic time scales of the impulse voltage, the same experiments are performed with standard switching impulse voltages. The standard switching impulse is defined by the IEC 60060-1 as a 250/2500 impulse and subsequently called switching impulse voltage. Hence, the impulse is characterized by a time to peak of  $t = 250 \mu\text{s}$  and a time to half value of  $t = 2500 \mu\text{s}$ . This leads to an impulse with a significantly longer duration and to different characteristic time scales (see Table 7.2) compared to lightning impulse voltages. Even if the characteristic time scales are increased compared to lightning impulse voltages, the characteristic time scales are still lower than the characteristic timescale of the typical droplet oscillations given under the influence of alternating electric fields. All experiments are performed with a single set of droplets to rule out any influence of droplet contamination or changed droplet size. The experiments are performed with the same procedure as for the lightning impulse.

The resulting frozen fraction of the droplet ensemble under the influence of switching impulse voltages after a duration of  $t = 1.5 \text{ s}$ , depending on

## 9 Results using supercooled sessile droplets

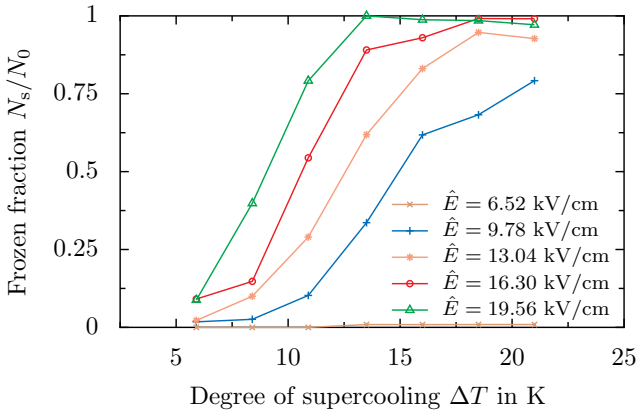


Figure 9.23: Frozen fraction  $N_s/N_0$  depending on the supercooling  $\Delta T$  as well as the electric field strength  $\hat{E}$  for a switching impulse voltage. Reprinted (adapted) with permission from [159], under the Creative Common License - Attribution 4.0 International (CC BY 4).

the electric field strength  $\hat{E}$  and the degree of supercooling  $\Delta T$ , is shown in Fig. 9.23. For the experiments performed with switching impulse voltages a minimum of 95 nucleation events for each combination of electric field strength and degree of supercooling is analysed to ensure a high statistical significance of the data. Only for an electric field strength of  $\hat{E} = 19.56$  kV/cm the number of nucleation events taken into account for constant conditions is lowered to 35 nucleation events. The reason for the lowered number of nucleation events is given by the influence of the electric field itself. At such high electric field strengths, the droplets are significantly deformed and release tiny droplets. This causes a continuous decrease of the droplet volume, which results in a reduced number of droplets being taken into account during the analysis. The effect of the electric field on the motion of the droplets is described later in more detail. The reduced number of the droplets ensures a well-defined droplet size during the experiments and repetitions, which enables the comparison of the different experiments. Although the number of nucleation events is reduced for the highest electric field strength, the obtained data is still sufficient to derive statistical significant effects of the electric field on ice nucleation.

Table 9.6: Approximated mean nucleation temperature  $\vartheta_{0.5}$  in dependence on the electric field strength  $\hat{E}$  for switching impulse voltage. The mean nucleation temperature correlates to  $N_s/N_0 = 0.5$  and characterizes the electric field strength to freeze half of the ensemble. Reprinted with permission from [159], under the Creative Common License - Attribution 4.0 International (CC BY 4).

$\hat{E}$ in kV/cm	$\vartheta_{0.5}$ in °C
9.78	-14.95
13.04	-12.56
16.30	-10.62
19.56	-9.05

Similar to lightning impulse voltages, low electric field strengths ( $\hat{E} \leq 6.52$  kV/cm) does not influence ice nucleation, independent of the electric field strength. None of the droplets within the ensemble are caused to freeze, independent of the degree of supercooling. The frozen fraction increases with increasing electric field strength and increasing degree of supercooling. The higher the electric field strength, the higher is the influence of the electric field on ice nucleation. The influence of switching impulse voltages is higher compared to lightning impulse voltages. Comparing the data of Figs. 9.21 and 9.23 reveals that the frozen fraction is higher for switching compared to lightning impulse voltages for fixed boundary conditions. While an electric field of  $\hat{E} = 9.78$  kV/cm yields a frozen fraction of about 12.5% at  $\Delta T = 21$  K for lightning impulse voltages, the same electric field strength causes about 80% of the droplets to freeze at  $\Delta T = 21$  K if the ensemble is exposed to switching impulse voltages. In addition, switching impulse voltages enhances the impact at low degrees of supercooling. While no ice nucleation is observed at a supercooling of  $\Delta T = 5$  K for lightning impulse voltages, switching impulse voltages cause up to approximately 12.5% of the droplet ensemble to freeze at such low degrees of supercooling. Furthermore, an electric field strength of  $\hat{E} = 16.30$  kV/cm already leads to a fully frozen ensemble at  $\Delta T = 21$  K, and thus is lower than the electric field strength in case

## 9 Results using supercooled sessile droplets

of a lightning impulse voltage. For the highest electric field strength a completely frozen ensemble is already achieved at  $\Delta T = 13.5$  K, which is significantly lower than for lightning impulse voltages ( $\Delta T = 21$  K) for a constant electric field strength of  $\hat{E} = 19.65$  kV/cm.

The impact of switching impulse voltages is also shown by the mean nucleation temperatures  $\vartheta_{0.5}$ . Similar to lightning impulse voltages, the mean nucleation temperature is approximated by the given data using a linear approximation of the frozen fractions the closest to  $N_s/N = 0.5$ . The resulting mean nucleation temperatures for droplets under the impact of switching impulse voltages are presented in Table 9.24. Increasing the electric field strength significantly reduces the mean nucleation temperature. Generally, the temperatures are higher compared to lightning impulse voltages (see Table 7.2). However, the increase from  $\hat{E} = 9.78$  kV/cm to  $\hat{E} = 19.56$  kV/cm leads to almost the same increase of the mean freezing temperature of  $\Delta\vartheta_{0.5} \approx 6$  K compared to lightning impulse voltages. Consequently, the general impact of transient electric fields on ice nucleation is independent of the impulse duration and characteristic timescales. Nevertheless, the impact of switching impulses is higher compared to lightning impulses. This increased influence is associated with the extended duration of the electric field. The longer the electric field is applied, the longer is the droplet influenced by the forces caused by the electric field, which results in a larger macroscopic reaction of the droplet. To determine the reason for this behaviour the motion of the droplets is analysed in more detail.

A time series of a part of the droplet ensemble is shown in Fig. 9.24. The droplets are held at a constant temperature of  $\vartheta = 5.9^\circ\text{C}$ . Initially the droplets are at rest as shown by Fig. 9.24a. An electric field with  $\hat{E} = 19.56$  kV/cm is triggered at  $t = 0$  ms and applied to the droplets. Due to the applied electric field the droplets are significantly deformed as shown in Figs. 9.24b and c. Mainly, the droplets closest to the electrodes (upper row) are affected the most by the electric field. The conical deformation of the droplets was also observed for droplets under the impact of constant electric fields and is called Taylor cone [259]. The formation of a Taylor cone can be associated with the release of tiny droplets from the tip of the Taylor cone. Generally, the formation of such droplets can be observed during the experiments. The tiny droplets come to rest in the space between the individual droplets of the ensemble, which can be observed in the pictures. The change in volume of the droplets is assumed to be negligible due to the fact that the volume of the released droplets

is rather small. However, many repetitions causes a significantly reduced volume of individual droplets. Note that also droplets in the centre of the ensemble might form a Taylor cone and release tiny droplets, even if it is not shown in the time series.

After  $t = 2$  ms the deformation of the droplets is the largest (Fig. 9.24b) and decreases afterwards (Figs. 9.24c). At  $t = 6$  ms the droplets are again in their initial position. Even though the droplets have been significantly deformed by the electric field the final shape and position of the droplets is almost not influenced. The appearance of the ensemble is almost the same before and after the impulse voltage is applied. It is noteworthy that the contact line of the droplets moves during the deformation, which results in a slightly changed position of the contact line after the impulse voltage. However, the change in position cannot be seen in the time series.

For lighting impulse voltages the formation of a Taylor was not observed during the experiments. As already shown in Chap. 7, the macroscopic movement and deformation of droplets exposed to lighting impulses is much lower compared to switching impulses. The same behaviour is observed in the present experiments. The general behaviour of single droplets was already presented in Figs. 7.2 and 7.3 and the conclusions are transferable to the present experiments. Due to the fact that the deformations and oscillations of the droplets are much smaller in case of lighting impulse voltages, no image series is shown for that case.

As discussed in Chap. 7, the characteristic time scales of the impulse and the charge relaxation time of water mainly affects the behaviour of the droplet under the influence of the electric field. Generally, the characteristic timescales of the impulse voltage is much smaller than the charge relaxation time of the droplet, so that the droplet can be assumed as a leaky-dielectric. Only the characteristic time to half value for the switching impulse is larger than the charge relaxation so that the droplet is assumed to be a perfect conductor during this period of the switching impulse. The formation of a Taylor cone is generally possible for conducting and non-conducting liquids [41]. However, the release of tiny droplets is only possible in case of a dielectric or leaky-dielectric liquid [41]. In case of a conducting liquid, the electric field inside the droplet completely vanishes and so does the force tangentially aligned to the interface of the droplet. These tangentially aligned forces on the interface of the droplet were identified to be necessary to cause the formation of tiny droplets [41]. Nevertheless, the formation of a Taylor cone and the possibly associated

## 9 Results using supercooled sessile droplets

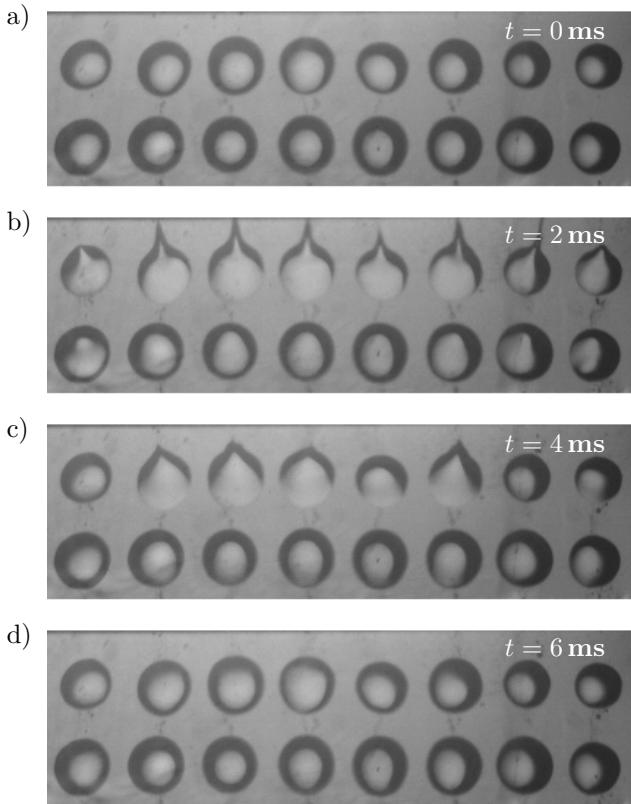


Figure 9.24: Part of a droplet ensemble during the impact of a switching impulse voltage with  $\hat{E} = 19.56$  kV/cm at  $\vartheta = -5.9^\circ\text{C}$  (no freezing is observed). Each image shows the droplets at a different time after triggering of the impulse. a) Time of trigger, b) deformation of the droplets after  $t = 2$  ms, c) after  $t = 4$  ms and d) after  $t = 6$  ms. The mean droplet diameter is  $\bar{a}_d = 1.01$  mm. Reprinted (adapted) with permission from [159], under the Creative Commons License - Attribution 4.0 International (CC BY 4).

generation of tiny droplets is only observed for switching impulse voltages, which is associated with the duration of the impulse. It seems that the duration of a lightning impulse is not long enough to cause a Taylor cone. Hence, the Taylor cone is assumed to be formed during the time to peak of a switching impulse voltage, which is significantly longer than the duration of a lightning impulse.

Ice nucleation is influenced by both impulse types, but the behaviour of the individual droplets mainly depends on the impulse type. Due to the fact that the switching impulse has an increased impact on ice nucleation, it is assumed that not only the presence of an electric field promotes ice nucleation but also the macroscopic motion caused by the electric field. The macroscopic motion and the possibly generated shear flow might promote ice nucleation [224]. It is assumed that the influence originates from the macroscopic motion rather than the molecular motion of water, because water molecules are able to follow electric fields with frequencies up to the GHz range [242]. Accordingly, the characteristic frequency for the orientation of the molecules is much lower than the characteristic time of the applied impulses and the molecules have always enough time to orient themselves in the electric field. In addition, the macroscopic motion can be clearly observed during the experiments. Even if the characteristic timescale of the impulse voltages are significantly higher than typical oscillation frequencies under the impact of alternating voltages, the resulting motion might significantly impact the shear flow inside the droplet, i.e. ice nucleation [224]. This might be an explanation for the increased impact of switching compared to lightning impulse voltages.

### 9.4.3 Singular vs. stochastic behaviour

In the previous subsections, the impact of the electric field was evaluated after a constant time of  $t = 1.5$  s, which revealed the long time effect of the electric field on ice nucleation. Using this approach, the individual droplets are categorized as frozen or unfrozen, which is associated to a singular point of view. However, it is well known that ice nucleation is a stochastic process, and thus a time-dependent process, regardless of any singular nature, when studied with an appropriate timescale [193, 265, 266]. To investigate the time-dependence of the process, the high temporal resolution of the high-speed camera is used to determine the exact moment ice nucleation with respect to the applied electric field.

9 Results using supercooled sessile droplets

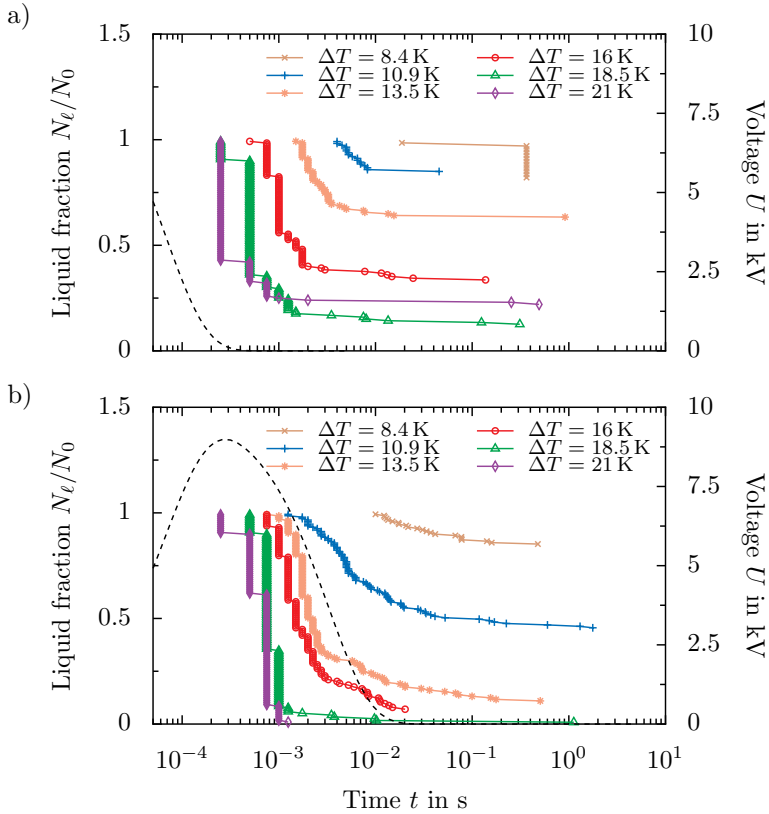


Figure 9.25: Liquid fraction  $N_\ell/N_0$  depending on time  $t$  and degree of supercooling  $\Delta T$  under the impact of transient electric fields with  $\hat{E} = 16.3 \text{ kV/cm}$ . a) shows the resulting liquid fraction for lightning and b) for a switching impulse voltage. Time  $t = 0 \text{ ms}$  refers to the instant when the transient electric field is triggered. The dashed line shows the trend of the applied impulse voltage. Reprinted (adapted) with permission from [159], under the Creative Common License - Attribution 4.0 International (CC BY 4).

The temporal evolution of the liquid fraction for the two impulse types is shown in Fig. 9.25 for a constant electric field strength of  $\vec{E} = 16.30 \text{ kV/cm}$ . Figure 9.25a corresponds to the lightning impulse voltage and shows the experimental data as symbols for various degrees of supercooling. In addition, the dashed line indicates the temporal evolution of the voltage signal, i.e. the temporal evolution of the electric field. The same illustration is used for Fig. 9.25b representing the data for the switching impulse voltage. The time  $t = 0 \text{ s}$  corresponds to the moment the electric field is generated. The camera and the electric field are synchronized by triggering both at the same time.

As shown by the data, the droplets do not freeze instantaneously after the electric field is applied and can have a significant nucleation delay up to  $t = 1.5 \text{ s}$ . Individual droplets freeze after this time, but these nucleation events are not taken into account due to the fact that these nucleation events cannot be clearly correlated to the presence of the electric field. Freezing delays larger than  $t > 1.5 \text{ s}$  might be related to the stochastic nature of ice nucleation, which can cause droplets to nucleate after a specific time even without the influence of an electric field. It is assumed that the impact of this process is rather small because such large freezing delays were only rarely observed during the experiments.

The first nucleation event is observed at  $t = 2.5 \cdot 10^{-4} \text{ s}$  for both impulse types and is associated with the temporal resolution of the camera. Using a frame rate of 4000 fps the maximum temporal resolution yields  $\Delta t = 2.5 \cdot 10^{-4} \text{ s}$ . Hence, any nucleation event occurring at  $t < 2.5 \cdot 10^{-4} \text{ s}$  is recognized at  $t = 2.5 \cdot 10^{-4} \text{ s}$ . The temporal resolution of the camera limits the investigation of the first moment of freezing. This results in an accumulation of freezing events at  $t = 2.5 \cdot 10^{-4} \text{ s}$ , which can be observed for lightning and switching impulse voltages. Even if the resolution is limited to very small timescales, the temporal evolution of the liquid fraction can be accurately measured for larger orders of time. This reveals the stochastic nature and the time dependence of ice nucleation. The individual nucleation events cover several orders of magnitude in time, which indicates that the droplets do not freeze at the same time.

For lightning impulse voltages and supercoolings  $\Delta T < 21 \text{ K}$  the majority of the droplets freeze significantly after the impulse is applied. Furthermore, in most cases the electric field has already decayed when the droplets freeze. For high supercoolings like  $\Delta T = 21 \text{ K}$  the exact moment of nucleation of the first droplets cannot be determined. Hence, it might

## 9 Results using supercooled sessile droplets

be possible that for large supercoolings the electric field is still present when the first droplets freeze. This observation supports the assumption that the impact of an electric field is not only caused by the presence of the electric field but also as a consequence of the macroscopic motion of the droplet in the presence of an electric field.

For switching impulse voltages the first nucleation events for  $\Delta T \geq 16$  K is observed slightly later than for lightning impulse voltages. However, the impact of the electric field is higher compared to lightning impulse voltages, which results in a faster decay of the liquid fraction. In contrast, for supercoolings  $\Delta T < 16$  K the first nucleation event is observed later than for lightning impulse voltages. Even though ice nucleation is initiated at a later time, it is more pronounced for switching impulse voltages. For constant conditions, the decay of the liquid fraction is generally larger for switching compared to lightning impulse voltages. Accordingly, switching impulse voltages have a higher impact on ice nucleation and promote ice nucleation more than lightning impulse voltages. The general onset of nucleation is observed shortly after the maximum electric field strength is applied for large supercoolings  $\Delta T > 8.4$  K. Hence, the majority of the ensemble freezes during the electric field is applied. Only for small supercoolings  $\Delta T < 13.5$  K droplets freeze after the electric field has already decayed. In contrast, the onset of nucleation spreads over approximately two orders of magnitude for the lightning impulse voltage.

Both impulse types significantly promote ice nucleation. However, the different impulse voltages lead to a different temporal decay of the liquid fraction. Even though the characteristic time scales of both impulses differ by almost two decades, the overall nucleation behaviour is comparable for both impulse types. In addition, a counter-intuitive behaviour could be observed. An increasing characteristic timescale of the impulse leads to a decreasing time span for the onset of nucleation. The larger the degree of supercooling, the lower is the difference in the onset of nucleation with respect to time between the different impulse types.

To further analyse the behaviour of the droplets, the experimental data is used to calculate the time-dependent nucleation rate  $\mathcal{J}$ . Assuming that the freezing of the droplets is initiated by heterogeneous ice nucleation, the nucleation rate is determined with the wetted area  $A_{\text{wet}}$ . For nucleation events at constant temperature the time-dependent nucleation rate can

be calculated by [102, 266]

$$\frac{N_\ell}{N_0} = \exp \left[ - \int_0^t A_{\text{wet}} \mathcal{J}_{\text{surf}}(t) dt \right]. \quad (9.1)$$

The resulting nucleation rate defines the probability of freezing per unit surface area and time and has the unit  $\text{m}^{-2}\text{s}^{-1}$ . Using the survival curves obtained from the experimental data the nucleation rate is given by

$$\mathcal{J}_{\text{surf}}(t) = - \frac{1}{A_{\text{wet}}} \frac{d \left[ \ln \frac{N_\ell(t)}{N_0} \right]}{dt}. \quad (9.2)$$

The calculated nucleation rate for lightning and for switching impulse voltages for a constant temperature of  $\vartheta = -13.5^\circ\text{C}$  is shown in Fig. 9.26 as semi-logarithmic diagram to ensure a detailed presentation of the data over a wide time span. Note that the data presented in Fig. 9.26 is reduced compared to Fig. 9.25. Only the data used for the calculation of the nucleation rate is shown. In addition, the figure shows the dependence on the electric field for a constant temperature, so that the number of curves is reduced in Fig. 9.26a because an electric field strength  $\hat{E} < 13.30 \text{ kV/cm}$  has no impact on ice nucleation for lightning impulse voltage at the given temperature. For both, lightning and switching impulse voltages, the nucleation rate is characterized by a steep increase until the maximum nucleation rate is reached and a steep decrease afterwards. Even though the different impulse types have significantly different timescales, the maximum of the nucleation rate appears at almost the same time instant for both impulses. The maximum nucleation rate is reached after approximately  $t \approx 2-4 \text{ ms}$ . In case of lightning impulse voltages, the electric field has already decayed at this time. Hence, the impact of the electric field is associated with a physical mechanism on a larger timescale as given by the impulse voltage. The exact time until the maximum is reached depends on the degree of supercooling. The analysis of the other temperatures revealed that an increasing degree of supercooling causes the maximum nucleation rate to appear earlier in time. In addition to the temperature, the maximum nucleation rate is affected by the electric field strength. The higher the electric field strength, the higher is the maximum nucleation rate. As shown in Fig. 9.26 the maximum nucleation rate is almost identical for an electric field strength  $\hat{E} = 19.56 \text{ kV/cm}$  independent of the impulse type. However, for smaller electric field strengths, the maximum nucleation rate differs for lightning and switching impulse voltages. Over-

## 9 Results using supercooled sessile droplets

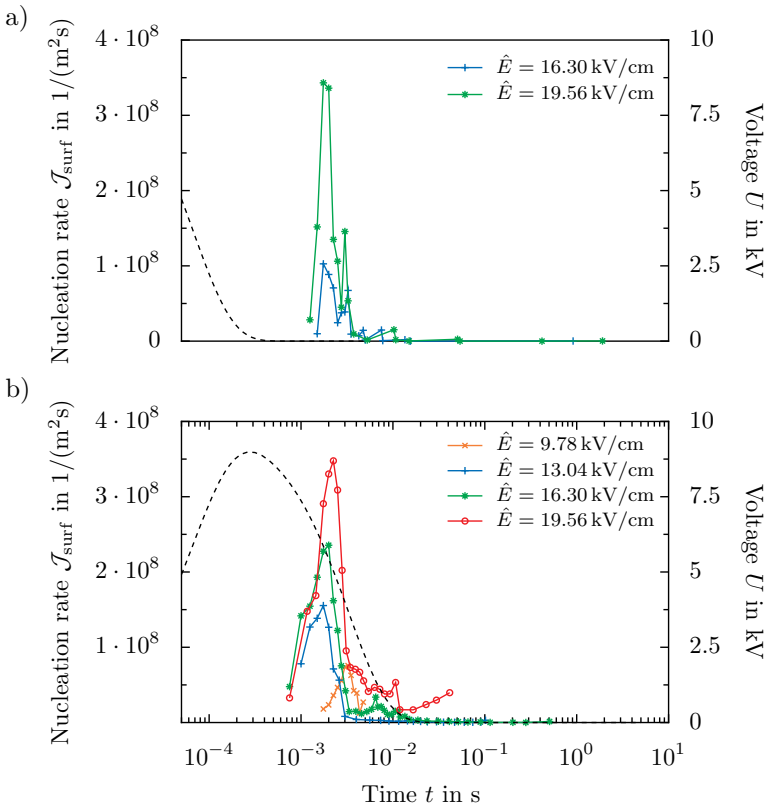


Figure 9.26: Temporal evolution of the nucleation rate  $\mathcal{J}_{\text{surf}}$  depending on the electric field strength  $\hat{E}$  at a temperature of  $\vartheta = -13.5^\circ\text{C}$ , shown for a) lightning impulse voltage and b) switching impulse voltage. Time  $t = 0$  s refers to the instant when the transient electric field is triggered. The dashed line shows the evolution of the applied impulse voltage. Reprinted (adapted) with permission from [159], under the Creative Common License - Attribution 4.0 International (CC BY 4).

all, the general behaviour and the order of magnitude of the nucleation rate is very similar for the different impulse types.

Due to the fact that some droplets freeze after the electric field has already decayed, which is assisted by the maximum nucleation rate appearing at  $t \approx 2-4$  ms, the impact of the electric field is assumed to only influence ice nucleation indirectly. As shown in the previous subsection, the presence of an electric field leads to a deformation of the droplet. Furthermore, the introduced disturbances at the three-phase contact line and the resulting droplet oscillation are associated with a macroscopic motion of the droplet. Based on the observation that the wetted area of the droplet is almost not influenced by the electric field, it is assumed that a shear flow is induced by the electric field. Directly at the substrate, the no-slip condition has to be fulfilled. Simultaneously, the bulk of the droplet oscillates, and a flow profile inside the droplet is generated, which is associated with shear. The larger the droplet motion, the larger is the shear inside the droplet, which is known to possibly affect ice nucleation [224]. Therefore, it is evident that transient electric fields promote ice nucleation by inducing a macroscopic motion. Generally, ice nucleation is promoted by both, lightning and switching impulse voltages, but the impact of switching impulse voltages is higher compared to lightning impulse voltages. This effect is caused by the larger fluid motion generated by the switching impulse voltages.

#### 9.4.4 Conclusions

In addition to alternating electric fields, transient electric fields significantly promote ice nucleation. Both standard lightning and switching impulse voltages can generate electric fields, which can promote ice nucleation. While electric fields with an electric field strength of  $\hat{E} \leq 6.52$  kV/cm are identified to have no impact on ice nucleation independent of the degree of supercooling, higher electric field strengths promote ice nucleation. An electric field strength of  $\hat{E} > 19.56$  kV/cm leads to a fully frozen ensemble depending on the degree of supercooling. Generally, the higher the electric field strength, the higher is the impact on ice nucleation. In addition to the electric field strength, the degree of supercooling influences the nucleation behaviour of the individual droplets. The higher the degree of supercooling, the more prone are the droplets to nucleate. Accordingly, applying an electric field can force ice nucleation of the droplet ensemble.

## 9 Results using supercooled sessile droplets

The nucleation behaviour was investigated with respect to different time scales. The frozen fraction was analysed after  $t = 1.5$  s and revealed the long time effect of the transient electric fields, which corresponds to a singular point of view. A more detailed analysis of the nucleation behaviour with respect to time revealed that the individual droplets do not freeze at the same time. Individual droplets experience a significant nucleation delay of up to  $t = 1.5$  s. Consequently, nucleation is a stochastic and time dependent process independent of the presence of a singular behaviour.

The impact of switching impulse voltages is observed to be higher compared to lighting impulse voltages for the same electric field strength. The formation of a Taylor cone, which is associated with the release of tiny droplets, is only observed for switching impulse voltages. In addition, the macroscopic motion caused by the impulse is also higher in case of switching compared to lighting impulse voltages. Due to the fact that several droplets freeze after the electric field has completely decayed, the influence of the electric field is not only associated with the electric field strength but also with the droplet motion caused by the presence of an electric field. Thus, the impact of the electric field on ice nucleation is presumably not caused by fast physical processes like the molecule orientation, but by slow processes like droplet oscillations and the shear inside the droplet.

# 10 Results of emulsified supercooled droplets

While sessile droplets are always in contact with a substrate which inevitably leads to heterogeneous ice nucleation, emulsified droplets are only in contact with the surrounding fluid. Thus, emulsified droplets can be used to investigate homogeneous ice nucleation as reported in literature by various authors [226, 255, 258]. However, the impact of electric fields on homogeneous ice nucleation is rarely investigated experimentally, amongst others by Stan et al. [247]. Using an emulsion to investigate ice nucleation overcomes two major problems: the presence of a substrate, which leads to heterogeneous nucleation and a high sensitivity of the process caused by the large number of droplets [129]. The major challenge to investigate homogeneous ice nucleation under the impact of electric fields is to stabilize the individual droplets and to prevent coalescence of the droplets, because it is already known that electric fields can cause coalescence [72]. Electro-coalescence is often used to merge nearby droplets. Consequently, the droplets have to be stabilized, which is often achieved by adding a surfactant [105], but this surfactant should not influence ice nucleation. Using a commercially available surfactant and performing the experiments carefully with respect to the application of the electric field, the influence of electric fields on homogeneous ice nucleation could be successfully investigated. The absence of a substrate reveals the general impact of electric fields on ice nucleation. A summary of the experimental conditions for constant electric fields is shown in Table 10.1.

Table 10.1: Overview of tested parameters and their quantities to investigate the influence of constant electric fields on heterogeneous ice nucleation.

Parameter	Quantity
Mean droplet diameter $\bar{d}_d$ in $\mu\text{m}$	$124.8 \pm 18.7$
Electric field strength $E$ in $\text{kV/cm}$	$0, \dots, 13.06$
Cooling rate $\dot{T}$ in $\text{K/min}$	5

## 10.1 Constant electric fields

Each experiment is performed with a new droplet ensemble, because of droplet coalesce during thawing. As already mentioned in Subsec. 8.2.3 the use of different droplet ensembles leads to variations of the nucleation behaviour resulting in a larger scatter of the data. The reported scatter of the data is influenced by the number of droplets, so that the number of nucleation events should be as high as possible to ensure reliable results. Using the closely packed emulsion, a minimum of 1500 nucleation events can be observed for each electric field strength. Hence, the number of nucleation events is significantly higher compared to sessile droplets.

All experiments are performed using a constant cooling rate of  $\dot{T} = 5 \text{ K/min}$ . At first, each ensemble is held at a constant temperature of  $\vartheta_d = 14^\circ\text{C}$  for five minutes to ensure constant boundary conditions while the electric field strength is slowly increased to the desired field strength. The field strength has to be increased slowly to avoid droplet coalescence. Only without droplet coalescence during the experiments the impact of the electric field strength on ice nucleation can be investigated. An exemplary time series of the nucleation experiment for emulsified droplets is shown in Fig. 10.1. Compared to sessile droplets, the first freezing event is observed at significantly lower temperatures. The nucleation of the individual droplets is determined by the colour change of the droplets as

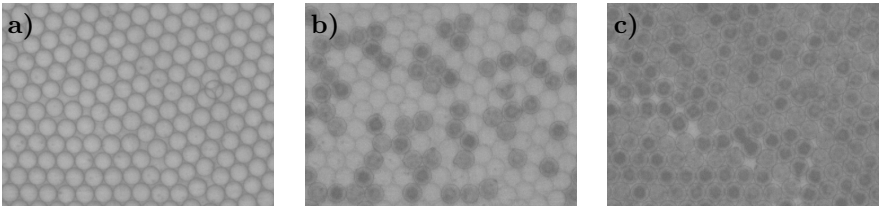


Figure 10.1: Exemplary time series of a nucleation experiment of emulsified droplets. The images show a section of the complete ensemble observed in the experiments, where a) contains unfrozen droplets at  $\vartheta_d = -22.56^\circ\text{C}$ , b) a partially frozen droplet ensemble at  $\vartheta_d = -33.97^\circ\text{C}$  and c) a completely frozen droplet ensemble at  $\vartheta_d = -35.30^\circ\text{C}$ .

shown in Fig. 10.1. While liquid droplets are transparent, frozen droplets are non-transparent leading to a darker appearance. The results of the individual experiments with various electric field strengths are analysed in the same manner as for sessile droplets.

The fraction of liquid droplets  $N_\ell/N_0$  in dependence of the current droplet temperature  $\vartheta_d$  and the applied electric field strength  $E$  is shown in Fig. 10.2. All survival curves exhibit the typical 'S'-shaped trend, which indicates a very clean and careful experimental procedure and reflects the contamination within the droplets [212]. The first droplets nucleate at a temperature of  $\vartheta_d \approx -22^\circ\text{C}$  almost independent of the electric field strength. Furthermore, the lowest nucleation temperature of  $\vartheta_d \approx -35^\circ\text{C}$  is also very constant and does not depend on the applied electric field strength. Compared to the experiments with sessile droplets, the nucleation temperatures of the individual droplets are significantly lower and in the right order of magnitude for homogeneous ice nucleation as reported in literature [96, 130]. This is also a good indicator that the dominant mechanism is given by homogeneous ice nucleation instead of heterogeneous ice nucleation. As indicated by the almost identical trend of all survival curves, the influence of a constant electric field seems negligible. The slight variation between the individual curves is caused by the changed droplet ensemble and the stochastic nature of ice nucleation.

In addition to the survival curves, the nucleation rate  $\mathcal{J}$  is shown in Fig. 10.2b. The nucleation rate is calculated according to Eq. (3.16) by the liquid fraction, the volume of the droplets as well as the constant cooling rate instead of the time. As already indicated by the survival curves, the trend of the different nucleation rates is almost identical, independent of the applied electric field strength. The gradient of the nucleation rates is almost linear for a temperature between  $\vartheta_d \approx -32.56^\circ\text{C}$  and  $\vartheta_d \approx -36^\circ\text{C}$ , which indicates a stochastic nucleation behaviour [193]. For higher temperatures ( $\vartheta_d > -32.5^\circ\text{C}$ ) the gradient of the nucleation curves decreases, but is still almost constant up to a temperature of  $\vartheta_d \approx -25^\circ\text{C}$ . Note, the maximum and minimum of the nucleation rate are mainly defined by the droplet size and the resolution of the liquid fraction. The given boundary conditions yields  $\mathcal{J}_{\max} \approx 4 \cdot 10^{13} \text{ m}^{-3}\text{s}^{-1}$  and  $\mathcal{J}_{\min} \approx 4 \cdot 10^8 \text{ m}^{-3}\text{s}^{-1}$  as maximum and minimum nucleation rates, respectively.

To investigate the influence of the electric field on ice nucleation in more detail the characteristic temperatures of the survival curves are analysed.

10 Results of emulsified supercooled droplets

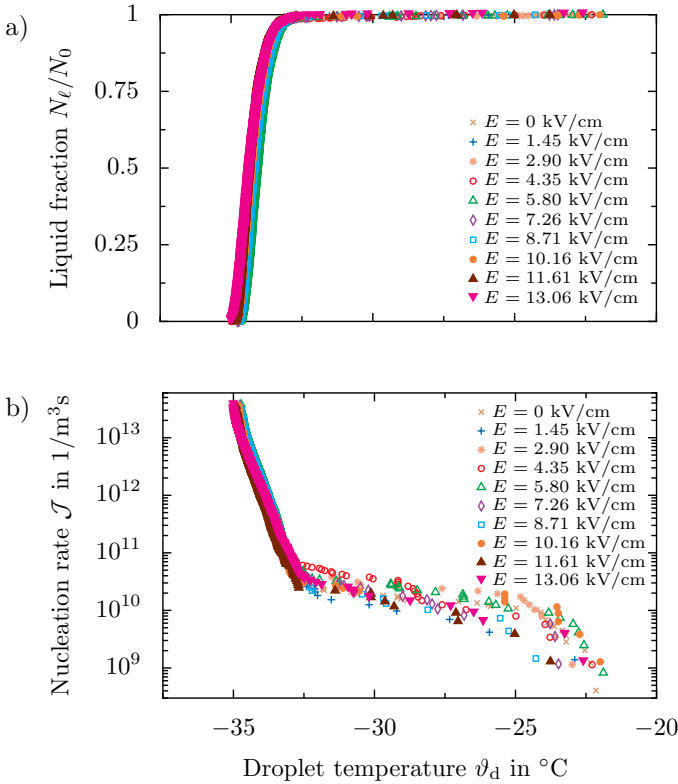


Figure 10.2: Experimental data to obtain the influence of constant electric fields on emulsified droplets. a) Liquid fraction  $N_\ell/N_0$  and b) corresponding nucleation rate  $\mathcal{J}$  depending on the droplet temperature  $\vartheta_d$  and the electric field strength  $E$ .

Each characteristic temperature  $\vartheta_i$  corresponds to the liquid fraction  $N_\ell/N_0 = i$ . Typical liquid fraction ratios are chosen to determine the impact of different electric field strengths and to reveal even small influences, which might be masked by the illustration of survival curves. The resulting characteristic temperatures  $\vartheta_i$  depending on the electric field strength  $E$  are shown in Fig. 10.3, where the characteristic temperature  $\vartheta_1$  defines the highest nucleation temperature and  $\vartheta_0$  the lowest nucle-

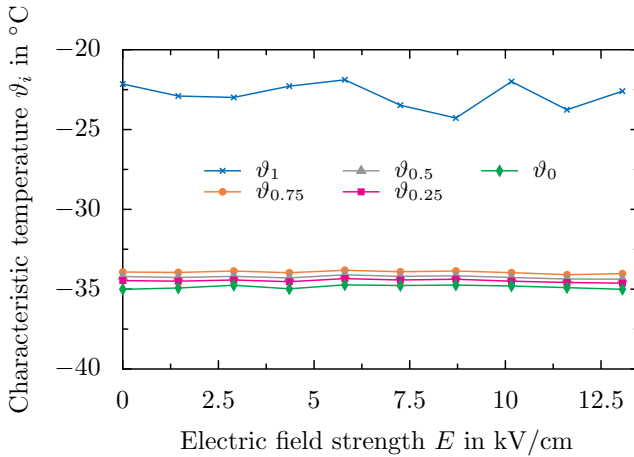


Figure 10.3: Characteristic temperatures  $\vartheta_i$  for the decay of a droplet ensemble depending on the electric field strength  $E$  (constant electric field). The present data corresponds to the experimental series already shown in Fig. 10.2. The temperature  $\vartheta_i$  of an ensemble represents the temperature, where  $N_\ell/N_0 = i$ .

ation temperature. The characteristic temperatures are almost perfectly constant independent of the electric field strength. Only  $\vartheta_1$  varies slightly for the range of applied electric field strength. Nevertheless, no clear trend is observable. The slight variations of the nucleation temperature of the droplets freezing first might be caused by the different droplet ensembles. Even if the droplets are produced from the same bulk the individual droplet contain a different spectrum of unwanted ice nucleating particles [267], which result from water and sample preparation being not perfectly clean.

Hence, homogeneous ice nucleation of water droplets is not affected by constant electric fields up to  $E = 13.06$  kV/cm. The electric field strength could not be further increased because such high electric field strength lead to a destabilization of the droplets, which results in droplet coalescence. Hence, it is still not clear if higher electric field strengths would influence ice nucleation. Such high electric fields might occur in clouds, but in most technical systems the electric field strength is limited. In case of high-voltage insulators the maximum electric field strength amounts

to  $E_{\text{RMS}} \approx 4.5 \text{ kV/cm}$  [209]. As already shown in Sec. 9.2 the impact of constant electric fields on heterogeneous ice nucleation is rather small and might be masked by the stochastic nature of ice nucleation for small electric field strength. This might be also the case for homogeneous nucleation. Polen et al. [212] reported a significant variance between the individual runs and repetitions even if high purity water is used. Consequently, the scatter of the data originate from the water being not perfectly clean. In general, no influence of a constant electric field in homogeneous ice nucleation could be determined for the tested electric field strength, which is in good agreement with the results reported by Stan et al. [247]. However, Stan et al. [247] investigated the impact of alternating electric fields with significantly lower electric field strength. Therefore, the present experiments enhance the knowledge of the impact of constant electric fields on homogeneous ice nucleation, especially for high electric field strengths.

## 10.2 Alternating and transient electric fields

For heterogeneous nucleation it was shown that the impact of alternating and transient electric fields is much more significant than for constant electric fields. This might also be the case for homogeneous ice nucleation. While electro-coalescence was already observed for constant electric fields if the electric field was switched on or the electric field strength was increased too fast, the droplets could not be stabilized under the impact of alternating and transient electric fields. Applying the electric field always leads to a destabilization of the droplets for alternating and transient electric fields. Even if the alternating voltage is increased very slowly, electro-coalescence could be observed for very small electric field strengths. Electric fields are known to promote coalescence [72]. Consequently, the presented method to stabilize the droplets cannot be used to determine the impact of alternating or transient electric fields on homogeneous ice nucleation. However, using other methods to stabilize the droplets even under the impact of alternating or transient electric fields might reveal new insights of the influencing factors of homogeneous ice nucleation. Even though homogeneous ice nucleation could not be observed, the macroscopic interaction of the emulsified droplets and the electric field could be clearly observed by coalescence of the droplets.

**Part V**

**REMARKS AND OUTLOOK**



# 11 Summary

In this study two main subjects have been investigated, namely the impact of electric fields on the hydrodynamic behaviour of sessile droplets at ambient conditions and on supercooled droplets, i.e. on ice nucleation. The two topics involve different physical mechanisms which were experimentally investigated. Generic experimental setups were used to generate well-defined boundary conditions to determine the impact of the various influencing factors. Several new results and conclusions were obtained by the experiments and their analysis.

Sessile water droplets are highly affected by the presence of electric fields. The general behaviour of the droplets is already known and has been widely investigated. Electric fields induce a deformation or oscillation of the water droplets, depending on the electric field strength, frequency of the electric field, droplet volume and substrate properties. Large electric field strengths might even lead to a motion of the droplet. As part of this study, the impact of electric charges on the behaviour of water droplets under alternating electric fields is investigated using a high-speed camera. The electric charge of the droplet is revealed to significantly influence the oscillation behaviour of sessile droplets. The oscillation of the droplets is investigated for the first three resonance modes. While uncharged droplets always oscillate with twice the frequency of the applied voltage, charged droplets oscillate with the same frequency as the applied voltage signal. The frequency of the droplet oscillation is mainly determined by the dominant force acting on the droplet, and thus is defined by the electric field strength and the charge present on the droplet.

In case of a highly charged droplet and a low electric field strength, the Coulomb force causes the droplet to oscillate with the same frequency as the applied voltage. In contrast, a dominant dielectric and electrostrictive force leads to an oscillation with twice the frequency of the applied voltage. Both forces are generally present at the same time, because a perfectly uncharged droplet cannot be produced in reality. To characterize the behaviour of the droplets a regime map is derived by the experimental data, depending on the electric charge and the Bond number of the droplet. In addition, the onset charge necessary for the change in behaviour, depending on the droplet volume and the electric field strength, is determined. Besides the electric charge, the electric field strength is identified to have a large impact on the droplet behaviour. Sufficiently high electric field

## 11 Summary

strengths always cause the droplet to oscillate with twice the frequency of the applied voltage, because the amount of charge on a droplet is limited by the Rayleigh limit. Especially small droplets exposed to small electric field strengths are highly affected by the presence of electric charges. While this behaviour is valid for the second and third resonance mode, a droplet oscillating in the first resonance mode is not affected by the presence of electric charges. In the first resonance mode, the droplets always oscillate with the same frequency as the applied voltage, and thus behaves like a charged droplet even in absence of electric charges. Consequently, the behaviour of droplets under the impact of alternating electric field mainly depends on the electric field strength, electric charge, droplet volume and frequency of the electric field.

In addition to the general behaviour of the droplets and the influence of electric charges, the partial discharge inception of sessile droplets under the impact of alternating electric field is investigated. Due to the fact that water droplets are significantly deformed under high electric field strengths, which results in a complicated shape of the droplet, inflexible droplets made out of a gelatin-water mixture are used to determine the general partial discharge inception field strength of non-moving droplets. The occurring partial discharge patterns obtained by a UV-camera of inflexible droplets and water droplets are compared and identified to be almost identical with respect to the electrical properties of the inflexible droplets. Furthermore, the partial discharges are localized with high resolution and originate from the three-phase contact line. The partial discharge inception is influenced by several influencing factors such as the droplet volume, surface wettability or droplet-droplet separation. The larger the droplet volume, the lower is the partial discharge inception field strength. Furthermore, the lower the wettability of the substrate, the higher is the electric field strength necessary to cause partial discharges. In addition, a lower separation of the two droplets leads to a lower partial discharge inception field strength.

The interaction of nearby droplets mainly depends on the droplet-droplet separation and the droplet volume. Larger droplets can interact over a larger distance. A sufficiently large separation of the droplets prevents the interaction. In case of water droplets, the oscillation behaviour of the droplet, namely the specific resonance modes, have an impact on the occurrence of partial discharges. The higher the frequency of the resonance mode, the lower is the partial discharge inception field strength. Similarly, an increasing droplet volume promotes the generation of partial

discharges. In addition, electric charges are identified to further promote the occurrence of partial discharges. The higher the electric charge, the lower is the partial discharge inception field strength. Under the impact of an electric field water droplets adapt a complex shape, which significantly complicates the prediction of the inception field strength for partial discharges. All boundary conditions, like the electric field strength, droplet volume and shape, electric charges and the wetting properties, have to be taken into account to describe the partial discharge behaviour of a sessile water droplet under the impact of an alternating electric field.

While inflexible droplets were used to investigate the interaction of neighbouring droplets with respect to partial discharges, the coalescence of nearby droplets is investigated using water droplets. Transient electric fields generated by standard lighting and switching impulse voltages are used to determine the behaviour of single and two neighbouring droplets depending on the droplet volume, the electric field strength, type of the electric field and the droplet-droplet separation. Switching impulse voltages are identified to have a larger impact on the droplet behaviour compared to lightning impulse voltages. The transient electric field causes a movement of the three-phase contact line and initiates surface waves on the droplet interface, which finally results in a droplet oscillation. This oscillation of the droplets might cover the separation of nearby droplets and can lead to coalescence of the droplets. A regime map is generated for both impulse types to characterize the behaviour of the droplets depending on the electrical Bond number and the droplet volume. In case of lightning impulses, larger droplets are generally more prone to interaction than small droplets. In addition, increasing the electric field strength or decreasing the droplet-droplet separation also promotes an interaction of the droplets. In case of a switching impulse the inception of the interaction of nearby droplets does not depend on the droplet volume, but on the droplet-droplet separation and the electric field strength. Consequently, the presence of a transient electric field impacts the droplet size and distribution at the surface of a high-voltage insulator.

The experimental results show that the behaviour of sessile droplets under ambient conditions is influenced by various factors. The prediction of the behaviour is rather complex and challenging. All influencing factors, as for instance the electric charge or the deformation of the droplet, have to be taken into account to ensure reliable results. Especially, the influence of factors investigated in this study might have been underes-

## 11 Summary

timated in previous studies, and the necessity of conducting careful and clean experiments has been underlined.

A careful and clean experiment is not only important for droplets under ambient conditions but also to investigate the impact of electric fields on ice nucleation. An experimental setup was developed and built to generate well-defined conditions with respect to the electric field strength and temperature. All boundary conditions are controlled very precisely to investigate the impact of electric fields on ice nucleation inside sessile and emulsified droplets. The droplets are subjected to a constant cooling rate or a constant temperature and exposed to constant, alternating as well as transient electric fields. Droplet survival curves and the nucleation site density/nucleation rate are used to quantify the influence of the electric field strength, the frequency of the electric field and the type of the electric field. The same droplet ensemble is used for a specific set of experiments to rule out the influence of a changed droplet position or contamination of the water.

Constant electric fields are shown to slightly affect heterogeneous ice nucleation. The impact of the constant electric field is rather small and only observable for high electric field strengths. The mean nucleation temperature is decreased with increasing electric field strength. Accordingly, ice nucleation is promoted by the presence of a constant electric field. In addition, the nucleation behaviour is mainly of singular nature due to the fact that the nucleation temperature of the individual droplets is almost constant for all repetitions. Consequently, ice nucleation inside the droplets is associated with an almost constant and characteristic temperature. Furthermore, the formation of a Taylor cone, which is associated with the formation of tiny satellite droplets, is observed during the experiments. The periodical appearance of the Taylor cone results in droplet oscillations, which is a possible reason for the impact of constant electric fields on ice nucleation.

Besides the investigation of constant electric fields, the impact of alternating electric fields on heterogeneous ice nucleation is investigated, depending on the electric field strength and the frequency of the electric field. For the investigation of the electric field strength a constant frequency of  $f = 50 \text{ Hz}$  is used. In comparison to constant electric fields, alternating electric fields have a higher impact on ice nucleation. Increasing the electric field strength significantly promotes ice nucleation, i.e. causes the droplets to freeze at higher temperatures. While low electric

field strengths have a negligible influence on ice nucleation, an increase of the electric field strength leads to a higher impact on ice nucleation.

The influence of the electric field is identified to be twofold. The temperature range of droplet freezing is significantly increased due to the fact that the nucleation temperature of individual droplets is increased by the electric field, while the lowest nucleation temperature is almost not affected. In addition, the shape of the droplet survival curves is significantly altered by the electric field. Hence, the electric field mainly promotes ice nucleation inside droplets, which are already prone to ice nucleation at moderate or low degrees of supercooling. As a result the mean nucleation temperatures can be significantly increased by applying an alternating electric field. Generally, ice nucleation inside the droplet is only affected by the conditions present at the moment of nucleation. Thus, the electric field influences ice nucleation on a rather short timescale. A previous exposure of the droplets to an electric field did not influence subsequent ice nucleation in the experiments.

Similar to the nucleation behaviour under the influence of constant electric fields, the nucleation temperature of the individual droplets is almost constant for all experiments. Each droplet has a characteristic temperature of nucleation, which is described by the singular nature of ice nucleation. In addition, not only the temperature reveals a singular behaviour but also the electric field. During the different experiments, usually the same droplets are affected by the electric field, so that the impact of the electric field is not equal for all droplets of one ensemble. Instead, only specific droplets are affected by the electric field. However, the number of droplets affected by the electric field increases with increasing electric field strength. Consequently, the droplets do not only have a characteristic temperature but also a characteristic electric field strength necessary to impact ice nucleation. Furthermore, the frequency of the electric field has a significant influence on ice nucleation. Specific frequencies are able to promote ice nucleation. The influence of the frequency is assumed to be associated with the droplet oscillation and the fluid motion inside the droplet. Hence, alternating electric fields significantly promote ice nucleation depending on the electric field strength and the frequency.

The impact of transient electric fields is investigated using standard lighting and switching impulse voltages to generate electric fields on different characteristic time scales. For this kind of experiment the droplet ensemble is cooled down to a specific temperature, which is kept constant during the experiment. The impact of the transient electric fields is anal-

## 11 Summary

used by the frozen fraction after a specific time interval. Low electric field strengths do not influence ice nucleation, independent of the characteristic time scales of the electric field. In contrast, increasing the electric field strength forces the droplets to freeze, depending on the electric field strength and the degree of supercooling. The higher the degree of supercooling, the more droplets are affected by the electric field.

Generally, the impact of electric fields generated by switching impulse voltages are higher compared to lightning impulse voltages. Hence, a larger number of droplets freeze in case of a switching impulse voltage compared to a lightning impulse voltage for the same conditions with respect to temperature and electric field strength. In addition, droplets exposed to switching impulse voltages are significantly deformed by the electric field, as already seen under ambient conditions. The deformation of the droplet appears as a Taylor cone and results in the release of tiny droplets. Consequently, the droplets are disintegrated over time by the electric field.

The experiments revealed not only long term effects but also effects on a short timescale. A high-speed camera is used to investigate the moment of nucleation and revealed that the individual droplets have a significant nucleation delay with respect to the electric field. The impact of the transient electric field does not only impact nucleation on a molecular scale but also on a macroscopic scale. Due to the fact that numerous droplets freeze after the electric field has already decayed it is assumed that the droplet motion and oscillation as well as the associated shear flow inside the droplet might impact the nucleation. In summary, transient electric fields can be used to force ice nucleation inside sessile droplets.

The investigation of the impact of electric fields on homogeneous ice nucleation was limited to constant electric fields because the emulsified droplets could not be stabilized under the impact of alternating and transient electric fields. To prevent coalescence of the droplets, the electric field strength has to be increased very slowly. For the tested electric field strengths no significant influence on ice nucleation could be observed.

In summary, the conducted experiments expand the knowledge about the behaviour of sessile water droplets under the influence of electric fields under various different conditions. Several influencing factors are identified to significantly impact the behaviour of the droplets. The control of these parameters enable an active manipulation of the droplet behaviour. However, to control these parameters fundamental knowledge of the associated physical mechanisms is necessary. The present study contributes

to a better understanding of these physical mechanisms and might be the base for further investigations finally resulting in optimized applications. Especially, the extended knowledge about the impact of electric charges, the partial discharge inception of water droplets and the impact of electric fields on ice nucleation is important for the development, operation and optimization of high-voltage insulators to ensure a reliable and efficient power transmission and distribution under various different conditions.



## 12 Conclusions and outlook

The results of this study extend the knowledge of the behaviour of water droplets under the impact of high electric fields under various ambient conditions. The various experiments performed under well-defined conditions allow clear conclusions about the physical mechanisms and the influencing factors involved. Simultaneously, the research questions defined in the opening of the study are largely answered and the following objectives have been met:

### *Droplets under ambient conditions*

- ✓ Impact of electric charges on the motion and oscillation of sessile droplets depending on the droplet volume, droplet charge, electric field strength, frequency and type of the electric field.
- ✓ Influence of electric charges on the partial discharge inception field strength of sessile single and multiple droplets depending on the droplet volume, droplet charge, electric field strength and frequency of the electric field.
- ✓ Interaction of two nearby droplets under the impact of transient electric fields depending on the electric field strength, impulse type, droplet volume and droplet-droplet separation.

### *Supercooled droplets - ice nucleation*

- ✓ Development and build of an experimental setup to investigate the impact of electric fields on ice nucleation under well defined conditions with respect to the electric field and temperature.
- ✓ Influence of electric fields on ice nucleation depending on the electric field strength, type of the electric field, frequency, droplet ensemble and temperature.
- (✓) Difference between homogeneous and heterogeneous ice nucleation under the impact of electric fields.

The impact of alternating and transient electric fields on homogeneous ice nucleation is not yet completely clear and needs further investigation. Hence, this objective has only partially been achieved.

In addition, the performed experiments revealed new results and conclusions, which raised further questions about the underlying physical mechanisms and the influencing factors. These questions have to be

investigated and answered in future studies. Subsequently, the open questions are defined and highlighted for the different boundary conditions.

### **Droplets under ambient conditions**

The impact of electric charges on the motion of a sessile droplet was identified within this work. However, the motion of a droplet oscillating in the first resonance mode was not affected by the presence of electric charges. Instead, the droplet always behaves as a charged droplet, independent of the amount of charge present on the droplet. The physical reason for this behaviour is still unknown and requires further investigation. A possible reason is the non-axisymmetric motion of the droplet, which results in an internal flow inside the droplet causing the droplet to oscillate with the same frequency as the applied voltage. Hence, the internal flow of a droplet oscillating in first resonance should be investigated using particle image velocimetry or numerical simulations to reveal whether the behaviour is caused by the internal flow of the droplet.

Furthermore, the impact of charges on the inception of partial discharges was investigated. It was shown that the prediction of the partial discharge inception field strength is rather complicated for water droplets, because of the deformation of the droplets under the influence of large electric fields. Thus, reliable theoretical models for prediction of the partial discharge inception field strength are still missing. The newly achieved results together with already existing results can be used to develop new theoretical models to predict the occurrence of partial discharges for sessile water droplets. This might lead to an increased knowledge about the ageing behaviour of high-voltage insulators. Finally, more reliable prediction models to determine the lifetime of high-voltage insulators can be developed with the extended knowledge.

While the behaviour of single and two adjacent droplets was investigated with respect to the inception of partial discharges and the coalescence of the neighbouring droplets, the interaction of multiple sessile droplets with differing sizes is still unknown. The investigation of more complex systems including multi-droplet arrangements, might reveal different interaction mechanisms. In addition, the interaction of multiple droplets might have an impact on the behaviour of each individual droplet and the inception of partial discharges. Such investigations would not only

extend the knowledge to develop reliable prediction models for partial discharges, but would also reproduce conditions present in applications more accurately.

## **Supercooled droplets - ice nucleation**

The influence of electric fields on ice nucleation was extensively studied in this work. However, existing theoretical models were unable to describe the observed behaviour. While the theoretical models are generally developed for constant electric fields, the impact of a varying frequency or transient electric fields on ice nucleation is not captured by the theoretical models. Consequently, the existing models presumably are based on a different physical mechanism as it is present in the experiments.

For the development of such physics based theoretical models the experimental investigations should be enlarged to examine the impact of the frequency of an electric field on ice nucleation in more detail. As part of this work it was shown that the frequency significantly influences ice nucleation. The interaction of the droplet oscillation and the frequency of the electric field on ice nucleation was not investigated in detail. It is assumed that mainly the oscillation, especially in resonance, of the droplets affects ice nucleation, which still has to be confirmed using additional investigations. The results will improve the understanding of the underlying mechanisms and might help to develop theoretical models.

While the present work focuses on the investigation of the underlying physical mechanisms, the results can still be used to optimize applications. The field of anti-icing research, including the development of anti-icing surface and methods, is of increasing importance for aircraft or power transmission and distribution systems. Repeating the conducted experiments with different substrates can reveal additional applications, which possibly benefit from the presence of an actively controlled electric field. Hence, the existing anti-icing methods or surfaces could be improved and further optimized based on these experiments.

The impact of alternating and transient electric fields on emulsified droplets could not be investigated within the scope of this study. The emulsified droplets could not be stabilized to resist coalescence under the impact of time-variant electric field. Thus, a new method should be developed to stabilize emulsified droplets. The new method should prevent

## *12 Conclusions and outlook*

coalescence of the droplet with and without the presence of alternating and transient electric fields and should have a negligible impact on homogeneous ice nucleation. The results of further experiments possibly reveal the physical mechanism behind the influence of electric fields on ice nucleation, and thus are essential for the development of theoretical models.

In conclusion, the existing experiments should be extended to determine the impact of influencing factors in more detail. Furthermore, the experimental investigations should be used to develop theoretical models. Both, the experimental investigations and the prediction models generally expand the knowledge of the impact of electric fields on sessile water droplets and enable the optimization of certain applications.

# Appendix

## A Electrical circuit for the measurement of partial discharges

A schematic of the electrical circuit for the measurement of partial discharges (PDs) according to IEC 60270 is shown in Fig. A.1. An alternating voltage  $U$  generated by a high-voltage transformer is supplied to the specimen  $C_a$ . The impedance  $Z$  (ohmic resistor) acts as a filter and limits the current in case of a breakdown of the specimen. Furthermore, it prevents charges to flow towards the high-voltage source to ensure an accurate measurement of the PD impulses. A coupling capacitor  $C_k$  is used to determine the (apparent) charge of the PDs. The PDs generated by the specimen cause electric charges to flow from the coupling capacitor to the specimen. A calibration of the charge prior to the measurement enables the accurate measurement of the charge, i.e. the PD impulse. The measurement instrument MI is connected with a connection cable CC to the coupling device CD. The change of charge on the coupling capacitor is recognized by the measurement instrument and correlated to the applied voltage. For the present work, the PD measurement system MPD 600 from Omicron is used. The calibration and the measurement are performed according to the IEC 60270 standard.

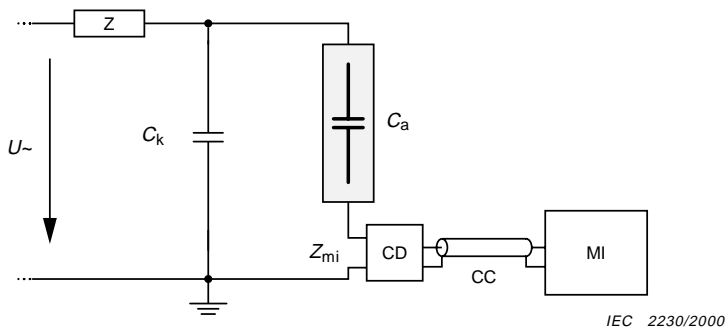


Figure A.1: Electrical circuit for the measurement of partial discharges according to IEC 60270. Reproduced from IEC 60270 ed.3.0, Copyright © 2000 IEC Geneva, Switzerland. [www.iec.ch](http://www.iec.ch).

## B Measurement setup to determine the electric surface potential on silicone rubber

---

---

The content of this chapter is partly based on the Master thesis of Jan Engelhardt [58], and has already been partially published in the following publication and conference proceeding:

- [152] Löwe, J.-M., Secklehner, M., and Hinrichsen, V. Investigation of Surface Charges on Polymeric Insulators and the Influence of Sessile Water Droplets. In *2017 INSUCON - 13th International Electrical Insulation Conference (INSUCON)*, pages 1–7. IEEE, 2017. ISBN 978-1-9998-1569-1. doi:10.23919/INSUCON.2017.8097170
- [155] Löwe, J.-M., Engelhardt, J., Secklehner, M., and Hinrichsen, V. Determination of the Spatial Impulse Response of Compensating Electrostatic Voltmeters. *IEEE Transactions on Dielectrics and Electrical Insulation*, 27(1):49–57, 2020. doi:10.1109/TDEI.2019.008305

---

---

The measurement of the electric surface potential is performed with an electrostatic voltmeter (TREK Model 431B) equipped with a non-contact square shaped probe (3455ET) and a two-axis positioning system. The measurement setup is shown in Fig. B.2. The specimen is placed on the sample holder, which is mounted on the two-axis positioning system. Two stepper motors (Nema 23) connected to spindle drives are used to independently control the position of the specimen in each direction ( $x$  and  $y$  direction) with a positioning accuracy of up to 40  $\mu\text{m}$ . The position of the specimen is continuously measured by two potentiometers to accurately control the position with respect to the probe of the electrostatic voltmeter. The probe is mounted above the specimen using a height adjustable tripod. The distance between the probe and the surface is fixed for each measurement and is adjusted prior to the measurement. However, the distance is continuously monitored with a laser distance sensor (Waycon LAR-30) during the measurement to determine variations of the distance (e.g., by an uneven surface of the specimen), which would influ-

## B Measurement setup to determine the electric surface potential on silicone rubber

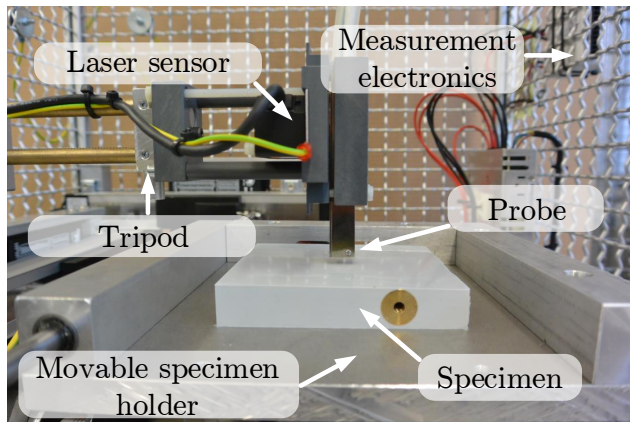


Figure B.2: Experimental setup for automated measurement of the electric surface potential. Not shown: spindle drive, stepper motors and computer.

ence the accuracy of the measurement. The stepper motors are driven with conventional stepper drivers (DQ542MA), which are controlled by an in-house LabVIEW<sup>TM</sup> program. An automated routine continuously changes the position of the specimen below the probe of the electrostatic voltmeter following a specified pattern. For the measurement of the electric surface potential the motion of the specimen is stopped. This ensures an accurate measurement of the electric surface potential with an accuracy of  $\Delta\phi = \pm 1\text{ V}$ . The high accuracy is achieved by a calibration of the sensor depending on the substrate-sensor distance and the probe geometry. A more detailed description of the calibration procedure can be found in [155]. The calibration is necessary to compensate the influence of the surrounding on the measurement of the electric surface potential directly below the probe. Due to the capacitive measurement principle of the electrostatic voltmeter the measurement device can only determine the electric surface potential of a single spot by compensating the effect of nearby influences. In addition to the position of the specimen, the environmental conditions like the pressure, temperature and humidity are continuously logged. The data is captured by a data acquisition system from National Instruments (cDAQ-9174, NI 9229, NI 9401, NI 9219). The measured data is saved by the LabVIEW<sup>TM</sup> program and analysed with

an in-house Matlab<sup>®</sup> code. The automated system enables the selection of the scanned area, speed and resolution.

## C Electric surface potential measurement on silicone rubber

Figure C.3 and C.4 show the electric surface potential distribution on an untreated and a cleaned substrate, respectively. Compared to the illustration presented in Sec. 4.2 both figures are scaled individually to illustrate the maximum, the minimum and the distribution of the electric surface potential in more detail. For an untreated surface the electric surface potential is very inhomogeneous with spots of high positive electric potential ( $\phi > 4$  kV). However, generally the substrate has a negative electric surface potential. Individual locations on the surface have an electric surface potential of  $|\phi| > 5$  kV. In contrast, Fig. C.4 illustrates the mean electric surface potential of ten measurements of a cleaned substrate. The scale was adjusted to visualize the electric potential distribution in more detail. Generally, the spots of high negative or positive electric surface potential

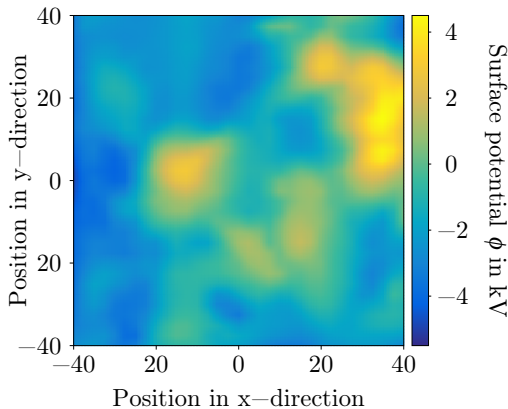


Figure C.3: Measured electric surface potential  $\phi$  of an untreated substrate after it has been stored in a cabinet. Reprinted (adapted) with permission from [152], © 2017 IEEE.

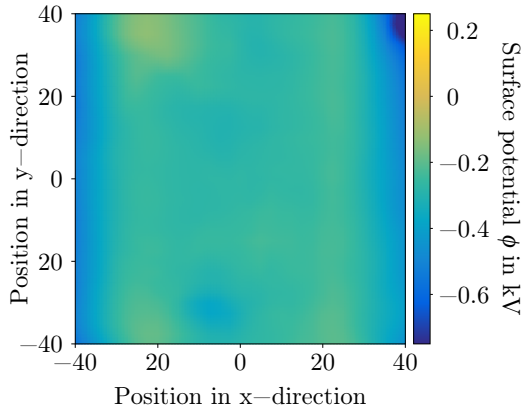


Figure C.4: Mean electric surface potential  $\phi$  for a cleaned substrate. The distribution is determined by the mean of ten measurements. Reprinted figure with permission from [156]. Copyright 2020 by the American Physical Society.

are removed, so that the distribution of the electric surface potential is more homogeneous. The entire surface of the substrate has an electric surface potential of almost zero. Especially, the electric surface potential at the centre of the substrate is very homogeneous. Consequently, the accumulated surface charges were reduced and residual charges are assumed to have a negligible effect.

## **D Calibration of the electric charge measurement**

The accuracy of the electric charge measurement was determined using a well-defined electric charge. This charge was generated by a charge calibrator (Kistler 5357 B) which was directly connected to the Faraday cup. Simultaneously, the electric charge of the Faraday cup was measured by an electrometer (Keithley 6514). The dependence of the measured on the applied electric charge is shown in Fig. D.5. The solid line indicates the perfect agreement between the measured and applied electric charge. The

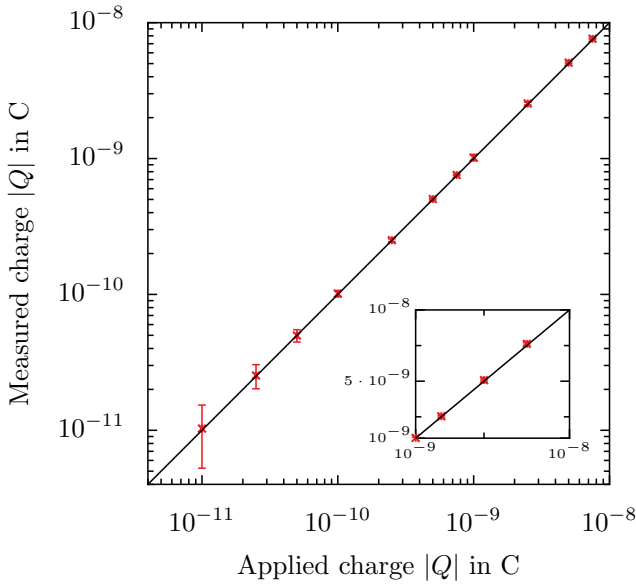


Figure D.5: Measured electric charge  $|Q|$  of the electrometer depending on the applied electric charge  $|Q|$  of the charge calibrator for a large range of electric charges. Reprinted figure with permission from [156]. Copyright 2020 by the American Physical Society.

red crosses show the experimental data. Each experiment was performed at least three times. The error bars represent the measurement uncertainty of the complete measurement chain. All experiments are almost perfectly aligned on the diagonal, so that the measured charge almost perfectly equals the applied charge. Note that the error bars for small amounts of charge appear larger than for high amounts of charge because of the logarithmic scale. Especially in the range of  $Q \approx 10^{-9}$  C, the measurement error is almost negligible. It was also found that the polarity of the electric charge does not have any influence on the measurement accuracy. The measured charge has a high accuracy with a maximum error of  $\Delta Q = 8.12 \cdot 10^{-9}$  C for the full range and  $\Delta Q = 5.5 \cdot 10^{-9}$  C for the range used in this work [156]. The generated droplet charge depends on the needle diameter, the applied voltage between the electrodes of the droplet charger and the droplet volume. The dependence of the droplet charge on

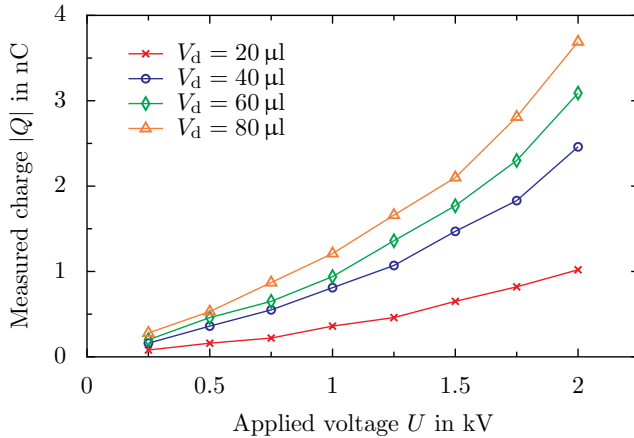


Figure D.6: Resulting electric charge  $|Q|$  of a droplet depending on the droplet volume  $V_d$  and the applied voltage  $U$  between the electrodes of the droplet charger for a needle diameter of  $d = 0.7$  mm.

these parameters for a needle with a diameter of  $d = 0.7$  mm is shown in Fig. D.6. Generally, the behaviour is similar to the presented data for a needle with a diameter of  $d = 0.5$  mm, but the resulting charge is smaller for a larger needle size. The reason for this behaviour is the size of the detaching droplets. The smaller the needle, the smaller are the individual droplets detaching from the needle. The cumulative charge of several small droplets is larger than the cumulative charge of larger droplets with the same resulting volume. Hence, the charge of the droplets produced with a smaller needle diameter is higher.

## E Additional data for charged and uncharged droplets under the influence of alternating electric fields

The presence of the transition region mainly depends on the droplet volume. Both the transition region and the distinct transition can be observed in second and third resonance mode. While no distinct transi-

## Appendix

tion between the regimes can be observed for a droplet with a volume  $V_d = 20 \mu\text{l}$  oscillating in third resonance, a distinct transition is observable for a droplet with a volume of  $V_d = 60 \mu\text{l}$ . The corresponding data is shown in Fig. E.7. The dimensionless frequency ratio, depending on the characteristic ratio of the electric forces, is presented for varying electric charge of the droplet. The dashed line shows the critical characteristic ratio of  $\xi^* = 18.47$ . The corresponding minimum charge  $Q^*$  to change the oscillation behaviour of the droplet yields  $Q^* = 1.29 \text{ nC}$ . It is assumed that the occurrence of the transition region is associated with slightly varying boundary conditions with respect to the electric charge on the droplet or the electric charge on the substrate. The behaviour of the droplet is very sensitive to a change of the electric charge and even small deviations can significant influence the behaviour of the droplets as seen for the distinct transition between the different regimes.

The critical characteristic ratio and corresponding minimum onset charge are determined for all droplet volumes using a representation similar to Fig. E.7. For convenience, not all figures for the different volumes and resonance frequencies are shown. The data of the other volumes follow the

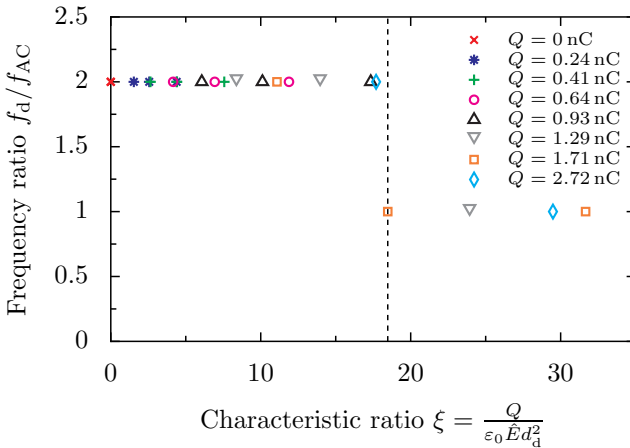


Figure E.7: Dimensionless frequency ratio  $f_d/f_{AC}$  depending on the characteristic ratio  $\xi$  for a droplet oscillating in third resonance mode with a volume of  $V_d = 60 \mu\text{l}$ . The dashed line shows the critical characteristic ratio  $\xi^*$  for the change of the behaviour.

same trend and are indirectly presented by the analysis of the minimum onset charge depending on the droplet volume, see Figs. 5.5 and 5.9 for the second and third resonance mode respectively.

## **F Measurement of electrical properties of gelatin droplets**

A water-gelatin mixture is used to generate inflexible droplets to measure the inception field strength in the absence of any motion of the droplet. However, to accurately reproduce the electrical situation with respect to the field distribution, the gelatin-water mixture must have similar electrical/dielectrical properties compared to water. The electrical/dielectrical properties, namely, the electrical conductivity and the relative permittivity of the water-gelatin mixture, were measured with a Novocontrol Alpha-N High Resolution Dielectric Analyzer with actively controlled temperature (Novocontrol Quatro)<sup>6</sup>.

The electrical conductivity  $\kappa_{\text{el}}$  of the gelatin-water mixture and pure water, depending on the frequency  $f$  and the temperature  $\vartheta$ , is shown in Fig. F.8. The electrical conductivity of the gelatin-water mixture is almost constant for frequencies  $f > 10^2$  Hz and decreases with decreasing frequency. The gradient at low frequencies is constant in the double logarithmic scaled illustration. Generally, the electrical conductivity of the gelatin-water mixture is higher than the electrical conductivity of water for high frequencies ( $f > 10^2$  Hz) and is in the same order of magnitude for smaller frequencies. The characterization of the behaviour of a material under the influence an electric field is mainly defined by the charge relaxation time, which in turn is defined by the electrical conductivity and the relative permittivity.

The relative permittivity  $\varepsilon_r$  of the gelatin-water mixture and pure water, depending on the frequency  $f$  and the temperature  $\vartheta$ , is shown in Fig. F.9. The relative permittivity of water is given as a reference. Generally, the relative permittivity of water is assumed to be constant and yields  $\varepsilon_{r,\text{wa}} \approx 80$ , which can be observed for  $f > 10^4$  Hz. At such high frequencies the relative permittivity of the water is constant. However, decreasing the frequency leads to an increasing relative permittivity. The

---

<sup>6</sup>at the Institute for Condensed Matter Physics (TU Darmstadt) in collaboration with Florian Pabst.

## Appendix

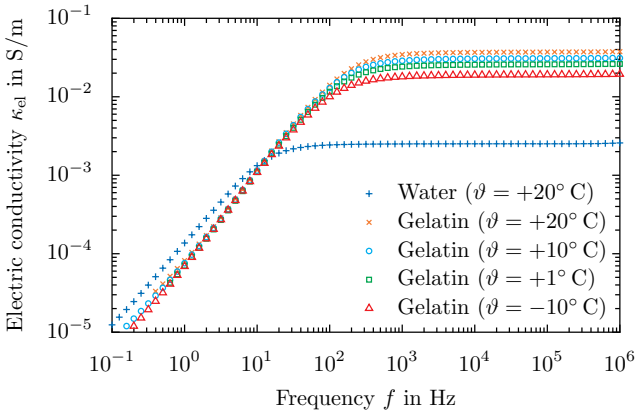


Figure F.8: Measured electrical conductivity  $\kappa_{el}$  depending on the frequency  $f$  and the temperature  $\vartheta$  for water and gelatin.

reason for the increasing relative permittivity is associated with the electrode polarization caused by ionic conduction of water [5] and is also known as Maxwell-Wagner-Sillars polarization [132]. Although deionized water is used, the water might contain free dissolved ions. The presence of an electric field leads to a motion of the ions towards one of the electrodes (depending on their polarity) resulting in the formation of an electric double layer at the interface of the electrode [110, 132]. The electric potential drops rapidly in this double layer, which indicates a huge electrical polarization of the material [110]. Such an electric polarization is associated with an almost field-free bulk. Especially for low frequencies, the electrode polarization can dominate during the measurement of the relative permittivity [110]. The electrode polarization is mainly observed for materials with high electrical conductivity and always appears during the measurement of dielectric properties, leading to extremely large values [132]. Note that the electrode polarization depends on several influencing factors such as the electrode geometry, but cannot be completely prevented during the measurement [110, 132]. Due to the artificial increase caused by the measurement procedure, it is generally assumed that the relative permittivity of water is constant even for low frequencies and yields  $\varepsilon_{r,wa} \approx 80$  [5]. At high frequencies ( $f > 10^5$  Hz) the measured relative permittivity is in good agreement with values from literature.

The same frequency dependence as shown for water is also observed for

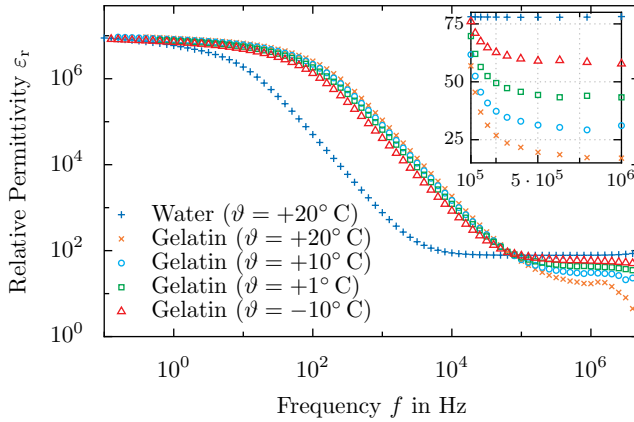


Figure F.9: Measured relative permittivity  $\epsilon_r$  depending on the frequency  $f$  and the temperature  $\vartheta$  for water and gelatin. Reprinted figure (adapted) with permission from [157]. Copyright 2020 by the American Physical Society.

the gelatin-water mixture. The electrode polarization is observed at even higher frequencies which results from the higher electrical conductivity of the water-gelatin mixture compared to water. Due to the fact that the huge increase in relative permittivity is caused by the electrode polarization and is only an artificial effect, the same assumption as for water is applied to the gelatin-water mixture. Hence, the relative permittivity is assumed to be constant independent of the frequency. Similarly, the relative permittivity is determined at high frequencies, where the relative permittivity is constant. Besides the electrical conductivity, the relative permittivity also depends on the temperature of the gelatin-water mixture. The lower the temperature, the higher is the relative permittivity as shown in the insert in Fig. F.9.

## G Accuracy of image processing and droplet motion analysis

The accuracy of the image processing is analysed using three different reference arrangements, which consist of drop like shapes resting on a flat

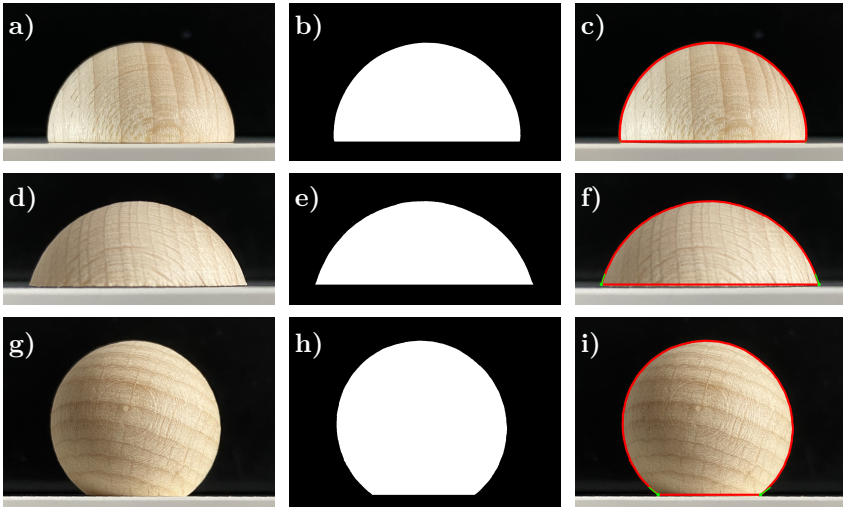


Figure G.10: Different steps of image analysis for various reference objects. For each reference object an original image, a black and white image of the detected shape after edge detection and morphological operations and an image of the detected contour superimposed on the original image is shown. a)-c) images of a half sphere, d)-f) images of reference object imitating a hydrophilic droplet ( $\theta < 90^\circ$ ) and g)-i) images of reference object imitating a hydrophobic droplet ( $\theta < 90^\circ$ ).

surface. Each arrangement replicates the shape of a droplet resting on a surface. The shape of the droplet is mainly influenced by the wetting properties of the substrate, and so a half sphere, a hydrophobic droplet and a hydrophobic droplet are reproduced. An image of each arrangement is analysed in the same manner as the images of the moving droplets. Different steps of the analysis are shown in Fig. G.10. For each arrangement an original image, an image of the detected shape of the droplet and the result from the image detection superimposed on the original image is shown. The visual comparison already reveals a high accuracy of the image detection in all cases. To further classify the accuracy of the procedure the data obtained by the image analysis is compared to the known dimensions. Note that in case of a half sphere the projected area is known

by the dimensions of the half sphere, and thus can be used for the comparison. A comparison of the diameter, the height, the projected area and the contact angles of the arrangements is shown in Table G.2. The reference values of the contact angles are determined using the software ImageJ and the contact angle extension. The analysis is performed by hand.

In case of the half sphere the maximum deviation between the reference value and the data obtained from the image analysis is given for the pro-

Table G.2: Comparison of the data obtained by the image analysis and known dimensions for the different cases shown in Fig. G.10. In this analysis  $d$  is the diameter,  $h$  is the height,  $A_{\text{proj}}$  is the projected area and  $\theta_{\text{right}}$ ,  $\theta_{\text{left}}$  are the right and left contact angle, respectively.

Case	Parameter	Reference	Image analysis
Half sphere			
	$d$ in cm	2.99	2.98
	$h$ in cm	1.54	1.57
	$A_{\text{proj}}$ in cm <sup>2</sup>	3.51	3.73
$\theta < 90^\circ$			
	$d$ in cm	2.80	2.92
	$h$ in cm	1.11	1.11
	$\theta_{\text{right}}$ in $^\circ$	73.9	70.9
	$\theta_{\text{left}}$ in $^\circ$	74.5	69.5
$\theta > 90^\circ$			
	$d$ in cm	3.06	3.09
	$h$ in cm	2.78	2.79
	$\theta_{\text{right}}$ in $^\circ$	143.4	142.6
	$\theta_{\text{left}}$ in $^\circ$	144.1	144.0

## Appendix

jected area and yields  $\Delta A_{\text{proj}} = 6.25\%$ . For the diameter and the height the deviations are  $\Delta d = 0.27\%$  and  $\Delta h = 2.21\%$ , respectively. In case of  $\theta < 90^\circ$  the maximum deviation is given for the left contact angle  $\Delta\theta_{\text{left}} = 7.19\%$ . For the diameter and the right contact angle the deviations are  $\Delta d = 4.1\%$  and  $\Delta\theta_{\text{right}} = 4.23\%$ , respectively. For  $\theta > 90^\circ$  the deviation between the reference and the image analysis yields  $\Delta d = 0.97\%$  for the diameter,  $\Delta h = 0.35\%$  for the height as well as  $\Delta\theta_{\text{right}} = 0.56\%$  and  $\Delta\theta_{\text{left}} = 0.1\%$  for the right and left contact angle, respectively. Thus, the shape of the droplet can be analysed with high accuracy. The overall accuracy of the method mainly depends on the accurate detection of the droplet boundary because parameters like droplet height, width, area or contact angle are derived from the detected boundary. The more accurate the detection of the droplet boundary, the more accurate is the temporal evolution of these parameters. Due to the fact that the video data is analysed frame by frame the detection accuracy is assumed to be constant during the analysis. This assumption is valid because the recording rate of the camera is high enough so that the droplet appears to be stationary in each frame. Furthermore, the motion of the droplet is rather small, and thus does not affect the image quality with respect to the illumination or contrast.

Besides the image detection the accuracy of the mathematical operations to determine the frequency of the signal are important. To verify the correct analysis of the signals several test signals were tested. To ensure accurate results, the FFT was performed with respect to the Nyquist criterion. In addition, the sampling frequency of the video data was chosen to be at least ten times higher than the highest expected frequency. The test signals confirmed the proper functionality of the routine for the given frequencies.

Consequently, the automated analysis performed with the in-house Matlab<sup>®</sup> code has a high accuracy. Furthermore, the fixed criteria for the analysis (detection of the droplet boundary) lead to repeatable results. In contrast, an analysis by hand is less repeatable because the criterion to determine the droplet contour is not fixed and influenced by the subjective impression of the analyser. Besides the good accuracy, the automated analysis of the experiments enables the analysis of numerous experiments in a short time.

## **H Measurement of electric charge of raindrops**

---

---

The content of this chapter is partly based on the Bachelor theses of Henrik Scholz [234] and Johannes Hollerith [104].

---

---

The measurement of the electric charge of raindrops is performed with a specifically designed measurement setup. A schematic of the setup is shown in Fig. H.11, which consists of three main components, namely, the Faraday cup, a tank to collect water and a waterproof box protecting the electronics and measurement devices. The measurement of the electric charge and the amount of the liquid is separated to ensure an accurate measurement of each quantity. The charge is determined using a Faraday cup, similar to the procedure shown in Chap. 4. As a measurement device a charge amplifier (Kistler 5073A) is used, because it has a small design and a good accuracy. The charge amplifier is directly connected to the Faraday cup with a shielded cable. Prior to the measurements the charge amplifier was calibrated using a charge calibrator (Kistler 5357B). The obtained results are almost similar to the results shown in App. D. The charge measurement is automatically activated as soon as rain is detected. The rain is collected by a tank and the water level is continuously measured (Adafruit eTape Liquid Level Sensor). An increasing liquid level in the tank is detected and activates the charge measurement. The measurement is controlled by an Arduino Uno. The charge is continuously measured as long as the liquid level increases. Once, the liquid level is constant the charge is measured for three more minutes and is subsequently paused. The liquid tank is automatically emptied by an automatic valve if the tank is full. In contrast, the Faraday cup is not emptied, because the size of the Faraday cup was chosen appropriately to prevent a completely filling of the cup. Generally, the evaporation of the water is used to empty the Faraday cup. However, in exceptional circumstances the cup might also be complete filled. The collected data is saved on a memory card. In addition to the charge and the liquid level, the actual time, humidity and temperature (Adafruit SHT10) are also recorded. The measurement setup is powered by two 12 V batteries and can autonomously perform measurements for several days. The roof of the high-voltage laboratories was chosen as installation location to ensure a safe and unhindered rain collection.

## Appendix

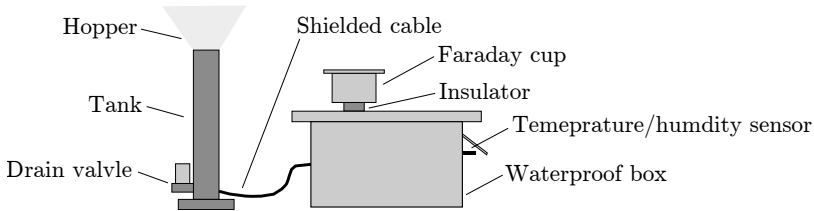


Figure H.11: Schematic of the measurement setup to determine the electric charge of rain.

Note that this device is not able to measure the charge of single raindrops, but rather measures the net charge of a specific amount of liquid. This is due to the limited accuracy and sensitivity of the measurement of the liquid level. Furthermore, the measurement is based on the assumption that both the Faraday cup and the tank are exposed to the same amount of rain per square meter. Thus, the estimated liquid volume and the measured charge are correlated. A direct measurement of the liquid volume present in the Faraday cup is not possible.

The measurements revealed that the collected rain almost always contains a positive or negative net charge. Consequently, it is assumed that sessile droplets formed by rain are also charged. This assumption is also supported by other investigations reported in literature [36, 91, 246, 256].

## I Measurement of electrical properties of ice

During the experiments to determine the influence of an electric field on ice nucleation, the temperature of water is varied over a wide range. In addition, the water undergoes a phase change from liquid to solid. The phase transition and the temperature change can significantly influence the electric/dielectric properties of water. Hence, the electric/dielectric properties, namely the electrical conductivity and the relative permittivity, of water in liquid and solid state are investigated. Similar to the gelatin-water mixture, the measurement was performed with a Novocontrol Alpha-N High Resolution Dielectric Analyzer with actively controlled temperature (Novocontrol Quatro)<sup>7</sup>.

<sup>7</sup>at the Institute for Condensed Matter Physics (TU Darmstadt) in collaboration with Florian Pabst.

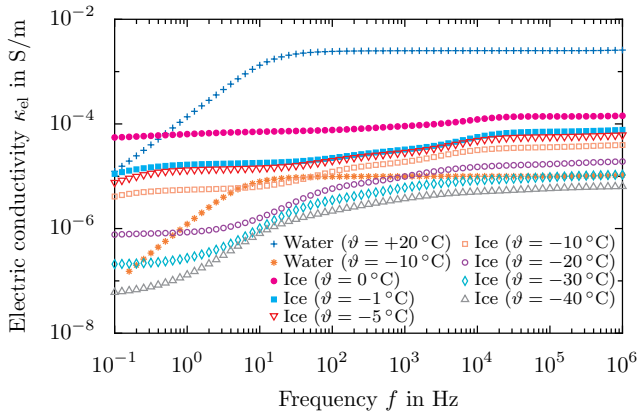


Figure I.12: Measured electrical conductivity  $\kappa_{\text{el}}$  depending on the frequency  $f$  and the temperature  $\vartheta$  for water and ice.

The resulting electrical conductivity  $\kappa_{\text{el}}$  of water and ice depending on the temperature  $\vartheta$  and the frequency  $f$  are shown in Fig. I.12. For high frequencies the electrical conductivity is constant and decreases for a decreasing frequency. While the electrical conductivity decreases with a constant gradient at low frequencies, the electrical conductivity has no constant gradient in case of ice, independent of the temperature. In addition, the gradient is much smaller for ice compared to water. Both the electrical conductivity of water and ice strongly depends on the temperature. A decreasing temperature leads to a decreasing electrical conductivity. Note that water at  $\vartheta = -10^\circ\text{C}$  is still liquid in this case but in a supercooled state. Decreasing the temperature, decreases the electrical conductivity by several orders of magnitude.

In addition to the electrical conductivity, the relative permittivity  $\varepsilon_r$ , depending on the temperature  $\vartheta$  and the frequency  $f$ , is measured for ice and water. The results are shown in Fig. I.13. As already mentioned in App. F the increase of the relative permittivity is caused by electrode polarization and artificially increases the permittivity. Hence, the relative permittivity of water and ice is mainly determined at high frequencies. For liquid water, the relative permittivity increases with decreasing temperature. As soon as the water is frozen, the relative permittivity is significantly reduced compared to liquid water. The relative permittivity of ice still depends on the temperature and decreases with decreasing tempera-

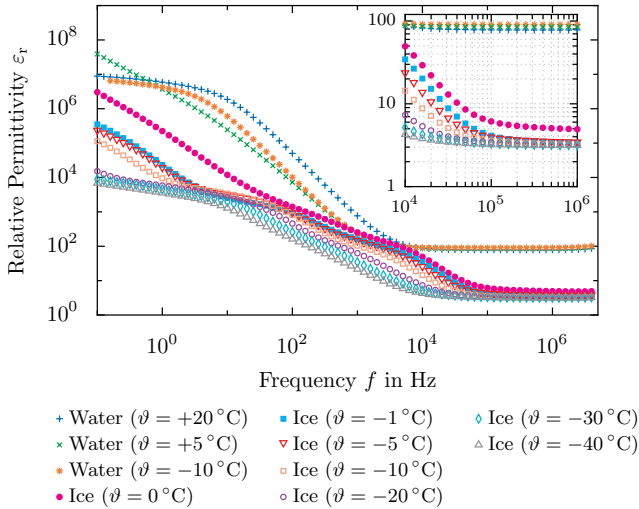


Figure I.13: Measured relative permittivity  $\epsilon_r$  depending on the frequency  $f$  and the temperature  $\vartheta$  for water and ice.

ture. The measured relative permittivity of ice is assumed to be constant, similar to water. Comparing the relative permittivity of ice at high frequencies with values from literature ( $\epsilon_{r,ice} = 3.07, \dots, 3.3$  at  $\vartheta = -40^\circ\text{C}$ ) reveals a very good agreement [102]. Consequently, the relative permittivity and conductivity of frozen droplets are significantly reduced compared to liquid droplets. This significantly impacts the electric field distribution around the droplet.

## J Distorted electric field distribution

The electric field is generated using two high-voltage sources to generate a homogeneous electric field tangentially aligned to the sapphire substrate. The reason for the use of two high-voltage sources with opposite polarity is given by the grounded aluminium foil below the ceramic body. This grounded foil protects the electronics below the ceramic body from the electric field but also influences the electric field distribution. Using only one high-voltage source leads to a distorted electric field distribution as shown in Fig. J.14. The results are obtained from a numerical simulation

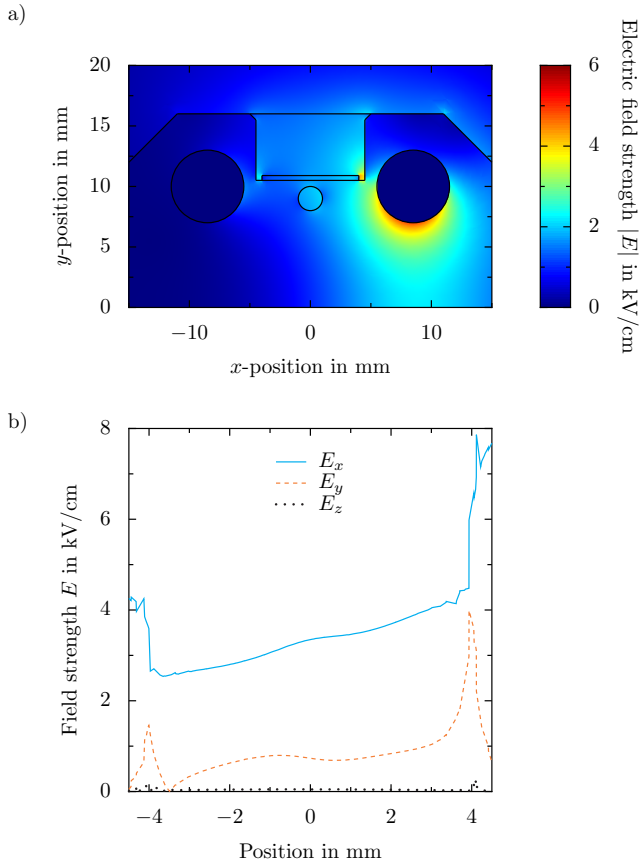


Figure J.14: Numerically obtained electric field distribution in the  $x - y$  plane of the ceramic without droplets using only one high-voltage source in a) and the corresponding components of the electric field strength  $E_i$  along the  $x$  direction in the centre of the ceramic at the sapphire substrate surface in b). The electric field is generated using a single voltage signal of  $\hat{U} = 4.0$  kV in combination with a grounded electrode. Note that the field distribution is qualitatively the same for other types of electric fields. Reprinted (adapted) with permission from [160], under the Creative Common License - Attribution 4.0 International (CC BY 4).

performed with COMSOL Multiphysics<sup>®</sup>. One electrode is connected to the high-voltage source and the other electrode is grounded. Due to the fact that the grounded foil below the ceramic body and one electrode have the same electric potential, the electric field is not homogeneous at the position of the droplets. As shown in Fig. J.14b the electric field strength is not constant at the position of the droplets and depends on the position of the individual droplets. The electric field strength decreases with increasing distance from the right electrode. Hence, the individual droplets are exposed to different electric field strengths, which clearly limits the comparability of the individual nucleation events. Consequently, two high-voltage sources with opposite polarity have to be used to protect the electronics and to generate a well-defined and tangentially aligned electric field.

## K Literature review of ice nucleation investigations

In the past, several investigations were performed to determine the impact of electric fields on ice nucleation. An overview of the most important literature is shown in Table K.3. Although the table may not include all previous investigations, still a wide range of electric field strengths including high and low electric field strengths have been investigated for constant electric fields. In contrast, only low electric field strengths are investigated for alternating electric fields. Comparing the electric field strength applied during the present experiments to the electric field strength of previous investigations reveals that the employed electric field strength in this study are much larger. In addition, the investigated frequencies of the previous investigations are generally much higher  $f > 10^3$  Hz. Note that the impact of electric fields with low frequencies relevant for power transmission and distribution have not been investigated in detail. Hence, the present study provides an extension of available data and aims to determine the impact of low frequency electric fields on ice nucleation.

In addition to constant and alternating electric fields, transient electric fields were already investigated and proven to impact ice nucleation. However, the number of investigations is limited and is extended with the presented experiments.

Table K.3 includes experimental investigations and molecular dynamics

simulations. Due to the different experimental setups and boundary conditions the comparability between the different investigations is limited.

Table K.3: Overview of the most important investigations focusing on the impact of electric fields on ice nucleation. The overview contains experimental investigations and molecular dynamic simulations.

Author & reference	Type	$f_E$ in Hz	$\hat{E}_{\max}$ in kV/cm
Rau [222]	DC	0	60
Pruppacher [214]	DC	0	30
Rouleau et al. [227]	DC	0	n.a. <sup>8</sup>
Doolittle and Vali [53]	DC	0	6
Marand and Stein [168]	DC	0	100
Svishchev and Kusalik [253]	DC	0	$5 \cdot 10^4$
Svishchev and Kusalik [254]	DC	0	$1 \cdot 10^5$
Zangi and Mark [293]	DC	0	$5 \cdot 10^4$
Wei et al. [277]	DC	0	1
Orlowska et al. [197]	DC	0	60
Yan and Patey [287]	DC	0	$5 \cdot 10^4$
Xanthakis et al. [283]	DC	0	n.a. <sup>9</sup>
Nie et al. [192]	DC	0	$5 \cdot 10^5$
Carpenter and Bahadur [31]	DC	0	800
Dawson and Cardell [47]	DC	0	4
Wilson et al. [279]	DC	0	0.5
Peleg et al. [203]	DC	0	$10^3$
Salt [232]	AC	60	n.a. <sup>10</sup>

<sup>8</sup>No information about the electric field, up to 8kV applied to a wire

<sup>9</sup>No information about the electric field, 12kV applied to the sample with 6 mm thickness and a small air gap

<sup>10</sup>No information about the electric field, up to 15 kV applied to the sample

Continuation of Table K.3			
Author & reference	Type	$f_E$ in Hz	$\hat{E}_{\max}$ in kV/cm
Sun et al. [251]	AC	$10^3, \dots, 2 \cdot 10^5$	$5 \cdot 10^{-3}$
Koizumi et al. [127]	AC	$1, \dots, 9 \cdot 10^6$	0.8
Stan et al. [247]	AC	$3, \dots, 100 \cdot 10^3$	1.6
Yahong et al. [286]	AC	$0.5, \dots, 10 \cdot 10^6$	$\approx 0.25$
Ma et al. [165]	AC	$10^5, \dots, 10^7$	1
Peleg et al. [203]	AC	$0.01, \dots, 10^5$	$10^3$
Braslavsky and Lipson [24]	Transient	-	n.a. <sup>11</sup>
Mandal and Pradeep Kumar [167]	Transient	-	$\approx 10$
Petersen et al. [205]	Transient	-	n.a. <sup>12</sup>
Yang et al. [290]	Transient	-	$4.5 \cdot 10^5$
End of Table			

## L Temperature calibration for emulsified droplets

The temperature calibration described in Löwe et al. [160] was performed with a sapphire glass sheet and sessile droplets. In contrast, the investigation of emulsified droplets uses a different sample holder, which supersedes the calibration using the glass sheet. The temperature correlation between the temperature measurement inside the ceramic block and the droplet position significantly depends on the geometry of the sample holder. To ensure an accurate temperature measurement, the calibration is repeated using the new sample holder. During the calibration the experimental setup should reproduce the situation during the experiments with emulsified droplets as accurately as possible. Hence, the temperature sensor

<sup>11</sup>No information about the electric field, up to 10 kV applied to the sample

<sup>12</sup>No information about the electric field, up to 6.5 kV applied to the sample

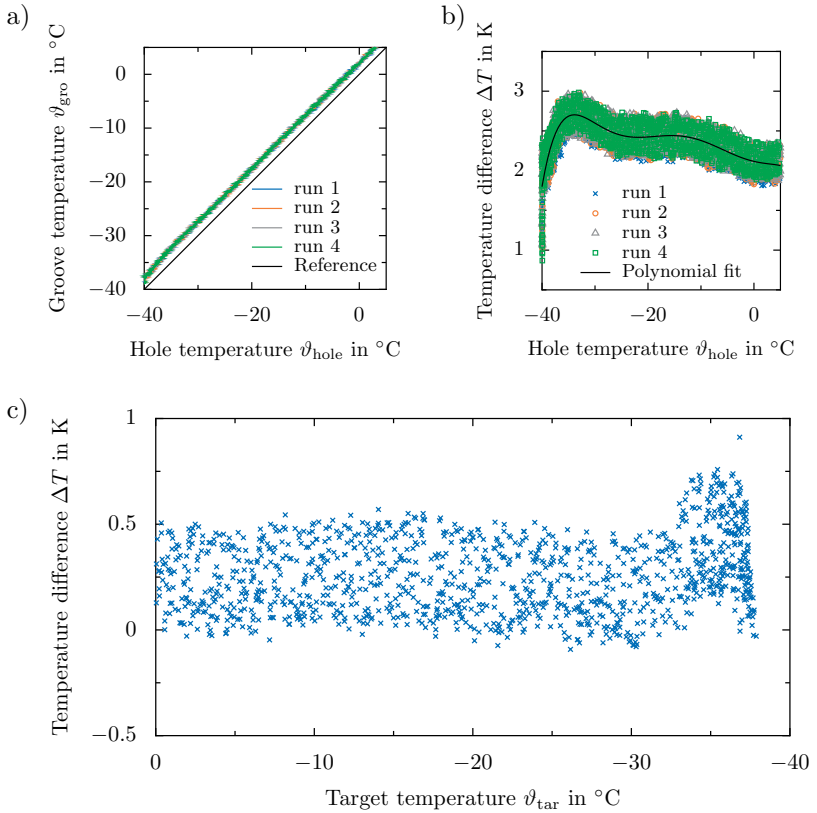


Figure L.15: a) Temperature at the droplet position  $\vartheta_{\text{gro}}$ , depending on the temperature inside the ceramic  $\vartheta_{\text{hole}}$ . b) Temperature difference  $\Delta T = |\vartheta_{\text{gro}} - \vartheta_{\text{hole}}|$ , depending on the temperature inside the ceramic and c) temperature difference between target temperature and current temperature  $\Delta T$ , depending on the target temperature  $\vartheta_{\text{tar}}$ .

has to be placed inside the fluid channel of the sample holder directly at the position of the emulsified droplets. A type K thermocouple is inserted into the fluid channel and the sample holder is placed in the groove inside the ceramic body. The sample holder and the air gap between the

## Appendix

sample holder and the groove are filled with Novec<sup>TM</sup> 7500 to reproduce the experimental configuration as accurate as possible. Afterwards, the sample is cooled down with a constant cooling rate of  $\dot{T} = 5 \text{ K/min}$  and both the temperature inside the ceramic body and at the droplet position are recorded. The experiment is repeated four times to minimize the influence of the statistical scatter. The temperature at the droplet position  $\vartheta_{\text{gro}}$ , depending on the temperature inside the ceramic body  $\vartheta_{\text{hole}}$  down to temperature of  $\vartheta = -40^\circ\text{C}$ , is shown in Fig. L.15a. The solid black line indicates the perfect agreement between both temperatures, resulting in a vanishing temperature difference between the droplets position and the ceramic body. As shown by the data, the temperature of the droplets  $\vartheta_{\text{gro}}$  is always higher than the temperature of the ceramic body  $\vartheta_{\text{hole}}$ . The temperature difference  $\Delta T = |\vartheta_{\text{hole}} - \vartheta_{\text{gro}}|$ , depending on the temperature inside the ceramic, is shown in Fig. L.15b. The higher the degree of supercooling, the higher is the deviation between both temperatures. Note that the temperature difference  $\Delta T$  decreases for supercoolings in the range of  $\vartheta \approx -38^\circ\text{C}$  because at such low temperatures the experimental setup cannot follow the desired cooling rate of  $\dot{T} = 5 \text{ K/min}$  any more. In this case the groove temperature converges towards the temperature of the ceramic block, which leads to a smaller deviation between both temperatures. Even if the experimental setup cannot follow the desired cooling rate at such high degrees of supercooling, the experimental setup has an accurate temperature control.

In general, ice nucleation in water droplets is observed at temperatures higher than  $\vartheta = -40^\circ\text{C}$ , so that the experimental setup is only operated in the calibrated range with a high accuracy. To accurately determine the temperature of the droplets, depending on the measured temperature inside the ceramic body, the calculated temperature difference  $\Delta T$  of the four runs is fitted by a polynomial of sixth degree. The polynomial is used to calculate the droplet temperature depending on the current temperature inside the ceramic. The accuracy of the correction is tested by comparing the deviation between the desired target temperature and the current temperature of the droplets  $\Delta T$ . The deviation of the temperatures, depending on the desired target temperature  $\vartheta_{\text{tar}}$ , is shown in Fig. L.15c. As shown by the data the temperature of the droplets only varies about 0.5 K down to temperature of  $\vartheta \approx -35^\circ\text{C}$ . For larger a supercooling the deviation increases because the experimental setup is approaching the lowest temperature possible for the given configuration. Taken into account the accuracy of the temperature sensor (Fiso FOT-

### *L Temperature calibration for emulsified droplets*

L-SD)  $\delta T = \pm 1$  K, the maximum temperature uncertainty is given by  $\delta T = 1.5$  K down to a temperature of  $\vartheta \approx -35$  °C. Thus, the temperature of the droplets can be accurately controlled.



## Bibliography

- [1] Acharya, P. V. and Bahadur, V. Fundamental Interfacial Mechanisms Underlying Electrofreezing. *Advances in Colloid and Interface Science*, 251:26–43, 2018. doi:10.1016/j.cis.2017.12.003.
- [2] Akbar, M., Ullah, R., and Alam, S. Aging of Silicone Rubber-based Composite Insulators under Multi-stressed Conditions: An Overview. *Materials Research Express*, 6(10):102003, 2019. doi:10.1088/2053-1591/ab3f0d.
- [3] Alsabagh, A. S. Y., Tiu, W., Xu, Y., and Virk, M. S. A Review of the Effects of Ice Accretion on the Structural Behavior of Wind Turbines. *Wind Engineering*, 37(1):59–70, 2013. doi:10.1260/0309-524X.37.1.59.
- [4] Amin, M., Akbar, M., and Salman, M. Composite Insulators and their Aging: An Overview. *Science in China Series E: Technological Sciences*, 50(6):697–713, 2007. doi:10.1007/s11431-007-0053-x.
- [5] Angulo-Sherman, A. and Mercado-Uribe, H. Dielectric Spectroscopy of Water at Low Frequencies: The Existence of an Isopermittive Point. *Chemical Physics Letters*, 503(4-6):327–330, 2011. doi:10.1016/j.cplett.2011.01.027.
- [6] Atkinson, J. D., Murray, B. J., Woodhouse, M. T., Whale, T. F., Baustian, K. J., Carslaw, K. S., Dobbie, S., O’Sullivan, D., and Malkin, T. L. The Importance of Feldspar for Ice Nucleation by Mineral Dust in Mixed-phase Clouds. *Nature*, 498(7454):355–358, 2013. doi:10.1038/nature12278.
- [7] Atkinson, J. D., Murray, B. J., and O’Sullivan, D. Rate of Homogenous Nucleation of Ice in Supercooled Water. *The Journal of Physical Chemistry. A*, 120(33):6513–6520, 2016. doi:10.1021/acs.jpca.6b03843.
- [8] Baars, W., Stearman, R., and Tinney, C. A Review on the Impact of Icing on Aircraft Stability and Control. *ASD Journal*, 2:35–52, 2010.
- [9] Barlow, T. W. and Haymet, A. D. J. ALTA: An Automated Lag-time Apparatus for Studying the Nucleation of Supercooled

## Bibliography

- Liquids. *Review of Scientific Instruments*, 66(4):2996–3007, 1995. doi:10.1063/1.1145586.
- [10] Bartels, F. Droplet-Driven Electrowetting Displays. In Chen, J., Cranton, W., and Fihn, M., editors, *Handbook of Visual Display Technology*, pages 1747–1759. Springer Berlin Heidelberg, Berlin, Heidelberg, 2012. ISBN 978-3-540-79566-7. doi:10.1007/978-3-540-79567-4\_104.
- [11] Battino, R., Seybold, P. G., and Campanell, F. C. Correlations Involving the Solubility of Gases in Water at 298.15 K and 101325 Pa. *Journal of Chemical & Engineering Data*, 56(4):727–732, 2011. doi:10.1021/je101070h.
- [12] Becker, R. and Döring, W. Kinetische Behandlung der Keimbildung in übersättigten Dämpfen. *Annalen der Physik*, 416(8):719–752, 1935. doi:10.1002/andp.19354160806.
- [13] Benteitis, N. and Krause, S. Droplet Deformation in DC Electric Fields: The Extended Leaky Dielectric Model. *Langmuir : the ACS Journal of Surfaces and Colloids*, 21(14):6194–6209, 2005. doi:10.1021/la0472448.
- [14] Berg, G., Lundgaard, L. E., and Abi-Chebel, N. Electrically Stressed Water Drops in Oil. *Chemical Engineering and Processing: Process Intensification*, 49(12):1229–1240, 2010. doi:10.1016/j.cep.2010.09.008.
- [15] Berg, J. C., editor. *Wettability*, volume 49 of *Surfactant Science Series*. Dekker, New York, 1993. ISBN 0-8247-9046-4.
- [16] Berge, B. and Peseux, J. Variable Focal Lens Controlled by an External Voltage: An Application of Electrowetting. *The European Physical Journal E*, 3(2):159–163, 2000. doi:10.1007/s101890070029.
- [17] Bernoulli, D. *Danielis Bernoulli ... Hydrodynamica, sive de viribus et motibus fluidorum commentarii : opus academicum ab auctore, dum Petropoli ageret, congestum*. sumptibus Johannis Reinholdi Dulseckeri and Typis Joh. Deckeri, typographi Basiliensis, 1738.
- [18] Berthier, J. *Micro-Drops and Digital Microfluidics*. Micro and Nano Technologies. Elsevier Science, Burlington, 2. edition, 2012. ISBN 978-1-4557-2550-2.

- [19] Bienia, M., Vallade, M., Quilliet, C., and Mugele, F. Electrical-field-induced Curvature Increase on a Drop of Conducting Liquid. *Europhysics Letters*, 74(1):103–109, 2006. doi:10.1209/epl/i2006-10003-3.
- [20] Bigg, E. K. The Supercooling of Water. *Proceedings of the Physical Society. Section B*, 66(8):688–694, 1953. doi:10.1088/0370-1301/66/8/309.
- [21] Bigg, E. K. The Formation of Atmospheric Ice Crystals by the Freezing of Droplets. *Quarterly Journal of the Royal Meteorological Society*, 79(342):510–519, 1953. doi:10.1002/qj.49707934207.
- [22] Borzák, I. and Cummings, P. T. Electrofreezing of Water in Molecular Dynamics Simulation Accelerated by Oscillatory Shear. *Physical Review E*, 56(6):R6279–R6282, 1997. doi:10.1103/PhysRevE.56.R6279.
- [23] Brandenbourger, M. and Dorbolo, S. Electrically Charged Droplet: Case Study of a Simple Generator. *Canadian Journal of Physics*, 92(10):1203–1207, 2014. doi:10.1139/cjp-2013-0479.
- [24] Braslavsky, I. and Lipson, S. G. Electrofreezing Effect and Nucleation of Ice Crystals in Free Growth Experiments. *Applied Physics Letters*, 72(2):264, 1998. doi:10.1063/1.120705.
- [25] Braunsberger, T., Dziubek, A., and Kurrat, M. Water Drop Corona on Hydrophobic Epoxy. In *Proceedings of the 2004 IEEE International Conference on Solid Dielectrics*, pages 439–442, 5-9 July 2004. doi:10.1109/ICSD.2004.1350385.
- [26] Breeze, P. A. *Hydropower*. The Power Generation Series. Academic Press, London, 2018. ISBN 978-0-12-812906-7.
- [27] Brutin, D. *Droplet Wetting and Evaporation: From Pure to Complex Fluids*. Elsevier Science, Burlington, 2015. ISBN 978-0-12-800722-8.
- [28] Budke, C. and Koop, T. BINARY: An Optical Freezing Array for Assessing Temperature and Time Dependence of Heterogeneous Ice Nucleation. *Atmospheric Measurement Techniques*, 8(2):689–703, 2015. doi:10.5194/amt-8-689-2015.

## Bibliography

- [29] Callen, H. B. *Thermodynamics and an Introduction to Thermostatistics*. Wiley, New York, 2. edition, 1985. ISBN 978-0-471-86256-7.
- [30] Campbell, J. M., Meldrum, F. C., and Christenson, H. K. Is Ice Nucleation from Supercooled Water Insensitive to Surface Roughness? *The Journal of Physical Chemistry C*, 119(2):1164–1169, 2015. doi:10.1021/jp5113729.
- [31] Carpenter, K. and Bahadur, V. Electrofreezing of Water Droplets under Electrowetting Fields. *Langmuir : the ACS Journal of Surfaces and Colloids*, 31(7):2243–2248, 2015. doi:10.1021/la504792n.
- [32] Carte, A. E. The Freezing of Water Droplets. *Proceedings of the Physical Society. Section B*, 69(10):1028–1037, 1956. doi:10.1088/0370-1301/69/10/309.
- [33] Carte, A. E. Probability of Freezing. *Proceedings of the Physical Society*, 73(2):324, 1959. doi:10.1088/0370-1328/73/2/126.
- [34] Carte, A. E. Air Bubbles in Ice. *Proceedings of the Physical Society*, 77(3):757–768, 1961. doi:10.1088/0370-1328/77/3/327.
- [35] Cebeci, T. and Kafyke, F. Aircraft Icing. *Annual Review of Fluid Mechanics*, 35(1):11–21, 2003. doi:10.1146/annurev.fluid.35.101101.161217.
- [36] Chalmers, J. A. and Pasquill, F. The Electric Charges on Single Raindrops and Snowflakes. *Proceedings of the Physical Society*, 50(1):1–16, 1938. doi:10.1088/0959-5309/50/1/302.
- [37] Chandrasekar, S., Kalaivanan, C., Montanari, G., and Cavallini, A. Partial Discharge Detection as a Tool to Infer Pollution Severity of Polymeric Insulators. *IEEE Transactions on Dielectrics and Electrical Insulation*, 17(1):181–188, 2010. doi:10.1109/TDEI.2010.5412016.
- [38] Chiu, C.-P., Chiang, T.-J., Chen, J.-K., Chang, F.-C., Ko, F.-H., Chu, C.-W., Kuo, S.-W., and Fan, S.-K. Liquid Lenses and Driving Mechanisms: A Review. *Journal of Adhesion Science and Technology*, 26(12-17):1773–1788, 2012. doi:10.1163/156856111X600514.

- [39] Choi, D., Lee, H., Im, D. J., Kang, I. S., Lim, G., Kim, D. S., and Kang, K. H. Spontaneous Electrical Charging of Droplets by Conventional Pipetting. *Scientific Reports*, 3:2037, 2013. doi:10.1038/srep02037.
- [40] Cicekdagli, D. Verifizierung/Validierung und Optimierung eines Versuchsaufbaus zum definierten Laden von Tropfen. Studienarbeit, Technische Universität Darmstadt, Darmstadt, Germany, 2017. (unpublished and not publicly available), Advisor: Jens-Michael Löwe, M.Sc.
- [41] Collins, R. T., Jones, J. J., Harris, M. T., and Basaran, O. A. Electrohydrodynamic Tip Streaming and Emission of Charged Drops from Liquid Cones. *Nature Physics*, 4(2):149–154, 2007. doi:10.1038/nphys807.
- [42] Collins, R. T., Sambath, K., Harris, M. T., and Basaran, O. A. Universal Scaling Laws for the Disintegration of Electrified Drops. *Proceedings of the National Academy of Sciences of the United States of America*, 110(13):4905–4910, 2013. doi:10.1073/pnas.1213708110.
- [43] Connolly, P. J., Möhler, O., Field, P. R., Saathoff, H., Burgess, R., Choularton, T., and Gallagher, M. Studies of Heterogeneous Freezing by Three Different Desert Dust Samples. *Atmospheric Chemistry and Physics*, 9(8):2805–2824, 2009. doi:10.5194/acp-9-2805-2009.
- [44] Dalvi-Isfahan, M., Hamdami, N., Le-Bail, A., and Xanthakis, E. The Principles of High Voltage Electric Field and its Application in Food Processing: A Review. *Food Research International*, 89(Pt 1): 48–62, 2016. doi:10.1016/j.foodres.2016.09.002.
- [45] Dalvi-Isfahan, M., Hamdami, N., Xanthakis, E., and Le-Bail, A. Review on the Control of Ice Nucleation by Ultrasound Waves, Electric and Magnetic Fields. *Journal of Food Engineering*, 195:222–234, 2017. doi:10.1016/j.jfoodeng.2016.10.001.
- [46] David, R. O., Cascajo-Castresana, M., Brennan, K. P., Rösch, M., Els, N., Werz, J., Weichlinger, V., Boynton, L. S., Bogler, S., Borduas-Dedekind, N., Marcolli, C., and Kanji, Z. A. Development of the DRoplet Ice Nuclei Counter Zurich (DRINCZ): Validation and Application to Field-collected Snow Samples. *Atmospheric Measurement Techniques*, 12(12):6865–6888, 2019. doi:10.5194/amt-12-6865-2019.

## Bibliography

- [47] Dawson, G. A. and Cardell, G. R. Electrofreezing of Supercooled Waterdrops. *Journal of Geophysical Research*, 78(36):8864–8866, 1973. doi:10.1029/JC078i036p08864.
- [48] de Gennes, P.-G., Brochard-Wyart, F., Quéré, D., and Reisinger, A. *Capillarity and Wetting Phenomena: Drops, Bubbles, Pearls, Waves*. Springer, New York, 2004. ISBN 0-387-00592-7.
- [49] Dehghani-Sanij, A. R., Dehghani, S. R., Naterer, G. F., and Muzychka, Y. S. Sea Spray Icing Phenomena on Marine Vessels and Offshore Structures: Review and Formulation. *Ocean Engineering*, 132:25–39, 2017. doi:10.1016/j.oceaneng.2017.01.016.
- [50] Dickinson, H. C. *Latent Heat of Fusion of Ice (Classic Reprint)*. FB & c Ltd, London, 2016. ISBN 978-1334261039.
- [51] Dietzmann-Kolbe, M. Untersuchung des Verhaltens von aufsitzenden Wassertropfen unter Stoßspannungsbeanspruchung. Master's thesis, Technische Universität Darmstadt, Darmstadt, Germany, 2018. (unpublished and not publicly available), Advisor: Jens-Michael Löwe, M.Sc.
- [52] Dong, L., Chaudhury, A., and Chaudhury, M. K. Lateral Vibration of a Water Drop and its Motion on a Vibrating Surface. *The European Physical Journal E, Soft Matter*, 21(3):231–242, 2006. doi:10.1140/epje/i2006-10063-7.
- [53] Doolittle, J. B. and Vali, G. Heterogeneous Freezing Nucleation in Electric Fields. *Journal of the Atmospheric Sciences*, 32(2):375–379, 1975. doi:10.1175/1520-0469(1975)032<0375:HFNIEF>2.0.CO;2.
- [54] Dorau, T., Hülsebrock, M., Weis, P., and Wenzel, J. Konstruktion eines Aufbaus zur experimentellen Untersuchung des Nukleationsverhaltens unterkühlter Wassertropfen im elektrischen Feld. Advanced Design Project (ADP), Technische Universität Darmstadt, Darmstadt, Germany, 2017. (unpublished and not publicly available), Advisor: Jens-Michael Löwe, M.Sc. and Dr.-Ing. Markus Schreimb.
- [55] Doyle, A., Moffett, D., and Vonnegut, B. Behavior of Evaporating Electrically Charged Droplets. *Journal of Colloid Science*, 19(2): 136–143, 1964. doi:10.1016/0095-8522(64)90024-8.

- [56] Drygiannakis, A. I., Papathanasiou, A. G., and Boudouvis, A. G. On the Connection between Dielectric Breakdown Strength, Trapping of Charge, and Contact Angle Saturation in Electrowetting. *Langmuir*, 25(1):147–152, 2009. doi:10.1021/la802551j.
- [57] Durant, A. J. Evaporation Freezing by Contact Nucleation Inside-out. *Geophysical Research Letters*, 32(20), 2005. doi:10.1029/2005GL024175.
- [58] Engelhardt, J. Entwicklung eines Versuchsstandes zur automatisierten Messung von Oberflächenpotentialen auf isolierenden Oberflächen. Master's thesis, Technische Universität Darmstadt, Darmstadt, Germany, 2017. (unpublished and not publicly available), Advisor: Jens-Michael Löwe, M.Sc.
- [59] Eow, J. S., Ghadiri, M., and Sharif, A. Deformation and Break-up of Aqueous Drops in Dielectric Liquids in High Electric Fields. *Journal of Electrostatics*, 51-52:463–469, 2001. doi:10.1016/S0304-3886(01)00035-3.
- [60] Epstein, P. S. and Plesset, M. S. On the Stability of Gas Bubbles in Liquid–Gas Solutions. *The Journal of Chemical Physics*, 18(11): 1505–1509, 1950. doi:10.1063/1.1747520.
- [61] Eriksson, A., Stringfellow, M., and Meal, D. Lighting - Induced Overvoltages on Overhead Distribution Lines. *IEEE Transactions on Power Apparatus and Systems*, PAS-101(4):960–968, 1982. doi:10.1109/TPAS.1982.317162.
- [62] Farzaneh, M. Ice Accretions on High-Voltage Conductors and Insulators and Related Phenomena. *Philosophical Transactions of the Royal Society A: Mathematical, Physical and Engineering Sciences*, 358(1776):2971–3005, 2000. doi:10.1098/rsta.2000.0692.
- [63] Farzaneh, M. *Atmospheric Icing of Power Networks*. Springer Netherlands, s.l., 1. edition, 2008. ISBN 978-1-4020-8530-7.
- [64] Farzaneh, M. and Chisholm, W. A. *Insulators for Icing and Polluted Environments*. IEEE Press Series on Power Engineering. Wiley-Blackwell, Oxford, 2009. ISBN 978-0-470-28234-2.
- [65] Farzaneh, M. and Kiernicki, J. Flashover Problems Caused by Ice Build up on Insulators. *IEEE Electrical Insulation Magazine*, 11(2): 5–17, 1995. doi:10.1109/57.372510.

## Bibliography

- [66] Feier-Iova, S. *The Behaviour of Water Drops on Insulating Surfaces Stressed by Electric Field*. PhD thesis, Technische Universität Darmstadt, Darmstadt, 01.01.2009. URL <http://tuprints.ulb.tu-darmstadt.de/2008/>.
- [67] Findeisen, W., Volken, E., Giesche, A. M., and Brönnimann, S. Colloidal Meteorological Processes in the Formation of Precipitation: *Meteorologische Zeitschrift*, 24(4), 443-454. *Meteorologische Zeitschrift*, 24(4):443–454, 2015. doi:10.1127/METZ/2015/0675.
- [68] Ford, I. J. Statistical Mechanics of Nucleation: A Review. *Proceedings of the Institution of Mechanical Engineers, Part C: Journal of Mechanical Engineering Science*, 218(8):883–899, 2004. doi:10.1243/0954406041474183.
- [69] Fortes, M. A. Microscopic and Macroscopic Contact Angles. *Journal of the Chemical Society, Faraday Transactions 1: Physical Chemistry in Condensed Phases*, 78(1):101, 1982. doi:10.1039/F19827800101.
- [70] Franks, F., editor. *Water and Aqueous Solutions at Subzero Temperatures*, volume 7 of *Water, A Comprehensive Treatise*. Springer US, Boston, 1982. ISBN 9781475769548.
- [71] Frenkel, J. A General Theory of Heterophase Fluctuations and Pre-transition Phenomena. *The Journal of Chemical Physics*, 7(7):538–547, 1939. doi:10.1063/1.1750484.
- [72] Frey, C., Göpfrich, K., Pashapour, S., Platzman, I., and Spatz, J. P. Electrocoalescence of Water-in-Oil Droplets with a Continuous Aqueous Phase: Implementation of Controlled Content Release. *ACS Omega*, 5(13):7529–7536, 2020. doi:10.1021/acsomega.0c00344.
- [73] Frohn, A. and Roth, N. *Dynamics of Droplets*. Experimental Fluid Mechanics. Springer, Berlin and Heidelberg, 2000. ISBN 978-3-662-04040-9.
- [74] Frohne, H. and Moeller, F. *Moeller Grundlagen der Elektrotechnik: Mit 182 Beispielen*. Studium. Vieweg + Teubner, Wiesbaden, 22. edition, 2011. ISBN 9783834808981.

- [75] Fujii, O., Honsali, K., Mizuno, Y., and Naito, K. A Basic Study on the Effect of Voltage Stress on a Water Droplet on a Silicone Rubber Surface. *IEEE Transactions on Dielectrics and Electrical Insulation*, 16(1):116–122, 2009. doi:10.1109/TDEL.2009.4784558.
- [76] Fujii, O., Honsali, K., Mizuno, Y., and Naito, K. Vibration of a Water Droplet on a Polymeric Insulating Material Subjected to AC Voltage Stress. *IEEE Transactions on Dielectrics and Electrical Insulation*, 17(2):566–571, 2010. doi:10.1109/TDEL.2010.5448113.
- [77] Gadd, G. E. A Note on the Undercarriage Aquaplaning of Aircraft Landing on Water-covered Runways. *The Journal of the Royal Aeronautical Society*, 67(627):189–191, 1963. doi:10.1017/S0368393100078184.
- [78] Gao, L. and McCarthy, T. J. Contact Angle Hysteresis Explained. *Langmuir*, 22(14):6234–6237, 2006. doi:10.1021/la060254j.
- [79] Garstecki, P., Fuerstman, M. J., Stone, H. A., and Whitesides, G. M. Formation of Droplets and Bubbles in a Microfluidic T-junction-Scaling and Mechanism of Break-up. *Lab on a Chip*, 6(3):437–446, 2006. doi:10.1039/B510841A.
- [80] Geng, H. and Cho, S. K. Dielectrowetting for Digital Microfluidics: Principle and Application. A Critical Review. *Reviews of Adhesion and Adhesives*, 5(3):268–302, 2017. doi:10.7569/RAA.2017.097308.
- [81] Ghosh, D. and Khastgir, D. Degradation and Stability of Polymeric High-Voltage Insulators and Prediction of Their Service Life through Environmental and Accelerated Aging Processes. *ACS Omega*, 3(9):11317–11330, 2018. doi:10.1021/acsomega.8b01560.
- [82] Gibbs, J. W., Bumstead, H. A., and van Name, R. G. *Scientific Papers of J. Willard Gibbs: Band 1 - Thermodynamics*. Landmarks of Science. Longmans, Green and co., 1906.
- [83] Girshick, S. L. and Chiu, C.-P. Kinetic Nucleation Theory: A New Expression for the Rate of Homogeneous Nucleation from an Ideal Supersaturated Vapor. *The Journal of Chemical Physics*, 93(2):1273–1277, 1990. doi:10.1063/1.459191.
- [84] Glycerine Producers' Association. *Physical Properties of Glycerine and its Solutions*. Glycerine Producers' Association, 1963.

## Bibliography

- [85] Good, R. J. Contact Angles and the Surface Free Energy of Solids. In Good, R. J. and Stromberg, R. R., editors, *Surface and Colloid Science*, pages 1–29. Springer US, Boston, 1979. ISBN 978-1-4615-7971-7. doi:10.1007/978-1-4615-7969-4\_1.
- [86] Gorur, R. S. High Voltage Outdoor Insulation Technology. In *Analysis and Control System Techniques for Electric Power Systems, Part 4 of 4*, volume 44 of *Control and Dynamic Systems*, pages 131–191. Elsevier, 1991. ISBN 9780120127443. doi:10.1016/B978-0-12-012744-3.50008-4.
- [87] Goudie, J. L., Owen, M. J., and Orbeck, T. A Review of Possible Degradation Mechanisms of Silicone Elastomers in High Voltage Insulation Applications. In *1998 Annual Report Conference on Electrical Insulation and Dielectric Phenomena (Cat. No.98CH36257)*, pages 120–127. IEEE, 1998. ISBN 0-7803-5035-9. doi:10.1109/CEIDP.1998.733878.
- [88] Grace, J. M. and Marijnissen, J. A Review of Liquid Atomization by Electrical Means. *Journal of Aerosol Science*, 25(6):1005–1019, 1994. doi:10.1016/0021-8502(94)90198-8.
- [89] Gray, W. E. Aquaplaning on Runways. *The Journal of the Royal Aeronautical Society*, 67(629):302–304, 1963. doi:10.1017/S0368393100078640.
- [90] Griffiths, D. J. *Introduction to Electrodynamics*. Cambridge University Press, Cambridge, fourth edition edition, 2017. ISBN 978-1108420419.
- [91] Gunn, R. and Devin, C. Raindrop Charge and Electric Field in Active Thunderstorms. *Journal of Meteorology*, 10(4):279–284, 1953. doi:10.1175/1520-0469(1953)010<0279:RCAEFI>2.0.CO;2.
- [92] Hackam, R. Outdoor High Voltage Polymeric Insulators. In *Proceedings of 1998 International Symposium on Electrical Insulating Materials*, pages 1–16, Tokyo and Piscataway, N.J, 1998. Institute of Electrical Engineers of Japan. ISBN 4-88686-050-8. doi:10.1109/ISEIM.1998.741674.
- [93] Harris, D. M., Liu, T., and Bush, J. W. M. A Low-cost, Precise Piezoelectric Droplet-on-Demand Generator. *Experiments in Fluids*, 56(4):516, 2015. doi:10.1007/s00348-015-1950-6.

- [94] Harrison, A. D., Whale, T. F., Rutledge, R., Lamb, S., Tarn, M. D., Porter, G. C. E., Adams, M. P., McQuaid, J. B., Morris, G. J., and Murray, B. J. An Instrument for Quantifying Heterogeneous Ice Nucleation in Multiwell Plates Using Infrared Emissions to Detect Freezing. *Atmospheric Measurement Techniques*, 11(10):5629–5641, 2018. doi:10.5194/amt-11-5629-2018.
- [95] Henke, H. *Elektromagnetische Felder: Theorie und Anwendung*. Springer-Lehrbuch. Springer Vieweg, Berlin and Heidelberg, 5. edition, 2015. ISBN 978-3-662-46918-7.
- [96] Herbert, R. J., Murray, B. J., Dobbie, S. J., and Koop, T. Sensitivity of Liquid Clouds to Homogenous Freezing Parameterizations. *Geophysical Research Letters*, 42(5):1599–1605, 2015. doi:10.1002/2014GL062729.
- [97] Heverly, J. R. Supercooling and Crystallization. *Transactions, American Geophysical Union*, 30(2):205, 1949. doi:10.1029/TR030i002p00205.
- [98] Heymsfield, A. J. and Miloshevich, L. M. Homogeneous Ice Nucleation and Supercooled Liquid Water in Orographic Wave Clouds. *Journal of the Atmospheric Sciences*, 50(15):2335–2353, 1993. doi:10.1175/1520-0469(1993)050%3C2335:HINASL%3E2.0.CO;2.
- [99] Higashiyama, Y., Yanase, S., and Sugimoto, T. DC Corona Discharge from Water Droplets on a Hydrophobic Surface. *Journal of Electrostatics*, 55(3-4):351–360, 2002. doi:10.1016/S0304-3886(01)00217-0.
- [100] Hillig, W. B. Measurement of Interfacial Free Energy for Ice/Water System. *Journal of Crystal Growth*, 183(3):463–468, 1998. doi:10.1016/S0022-0248(97)00411-9.
- [101] Hirano, Y., Inohara, T., Toyoda, M., Murase, H., and Kosakada, M. Accelerated Weatherability of Shed Materials for Composite Insulators. *IEEE Transactions on Dielectrics and Electrical Insulation*, 8(1):97–103, 2001. doi:10.1109/94.910431.
- [102] Hobbs, P. V. *Ice Physics*. Oxford Classic Texts in the Physical Sciences. Oxford Univ. Press, Oxford, 2010. ISBN 9780199587711.

## Bibliography

- [103] Holden, M. A., Whale, T. F., Tarn, M. D., O’Sullivan, D., Walshaw, R. D., Murray, B. J., Meldrum, F. C., and Christenson, H. K. High-speed Imaging of Ice Nucleation in Water Proves the Existence of Active Sites. *Science Advances*, 5(2):eaav4316, 2019. doi:10.1126/sciadv.aav4316.
- [104] Hollerith, J. F. A. Optimierung eines Versuchsaufbaus zur Untersuchung von Ladung auf Regentropfen. Bachelor’s thesis, Technische Universität Darmstadt, Darmstadt, Germany, 2019. (unpublished and not publicly available), Advisor: Jens-Michael Löwe, M.Sc.
- [105] Holtze, C., Rowat, A. C., Agresti, J. J., Hutchison, J. B., Angilè, F. E., Schmitz, C. H. J., Köster, S., Duan, H., Humphry, K. J., Scanga, R. A., Johnson, J. S., Pisignano, D., and Weitz, D. A. Biocompatible Surfactants for Water-in-Fluorocarbon Emulsions. *Lab on a Chip*, 8(10):1632–1639, 2008. doi:10.1039/b806706f.
- [106] Hoose, C. and Möhler, O. Heterogeneous Ice Nucleation on Atmospheric Aerosols: A Review of Results from Laboratory Experiments. *Atmospheric Chemistry and Physics*, 12(20):9817–9854, 2012. doi:10.5194/acp-12-9817-2012.
- [107] Huang, X., He, L., Luo, X., and Yin, H. Droplet Dynamic Response in Low-viscosity Fluid Subjected to a Pulsed Electric Field and an Alternating Electric Field. *AIChE Journal*, 66(4), 2020. doi:10.1002/aic.16869.
- [108] IEEE-DEIS-EHD Technical Committee. Recommended International Standard for Dimensionless Parameters Used in Electrohydrodynamics. *IEEE Transactions on Dielectrics and Electrical Insulation*, 10(1):3–6, 2003. doi:10.1109/TDEI.2003.1176545.
- [109] International Electrotechnical Commission. IEC 60038:2009 - IEC standard voltages, 17.06.2009. URL <https://webstore.iec.ch/publication/153>.
- [110] Ishai, P. B., Talary, M. S., Caduff, A., Levy, E., and Feldman, Y. Electrode Polarization in Dielectric Measurements: A Review. *Measurement Science & Technology*, 24(10):102001, 2013. doi:10.1088/0957-0233/24/10/102001.

- [111] Jelle, B. P., Gao, T., Mofid, S. A., Kolås, T., Stenstad, P. M., and Ng, S. Avoiding Snow and Ice Formation on Exterior Solar Cell Surfaces – A Review of Research Pathways and Opportunities. *Procedia Engineering*, 145:699–706, 2016. doi:10.1016/j.proeng.2016.04.084.
- [112] Jha, P. K., Sadot, M., Vino, S. A., Jury, V., Curet-Ploquin, S., Rouaud, O., Havet, M., and Le-Bail, A. A Review on Effect of DC Voltage on Crystallization Process in Food Systems. *Innovative Food Science & Emerging Technologies*, 42:204–219, 2017. doi:10.1016/j.ifset.2017.06.002.
- [113] Kabelac, S., editor. *VDI-Wärmeatlas: Berechnungsunterlagen für Druckverlust, Wärme- und Stoffübergang*. Springer, Berlin, 10. edition, 2006. ISBN 978-3-540-25504-8.
- [114] Kanji, Z. A., Ladino, L. A., Wex, H., Boose, Y., Burkert-Kohn, M., Cziczo, D. J., and Krämer, M. Overview of Ice Nucleating Particles. *Meteorological Monographs*, 58:1.1–1.33, 2017. doi:10.1175/AMSMONOGRAPHS-D-16-0006.1.
- [115] Karniadakis, G., Beşkök, A., and Aluru, N. *Microflows and Nanoflows: Fundamentals and Simulation*, volume 29 of *Interdisciplinary Applied Mathematics*. Springer, New York, 2005. ISBN 978-0-387-22197-7.
- [116] Karthika, S., Radhakrishnan, T. K., and Kalaichelvi, P. A Review of Classical and Nonclassical Nucleation Theories. *Crystal Growth & Design*, 16(11):6663–6681, 2016. doi:10.1021/acs.cgd.6b00794.
- [117] Kaščiev, D. *Nucleation: Basic Theory with Applications*. Butterworth Heinemann, Oxford, 2003. ISBN 978-0-7506-4682-6.
- [118] Kashchiev, D. Nucleation in External Electric Field. *Journal of Crystal Growth*, 13-14:128–130, 1972. doi:10.1016/0022-0248(72)90074-7.
- [119] Kashchiev, D. On the Influence of the Electric Field on Nucleation Kinetics. *Philosophical Magazine*, 25(2):459–470, 1972. doi:10.1080/14786437208226816.
- [120] Kashchiev, D. Nucleation. In van der Eerden, J. P. and Bruinsma, O. S. L., editors, *Science and Technology of Crystal Growth*, pages 53–66. Springer Netherlands, Dordrecht, 1995. ISBN 978-94-010-4062-4. doi:10.1007/978-94-011-0137-0\_5.

## Bibliography

- [121] Katada, K., Takada, Y., Takano, M., Nakanishi, T., Hayashi, Y., and Matsuoka, R. Corona Discharge Characteristics of Water Droplets on Hydrophobic Polymer Insulator Surface. In *6th International Conference on Properties and Applications of Dielectric Materials*, pages 781–784, 21–26 June 2000. doi:10.1109/ICPADM.2000.876346.
- [122] Ketcham, W. M. and Hobbs, P. V. An Experimental Determination of the Surface Energies of Ice. *Philosophical Magazine*, 19(162): 1161–1173, 1969. doi:10.1080/14786436908228641.
- [123] Khan, H., Amin, M., and Ahmad, A. Characteristics of Silicone Composites for High Voltage Insulations. *Reviews on Advanced Materials Science*, 56(1):91–123, 2018. doi:10.1515/rams-2018-0040.
- [124] Kim, D. Y., Kim, M.-J., Sung, G., and Sun, J.-Y. Stretchable and Reflective Displays: Materials, Technologies and Strategies. *Nano Convergence*, 6(1):21, 2019. doi:10.1186/s40580-019-0190-5.
- [125] Kleissl, K. and Georgakis, C. Bridge Ice Accretion and De- and Anti-Icing Systems: A Review. In *The 7th International Cable Supported Bridge Operators' Conference*, pages 161–167, 2010.
- [126] Knauel, J., Wagner, A., and Puffer, R. Behavior of Water Droplets on Polymeric Insulation Surfaces under Hybrid Field Stress. In *IEEE Conference on Electrical Insulation and Dielectric Phenomena - (CEIDP 2014)*, pages 243–246, 2014. doi:10.1109/CEIDP.2014.6995871.
- [127] Koizumi, H., Fujiwara, K., and Uda, S. Role of the Electric Double Layer in Controlling the Nucleation Rate for Tetragonal Hen Egg White Lysozyme Crystals by Application of an External Electric Field. *Crystal Growth & Design*, 10(6):2591–2595, 2010. doi:10.1021/cg901621x.
- [128] König, D. and Rao, Y. N. *Teilentladungen in Betriebsmitteln der Energietechnik*. VDE-Verl., Berlin, 1993. ISBN 3800717646.
- [129] Koop, T. Homogeneous Ice Nucleation in Water and Aqueous Solutions. *Zeitschrift für physikalische Chemie (Frankfurt am Main, Germany)*, 218(11-2004):1231–1258, 2004. doi:10.1524/zpch.218.11.1231.50812.

- [130] Koop, T. and Murray, B. J. A Physically Constrained Classical Description of the Homogeneous Nucleation of Ice in Water. *The Journal of Chemical Physics*, 145(21):211915, 2016. doi:10.1063/1.4962355.
- [131] Kories, R. and Schmidt-Walter, H. *Taschenbuch der Elektrotechnik: Grundlagen und Elektronik*. Edition Harri Deutsch. Verlag Europa-Lehrmittel, Haan-Gruiten, 10. edition, 2013. ISBN 9783808556696.
- [132] Kremer, F. and Schönhals, A., editors. *Broadband Dielectric Spectroscopy*. Springer, Berlin, Heidelberg and s.l., 2003. ISBN 978-3-642-56120-7.
- [133] Küchler, A. *High Voltage Engineering: Fundamentals - Technology - Applications*. VDI-Buch. Springer Vieweg, Berlin, 2018. ISBN 9783642119927.
- [134] Kuhn, T., Earle, M. E., Khalizov, A. F., and Sloan, J. J. Size Dependence of Volume and Surface Nucleation Rates for Homogeneous Freezing of Supercooled Water Droplets. *Atmospheric Chemistry and Physics*, 11(6):2853–2861, 2011. doi:10.5194/acp-11-2853-2011.
- [135] Kumar, S. S., Anupam, K., Scarpas, T., and Kasbergen, C. Study of Hydroplaning Risk on Rolling and Sliding Passenger Car. *Procedia, Social and Behavioral Sciences*, 53:1019–1027, 2012. doi:10.1016/j.sbspro.2012.09.951.
- [136] La Fernández de Mora, J. The Fluid Dynamics of Taylor Cones. *Annual Review of Fluid Mechanics*, 39(1):217–243, 2007. doi:10.1146/annurev.fluid.39.050905.110159.
- [137] Laaksonen, A., Talanquer, V., and Oxtoby, D. W. Nucleation: Measurements, Theory, and Atmospheric Applications. *Annual Review of Physical Chemistry*, 46:489–524, 1995. doi:10.1146/annurev.pc.46.100195.002421.
- [138] Lamb, H. *Hydrodynamics*. Univ. Press, Cambridge, 1895. ISBN 9780521458689.
- [139] Landau, L. D. and Lifšic, E. M. *The Classical Theory of Fields*, volume by L. D. Landau and E. M. Lifshitz ; Vol. 2 of *Course of Theoretical Physics*. Pergamon Press, Oxford, 4. edition, 1975. ISBN 978-0750627689.

## Bibliography

- [140] Langham, E. J., Mason, B. J.-N., and Bernal, J. D. The Heterogeneous and Homogeneous Nucleation of Supercooled Water. *Proceedings of the Royal Society of London. Series A. Mathematical and Physical Sciences*, 247(1251):493–504, 1958. doi:10.1098/rspa.1958.0207.
- [141] Law, K.-Y. Definitions for Hydrophilicity, Hydrophobicity, and Superhydrophobicity: Getting the Basics Right. *The Journal of Physical Chemistry Letters*, 5(4):686–688, 2014. doi:10.1021/jz402762h.
- [142] Lee, M. W., Latthe, S. S., Yarin, A. L., and Yoon, S. S. Dynamic Electrowetting-on-Dielectric (DEWOD) on Unstretched and Stretched Teflon. *Langmuir*, 29(25):7758–7767, 2013. doi:10.1021/la401669w.
- [143] Levine, J. Statistical Explanation of Spontaneous Freezing of Water Droplets, NACA Technical Note. Technical Report NACA-TN-2234, National Advisory Committee for Aeronautics, 1950.
- [144] Lima, N. C., Cavalli, A., Mishra, K., and Mugele, F. Numerical Simulation of Astigmatic Liquid Lenses Tuned by a Stripe Electrode. *Optics Express*, 24(4):4210–4220, 2016. doi:10.1364/OE.24.004210.
- [145] Lings, R. J. and Electric Power Research Institute. *EPRI AC Transmission Line Reference Book: 200 kV and above, Third Edition*. Electric Power Research Institute, 2005.
- [146] Lippmann, G. Beziehungen zwischen den Capillaren und Elektrischen Erscheinungen. *Annalen der Physik*, 225(8):546–561, 1873. doi:10.1002/andp.18732250807.
- [147] Lohse, D. and Zhang, X. Surface Nanobubbles and Nanodroplets. *Reviews of Modern Physics*, 87(3):981–1035, 2015. doi:10.1103/RevModPhys.87.981.
- [148] Lopes, I., Jayaram, S. H., and Cherney, E. A. Partial Discharge Patterns for Silicone Rubber Insulators under Salt-fog. In *2001 Annual Report Conference on Electrical Insulation and Dielectric Phenomena*, pages 452–455, 14-17 Oct. 2001. doi:10.1109/CEIDP.2001.963579.
- [149] Lopes, I., Jayaram, S. H., and Cherney, E. A. A Study of Partial Discharges from Water Droplets on a Silicone Rubber Insulating

- Surface. *IEEE Transactions on Dielectrics and Electrical Insulation*, 8(2):262–268, 2001. doi:10.1109/94.919951.
- [150] Löwe, J.-M. and Hinrichsen, V. Experimental Investigation of the Influence of Electric Charge on the Behavior of Water Droplets in Electric Fields. In *2019 IEEE 20th International Conference on Dielectric Liquids (ICDL)*, pages 1–6. IEEE, 2019. ISBN 978-1-7281-1718-8. doi:10.1109/ICDL.2019.8796707.
- [151] Löwe, J.-M., Hinrichsen, V., Schremb, M., Dorau, T., and Tropea, C. Experimental Investigation of Electro-freezing of Supercooled Droplets. In *9th World Conference on Experimental Heat Transfer, Fluid Mechanics and Thermodynamics*, Foz do Iguacu, Brasilien, 2017.
- [152] Löwe, J.-M., Secklehner, M., and Hinrichsen, V. Investigation of Surface Charges on Polymeric Insulators and the Influence of Sessile Water Droplets. In *2017 INSUCON - 13th International Electrical Insulation Conference (INSUCON)*, pages 1–7. IEEE, 2017. ISBN 978-1-9998-1569-1. doi:10.23919/INSUCON.2017.8097170.
- [153] Löwe, J.-M., Hinrichsen, V., and Tropea, C. Droplet Behavior Under the Impact of Lightning and Switching Impulse Voltage. In *2018 IEEE Electrical Insulation Conference (EIC)*, pages 443–447. IEEE, 2018. ISBN 978-1-5386-4178-1. doi:10.1109/EIC.2018.8480884.
- [154] Löwe, J.-M., Schremb, M., Hinrichsen, V., and Tropea, C. Ice Nucleation in the Presence of Electric Fields: An Experimental Study. In SAE International, editor, *International Conference on Icing of Aircraft, Engines, and Structures*, SAE Technical Paper Series. SAE International400 Commonwealth Drive, Warrendale, PA, United States, 2019. doi:10.4271/2019-01-2020.
- [155] Löwe, J.-M., Engelhardt, J., Secklehner, M., and Hinrichsen, V. Determination of the Spatial Impulse Response of Compensating Electrostatic Voltmeters. *IEEE Transactions on Dielectrics and Electrical Insulation*, 27(1):49–57, 2020. doi:10.1109/TDEI.2019.008305.
- [156] Löwe, J.-M., Hinrichsen, V., Roisman, I. V., and Tropea, C. Behavior of Charged and Uncharged Drops in High Alternating Tangential Electric Fields. *Physical Review E*, 101(2):023102, 2020. doi:10.1103/PhysRevE.101.023102.

## Bibliography

- [157] Löwe, J.-M., Hinrichsen, V., Roisman, I. V., and Tropea, C. Impact of Electric Charge and Motion of Water Drops on the Inception Field Strength of Partial Discharges. *Physical Review E*, 102(6):063101, 2020. doi:10.1103/PhysRevE.102.063101.
- [158] Löwe, J.-M., Hinrichsen, V., Schremb, M., and Tropea, C. Ice Nucleation in High Alternating Electric Fields: Effect of Electric Field Strength and Frequency. *Physical Review E*, 103(1):012801, 2021. doi:10.1103/PhysRevE.103.012801.
- [159] Löwe, J.-M., Hinrichsen, V., Schremb, M., and Tropea, C. Ice nucleation forced by transient electric fields. *Physical Review E*, 104(6):064801, 2021. doi:10.1103/PhysRevE.104.064801.
- [160] Löwe, J.-M., Schremb, M., Hinrichsen, V., and Tropea, C. Experimental Methodology and Procedure for SAPPHIRE: a Semi-automatic APParatus for High-voltage Ice nucleation REsearch. *Atmospheric Measurement Techniques*, 14(1):223–238, 2021. doi:10.5194/amt-14-223-2021.
- [161] Lowell, J. and Rose-Innes, A. C. Contact Electrification. *Advances in Physics*, 29(6):947–1023, 2006. doi:10.1080/00018738000101466.
- [162] Luo, X., Yin, H., Yan, H., Huang, X., Yang, D., and He, L. Electrocoalescence of Two Drops with Different Surfactant Concentrations Suspended in Oil. *The Journal of Physical Chemistry C*, 122(39):22615–22621, 2018. doi:10.1021/acs.jpcc.8b07619.
- [163] Lüönd, F., Stetzer, O., Welti, A., and Lohmann, U. Experimental Study on the Ice Nucleation Ability of Size-selected Kaolinite Particles in the Immersion Mode. *Journal of Geophysical Research*, 115(D14), 2010. doi:10.1029/2009JD012959.
- [164] Lyubimov, D. V., Lyubimova, T. P., and Shklyaev, S. V. Non-axisymmetric Oscillations of a Hemispherical Drop. *Fluid Dynamics*, 39(6):851–862, 2004. doi:10.1007/s10697-004-0002-3.
- [165] Ma, Y., Zhong, L., Gao, J., Liu, L., Hu, H., and Yu, Q. Manipulating Ice Crystallization of 0.9 wt. % NaCl Aqueous Solution by Alternating Current Electric Field. *Applied Physics Letters*, 102(18):183701, 2013. doi:10.1063/1.4804287.

- [166] Macky, W. A. Some Investigations on the Deformation and Breaking of Water Drops in Strong Electric Fields. *Proceedings of the Royal Society A: Mathematical, Physical and Engineering Sciences*, 133 (822):565–587, 1931. doi:10.1098/rspa.1931.0168.
- [167] Mandal, G. and Pradeep Kumar, P. A Laboratory Study of Ice Nucleation due to Electrical Discharge. *Atmospheric Research*, 61 (2):115–123, 2002. doi:10.1016/S0169-8095(01)00129-6.
- [168] Marand, H. and Stein, R. S. Isothermal Crystallization of Poly(vinylidene fluoride) in the Presence of High Static Electric Fields. II. Effect of Crystallization Temperature and Electric Field Strength on the Crystal Phase Content and Morphology. *Journal of Polymer Science Part B: Polymer Physics*, 27(5):1089–1106, 1989. doi:10.1002/polb.1989.090270510.
- [169] Marand, H. L., Stein, R. S., and Stack, G. M. Isothermal Crystallization of Poly(vinylidene fluoride) in the Presence of High Static Electric Fields. I. Primary Nucleation Phenomenon. *Journal of Polymer Science Part B: Polymer Physics*, 26(7):1361–1383, 1988. doi:10.1002/polb.1988.090260703.
- [170] Marcolli, C., Gedamke, S., Peter, T., and Zobrist, B. Efficiency of Immersion Mode Ice Nucleation on Surrogates of Mineral Dust. *Atmospheric Chemistry and Physics*, 7(19):5081–5091, 2007. doi:10.5194/acp-7-5081-2007.
- [171] Martin, G. D., Hoath, S. D., and Hutchings, I. M. Inkjet Printing - The Physics of Manipulating Liquid Jets and Drops. *Journal of Physics: Conference Series*, 105:012001, 2008. doi:10.1088/1742-6596/105/1/012001.
- [172] Melcher, J. R. Electrohydrodynamic Charge Relaxation and Interfacial Perpendicular-Field Instability. *Physics of Fluids*, 12(4):778, 1969. doi:10.1063/1.1692556.
- [173] Meschede, D. and Gerthsen, C., editors. *Gerthsen Physik*. Springer-Lehrbuch. Springer, Berlin, 24. edition, 2010. ISBN 978-3-642-12893-6.
- [174] Mhatre, S., Deshmukh, S., and Thaokar, R. M. Electrocoalescence of a Drop Pair. *Physics of Fluids*, 27(9):092106, 2015. doi:10.1063/1.4931592.

## Bibliography

- [175] Miller, A. J., Brennan, K. P., Mignani, C., Wieder, J., David, R. O., and Borduas-Dedekind, N. Development of the Drop Freezing Ice Nuclei Counter (FINC), Intercomparison of Droplet Freezing Techniques, and use of Soluble Lignin as an Atmospheric Ice Nucleation Standard. *Atmospheric Measurement Techniques*, 14(4):3131–3151, 2021. doi:10.5194/amt-14-3131-2021.
- [176] Milne, A. J. B., Defez, B., Cabrerizo-Vilchez, M., and Amirfazli, A. Understanding (Sessile/Constrained) Bubble and Drop Oscillations. *Advances in Colloid and Interface Science*, 203:22–36, 2014. doi:10.1016/j.cis.2013.11.006.
- [177] Mishra, K., Murade, C., Carreel, B., Roghair, I., Oh, J. M., Manukyan, G., van den Ende, D., and Mugele, F. Optofluidic Lens with Tunable Focal Length and Asphericity. *Scientific Reports*, 4: 6378, 2014. doi:10.1038/srep06378.
- [178] Mishra, K., van den Ende, D., and Mugele, F. Recent Developments in Optofluidic Lens Technology. *Micromachines*, 7(6), 2016. doi:10.3390/mi7060102.
- [179] Moghadam, M. K., Taheri, M., Gharazi, S., Keramati, M., Bahrami, M., and Riahi, N. A Study of Composite Insulator Aging using the Tracking Wheel Test. *IEEE Transactions on Dielectrics and Electrical Insulation*, 23(3):1805–1811, 2016. doi:10.1109/TDEI.2016.005427.
- [180] Möhler, O., Field, P. R., Connolly, P., Benz, S., Saathoff, H., Schnaiter, M., Wagner, R., Cotton, R., Krämer, M., Mangold, A., and Heymsfield, A. J. Efficiency of the Deposition Mode Ice Nucleation on Mineral Dust Particles. *Atmospheric Chemistry and Physics*, 6(10):3007–3021, 2006. doi:10.5194/acp-6-3007-2006.
- [181] Moreno, V. M. and Gorur, R. S. Effect of Long-term Corona on Non-ceramic Outdoor Insulator Housing Materials. *IEEE Transactions on Dielectrics and Electrical Insulation*, 8(1):117–128, 2001. doi:10.1109/94.910434.
- [182] Moreno, V. M., Gorur, R. S., and Kroese, A. Impact of Corona on the Long-term Performance of Nonceramic Insulators. *IEEE Transactions on Dielectrics and Electrical Insulation*, 10(1):80–95, 2003. doi:10.1109/TDEI.2003.1176565.

- [183] Mugele, F. and Baret, J.-C. Electrowetting: From Basics to Applications. *Journal of Physics: Condensed Matter*, 17(28):R705–R774, 2005. doi:10.1088/0953-8984/17/28/R01.
- [184] Murray, B. J., O’Sullivan, D., Atkinson, J. D., and Webb, M. E. Ice Nucleation by Particles Immersed in Supercooled Cloud Droplets. *Chemical Society Reviews*, 41(19):6519–6554, 2012. doi:10.1039/c2cs35200a.
- [185] Nardone, M. and Karpov, V. G. Nucleation of Metals by Strong Electric Fields. *Applied Physics Letters*, 100(15):151912, 2012. doi:10.1063/1.3703611.
- [186] Nazemi, M. and Hinrichsen, V. Partial Discharge Inception Electric Field Strength of Water Droplets on Polymeric Insulating Surfaces. *IEEE Transactions on Dielectrics and Electrical Insulation*, 22(2): 1088–1096, 2015. doi:10.1109/TDEI.2015.7076810.
- [187] Nazemi, M. H. *Experimental Investigations on Water Droplets on Polymeric Insulating Surfaces under the Impact of High Electric Fields*. PhD thesis, Technische Universität Darmstadt, Darmstadt, 01.01.2016. URL <http://tuprints.ulb.tu-darmstadt.de/5363/>.
- [188] Nazemi, M. H. and Hinrichsen, V. Experimental Investigations on Water Droplet Oscillation and Partial Discharge Inception Voltage on Polymeric Insulating Surfaces under the Influence of AC Electric Field Stress. *IEEE Transactions on Dielectrics and Electrical Insulation*, 20(2):443–453, 2013. doi:10.1109/TDEI.2013.6508746.
- [189] Nazemi, M. H. and Hinrichsen, V. Partial Discharge Investigation and Electric Field Analysis of Different Oscillation Modes of Water Droplets on the Surface of Polymeric Insulator under Tangential AC Electric Field Stress. In *2013 IEEE International Conference on Solid Dielectrics (ICSD)*, pages 194–197, 2013. doi:10.1109/ICSD.2013.6619788.
- [190] Nelson, W. C. and Kim, C.-J. C. Droplet Actuation by Electrowetting-on-Dielectric (EWOD): A Review. *Journal of Adhesion Science and Technology*, 2012(26):1747–1771, 2012. doi:10.1163/156856111X599562.
- [191] Nguyen, N.-T. Micro-optofluidic Lenses: A Review. *Biomicrofluidics*, 4(3), 2010. doi:10.1063/1.3460392.

## Bibliography

- [192] Nie, G.-X., Wang, Y., and Huang, J.-P. Role of Confinement in Water Solidification under Electric Fields. *Frontiers of Physics*, 10 (5), 2015. doi:10.1007/s11467-015-0504-y.
- [193] Niedermeier, D., Shaw, R. A., Hartmann, S., Wex, H., Clauss, T., Voigtländer, J., and Stratmann, F. Heterogeneous Ice Nucleation: Exploring the Transition from Stochastic to Singular Freezing Behavior. *Atmospheric Chemistry and Physics*, 11(16):8767–8775, 2011. doi:10.5194/acp-11-8767-2011.
- [194] Noblin, X., Kofman, R., and Celestini, F. Ratchetlike Motion of a Shaken Drop. *Physical Review Letters*, 102(19):194504, 2009. doi:10.1103/PhysRevLett.102.194504.
- [195] Nolan, J. J. The Breaking of Water-Drops by Electric Fields. *Proceedings of the Royal Irish Academy. Section A: Mathematical and Physical Sciences*, 37:28–39, 1924.
- [196] Oh, J. M., Ko, S. H., and Kang, K. H. Shape Oscillation of a Drop in AC Electrowetting. *Langmuir*, 24(15):8379–8386, 2008. doi:10.1021/la8007359.
- [197] Orłowska, M., Havet, M., and Le-Bail, A. Controlled Ice Nucleation under High Voltage DC Electrostatic Field Conditions. *Food Research International*, 42(7):879–884, 2009. doi:10.1016/j.foodres.2009.03.015.
- [198] Ouedraogo, Y. *Modelling of Electrohydrodynamic Droplet Motion under the Influence of Strong Electric Fields*. PhD thesis, Technische Universität Darmstadt, Darmstadt, 2020. URL <https://doi.org/10.25534/tuprints-00014008>.
- [199] Paish, O. Small Hydro Power: Technology and Current Status. *Renewable and Sustainable Energy Reviews*, 6(6):537–556, 2002. doi:10.1016/S1364-0321(02)00006-0.
- [200] Panofsky, W. K. H. and Phillips, M. *Classical Electricity and Magnetism: Second Edition*. Dover Books on Physics. Dover Publications, Newburyport, 2012. ISBN 978-0486439242.
- [201] Papailiou, K. O. and Schmuck, F. *Silikon-Verbundisolatoren: Werkstoffe, Dimensionierung, Anwendungen*. Springer, Heidelberg, 2012. ISBN 978-3-642-23813-0.

- [202] Parent, O. and Ilinca, A. Anti-icing and De-icing Techniques for Wind Turbines: Critical Review. *Cold Regions Science and Technology*, 65(1):88–96, 2011. doi:10.1016/j.coldregions.2010.01.005.
- [203] Peleg, Y., Yoffe, A., Ehre, D., Lahav, M., and Lubomirsky, I. The Role of the Electric Field in Electrofreezing. *The Journal of Physical Chemistry C*, 123(50):30443–30446, 2019. doi:10.1021/acs.jpcc.9b09399.
- [204] Peters, F. and Arabali, D. Interfacial Tension Between Oil and Water Measured with a Modified Contour Method. *Colloids and Surfaces A: Physicochemical and Engineering Aspects*, 426:1–5, 2013. doi:10.1016/j.colsurfa.2013.03.010.
- [205] Petersen, A., Schneider, H., Rau, G., and Glasmacher, B. A New Approach for Freezing of Aqueous Solutions under Active Control of the Nucleation Temperature. *Cryobiology*, 53(2):248–257, 2006. doi:10.1016/j.cryobiol.2006.06.005.
- [206] Petrin, A. B. Electric Field Singularity on the Line of Wetting of Dielectric Surface. *High Temperature*, 46(1):19–24, 2008. doi:10.1134/s10740-008-1004-3.
- [207] Phillips, A. J., Childs, D. J., and Schneider, H. M. Aging of Nonceramic Insulators due to Corona from Water Drops. *IEEE Transactions on Power Delivery*, 14(3):1081–1089, 1999. doi:10.1109/61.772357.
- [208] Phillips, A. J., Childs, D. J., and Schneider, H. M. Water Drop Corona Effects on Full-scale 500 kV Non-ceramic Insulators. *IEEE Transactions on Power Delivery*, 14(1):258–265, 1999. doi:10.1109/61.736734.
- [209] Phillips, A. J., Kuffel, J., Baker, A., Burnham, J., Carreira, A., Cherney, E., Chisholm, W., Farzaneh, M., Gemignani, R., Gillespie, A., Grisham, T., Hill, R., Saha, T., Vancia, B., and Yu, J. Electric Fields on AC Composite Transmission Line Insulators. *IEEE Transactions on Power Delivery*, 23(2):823–830, 2008. doi:10.1109/TPWRD.2007.911127.
- [210] Pinnangudi, B., Gorur, R. S., and Kroese, A. J. Quantification of Corona Discharges on Nonceramic Insulators. *IEEE Transac-*

## Bibliography

- tions on Dielectrics and Electrical Insulation*, 12(3):513–523, 2005. doi:10.1109/TDEI.2005.1453456.
- [211] Plog, J., Löwe, J.-M., Jiang, Y., Pan, Y., and Yarin, A. L. Control of Direct Writing of Ink Droplets using Electrowetting. *Langmuir*, 2019. doi:10.1021/acs.langmuir.9b01061.
- [212] Polen, M., Brubaker, T., Somers, J., and Sullivan, R. C. Cleaning up our Water: Reducing Interferences from Nonhomogeneous Freezing of “Pure” Water in Droplet Freezing Assays of Ice-Nucleating Particles. *Atmospheric Measurement Techniques*, 11(9):5315–5334, 2018. doi:10.5194/amt-11-5315-2018.
- [213] Porter, D. A., Easterling, K. E., and Sherif, M. Y. *Phase Transformations in Metals and Alloys*. CRC press, Boca Raton, 3. edition, 2009. ISBN 978-1-4398-8357-0.
- [214] Pruppacher, H. R. The Effect of an External Electric Field on the Supercooling of Water Drops. *Journal of Geophysical Research*, 68(15):4463–4474, 1963. doi:10.1029/JZ068i015p04463.
- [215] Pruppacher, H. R. Electrofreezing of Supercooled Water. *Pure and Applied Geophysics (PAGEOPH)*, 104(1):623–634, 1973. doi:10.1007/BF00875907.
- [216] Pruppacher, H. R. and Klett, J. D. *Microphysics of Clouds and Precipitation*, volume 18. of *Atmospheric and Oceanographic Sciences Library*. Springer Science+Business Media B.V, Dordrecht, 1. edition, 2010. ISBN 978-0-306-48100-0.
- [217] Pruppacher, H. R. and Neiburger, M. The Effect of Water Soluble Substances on the Supercooling of Water Drops. *Journal of the Atmospheric Sciences*, 20(5):376–385, 1963. doi:10.1175/1520-0469(1963)020<0376:TEOWSS>2.0.CO;2.
- [218] Quéré, D. Wetting and Roughness. *Annual Review of Materials Research*, 38(1):71–99, 2008. doi:10.1146/annurev.matsci.38.060407.132434.
- [219] Quilliet, C. and Berge, B. Electrowetting: A Recent Outbreak. *Current Opinion in Colloid & Interface Science*, 6(1):34–39, 2001. doi:10.1016/S1359-0294(00)00085-6.

- [220] Rahmstorf, S. Ocean Circulation and Climate During the Past 120,000 Years. *Nature*, 419(6903):207–214, 2002. doi:10.1038/nature01090.
- [221] Rashid, T., Khawaja, H. A., and Edvardsen, K. Review of Marine Icing and Anti-/De-icing Systems. *Journal of Marine Engineering & Technology*, 15(2):79–87, 2016. doi:10.1080/20464177.2016.1216734.
- [222] Rau, W. Eiskeimbildung durch Dielektrische Polarisaton. *Zeitschrift für Naturforschung A*, 6(11):649–657, 1951. doi:10.1515/zna-1951-1115.
- [223] Rayleigh. On the Equilibrium of Liquid Conducting Masses Charged with Electricity. *Philosophical Magazine Series 5*, 14(87):184–186, 1882. doi:10.1080/14786448208628425.
- [224] Reguera, D. and Rubi, J. M. Homogeneous Nucleation in Inhomogeneous Media. II. Nucleation in a Shear Flow. *The Journal of Chemical Physics*, 119(18):9888–9893, 2003. doi:10.1063/1.1614777.
- [225] Reynders, J. P., Jandrell, I. R., and Reynders, S. M. Review of Aging and Recovery of Silicone Rubber Insulation for Outdoor Use. *IEEE Transactions on Dielectrics and Electrical Insulation*, 6(5): 620–631, 1999. doi:10.1109/94.798119.
- [226] Riechers, B., Wittbracht, F., Hütten, A., and Koop, T. The Homogeneous Ice Nucleation Rate of Water Droplets Produced in a Microfluidic Device and the Role of Temperature Uncertainty. *Physical Chemistry Chemical Physics : PCCP*, 15(16):5873–5887, 2013. doi:10.1039/c3cp42437e.
- [227] Roulleau, M., Evans, L. F., and Fukuta, N. The Electrical Nucleation of Ice in Supercooled Clouds. *Journal of the Atmospheric Sciences*, 28(5):737–740, 1971. doi:10.1175/1520-0469(1971)028<0737:TENOII>2.0.CO;2.
- [228] Rowland, S., Xiong, Y., Robertson, J., and Hoffmann, S. Aging of Silicone Rubber Composite Insulators on 400 kV Transmission Lines. *IEEE Transactions on Dielectrics and Electrical Insulation*, 14(1):130–136, 2007. doi:10.1109/TDEI.2007.302881.
- [229] Rowland, S. M. and Lin, F. C. Stability of Alternating Current Discharges between Water Drops on Insulation Surfaces.

## Bibliography

- Journal of Physics D: Applied Physics*, 39(14):3067–3076, 2006. doi:10.1088/0022-3727/39/14/029.
- [230] Saban, K. V., Thomas, J., Varughese, P. A., and Varghese, G. Thermodynamics of Crystal Nucleation in an External Electric Field. *Crystal Research and Technology*, 37(11):1188–1199, 2002. doi:10.1002/1521-4079(200211)37:11<1188::AID-CRAT1188>3.0.CO;2-5.
- [231] Sakata, S., Hirabayashi, S., and Inuishi, Y. Measurement of Temperature Rise on Insulator Surface Exposed to Partial Discharge. *Electrical Engineering in Japan*, 92(4):1–8, 1972. doi:10.1002/ej.4390920401.
- [232] Salt, R. W. Effect of Electrostatic Field on Freezing of Supercooled Water and Insects. *Science*, 133(3451):458–459, 1961. doi:10.1126/science.133.3451.458.
- [233] Sarang, B., Basappa, P., Lakdawala, V., and Shivaraj, G. Electric Field Computation of Water Droplets on a Model Insulator. In *2011 Electrical Insulation Conference (EIC) (Formerly EIC/EME)*, pages 377–381, 2011. doi:10.1109/EIC.2011.5996182.
- [234] Scholz, H. Entwicklung eines Versuchsaufbaus zur Untersuchung von Ladung auf Regentropfen. Bachelor’s thesis, Technische Universität Darmstadt, Darmstadt, Germany, 2017. (unpublished and not publicly available), Advisor: Jens-Michael Löwe, M.Sc.
- [235] Schremb, M. *Hydrodynamics and Thermodynamics of Ice Accretion through Impact of Supercooled Large Droplets: Experiments, Simulations and Theory*. PhD thesis, Technische Universität, Darmstadt, 2018. URL <http://tuprints.ulb.tu-darmstadt.de/7398/>.
- [236] Schremb, M. and Tropea, C. Solidification of Supercooled Water in the Vicinity of a Solid Wall. *Physical Review E*, 94(5-1):052804, 2016. doi:10.1103/PhysRevE.94.052804.
- [237] Schütte, T. and Hornfeldt, S. Dynamics of Electrically Stressed Water Drops on Insulating Surfaces. In *IEEE International Symposium on Electrical Insulation*, pages 202–207, 3-6 June 1990. doi:10.1109/ELINSL.1990.109741.

- [238] Schwab, A. J. *Field Theory Concepts*. Springer, Berlin, Heidelberg, 1988. ISBN 978-3-642-48943-3.
- [239] Seeley, L. H. and Seidler, G. T. Two-dimensional Nucleation of Ice from Supercooled Water. *Physical Review Letters*, 87(5):055702, 2001. doi:10.1103/physrevlett.87.055702.
- [240] Seeley, L. H., Seidler, G. T., and Dash, J. G. Apparatus for Statistical Studies of Heterogeneous Nucleation. *Review of Scientific Instruments*, 70(9):3664–3667, 1999. doi:10.1063/1.1149975.
- [241] Selvam, A. M., Manohar, G. K., Khemani, L. T., and Murty, B. V. R. Characteristics of Raindrop Charge and Associated Electric Field in Different Types of Rain. *Journal of the Atmospheric Sciences*, 34(11):1791–1796, 1977. doi:10.1175/1520-0469(1977)034<1791:CORCAA>2.0.CO;2.
- [242] Shafiei, M., Ojaghlo, N., Zamfir, S. G., Bratko, D., and Luzar, A. Modulation of Structure and Dynamics of Water under Alternating Electric Field and the Role of Hydrogen Bonding. *Molecular Physics*, 117(22):3282–3296, 2019. doi:10.1080/00268976.2019.1651919.
- [243] Shapiro, B., Moon, H., Garrell, R. L., and Kim, C.-J. C. Equilibrium Behavior of Sessile Drops under Surface Tension, Applied External Fields, and Material Variations. *Journal of Applied Physics*, 93(9): 5794–5811, 2003. doi:10.1063/1.1563828.
- [244] Shaw, R. A., Durant, A. J., and Mi, Y. Heterogeneous Surface Crystallization Observed in Undercooled Water. *The Journal of Physical Chemistry B*, 109(20):9865–9868, 2005. doi:10.1021/jp0506336.
- [245] Singh, A., Orsat, V., and Raghavan, V. A Comprehensive Review on Electrohydrodynamic Drying and High-Voltage Electric Field in the Context of Food and Bioprocessing. *Drying Technology*, 30(16): 1812–1820, 2012. doi:10.1080/07373937.2012.708912.
- [246] Smith, L. G. The Electric Charge of Raindrops. *Quarterly Journal of the Royal Meteorological Society*, 81(347):23–47, 1955. doi:10.1002/qj.49708134705.
- [247] Stan, C. A., Tang, S. K. Y., Bishop, K. J. M., and Whitesides, G. M. Externally Applied Electric Fields up to  $1.6 \times 10^5$  V/m

## Bibliography

- do not Affect the Homogeneous Nucleation of Ice in Supercooled Water. *The Journal of Physical Chemistry. B*, 115(5):1089–1097, 2011. doi:10.1021/jp110437x.
- [248] Stevenin, C., Béreaux, Y., Charneau, J.-Y., and Balcaen, J. Shaping Air Flow Characteristics of a High-Speed Rotary-Bell Sprayer for Automotive Painting Processes. *Journal of Fluids Engineering*, 137(11):111304, 2015. doi:10.1115/1.4030703.
- [249] Storelvmo, T. and Tan, I. The Wegener-Bergeron-Findeisen Process – Its Discovery and Vital Importance for Weather and Climate. *Meteorologische Zeitschrift*, 24(4):455–461, 2015. doi:10.1127/metz/2015/0626.
- [250] Stratton, J. A. *Electromagnetic Theory*. John Wiley & Sons, Inc, Hoboken, 2015. ISBN 9781119134640.
- [251] Sun, W., Xu, X., Sun, W., Ying, L., and Xu, C. Effect of Alternated Electric Field on the Ice Formation During Freezing Process of 0.9%K<sub>2</sub>MnO<sub>4</sub> Water. In *2006 IEEE 8th International Conference on Properties and applications of Dielectric Materials*, pages 774–777. IEEE, 26.06.2006 - 30.06.2006. ISBN 1-4244-0190-9. doi:10.1109/ICPADM.2006.284293.
- [252] Supeene, G., Koch, C. R., and Bhattacharjee, S. Deformation of a Droplet in an Electric Field: Nonlinear Transient Response in Perfect and Leaky Dielectric Media. *Journal of Colloid and Interface Science*, 318(2):463–476, 2008. doi:10.1016/j.jcis.2007.10.022.
- [253] Svishchev and Kusalik. Crystallization of Liquid Water in a Molecular Dynamics Simulation. *Physical Review Letters*, 73(7):975–978, 1994. doi:10.1103/PhysRevLett.73.975.
- [254] Svishchev, I. M. and Kusalik, P. G. Electrofreezing of Liquid Water: A Microscopic Perspective. *Journal of the American Chemical Society*, 118(3):649–654, 1996. doi:10.1021/ja951624l.
- [255] Taborek. Nucleation in Emulsified Supercooled Water. *Physical Review. B, Condensed Matter*, 32(9):5902–5906, 1985. doi:10.1103/PhysRevB.32.5902.
- [256] Takahashi, T. Measurement of Electric Charge of Cloud Droplets, Drizzle, and Raindrops. *Reviews of Geophysics*, 11(4):903, 1973. doi:10.1029/RG011i004p00903.

- [257] Tanaka, M. and Sato, M. Microwave Heating of Water, Ice, and Saline Solution: Molecular Dynamics Study. *The Journal of Chemical Physics*, 126(3):034509, 2007. doi:10.1063/1.2403870.
- [258] Tarn, M. D., Sikora, S. N. F., Porter, G. C. E., O’Sullivan, D., Adams, M., Whale, T. F., Harrison, A. D., Vergara-Temprado, J., Wilson, T. W., Shim, J.-u., and Murray, B. J. The Study of Atmospheric Ice-Nucleating Particles via Microfluidically Generated Droplets. *Microfluidics and Nanofluidics*, 22(5):19163, 2018. doi:10.1007/s10404-018-2069-x.
- [259] Taylor, G. Disintegration of Water Drops in an Electric Field. *Proceedings of the Royal Society A: Mathematical, Physical and Engineering Sciences*, 280(1382):383–397, 1964. doi:10.1098/rspa.1964.0151.
- [260] Taylor, G. Studies in Electrohydrodynamics. I. The Circulation Produced in a Drop by Electrical Field. *Proceedings of the Royal Society A: Mathematical, Physical and Engineering Sciences*, 291(1425):159–166, 1966. doi:10.1098/rspa.1966.0086.
- [261] Taylor, G. Electrically Driven Jets. *Proceedings of the Royal Society A: Mathematical, Physical and Engineering Sciences*, 313(1515):453–475, 1969. doi:10.1098/rspa.1969.0205.
- [262] Teng, P., Tian, D., Fu, H., and Wang, S. Recent Progress of Electrowetting for Droplet Manipulation: From Wetting to Superwetting Systems. *Materials Chemistry Frontiers*, 4(1):140–154, 2020. doi:10.1039/C9QM00458K.
- [263] Tropea, C., Yarin, A., and Foss, J. F., editors. *Springer Handbook of Experimental Fluid Mechanics*. Springer, Berlin u.a., 2007. ISBN 978-3-662-49162-1.
- [264] Turnbull, D. and Fisher, J. C. Rate of Nucleation in Condensed Systems. *The Journal of Chemical Physics*, 17(1):71–73, 1949. doi:10.1063/1.1747055.
- [265] Vali, G. Repeatability and Randomness in Heterogeneous Freezing Nucleation. *Atmospheric Chemistry and Physics*, 8(16):5017–5031, 2008. doi:10.5194/acp-8-5017-2008.

## Bibliography

- [266] Vali, G. Interpretation of Freezing Nucleation Experiments: Singular and Stochastic; Sites and Surfaces. *Atmospheric Chemistry and Physics*, 14(11):5271–5294, 2014. doi:10.5194/acp-14-5271-2014.
- [267] Vali, G. Revisiting the Differential Freezing Nucleus Spectra Derived from Drop-freezing Experiments: Methods of Calculation, Applications, and Confidence Limits. *Atmospheric Measurement Techniques*, 12(2):1219–1231, 2019. doi:10.5194/amt-12-1219-2019.
- [268] Vali, G. and Stansbury, E. J. Time-Dependent Characteristics of the Heterogeneous Nucleation of Ice. *Canadian Journal of Physics*, 44(3):477–502, 1966. doi:10.1139/p66-044.
- [269] Vali, G., DeMott, P. J., Möhler, O., and Whale, T. F. Technical Note: A proposal for Ice Nucleation Terminology. *Atmospheric Chemistry and Physics*, 15(18):10263–10270, 2015. doi:10.5194/acp-15-10263-2015.
- [270] Vallet, M., Vallade, M., and Berge, B. Limiting Phenomena for the Spreading of Water on Polymer Films by Electrowetting. *The European Physical Journal B*, 11(4):583–591, 1999. doi:10.1007/s100510051186.
- [271] Venkatesulu, B. and Thomas, M. J. Long-term Accelerated Weathering of Outdoor Silicone Rubber Insulators. *IEEE Transactions on Dielectrics and Electrical Insulation*, 18(2):418–424, 2011. doi:10.1109/TDEI.2011.5739445.
- [272] Volmer, M. and Weber, t. Keimbildung in übersättigten Gebilden. *Zeitschrift für physikalische Chemie (Frankfurt am Main, Germany)*, 119U(1), 1926. doi:10.1515/zpch-1926-11927.
- [273] Wang, J., Wu, Y., Cao, Y., Li, G., and Liao, Y. Influence of Surface Roughness on Contact Angle Hysteresis and Spreading Work. *Colloid and Polymer Science*, 298(8):1107–1112, 2020. doi:10.1007/s00396-020-04680-x.
- [274] Wang, L., Kong, W., Wang, F., and Liu, H. Temperature-Gradient Effects on Heterogeneous Ice Nucleation from Supercooled Water. *AIP Advances*, 9(12):125122, 2019. doi:10.1063/1.5133459.
- [275] Wang, L. K., Shammass, N. K., Selke, W. A., and Aulenbach, D. B. *Flotation Technology*. Humana Press, Totowa, 2010. ISBN 978-1-58829-494-4.

- [276] Wang, S. and Jiang, L. Definition of Superhydrophobic States. *Advanced Materials*, 19(21):3423–3424, 2007. doi:10.1002/adma.200700934.
- [277] Wei, S., Xiaobin, X., Hong, Z., and Chuanxiang, X. Effects of Dipole Polarization of Water Molecules on Ice Formation under an Electrostatic Field. *Cryobiology*, 56(1):93–99, 2008. doi:10.1016/j.cryobiol.2007.10.173.
- [278] Whale, T. F., Murray, B. J., O’Sullivan, D., Wilson, T. W., Umo, N. S., Baustian, K. J., Atkinson, J. D., Workneh, D. A., and Morris, G. J. A Technique for Quantifying Heterogeneous Ice Nucleation in Microlitre Supercooled Water Droplets. *Atmospheric Measurement Techniques*, 8(6):2437–2447, 2015. doi:10.5194/amt-8-2437-2015.
- [279] Wilson, P. W., Osterday, K., and Haymet, A. D. J. The Effects of Electric Field on Ice Nucleation may be Masked by the Inherent Stochastic Nature of Nucleation. *Cryo Letters*, 30(2):96–99, 2009.
- [280] Wood, S. E., Baker, M. B., and Swanson, B. D. Instrument for Studies of Homogeneous and Heterogeneous Ice Nucleation in Free-falling Supercooled Water Droplets. *Review of Scientific Instruments*, 73(11):3988–3996, 2002. doi:10.1063/1.1511796.
- [281] Wu, H., Dey, R., Siretanu, I., van den Ende, D., Shui, L., Zhou, G., and Mugele, F. Electrically Controlled Localized Charge Trapping at Amorphous Fluoropolymer-Electrolyte Interfaces. *Small*, 16(2):e1905726, 2020. doi:10.1002/smll.201905726.
- [282] Wu, Y. and Clark, R. L. Electrohydrodynamic Atomization: A Versatile Process for Preparing Materials for Biomedical Applications. *Journal of Biomaterials Science. Polymer Edition*, 19(5):573–601, 2008. doi:10.1163/156856208784089616.
- [283] Xanthakis, E., Havet, M., Chevallier, S., Abadie, J., and Le-Bail, A. Effect of Static Electric Field on Ice Crystal Size Reduction During Freezing of Pork Meat. *Innovative Food Science & Emerging Technologies*, 20:115–120, 2013. doi:10.1016/j.ifset.2013.06.011.
- [284] Xie, G., He, F., Liu, X., Si, L., and Guo, D. Sessile Multidroplets and Salt Droplets under High Tangential Electric Fields. *Scientific Reports*, 6:25002, 2016. doi:10.1038/srep25002.

## Bibliography

- [285] Xie, J., Jiang, J., Davoodi, P., Srinivasan, M. P., and Wang, C.-H. Electrohydrodynamic Atomization: A Two-decade Effort to Produce and Process Micro-/Nanoparticulate Materials. *Chemical Engineering Science*, 125:32–57, 2015. doi:10.1016/j.ces.2014.08.061.
- [286] Yahong, M., Lisheng, Z., Huiyu, H., Qinxue, Y., and Yewen, Z. A Micro Electro-freezing Chip Used in the Crystallization of Aqueous Solutions under AC Electric Field. In *ICPADM 2012*, pages 1–4, [Piscataway, N.J.], 2012. IEEE. ISBN 978-1-4673-2851-7. doi:10.1109/ICPADM.2012.6319024.
- [287] Yan, J. Y. and Patey, G. N. Heterogeneous Ice Nucleation Induced by Electric Fields. *The Journal of Physical Chemistry Letters*, 2(20):2555–2559, 2011. doi:10.1021/jz201113m.
- [288] Yan, J. Y. and Patey, G. N. Molecular Dynamics Simulations of Ice Nucleation by Electric Fields. *The Journal of Physical Chemistry, A*, 116(26):7057–7064, 2012. doi:10.1021/jp3039187.
- [289] Yan, J. Y., Overduin, S. D., and Patey, G. N. Understanding Electrofreezing in Water Simulations. *The Journal of Chemical Physics*, 141(7):074501, 2014. doi:10.1063/1.4892586.
- [290] Yang, F., Shaw, R. A., Gurganus, C. W., Chong, S. K., and Yap, Y. K. Ice Nucleation at the Contact Line Triggered by Transient Electrowetting Fields. *Applied Physics Letters*, 107(26):264101, 2015. doi:10.1063/1.4938749.
- [291] Young, T. An Essay on the Cohesion of Fluids. *Philosophical Transactions of the Royal Society of London*, 95(0):65–87, 1805. doi:10.1098/rstl.1805.0005.
- [292] Zajonz, F. Untersuchung des Einflusses von Ladung auf das Verhalten von Wassertropfen in elektrischen Wechselfeldern. Master’s thesis, Technische Universität Darmstadt, Darmstadt, Germany, 2018. (unpublished and not publicly available), Advisor: Jens-Michael Löwe, M.Sc.
- [293] Zangi, R. and Mark, A. E. Electrofreezing of Confined Water. *The Journal of Chemical Physics*, 120(15):7123–7130, 2004. doi:10.1063/1.1687315.

- [294] Zhang, X., Liu, X., Wu, X., and Min, J. Experimental Investigation and Statistical Analysis of Icing Nucleation Characteristics of Sessile Water Droplets. *Experimental Thermal and Fluid Science*, 99:26–34, 2018. doi:10.1016/j.expthermflusci.2018.07.027.
- [295] Zhu, Y., Haji, K., Otsubo, M., and Honda, C. Surface Degradation of Silicone Rubber Exposed to Corona Discharge. *IEEE Transactions on Plasma Science*, 34(4):1094–1098, 2006. doi:10.1109/TPS.2006.876498.
- [296] Zobrist, B., Koop, T., Luo, B. P., Marcolli, C., and Peter, T. Heterogeneous Ice Nucleation Rate Coefficient of Water Droplets Coated by a Nonadecanol Monolayer. *The Journal of Physical Chemistry C*, 111(5):2149–2155, 2007. doi:10.1021/jp066080w.
- [297] Zöllner, D. Untersuchung des Nukleationsverhaltens unterkühlter Wassertropfen in hohen elektrischen Feldern. Bachelor’s thesis, Technische Universität Darmstadt, Darmstadt, Germany, 2019. (unpublished and not publicly available), Advisor: Jens-Michael Löwe, M.Sc.
- [298] Zou, H., Zhang, Y., Guo, L., Wang, P., He, X., Dai, G., Zheng, H., Chen, C., Wang, A. C., Xu, C., and Wang, Z. L. Quantifying the Triboelectric Series. *Nature Communications*, 10(1):1427, 2019. doi:10.1038/s41467-019-09461-x.



# Own publications

## Peer-reviewed publications

- Jens-Michael Löwe, Volker Hinrichsen, Markus Schreimb, and Cameron Tropea. Ice nucleation forced by transient electric fields. *Physical Review E*, 104(6):064801, 2021.
- Jens-Michael Löwe, Volker Hinrichsen, Markus Schreimb, and Cameron Tropea. Ice Nucleation in High Alternating Electric Fields: Effect of Electric Field Strength and Frequency. *Physical Review E*, 103(1):012801, 2021.
- Jens-Michael Löwe, Markus Schreimb, Volker Hinrichsen, and Cameron Tropea. Experimental Methodology and Procedure for SAPPHIRE: a Semi-automatic APParatus for High-voltage Ice nucleation REsearch. *Atmospheric Measurement Techniques*, 14(1):223–238, 2021.
- Jens-Michael Löwe, Volker Hinrichsen, Ilia V. Roisman, and Cameron Tropea. Impact of Electric Charge and Motion of Water Drops on the Inception Field Strength of Partial Discharges. *Physical Review E*, 102(6):063101, 2020.
- Jens-Michael Löwe, Jan Engelhardt, Maximilian Secklehner, and Volker Hinrichsen. Determination of the Spatial Impulse Response of Compensating Electrostatic Voltmeters. *IEEE Transactions on Dielectrics and Electrical Insulation*, 27(1):49–57, 2020.
- Jens-Michael Löwe, Volker Hinrichsen, Ilia V. Roisman, and Cameron Tropea. Behavior of Charged and Uncharged Drops in High Alternating Tangential Electric Fields. *Physical Review E*, 101(2):023102, 2020.
- Jens-Michael Löwe, Jevon Plog, Yizhou Jiang, Yayue Pan, and Alexander L. Yarin. Drop Deposition Affected by Electrowetting in Direct Ink Writing Process. *Journal of Applied Physics*, 126(3):035302, 2019.
- Jevon Plog, Jens-Michael Löwe, Yizhou Jiang, Yayue Pan, and Alexander L. Yarin. Control of Direct Writing of Ink Droplets using Electrowetting. *Langmuir*, 2019.

## Conference publications

- Jens-Michael Löwe and Volker Hinrichsen. Experimental Investigation of the Influence of Electric Charge on the Behavior of Water Droplets in Electric Fields. In *2019 IEEE 20th International Conference on Dielectric Liquids (ICDL)*, pages 1–6. IEEE, 2019.
- Jens-Michael Löwe, Markus Schremb, Volker Hinrichsen, and Cameron Tropea. Ice Nucleation in the Presence of Electric Fields: An Experimental Study. SAE Technical Paper Series. SAE International400 Commonwealth Drive, Warrendale, PA, United States, 2019.
- Jens-Michael Löwe, Volker Hinrichsen, and Cameron Tropea. Droplet Behavior Under the Impact of Lightning and Switching Impulse Voltage. In *2018 IEEE Electrical Insulation Conference (EIC)*, pages 443–447. IEEE, 2018.
- Jens-Michael Löwe, Volker Hinrichsen, Markus Schremb, Tim Dorau, and Cameron Tropea. Experimental Investigation of Electro-freezing of Supercooled Droplets. In *9th World Conference on Experimental Heat Transfer, Fluid Mechanics and Thermodynamics*, Foz do Iguacu, Brasilien, 2017.
- Jens-Michael Löwe, Maximilian Secklehner, and Volker Hinrichsen. Investigation of Surface Charges on Polymeric Insulators and the Influence of Sessile Water Droplets. In *2017 INSUCON - 13th International Electrical Insulation Conference (INSUCON)*, pages 1–7. IEEE, 2017.
- Jens Löwe, Daniel Kintea, Arne Baumert, Stephan Bansmer, Ilia V. Roisman, and Cameron Tropea. Inception of Ice Accretion by Ice Crystal Impact. volume 745, page 032013, 2016.
- Jens-Michael Löwe and Ilia V. Roisman. Bubble formation under constant flow rate. In *ICLASS 2015, 13th Triennial International Conference on Liquid Atomization and Spray Systems*, 2015.

# Supervised theses

- Johannes Franz Alois Hollerith. Optimierung eines Versuchsaufbaus zur Untersuchung von Ladung auf Regentropfen. Bachelor's thesis, Technische Universität Darmstadt, Darmstadt, Germany, 2019. (unpublished and not publicly available), Advisor: Jens-Michael Löwe, M.Sc.
- David Zöller. Untersuchung des Nukleationsverhaltens unterkühlter Wassertropfen in hohen elektrischen Feldern. Bachelor's thesis, Technische Universität Darmstadt, Darmstadt, Germany, 2019. (unpublished and not publicly available), Advisor: Jens-Michael Löwe, M.Sc.
- Marvin Dietzmann-Kolbe. Untersuchung des Verhaltens von aufsitzenden Wassertropfen unter Stoßspannungsbeanspruchung. Master's thesis, Technische Universität Darmstadt, Darmstadt, Germany, 2018. (unpublished and not publicly available), Advisor: Jens-Michael Löwe, M.Sc.
- Franziska Zajonz. Untersuchung des Einflusses von Ladung auf das Verhalten von Wassertropfen in elektrischen Wechselfeldern. Master's thesis, Technische Universität Darmstadt, Darmstadt, Germany, 2018. (unpublished and not publicly available), Advisor: Jens-Michael Löwe, M.Sc.
- Duygu Cicekdagli. Verifizierung/Validierung und Optimierung eines Versuchsaufbaus zum definierten Laden von Tropfen. Studienarbeit, Technische Universität Darmstadt, Darmstadt, Germany, 2017. (unpublished and not publicly available), Advisor: Jens-Michael Löwe, M.Sc.
- Jan Engelhardt. Entwicklung eines Versuchsstandes zur automatisierten Messung von Oberflächenpotentialen auf isolierenden Oberflächen. Master's thesis, Technische Universität Darmstadt, Darmstadt, Germany, 2017. (unpublished and not publicly available), Advisor: Jens-Michael Löwe, M.Sc.
- Henrik Scholz. Entwicklung eines Versuchsaufbaus zur Untersuchung von Ladung auf Regentropfen. Bachelor's thesis, Technische Universität Darmstadt, Darmstadt, Germany, 2017. (unpublished and not publicly available), Advisor: Jens-Michael Löwe, M.Sc.
- Tim Dorau, Moritz Hülsebrock, Patrick Weis, and Julia Wenzel. Konstruktion eines Aufbaus zur experimentellen Untersuchung des Nuk-

## *Bibliography*

leationsverhaltens unterkühlter Wassertropfen im elektrischen Feld. Advanced Design Project (ADP), Technische Universität Darmstadt, Darmstadt, Germany, 2017. (unpublished and not publicly available), Advisor: Jens-Michael Löwe, M.Sc. and Dr.-Ing. Markus Schreimb.